
The Terminator Region of Tidally Locked M-dwarf Exoplanets in 3-D General Circulation Models

---

Maureen J. Cohen

Doctor of Philosophy

THE UNIVERSITY OF EDINBURGH

2023

To my dearly departed cat,

Lucy

Abstract

The impressive sensitivity of the James Webb Space Telescope has made it possible to study the atmospheres of planets beyond the solar system. It will soon be followed by space missions aiming specifically at this goal, such as the Ariel mission, Twinkle, and the Habitable Worlds Observatory. One category of exoplanet has drawn interest because of its potential to harbour temperate climates with liquid surface water—and therefore potentially life. These are rocky planets orbiting cool M-class stars, or "M-Earths." Stellar population trends and observing biases lead to a high proportion of potentially habitable, terrestrial planets falling into this category. Because of the low temperatures of their host stars, however, habitable worlds of this type are found in close orbits where they are likely to be tidally locked. As the solar system has no tidally locked planets, our knowledge of their atmospheric circulation is currently limited to theoretical modelling.

Past modelling work has shown that the asymmetrical irradiation of tidally locked planets results in characteristic circulation regimes which have profound consequences for observations. Atmospheric retrievals, which use statistical methods to fit 1-D atmospheric models to observational data and quantify the confidence of the fit, are not yet able to account for the 3-D nature of this circulation. For planets with large spatial variation in environmental conditions caused by tidal locking, 1-D models are not able to capture the differences and interconnections between planetary regions such as the dayside, nightside, and planetary limb or terminator. In addition, planetary atmospheres exhibit variation over time, potentially resulting in differences in retrieved properties between observing visits or even between different phases of a planet's orbit. Accounting for 4-D circulation effects in atmospheric retrievals first requires a theoretical understanding of the impact of global-scale phenomena such as atmospheric waves and horizontal transport on conditions at the planetary limb, and then requires incorporation of this knowledge into the retrieval pipeline in the form of, for example, parameterisations.

In this thesis, I address the first requirement: the theoretical understanding of the effects of fully modelled 4-D atmospheric circulation on the planetary limb, the region probed by transmission spectroscopy, on tidally locked planets. I focus in particular on effects caused by the global propagation of atmospheric waves and by horizontal transport of clouds and hazes.

In Chapter 2, I show that that the atmospheric dynamics on the tidally locked Proxima Centauri b support a longitudinally asymmetric stratospheric wind oscillation (LASO), analogous to Earth's quasi-biennial oscillation (QBO). The LASO has a vertical extent of 35–55 km, a period of 5–6.5 months, and a peak-to-peak wind speed amplitude of -70 to +130 ms^{-1} with a maximum at an altitude of 41 km. Unlike the QBO, the LASO displays longitudinal

asymmetries related to the asymmetric thermal forcing of the planet and to interactions with the resulting stationary Rossby waves. The equatorial gravity wave sources driving the LASO are localised in the deep convection region at the substellar point and in a jet exit region near the western terminator, unlike the QBO, for which these sources are distributed uniformly around the planet. Longitudinally, the western terminator experiences the highest wind speeds and undergoes reversals earlier than other longitudes. The antistellar point only experiences a weak oscillation with a very brief, low-speed westward phase. The QBO on Earth is associated with fluctuations in the abundances of water vapour and trace gases such as ozone which are also likely to occur on exoplanets if these gases are present. Strong fluctuations in temperature and the abundance of atmospheric species at the terminators will need to be considered when interpreting atmospheric observations of tidally locked exoplanets.

In Chapter 3, I investigate the presence of cloud cover at the planetary limb of water-rich Earth-like planets, which is likely to weaken chemical signatures in transmission spectra and impede attempts to characterise these atmospheres. Based on observations of Earth and solar system worlds, exoplanets with atmospheres should have both short-term weather and long-term climate variability, implying that cloud cover may be less during some observing periods. I identify and describe a mechanism driving periodic clear sky events at the terminators in simulations of tidally locked Earth-like planets. A feedback between dayside cloud radiative effects, incoming stellar radiation and heating, and the dynamical state of the atmosphere, especially the zonal wavenumber-1 Rossby wave identified in past work on tidally locked planets, leads to oscillations in Rossby wave phase speeds and in the position of Rossby gyres and results in advection of clouds to or away from the planet's eastern terminator. I study this oscillation in simulations of Proxima Centauri b, TRAPPIST 1-e, and rapidly rotating versions of these worlds located at the inner edge of their stars' habitable zones. I simulate time series of the transit depths of the 1.4 μm water feature and 2.7 μm carbon dioxide feature. The impact of atmospheric variability on the transmission spectra is sensitive to the structure of the dayside cloud cover and the location of the Rossby gyres, but none of my simulations have variability significant enough to be detectable with current methods.

In Chapter 4, I study the interaction between the atmospheric circulation and photochemical hazes and describe the resulting haze abundances at the terminator. Transmission spectroscopy supports the presence of unknown, light-scattering aerosols in the atmospheres of many exoplanets. The complexity of factors influencing the formation, 3-D transport, radiative impact, and removal of aerosols makes it challenging to match theoretical models to the existing data. My study simplifies these factors to focus on the interaction between planetary general circulation and haze distribution at the planetary limb. I use an intermediate complexity general circulation model, ExoPlaSim, to simulate idealised organic haze particles as radiatively active tracers in the atmospheres of tidally locked terrestrial planets for a range of rotation rates. I find three distinct 3-D spatial haze distributions, corresponding to three

circulation regimes, each with a different haze profile at the limb. All regimes display significant terminator asymmetry. In my parameter space, super-Earth-sized planets with rotation periods greater than 13 days have the lowest haze optical depths at the terminator, supporting the choice of slower rotators as observing targets.

My thesis supports the existence of characteristic forms of temporal and spatial variability on tidally locked planets which will undoubtedly impact observations and inform our understanding of climate conditions on the surface. Overall, the effects of purely dynamical variability may be too small to be detected for Earth-like planets (but potentially detectable for larger ones). The impact of the atmospheric circulation on the distribution of clouds and hazes, on the other hand, is likely to affect even observations of terrestrial planets due to the highly scattering nature of these aerosols and will need to be accounted for in atmospheric retrievals.

Lay Summary

Powerful new telescopes and sophisticated data processing techniques have made it possible to study the atmospheres of planets outside our solar system (“exoplanets”). The emerging field of exoplanet science will continue to grow rapidly in the coming decades, with observations coming in from the James Webb Space Telescope and the commissioning of further missions such as the Extremely Large Telescope, ARIEL (Atmospheric Remote-sensing Infrared Exoplanet Large-survey), and eventually the Habitable Worlds Observatory. Observing exoplanets will give us context for the history and evolution of the Earth and the solar system —and, of course, help us in the search for life on other worlds.

Some of the best candidates for planets that could support life are rocky worlds orbiting cool red dwarf stars. These stars make up the majority of the stellar population of the galaxy because they have long lifetimes, allowing them to outlast their larger and hotter burning neighbours. Many of them also host rocky planets. Because these stars are so cool, any planets that are around the right temperature to host life —the temperature range within which liquid water can exist on the planet’s surface – are found orbiting close to the star, so close that the gravitational pull of the star eventually slows the planet’s rotation until its day is the same length as its year. As a result, these close-in rocky worlds always present the same face to the star: they have a permanent day side, a permanent night side, and a permanent zone of twilight between the two, known as the terminator. This state is known as a tidally locked orbit.

Whether or not planets in this type of orbit can maintain atmospheres or a habitable region on their surfaces is the subject of many theoretical studies. Yet tidally locked planets pose additional challenges before the question of habitability is even broached. Their atmospheres can be observed when the planet eclipses the host star, whose light is filtered through the planetary atmosphere on its way to Earth. This type of observation thus captures light that has passed through the ring of atmosphere around the planet’s silhouette: the region of the terminator, the dividing line between day and night. Telescopes are observing a special part of the planet whose climate and atmospheric physics are known only from theoretical modelling, as our own solar system has no examples we could turn to as analogues.

To understand how tidally locked planets may appear in telescope observations, scientists use three-dimensional global models of the atmosphere and climate. In this thesis, I use two such models to study the terminator region of tidally locked planets, and specifically how phenomena that can only be represented in a full 3-D global climate model could affect the climate at the terminator and our observations.

In my first research chapter, I describe how winds in the upper atmosphere of my model periodically change direction, from eastward-flowing to westward-flowing, and how the amount of water vapour in the upper atmosphere of the terminator varies on the same timescale. This periodic variation in wind and water vapour is analogous to phenomena seen on Earth, Jupiter, and Saturn, and occurs when atmospheric waves transport momentum to the upper atmosphere and deposit it at different locations, causing winds at different levels to accelerate in opposite directions. Although the variations are too small for present telescopes to observe for Earth-like planets, the physical mechanism and the resulting oscillation could be present and observable on many types of larger planets.

In my second research chapter, I study another climate oscillation specific to tidally locked Earth-like planets, in which global-scale atmospheric waves shift gigantic vortices eastward and westward, sometimes carrying clouds towards the terminator and sometimes away from it. The presence of clouds inhibits observations, so if such an oscillation were to occur on a real planet, there might be better or worse days for observing, as there are for observation of Earth from space based on the daily weather. My study finds the cause of the oscillation in a complex feedback loop between clouds, heat, wind, and atmospheric waves not present on Earth or other known planets. The periodic variation in cloud cover at the terminator has a consistent effect on how difficult it is to observe water vapour there, but the difference does not appear to be large enough to be significant.

In the final research chapter, I use a simpler and faster climate model to simulate how the 3-D wind structure of planets with 32 different rotation rates results in a predictable 3-D distribution of photochemical haze, another atmospheric component that inhibits observations. The simulations fall into four distinct types, each with its own pattern of winds and haze. The outcome is that planets with rotation periods that fall into certain ranges may have less haze and atmospheres that are easier to observe. In particular, I find that slower rotation periods result in less hazy terminators and that there is an unusual “valley” at periods of around 2 or 3 days for which the simulations predict comparatively clear atmospheres.

My thesis demonstrates the importance of two three-dimensional phenomena that significantly affect the terminator on tidally locked planets: atmospheric waves and horizontal transport of these waves, as well as of clouds and photochemical hazes, by the global winds. These factors cannot be represented in the fast one-dimensional atmospheric models used to compare to observational data, but are too significant to be ignored. Future work should look at incorporating the insights from theoretical studies like those in this thesis into interpretations of telescope data. In the meantime, the results can already inform qualitative understandings of observations and potentially the choice of observing targets.

Acknowledgements

I would like to thank my supervisors, Dr Massimo Bollasina and Prof. Paul Palmer, for their guidance, advice, feedback, and support throughout my PhD process.

I also thank the members of the Exeter Exoplanet Theory Group for their invaluable technical assistance and advice.

I am grateful to Ilka Cohen and Charlotta A. Roberts for proofreading the text and for their encouragement.

Finally, I would like to thank Dr Weiping Lu for taking the time to teach a beginner how to do a research project.

This research was funded by the Natural Environment Research Council under grant number NE/S007407/1 and supported by the Edinburgh Earth, Ecology, and Environmental Doctoral Training Partnership.

Declaration

I declare that this thesis was composed by myself, that the work contained herein is my own except where explicitly stated otherwise in the text, and that this work has not been submitted for any other degree or professional qualification except as specified.

Maureen J. Cohen

Contents

Appendices

Figures and Tables

Figures

Tables

Chapter 1

Introduction

1.1 Exploring tidally locked exoplanets

Exoplanets are planets orbiting stars other than the Sun. In a foretaste of the diversity and exoticism of planetary discoveries to come, the first confirmed exoplanet was detected in 1992 around a pulsar (Wolszczan & Frail, 1992). Since then, exoplanet science has continued to challenge existing theories of planetary formation, possible planetary system architectures, and habitability.

What does it mean for a planet to be habitable? J. F. Kasting, Whitmire, and Reynolds (1993) established a widely used definition of the "circumstellar habitable zone". The habitable zone refers to the range of distances from a star at which a planet is temperate enough to support liquid water on its surface. The inner edge of the habitable zone is the orbital distance at which all a planet's water would exist in vapour form, and water photolysis and hydrogen escape would cause gradual water loss. The outer edge of the habitable zone is the condensation line for CO_2 (J. F. Kasting et al., 1993). A "habitable" planet does not necessarily harbour life, only liquid water. This definition does not account for forms of life that might not require water as a solvent, but it is a reasonable starting point in the search for habitable worlds.

We are interested in habitable exoplanets for several reasons. One is the search for Earth-like life—life we can recognise by analogy to that on our own planet. The search for chemical signatures of life on other planets, or "biosignatures," makes up a respectable portion of exoplanet literature (see Schwieterman et al. (2018) for a review). A second is comparative climatology: exoplanets can show us what the Earth may have been like in earlier periods of its history, when it may have been covered by photochemical haze (G. Arney et al., 2016; G. N. Arney et al., 2017; Trainer et al., 2004) or in a snowball state (Lucarini, Pascale, Boschi, Kirk, & Iro, 2013; Wordsworth, 2021), as well as how our climate might develop in the future (Popp, Schmidt, & Marotzke, 2016; Rushby, Johnson, Mills, Watson, & Claire, 2018). From a methodological perspective, adapting Earth system models for exoplanets allows us to test how these models perform when basic assumptions like the stellar spectrum or planetary rotation period are varied and deepen our theoretical understanding of habitability (Abbot et al., 2018; Hochman, Luca, & Komacek, 2022; Leconte, Forget, Charnay, Wordsworth,

& Pottier, 2013; Wordsworth, 2021). For example, simulations of the water cycle on tidally locked habitable planets have paralleled the intensification of precipitation patterns caused by anthropogenic climate change, motivating the search for underlying physical mechanisms (Labonté & Merlis, 2020; Seeley & Wordsworth, 2021). Finally, understanding the formation, development, prevalence, and characteristics of Earth-like planets is intrinsically useful to astronomers and astrophysicists seeking to understand topics like circumstellar disc evolution and the history of the solar system.

Early exoplanet catalogues were dominated by "hot Jupiters," "very hot Jupiters," and a few "ultra-short-period hot Jupiters" (Perryman, 2018). These terms describe gas giants roughly the size of Jupiter that orbit very close to their host star and, as a result, are strongly irradiated. Hot Jupiters overturned expectations in the astronomical community because theories of protoplanetary disc evolution and planet formation predicted that gas giants should form further from the star. According to this line of thought, more elements can condense into liquid or solid phases further from the star where temperatures are lower, providing more material for accretion of a planetary core, which can then capture hydrogen and helium from the disc due to its large mass and gravity. A leading theory for the existence of hot Jupiters is that these planets originally form far from the star and migrate inward over time through a variety of potential mechanisms. Their large mass and proximity to their host star made them the first to be detected due to their strong gravitational pull on the star. The star and planet orbit a common centre of gravity, causing the star to move slightly backward and forward in the line of sight from Earth and resulting in a Doppler shift of the stellar spectrum. Newer detection methods, however, have expanded the exoplanet bestiary far beyond planets of this size. Figure 1.1 lists the terms commonly used to classify exoplanets by size, with examples from the Solar System where available.

Earth-sized planets (0.1 to 2 Earth masses) and "Super-Earths" (2 to 10 Earth masses, the most common sub-type) now make up a substantial enough portion of known exoplanets to allow for prevalence estimates. Catanzarite and Shao (2011) calculated that $1-3\%$ of Sun-like stars have Earth-analogue planets, while Petigura, Howard, and Marcy (2013) put the figure at 22%. Kunimoto and Matthews (2020) used data from NASA's *Kepler* mission to estimate that F-, G-, and K-type stars have an average of 0.18 potentially habitable, terrestrial planets per star.

Impressive as these figures for Sun-like stars are, the expected prevalence of Earth-like planets around the far more abundant M-class stars ("M-dwarfs" or "red dwarfs") is even higher. In a search for terrestrial planets in the habitable zones of M-class stars, R. K. Kopparapu (2013) estimated 0.48 to 0.53 such planets per star based on *Kepler* data, depending on the definition of the habitable zone. Bonfils et al. (2013) came to a similar figure of 0.41 planets per star using the European Southern Observatory *HARPS* spectrograph. An analysis by

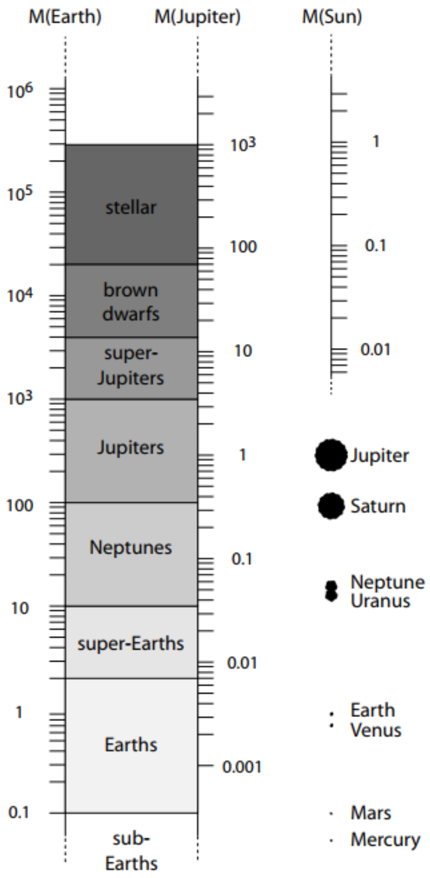

Figure 1.1: Types of exoplanets by size in masses (Perryman, 2018)

Dressing and Charbonneau (2015) found 0.24 Earth-sized planets and 0.21 super-Earths per M-dwarf. Hardegree-Ullman, Cushing, Muirhead, and Christiansen (2019) found a value of 1.19 planets per mid-M-class star based on data from *Kepler*. J.-Y. Yang, Xie, and Zhou (2020) estimated 2.8 planets per star in the M, K, G, and F classes.

Given that M-dwarf stars make up about $70-75\%$ (Heath, Doyle, Joshi, & Haberle, 1999; Henry et al., 2006) of the stellar population, these high prevalences indicate that a large percentage of habitable Earth-like planets may be found in the habitable zones of M-dwarfs (Heath et al., 1999; Scalo et al., 2007; Tarter et al., 2007; Wandel, 2018). As a result, M-class stars have become prime observational targets in the search for Earth-like and habitable exoplanets.

One reason even small rocky planets are comparatively easy to observe around M stars is their closer orbits and larger sizes relative to the host star (Catling & Kasting, 2017). These two characteristics make them amenable to detection by the transit method (see Section 1.2 for a description). In addition, closely orbiting stars will take less time to complete an orbit, passing in front of the star more often in a given observing period and allowing more data to be gathered (Catling & Kasting, 2017). Transit surveys—past, present, and future—yield a continuous stream of rocky planet detections around M-class stars from missions such as TESS (Barclay, Pepper, & Quintana, 2018), SPECULOOS (Sebastian et al., 2020), and Kepler (Feliz et al., 2021).

M-class stars differ from our G-class Sun in ways that will affect the climate of their planets. M-dwarfs are often highly active, especially when younger, with flares that may cause atmosphere stripping in the absence of a protective planetary magnetic field due to the impact of high-energy radiation and charged particles (Guenther et al., 2020; Tilley, Segura, Meadows, Hawley, & Davenport, 2018; Vida et al., 2019). High amounts of extreme ultraviolet and X-ray radiation during the hot early phase of the star may also cause a runaway greenhouse effect and loss of water to space (Turbet & Selsis, 2021). During their stable main sequence lifetime, these stars also emit a greater proportion of their radiation in redder parts of the spectrum. Eager-Nash et al. (2020) found that atmospheres with an Earth-like composition absorb more energy at these wavelengths, leading to a warmer planet than for a G-star. Turbet and Selsis (2021) examined in detail the impact stellar flux and its variations can have on the climate of an orbiting planet. They agree that lower-temperature stars like M-dwarfs warm Earth-like planets more efficiently because of greater absorption of longer wavelengths of light by the atmosphere, less Rayleigh scattering, and lower ice and snow surface albedo at longer wavelengths, somewhat compensating for the lack of stellar energy.

Perhaps most importantly, because M-dwarfs are so much cooler than Sun-like G-class stars, their habitable zones are far closer to the star, and any planets orbiting within the habitable zone are likely to be either in some form of synchronous orbit or fully tidally locked (Barnes, 2017; Pierrehumbert & Hammond, 2019). Tidal locking occurs because the star's gravitational pull on the near side of the planet and the centrifugal force on the far side elongate the planet's shape. While the planet is not yet tidally locked, different areas of its body are stretched or compressed as it moves through its orbit, dissipating energy through friction. The spin slows down until the rotation period is equal to the orbital period and this mechanism no longer dissipates energy (Pierrehumbert & Hammond, 2019). Despite the extreme difference in insolation between the planet's "dayside" and "nightside," general circulation models of the atmosphere have consistently shown that it can remain habitable thanks to heat redistribution from dayside to nightside (starting with Joshi, Haberle, and Reynolds (1997), see also A. Showman, Cho, and Menou (2010), A. P. Showman, Wordsworth, Merlis, and Kaspi (2013), Pierrehumbert and Hammond (2019)). Figure 1.2 shows the effect of single-hemisphere insolation: an extreme contrast in surface temperature between dayside and nightside, but largely equalised air temperatures, especially higher in the atmosphere.

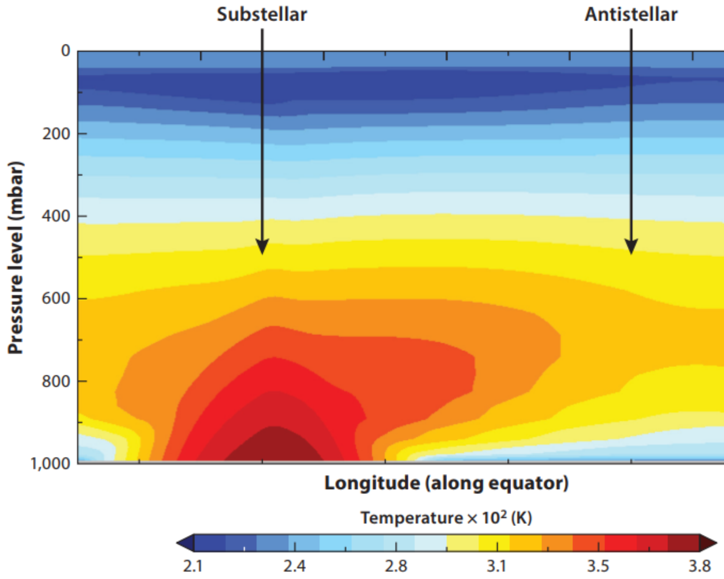

Figure 1.2: Atmospheric temperature cross-section of a tidally locked terrestrial planet. Warm air at the substellar point is transported to the antistellar point. The nightside surface is warmed only by outgoing long-wave radiation from the air stream above it and is colder than the atmosphere (Pierrehumbert & Hammond, 2019).

No planet in the Solar System is tidally locked, although Venus comes close with its very slow rotation rate. Earth's Moon and other Solar System moons like Titan are tidally locked to their planets (Folonier & Ferraz-Mello, 2017), but they are not powerfully irradiated on one side and in most cases (Titan excepted) lack a thick atmosphere. Not only does this orbital configuration profoundly impact the climate, it also presents unique challenges to interpreting the results of observations, above all of transmission spectroscopy.

1.2 Observing the terminator

The capabilities of astronomy have expanded to include detection of not only exoplanets, but their atmospheres (Catling & Kasting, 2017). For planets that pass between their host star and the Earth, atmospheres can be observed using phase curves, thermal emission and reflection spectroscopy, and transmission spectroscopy. To date, most of our information about exoplanet atmospheres comes from these transit methods, especially transmission spectroscopy (Madhusudhan, 2018, 2019).

If the plane of the planet's orbit is not too strongly inclined, the planet will, at some point during its orbit, pass in the line of sight between the Earth and the host star, causing a small drop in the amount of light telescopes detect from the star (see Figure 1.3 for the geometry of transit and Figure 1.4 for an example plot of the light curve). The decrease in light can be correlated to the radius of the planet relative to the radius of the star, allowing limits to be set on the planet's size (Catling & Kasting, 2017; Perryman, 2018). This method, the transit method, is used to detect the existence of exoplanets.

A telescope sensitive enough to resolve the light curve of *different* wavelengths can also provide data that allow us to infer constraints on the atmospheric composition. As light passes through the planetary limb, some wavelengths are preferentially absorbed or scattered by atmospheric constituents (Beichman et al., 2014). This makes the planet appear bigger or smaller at different wavelengths, depending on the height where a given wavelength is absorbed. The relative apparent size of the planet can be plotted against wavelength and correlated with known spectra of atmospheric species, as shown in Figure 1.5. This method of observation is called transmission spectroscopy.

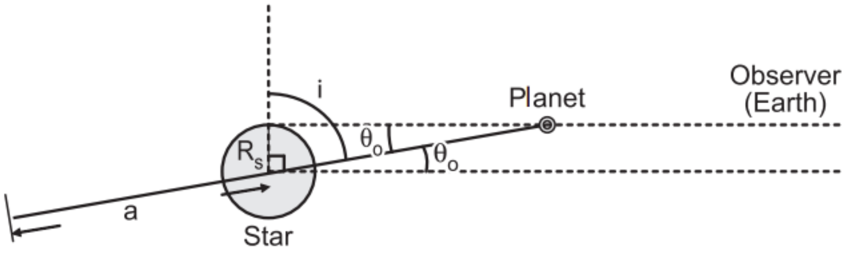

Figure 1.3: Geometry of the transit detection method, from J. Kasting (2012), reproduced by Catling and Kasting (2017)

A number of new and upcoming telescopes will be able to perform transmission spectroscopy of exoplanet atmospheres, including the James Webb Space Telescope (see Gialluca, Robinson, Rugheimer, and Wunderlich (2021), Mollière et al. (2017), Greene et al. (2016), Beichman et al. (2014) for discussion of JWST's capabilities, observational targets, and synthetic spectra), the Atmospheric Remote-sensing Infrared Exoplanet Large-survey (Edwards, Mugnai, Tinetti, Pascale, & Sarkar, 2019; Tinetti et al., 2018; Venot et al., 2018), the British commercial space mission Twinkle (Edwards, Rice, et al., 2019; Jason et al., 2016), and speculative missions like HabEx and LUVOIR (J. Wang et al., 2017). The next generation of ground-based telescopes like the Extremely Large Telescope and the Giant Magellan Telescope will also be able to characterise some exoplanet atmospheres (Diamond-Lowe, Berta-Thompson, Charbonneau, & Kempton, 2018).

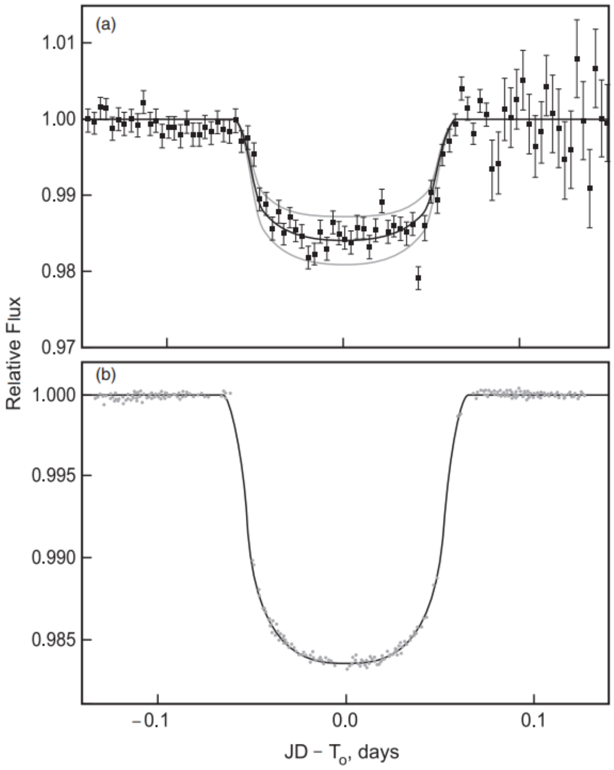

Figure 1.4: Light curve of a star-planet system as the planet passes in front of the star, from Charbonneau et al. (1999), reproduced by Catling and Kasting (2017))

Exoplanet atmosphere research using light curves and transmission spectroscopy had already begun with the Hubble Space Telescope (Brown, Charbonneau, Gilliland, Noyes, & Burrows, 2001; Tinetti et al., 2010; Tsiaras et al., 2016), and Spitzer Space Telescope (Knutson et al., 2007, 2008). Charbonneau, Brown, Noyes, and Gilliland (2002) found sodium in the atmosphere of HD 209458 b and Wyttenbach, Ehrenreich, Lovis, Udry, and Pepe (2015) in the atmosphere of HD 189733 b, both hot Jupiter planets, the first using Hubble Space Telescope data and the second data from the European Southern Observatory. Fossati et al. (2010) found sodium, tin, manganese, and other metals in the atmosphere of the hot Jupiter WASP-12 b with data from the Hubble Space Telescope. Tinetti et al. (2010) discovered a spectrum with water vapour, methane, carbon dioxide, and potentially carbon monoxide for the hot Jupiter XO-1 b, again with Hubble Space Telescope data. Fraine et al. (2014) reported water vapour and no clouds in the atmosphere of a Neptune-sized planet using observations from both Hubble and Spitzer.

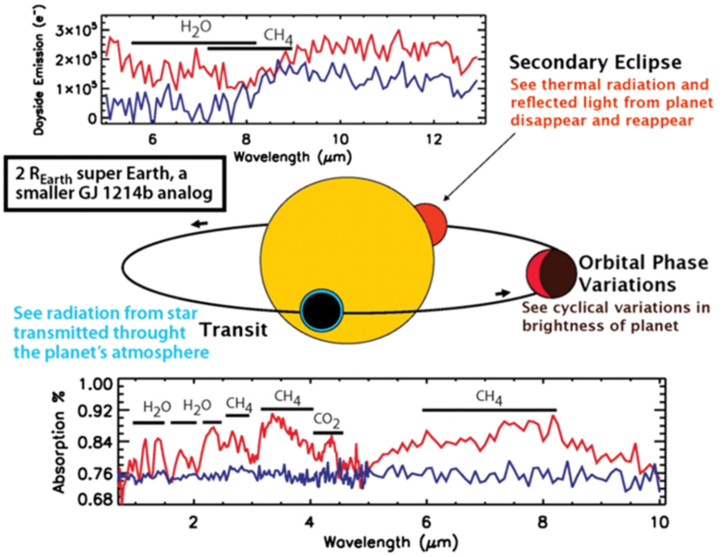

Figure 1.5: A schematic illustration of transit/transmission spectroscopy, thermal emission/reflection spectroscopy, phase curves, and simulated spectra (Beichman et al., 2014). The diagram depicts a planet passing in front of its host star and identifies important stages of its orbit: transit (planet in front of star), secondary eclipse (planet behind star), and orbital phase (illuminated part of planet varies with phase). Transmission spectroscopy uses light filtered through the planet's atmosphere while the planet is in transit.

Observations are not limited to atmospheric composition: Brogi et al. (2016) also inferred wind speeds on HD 189733 b using high-dispersion transmission spectroscopy. Nor are giant planets the only accessible targets. Tsiaras et al. (2016) detected an atmosphere around the super-Earth 55 Cancri e, and Demory et al. (2016) were able to measure the day-night temperature gradient of the same planet. Kreidberg et al. (2014) detected clouds or haze on the super-Earth GJ 1214 b. It is only a matter of time before this kind of data becomes available for Earth-sized planets such as the TRAPPIST-1 planets (Gillon et al., 2017), LP 890-9 b and c (Delrez et al., 2022), or Kepler-186 f (Quintana et al., 2014).

As Figure 1.5 also shows, transmission spectroscopy does not probe the entire planet. Only light filtered through the thin ring of atmosphere around the planetary disc and in the line of sight contributes to the observation (Caldas et al., 2019; Wardenier, Parmentier, & Lee, 2022). This region is known as the planetary limb. On a tidally locked planet, the limb is also the terminator line, the boundary between the dayside and nightside. Far from being a representative sample of the atmosphere, it is a unique transition zone where two different environments meet. The composition of the atmosphere at the terminator may be different from both the dayside and the nightside, and even the two halves of the terminator—the leading edge as the planet begins to transit the star and the trailing edge on the far side—may differ substantially. For example, in a study of the ultrahot gas giant WASP-76 b, Ehrenreich et al. (2020) found an absorption signature of iron at the planet's trailing limb, but none at the leading limb, which the authors interpret as nightside condensation of gaseous iron into iron rain. Modelling studies of ultra-hot Jupiters (Helling et al., 2021) and temperate terrestrial planets (Song & Yang, 2021) alike have found variations in cloud cover and chemical abundances across the dayside, nightside, and both terminators. An important conclusion to draw from this body of work is that, even though an unresolved planet is contained in a single pixel of data, we cannot simplify the planetary environment into a single spatial point. The spatial bias of transmission spectroscopy requires a three-dimensional understanding of the planet's atmosphere.

1.3 Comparing 1-D and 3-D models

The atmospheric properties of a planet are inferred from an observed spectrum by the process of atmospheric retrieval. Due to the computational expense involved in atmospheric retrievals, these methods use 1-D models of planetary atmospheres (Madhusudhan, 2018). A number of studies have predicted biases in retrievals based on 1-D models due to both observing geometry (Caldas et al., 2019) and inhomogeneities in atmospheric composition and climate, especially for tidally locked planets (Lacy & Burrows, 2020; Welbanks & Madhusudhan, 2022). As 3-D forward models of atmospheres cannot yet be used in retrievals, observers typically use parameterisations (if available) to incorporate insights from 3-D studies into 1-D models (Madhusudhan, 2018). For example, Parmentier, Showman, and Lian (2013) proposed a 1-D parameterisation of vertical eddy diffusivity based on vertical mixing of photochemical haze particles in a 3-D hot Jupiter simulation. 3-D models are especially necessary to understand the global circulation of a planet and the horizontal transport of atmospheric aerosols and chemical species, as these aspects cannot be simulated in a 1-D model.

3-D general circulation models have already been able to explain observed features of exoplanets. A prominent feature of tidally locked models of both terrestrial and gas planets is the presence of an equatorial superrotating jet (Hammond & Lewis, 2021; Hammond, Tsai, & Pierrehumbert, 2020; Joshi et al., 1997; Merlis & Schneider, 2010; Pierrehumbert & Hammond, 2019; A. Showman et al., 2010; A. P. Showman & Polvani, 2011; A. P. Showman et al., 2013). Superrotation means the wind is moving faster than the planet's surface; this phenomenon also occurs on Solar System worlds like Venus and Titan (Imamura et al., 2020; Read & Lebonnois, 2018), as well as in parts of the Earth's atmosphere (Kraucunas & Hartmann, 2005). The mechanisms driving superrotation are not necessarily the same on different worlds and the tidally locked case requires its own explanation.

Observations have supported the existence of an equatorial jet on hot Jupiter planets through the detection of a "hot spot shift" (Knutson et al., 2007, 2008). These studies find that the hottest part of the surface is shifted eastwards of the substellar point. Variable Doppler shifts of the leading and trailing planetary limbs, attributable to high eastward winds, have also been observed on hot Jupiters (Louden & Wheatley, 2015). These horizontal wind structures and their impacts cannot be simulated in 1-D models.

Based on 3-D modelling, A. P. Showman and Polvani (2011) proposed an analytic theory of equatorial superrotation on tidally locked planets. In their theory, the differential dayside-nightside heating generates large-scale waves in the atmosphere, which funnel angular momentum towards the equator. This thermal forcing pattern is analogous to longitudinally varying heating at Earth's equator in the equatorial wave theory developed by Matsuno (1966) and Gill (1980). The solutions to the equations of motions with longitudinally varying thermal forcing are accordingly called the Matsuno-Gill solutions. A. P. Showman and Polvani (2011) argue that the Matsuno-Gill model contains a physically inconsistent representation of vertical momentum transport and, when corrected, the model always predicts equatorial superrotation, regardless of the strength of the thermal forcing. This would account for the persistent appearance of an equatorial superrotating jet in tidally locked exoplanet GCMs.

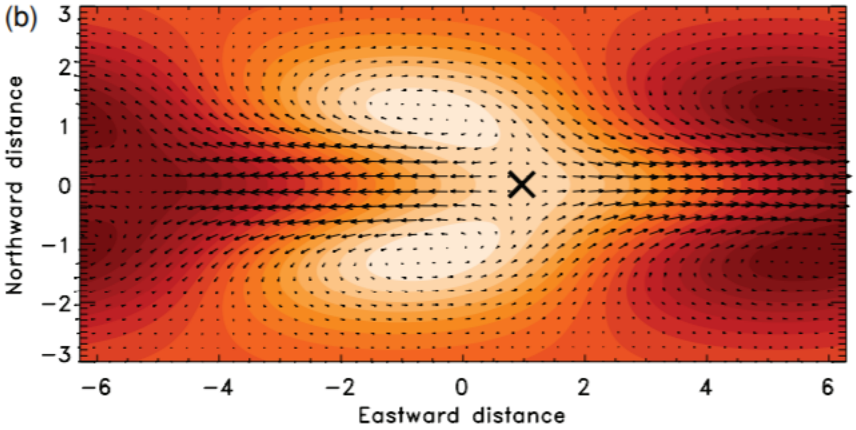

Figure 1.6: Analytic solution to the equations of motion on a tidally locked planet, showing the differential eastward-westward propagation of Kelvin and Rossby waves and the resulting formation of an eastward equatorial jet (A. P. Showman and Polvani (2011)). The brightness of the colours represents geopotential height (brighter shade equals higher geopotential height), while the arrows represent the horizontal wind vectors.

In A. P. Showman and Polvani (2011), the authors identify equatorial Kelvin and Rossby waves as the main drivers of equatorial superrotation. Kelvin waves form at the equator and propagate eastwards. Rossby waves form at midlatitudes and propagate westwards. This differential propagation causes the radiative-equilibrium height field to develop a northwest-southeast tilt in the northern hemisphere and a mirrored southwest-northeast tilt in the southern hemisphere. Wind vectors flow around the height field, transporting angular momentum from mid-latitudes towards the equator. Figure 1.6 depicts the shape of the radiative-equilibrium height field and the flow of wind around its contours. The wave theory underlying this pumping mechanism relies on a relatively strong Coriolis force, which slower-rotating tidally locked planets will lack; however, in their discussion the authors cite other mechanisms that may generate superrotation on slowly rotating planets, such as baroclinic instability (Del Genio & Zhou, 1996; Mitchell & Vallis, 2010).

The equatorial jet is not the only characteristic feature of the circulation on a tidally locked planet. A central element of the mechanism behind the jet, the planetary-scale standing Rossby waves, are ubiquitous in tidally locked models and have been discussed both as drivers of the equatorial jet (Hammond et al., 2020; A. P. Showman & Polvani, 2010, 2011) and for their other effects on the circulation and distribution of atmospheric species (Carone, Keppens, Decin, & Henning, 2018; Yates et al., 2020). These waves manifest as a pair of permanent gyres on the nightside and a matching pair rotating in the opposite direction on the dayside, superimposed on the equatorial jet (Hammond & Lewis, 2021). Carone et al. (2018) found that standing Rossby waves form either in the tropics or extratropics, depending on the planet's rotation rate, and that tropical Rossby waves confine atmospheric species to an equatorial belt, preventing them from being transported towards the poles. In a model of Proxima Centauri b with ozone chemistry, Yates et al. (2020) found that ozone collects in the cold nightside cyclones, where it is transported from the dayside by the atmospheric circulation and removed from photolysis by the star's radiation. Chen, Wolf, Kopparapu, Domagal-Goldman, and Horton (2018) likewise found spatial variations in abundances of atmospheric species, particularly between the dayside and nightside. These 3-D effects are beyond the capabilities of 1-D atmospheric models to simulate and indicate that predictions made by the latter may be sufficiently inaccurate to make atmospheric retrievals impossible.

Understanding horizontal transport is particularly important because the 3-D spatial distribution of light-scattering aerosols (clouds and hazes) in an atmosphere profoundly impacts transmission spectroscopy by ”flattening” the spectrum (Barstow, 2021; Dymont, Yu, Ohno, Zhang, & Fortney, 2021; Gao, Wakeford, Moran, & Parmentier, 2021). In a flat spectrum, the transit depth is uniform across all wavelengths, making it impossible to infer the presence of chemical species based on absorption features. Flat or near-flat spectra have been obtained for GJ 486 b (Moran et al., 2023), TRAPPIST-1 b, e, and f (Krishnamurthy et al., 2021), TRAPPIST-1 h (Garcia et al., 2022), GJ 436 b (Knutson, Benneke, Deming, & Homeier, 2014), GJ 1214 b (Bean et al., 2011; Berta et al., 2012; Kempton et al., 2023; Kreidberg et al., 2014), WASP-29 b (Gibson et al., 2013), GJ 1132 b (Libby-Roberts et al., 2022), L98-59 b (Damiano et al., 2022), GJ 3470 b (Crossfield, Barman, Hansen, & Howard, 2013), HD 189733 b (Pont, Knutson, Gilliland, Moutou, & Charbonneau, 2008), Kepler 51 b and d (Libby-Roberts et al., 2020), among others—planets which range from hot Jupiters to warm Neptune-sized gas dwarfs to sub-Earth-sized rocky worlds. Featureless spectra could be caused by the lack of an atmosphere, a heavy mean molecular weight atmosphere, a cloudy or hazy atmosphere, or insufficient instrument resolution. Distinguishing between these scenarios requires improvements in modelling and interpretation as well as observational techniques and instrumentation.

An advantage of 3-D models over their 1-D counterparts is the ability to predict the spatial distribution of clouds and hazes. For example, while clouds are likely to flatten transmission spectra on water-rich planets (Komacek, Fauchez, Wolf, & Abbot, 2020; Suissa et al., 2020), their concentration in the substellar region of tidally locked planets (J. Yang, Cowan, & Abbot, 2013) could allow for clear terminators on some planets at least some of the time. Terminator asymmetry predicted by 3-D models (Parmentier et al., 2013; Song & Yang, 2021; Steinrueck et al., 2021), with one terminator clearer than the other, may speak for separating data from the leading and trailing limb in analysis. Novel analytical techniques such as transmission strings (Grant & Wakeford, 2023) and eclipse mapping (Rauscher et al., 2007; Williams, Charbonneau, Cooper, Showman, & Fortney, 2006) are also beginning to produce 3-D information, which requires models to interpret. Ultimately, teasing out insights from featureless transmission spectra requires a more sophisticated 3-D understanding of exoplanet atmospheres and the incorporation of this understanding into atmospheric retrievals and interpretation of data.

1.4 Thesis structure

In this thesis, I study the 4-D (spatial and temporal) distribution of the atmospheric tracers of water vapour, clouds, and photochemical haze particles in general circulation model simulations of Earth-like tidally locked exoplanets. My focus falls particularly on global-scale atmospheric waves, including Rossby waves and gravity waves, which can only be simulated in 3-D models. These waves can affect the spatial distribution and temporal variability of atmospheric species, both directly through advection and indirectly through their impact on the general circulation of the planet.

In Chapter 2, I describe a stratospheric oscillation in wind direction and water vapour abundance on a tidally locked M-Earth. The oscillation is analogous to the quasi-biennial oscillation on Earth and is driven by gravity waves generated by convection on the planet's dayside. Simulated transit spectra show that for an Earth-like planet, the amplitude of the oscillation is too small to detect with current instruments. However, the dynamical mechanism driving the variability is not specific to rocky planets, and in fact analogous oscillations have been observed on Jupiter and Saturn. Such an oscillation could be observable on a gas giant. My study investigates differences between this phenomenon and Earth's quasi-biennial oscillation attributable specifically to the tidally locked orbital configuration.

In Chapter 3, I describe a periodic variation in cloud cover at the planetary limb of an Earth-like planet caused by a shift in the location of the stationary Rossby gyres characteristic of a tidally locked planet circulation. This oscillation is caused by corresponding variations in cloud cover at the substellar point, which affect the zonal wind speeds throughout the planet and therefore the phase speed and longitudinal location of the stationary Rossby waves. Simulated transmission spectra show a regular increase and decrease in the transit depths of specific absorption features with the same period as the cloud cover and Rossby wave oscillation. For some select planets, this oscillation could cause periods of low- to no cloud at the planetary limb, though there is no way to predict in advance when these will occur.

In Chapter 4, I study the impact of planetary rotation rate on the spatial distribution of photochemical haze particles on tidally locked planets. My parameter space of 32 rotation periods and two planets shows that the general circulation falls into three regimes: banded, double jet, and single jet, in agreement with previous studies. I find that the banded regime results in very high haze amounts throughout the planet, the double jet regime results in haze collected mainly within the stationary Rossby gyres, and the single jet regime results in both haze collection in the gyres and a high haze layer kept aloft by the increasing dominance of the overturning element of the circulation. These findings can help guide future observing target choices as well as haze parameterisations in 1-D forward models in atmospheric retrievals.

Chapter 2

Longitudinally asymmetric stratospheric oscillation on a tidally locked exoplanet

(**Author contributions:** This work has been published in Cohen et al. (2022). I ran the simulations, performed the analysis, and wrote the paper. Massimo Bollasina and Paul Palmer supervised the work and edited the text. Denis Sergeev, Ian Boutle, Nathan Mayne, and James Manners contributed to development of the model and provided feedback on the text.)

2.1 Introduction

Rocky planets orbiting M-class stars have become a prime target for exoplanet research due to their prevalence and potential habitability (Heath et al., 1999; R. K. Kopparapu, 2013; Scalo et al., 2007; Schwieterman et al., 2018; Wandel, 2018; J.-Y. Yang et al., 2020). As the habitable zones (HZ) of cool M stars are found close to the host star, planets within the HZ have a high chance of being tidally locked (Barnes, 2017; Pierrehumbert & Hammond, 2019). These planets receive stellar irradiation on only one hemisphere, an orbital configuration not found for planets in the solar system, which has a substantial impact on the planet's atmospheric dynamics and chemistry.

An accurate understanding of atmospheric dynamics is important both to assessing the theoretical habitability of tidally locked rocky planets and interpreting observations. Theoretical studies of tidally locked rocky exoplanets have used 3-D atmospheric general circulation models (GCMs) to explore their possible atmospheric dynamics and climate states (Boutle et al., 2017; Koll & Abbot, 2016; Komacek & Abbot, 2019; Wolf, 2017). A key finding of GCM studies is that tidally locked planets within the HZ of M-class stars can retain temperate climates in spite of their uneven thermal forcing as a result of winds redistributing heat from their hot daysides to their cold nightsides (Joshi et al., 1997; Merlis & Schneider, 2010; Pierrehumbert & Hammond, 2019; Wordsworth, 2015). The day-night temperature gradient of a tidally locked exoplanet has already been observed for some hot Jupiters (Komacek, Showman, & Tan, 2017; Wong et al., 2021), and even for a rocky planet (Demory et al., 2016). However, most past studies have examined mean climate states, masking time-dependent phenomena which may impact observations by upcoming instruments such as the James Webb Space Telescope's Near Infrared Spectrograph (NIRSpec) (Mollière et al., 2017; Morley, Kreidberg, Rustamkulov, Robinson, & Fortney, 2017) and the ESA Atmospheric Remote-sensing Infrared Exoplanet Large-survey mission (Tinetti et al., 2018; Venot et al., 2018). As observations are performed in a narrow time window, modes of variability with long periods such as analogues of the Earth's quasi-biennial oscillation (QBO) may result in observed temperatures or abundances that differ by an order of magnitude or more from predictions based on mean GCM states. Other studies have used GCMs, coupled with synthetic planetary spectrum generators, to simulate observations of transmission spectroscopy for transiting exoplanets (G. N. Arney et al., 2017; Boutle et al., 2020; Lines et al., 2018; May, Taylor, Komacek, Line, & Parmentier, 2021; Suissa et al., 2020), enhancing the value of these models as an aid to interpreting observational data (Brogi et al., 2016; Louden & Wheatley, 2015). However, gaps in our understanding of the physics driving atmospheric phenomena on tidally locked planets, partly driven by differences in model structure and parameterisations (Fauchez et al., 2022; Sergeev, Fauchez, et al., 2022; Sergeev et al., 2020; Turbet et al., 2022), may cause misinterpretations of atmospheric observations.

Global 3-D models of tidally locked planets exhibit an area of deep convection around the substellar point (Hammond & Lewis, 2021; R. k. Kopparapu et al., 2016; J. Yang et al., 2013), leading to permanent cloud cover and heavy precipitation in this region (Boutle et al., 2017; Labonté & Merlis, 2020; Sergeev et al., 2020; J. Yang et al., 2013). The tropospheric and stratospheric circulation is characterised by stationary Rossby waves of zonal wavenumber 1 induced by the day-night thermal forcing (Carone et al., 2018; Hammond & Lewis, 2021; Merlis & Schneider, 2010; A. P. Showman & Polvani, 2011). These waves have been identified as a driving source of the superrotating equatorial jets that develop in tidally locked simulations of both Earth-like planets and hot Jupiters (Debras, Mayne, Baraffe, Goffrey, & Thuburn, 2019; Debras et al., 2020; A. P. Showman & Polvani, 2010, 2011; Tsai, Dobbs-Dixon, & Gu, 2014). The jets are associated with two pairs of cyclones-anticyclones: one pair forms in the northern hemisphere, rotating clockwise on the dayside and anticlockwise on the nightside, while the other pair forms in the southern hemisphere and rotates in the opposite directions. The cyclones contribute a zonal wind vector component near the equator that points westward in the substellar region and eastward in the antistellar region. This results in a background flow which is more eastward on the nightside than on the dayside, a pattern that holds true in both the troposphere and the stratosphere. The day-night thermal forcing additionally creates a region of rising air on the dayside and subsiding air on the nightside (Hammond & Lewis, 2021; Joshi et al., 1997).

In the theory of the QBO, the background flow determines the structure of the oscillation. On Earth, the stratospheric zonal wind forms a pattern of vertically stacked jets flowing in opposite directions. The pattern propagates downwards from roughly $20-40$ km at a speed of 1 km per month such that the wind direction at a given height reverses over time with a mean periodicity of $26-28$ months, with substantial variation from cycle to cycle (Braesicke, 2015; Dunkerton, Anstey, & Gray, 2015). The oscillation of the zonal wind is accompanied by oscillations in air temperature and trace gases. The basic mechanism driving the QBO was described by Lindzen and Holton (1968) and Plumb (1977) and reproduced in a laboratory setting by Plumb and McEwan (1978). The minimum requirements for the QBO to occur are a background flow that is a function of altitude and at least two gravity waves propagating in opposite directions horizontally, as well as upwards vertically (Plumb, 1977). An eastward propagating gravity wave will travel upwards until it encounters an eastward perturbation in the background flow, where it is absorbed, accelerating the flow in the eastward direction. Westward propagating waves pass through this area of eastward flow until they reach a westward perturbation and are absorbed in turn. The resulting pattern of stacked jets propagates downwards over time as the bottom of each shear zone is accelerated and the lowest jet dissipates due to viscous diffusion (Dunkerton et al., 2015; Plumb, 1977). Although equatorially trapped Rossby and Kelvin waves were originally believed to contribute the necessary momentum flux, it has been estimated that anywhere from $25-80\%$ of the momentum flux driving the QBO is provided by convectively generated gravity waves, with more recent work tending towards higher percentages (Alexander & Holton, 1997; Dunkerton, 1997; Ern & Preusse, 2009; Evan, Alexander, & Dudhia, 2012; Lane, 2015; Piani, Durran, Alexander, & Holton, 2000). Gravity waves are generated when the forces of gravity or buoyancy react against vertical perturbations in a fluid medium. The waves travel internally within the fluid until they are absorbed at critical levels where the velocity of the background flow is comparable to the wave's horizontal phase speed (Booker & Bretherton, 1967), making the planet's mean flow an important element in the phenomenon.

Here, I describe the first reported simulation of a stratospheric oscillation, analogous to the QBO on Earth, on a tidally locked planet with an Earth-like atmospheric composition. This new stratospheric oscillation consists of periodic reversals in the direction of the zonal wind, an associated cooling and warming of the equatorial atmosphere, and fluctuations in the stratospheric water vapour content. While analogous to the QBO in its causal mechanism, the oscillation displays longitudinal asymmetries arising directly from the planet's tidally locked state. Accordingly, I refer to the oscillation on a tidally locked planet as a longitudinally asymmetric stratospheric oscillation (LASO) and reserve the term QBO for the phenomenon on Earth. To put my results into context, throughout the paper I compare and contrast key features of the tidally locked LASO with the QBO on Earth (Baldwin et al., 2001).

Section 2.2 describes the global 3-D model I use to describe atmospheric dynamics on a tidally locked planet, the metrics I use to characterize the LASO, and the radiative transfer model I use to simulate JWST observations of the fluctuations in atmospheric water vapour content caused by the LASO. Section 2.3 describes the mechanism underpinning the LASO and characteristics of the LASO that differ from those of the QBO. I also consider the effect of LASO-related water vapour fluctuations on transit observations. In Section 2.4 I discuss the implications of the LASO for future spectral atmospheric observations and the sensitivity of the LASO to differences in sub-grid scale model parameterisations. I conclude the paper in Section 2.5.

2.2 Methods

2.2.1 Model description

I use the Global Atmosphere 7.0 configuration of the Met Office Unified Model to simulate the atmosphere of a tidally locked Earth-like exoplanet, nominally Proxima Centauri b (Walters et al., 2019). For brevity, I provide a basic description of the model and refer the reader to Mayne, Baraffe, Acreman, Smith, Wood, et al. (2014), Boutle et al. (2017), and Sergeev et al. (2020) for more details.

I run the model at a horizontal resolution of 2° latitude by 2.5° longitude, and with 60 vertical levels from the surface to up to 85 km (Table 2.1). The atmospheric levels are identical to those in Boutle et al. (2017) up to 38 km. The remaining 47 km are accounted for by an additional 22 levels. Table 2.2 shows the orbital and planetary parameters used in this study, following Boutle et al. (2017), with data taken from Anglada-Escudé et al. (2016) and Turbet et al. (2016). Proxima Centauri b is simulated as an aquaplanet with a slab ocean (Frierson, Held, & Zurita-Gotor, 2006), with a heat capacity of 10^{7} J K^{-1} m^{-2} representing a mixing layer of 2.4 m. I specify an atmospheric composition of 100 % nitrogen with a trace fixed $\mathrm{CO_2}$ abundance of $5.941 \times 10^{-04}\mathrm{kgkg}^{-1}$. The model includes interactive water vapour and a full water cycle with unlimited evaporation from the slab ocean, precipitation in the liquid and ice phases, and a cloud scheme. The stellar spectrum for Proxima Centauri was taken from BT-Settl (Rajpurohit et al., 2013) with $T_{eff} = 3000$ K, g= $1000\mathrm{ms}^{-2}$, and metallicity $= 0.3$ dex. The star is treated as quiescent. I spin up the model for 900 Earth days from an equilibrium state taken from a previous run of the Proxima Centauri b model. The simulation was determined to be in equilibrium when the incoming and outgoing radiation at top-of-atmosphere were balanced, evaporation balanced precipitation in the global mean, and the surface temperature no longer showed a long-term upward or downward trend. The experiments I report were run

Level	1	2	3	4	5	6	7	8	9	10
Height (m)	10.0	49.9	130.0	249.99	410.0	610.0	849.9	1129.9	1449.9	1810.0
Level	11	12	13	14	15	16	17	18	19	20
Height (m)	2209.9	2650.0	3129.9	3650.0	4210.0	4810.0	5449.9	6129.9	6849.9	7609.9
Level	21	22	23	24	25	26	27	28	29	30
Height (m)	8409.9	9249.9	10130.0	11050.0	12001.0	13001.0	14050.0	15130.0	16250.0	17410.0
Level	31	32	33	34	35	36	37	38	39	40
Height (m)	18590.0	19770.1	20950.3	22131.3	23313.9	24499.5	25690.3	26889.2	28100.2	29328.5
Level	41	42	43	44	45	46	47	48	49	50
Height (m)	30580.3	31863.4	33186.9	34562.1	36001.5	37520.0	39134.3	40863.5	42729.0	44754.9
Level	51	52	53	54	55	56	57	58	59	60
Height (m)	46967.7	49396.9	52074.8	55036.7	58321.5	61971.1	66030.9	70550.2	75581.7	81182.4

Table 2.1: Vertical levels and heights (layer centres) used in the Unified Model to describe the atmospheric dynamics of an Earth-like tidally locked Proxima Centauri b.

Parameter	Value
Semi-major axis (AU)	0.0485
Stellar irradiance (W m^{-2})	881.7
Orbital period (Earth days)	11.186
Rotation speed (rad s^{-1})	6.501×10^{-6}
Eccentricity ($\cdot$)	0
Obliquity ($\cdot$)	0
Radius (km)	7160
Acceleration due to gravity (m s^{-2})	10.9

Table 2.2: Simulation parameters used to describe an Earth-like tidally locked Proxima Centauri b.

for 1800 Earth days in total, and I analysed a sampling period of 900 days after equilibrium, which is long enough to include multiple oscillations. I define the substellar point to be 0° longitude and latitude. The antistellar point is located at 180° longitude and the eastern and western terminators at 90°E and 90°W, respectively. Hereafter, days refer to Earth days.

Earth GCMs typically require both resolved and parameterised waves to generate a QBO (Garfinkel et al., 2021). Past studies have shown that the Unified Model can reproduce a realistic oscillation (Scaife et al., 2000; Scaife, Butchart, Warner, & Swinbank, 2002). The model can sustain resolved long wavelength gravity waves and inertio-gravity waves generated by physical and numerical imbalances in the flow (as discussed in Section 2.3). The model also includes a sub-grid scale non-orographic gravity wave parametrisation (A. C. Bushell et al., 2015; Warner & McIntyre, 1996, 2001). Within this parameterisation, an unsaturated spectrum of gravity waves is launched near the surface and carries a vertical flux of horizontal wave pseudo-momentum upwards in equal amounts towards the north, south, east, and west.

Upward-propagating flux is diminished by Doppler modification and density amplification. Wave pseudo-momentum is conserved by an opaque model lid which sets the outgoing flux to zero (A. Bushell, 2021). The scheme includes a scale factor for the vertical flux and a characteristic (spectrum peak) wavelength which must be tuned to the vertical resolution of the model to achieve a QBO. I use a factor enhancement for the vertical flux of horizontal pseudo-momentum of 1.2 and a characteristic wavelength of 4.3 km with model level heights shown in Table 2.1. These are the standard values used in the GA 7.0 for Earth with the model levels in Table 2.1 and I retain them in order to simulate Proxima Centauri b as an Earth-like planet. The gravity wave scheme can be run with two different gravity wave source locations: 1) a standard scheme in which the gravity wave launch flux is globally invariant, distributed uniformly around the model; and 2) an experimental scheme in which the gravity wave launch flux is determined by local precipitation, developed based on an empirical correlation found between gravity waves and precipitation on Earth (A. C. Bushell et al., 2015). A comparison of these two gravity source locations in producing an accurate QBO did not show any preference for either of them, with each source demonstrating some strengths and weaknesses (A. C. Bushell et al., 2020). My study is based on the standard globally invariant source.

In addition to the control experiment described below, I performed a sensitivity run to understand the influence of horizontal resolution by increasing it to 1° latitude by 1.25° longitude. I performed a separate sensitivity test by decreasing the timestep from 20 to 2 minutes. To test whether my results are robust against the location of the gravity wave source, I also ran the experimental precipitation-dependent scheme described above and found comparable results. I present more detailed results of these three sensitivity tests in Section 2.3.

2.2.2 Metrics used to characterise the LASO

Thermal wind equation

Holton and Hakim (2013) predict the amplitude of the QBO of temperature using the equatorial beta plane form of the thermal wind equation:

$$\frac{\partial \overline{u}}{\partial z} = -R(H\beta)^{-1}\frac{\partial^2 \overline{T}}{\partial y^2}, \tag{2.1}$$

where $\overline{u}$ is the zonal mean zonal wind at the equator, R is the specific gas constant, H is the atmospheric scale height, $\beta = \frac{2\Omega}{r} cos\theta$ is the beta parameter at the equator (with Ω the planetary rotation rate in radians and r the planet's radius), $\overline{T}$ is the zonal mean temperature perturbation, and ∂y is the meridional scale of the oscillation. The mean zonal wind and temperature satisfy thermal wind balance because the mean meridional and vertical motions are comparatively small, and Holton and Hakim (2013) successfully derive the observed amplitude of the temperature oscillation on Earth with this method.

Gravity wave-induced acceleration

To confirm that the reversal in the direction of the stratospheric jets is caused by absorption of gravity waves, I calculate the acceleration of the atmosphere in each model gridbox due to gravity waves, F, as:

$$F = \frac{\partial(u'w')}{\partial z}, \tag{2.2}$$

where u' is the high-pass filtered zonal anomaly of the zonal wind, w' is the time anomaly of the vertical wind, and z is the height. This definition is adapted from the formulation of the wave momentum flux described by Plumb (1977) and used in its original form by A. P. Showman, Tan, and Zhang (2019) to identify shear transition zones between alternating jets.

I modified u' to better describe the characteristic flow on a tidally locked planet. The zonal anomaly is usually defined as the deviation of that quantity from its zonal mean and, in a zonally symmetric baseline flow, identifies transient phenomena. However, tidally locked planets lack zonal symmetry. The planet's stationary Rossby waves skew the zonal anomaly so that it represents the Rossby waves rather than transient flows. To adapt u' to this asymmetrical background flow, I use a high-pass filter to remove the influence of waves with zonal wavenumber less than 5 (i.e., long Rossby waves), following Sugimoto et al. (2021). The remaining waves are resolved long wavelength gravity and inertio-gravity waves. Additionally, the zonal anomaly of the vertical wind w would be impractical for identifying waves because rising air on the dayside and subsiding air on the nightside cancel when a zonal mean is calculated. I instead use the time anomaly to distinguish transient, wave-like fluctuations in w from the background. The resulting metric identifies wave-induced acceleration caused by resolved gravity and inertio-gravity waves only.

Latitudinal extent

I expect that a QBO-like oscillation on an exoplanet may extend to higher latitudes than Earth's QBO, covering a larger portion of the terminators, which may affect transit spectroscopy. To characterise the latitudinal extent L of the LASO, I use a formula derived by Haynes (1998) for the latitudinal extent of the QBO:

$$L = (\frac{\sigma}{\alpha})^{1/4}(\frac{ND}{\beta_0})^{1/2}, \tag{2.3}$$

where σ is the frequency of time variation of the applied force, α is the radiative damping rate, N is the buoyancy frequency, D is the depth scale of the force, and β_0 is the meridional gradient of the Coriolis parameter evaluated at the equator. The applied force refers to the mechanical forcing of the oscillation by waves, the frequency of its time variation is equivalent to the frequency of the oscillation, and the depth scale is the approximate vertical distance between opposing jets in the vertical jet structure.

Period

The period of the LASO is of interest because the duration of the temperature and atmospheric composition oscillations may affect observations and in particular could cause discrepancies between repeated observations of the same target exoplanet. I determine the period T of the LASO using a wavelet analysis of the wind velocity time series at the altitude where the LASO has its greatest amplitude. Following Plumb (1977), the period of the oscillation is inversely proportional to the momentum flux:

$$T = \eta \frac{\hat{k}\hat{c}^3}{\hat{N}\hat{\mu}\hat{F}}, \tag{2.4}$$

where $\hat{k}$, $\hat{c}$, $\hat{N}$, $\hat{\mu}$, and $\hat{F}$ are scaling factors for the wavenumber and phase speed of the wave driving the oscillation, the buoyancy frequency, the thermal dissipation rate, and the momentum flux, respectively. The parameter η is a dimensionless number that depends on the specific details of the problem. In Plumb's simple numerical model, the wavenumber and phase speed of the waves can be specified, while in the real atmosphere the oscillation is driven by a broad spectrum of waves whose constituents vary with location and time. However, the inverse relationship between the period and the momentum flux at the lower boundary of the QBO shear zone is also accepted to exist for the real QBO (Dunkerton et al., 2015). I assume all other values are identical to those for Earth and focus on the impact of the wave momentum flux $\hat{F}$ on the period.

Lagrangian Rossby number

To understand how a tidally locked orbital configuration affects where gravity waves are generated on the planet I use the Lagrangian Rossby number, $Ro^{(L)}$, to identify resolved gravity wave sources. $Ro^{(L)}$ is not an exclusive measure of gravity wave sources, but is often used to detect unbalanced flows which give rise to gravity waves (Y.-L. Lin, 2007; Sugimoto et al., 2021; F. Zhang, Koch, Davis, & Kaplan, 2000). It is defined as the ratio of the acceleration of a parcel of air to the Coriolis acceleration and essentially measures the local departure from geostrophy:

$$Ro^{(L)} = \frac{\mid \frac{\partial v_h}{\partial t} + v_h \cdot \nabla v_h \mid}{f \mid v_h \mid}, \tag{2.5}$$

where v_h is the horizontal wind vector and *f* is the Coriolis parameter.

I modify $Ro^{(L)}$ in several respects to adapt the metric to a slowly rotating planet. Following Sugimoto et al. (2021), I disregard the local wind tendency term, $\frac{\partial v_h}{\partial t}$, and fix the value of *f* near the equator ($\leq \pm 10^{\circ}$) equal to *f* at 10° to extend the metric to cover the equatorial region. As the slowly rotating Proxima Centauri b is not in geostrophic balance, the resulting values of $Ro^{(L)}$ are very large. I normalise $Ro^{(L)}$ by dividing by the minimum value, which I consider the baseline ageostrophy for my simulation. A larger value indicates a relative local increase in imbalances in the flow. I also exclude the top five model levels and latitudes above $\pm 40^\circ$ to avoid interference from instability at the model top and poles.

2.2.3 NASA Planetary Spectrum Generator

To describe the spectrum of the atmospheric water vapour content that might be observed by the James Webb Space Telescope's NIRSpec instrument, I use the NASA Planetary Spectrum Generator (Villanueva, Smith, Protopapa, Faggi, & Mandell, 2018), publicly available at `https://psg.gsfc.nasa.gov/`. The NIRSpec instrument has a range of 0.6 to 5.3 $\mu\mathrm{m}$, covering water vapour features in the infrared at 1.4, 1.8, and 2.7 $\mu\mathrm{m}$, with spectral resolutions (R) of 100, 1000, and 2700. As inputs to the PSG, I use the basic orbital, planetary, and stellar parameters for the Proxima Centauri system, as well as pressure, temperature, altitude, H_2O, N_2, and CO_2 data from my UM simulations. I generate a transit spectrum for each latitude at both the eastern and western terminators (i.e., every 2° of latitude, for a total of 180 individual spectra) and average the outputs to get a final spectrum, following Suissa et al. (2020).

2.3 Results

2.3.1 Climatology

I briefly summarise the basic climatology of the model, originally presented in Boutle et al. (2017). The simulation develops a warm dayside with a maximum surface temperature of 290 K and a nightside characterised by cold traps between the equator and poles with a minimum temperature of 150 K. The dayside of the planet is largely covered in clouds, primarily ice clouds, up to about 15 km. The substellar region has an atmospheric humidity on the order of 10^{-4} kg/kg near the surface and experiences deep convection, while the nightside is extremely arid, with a water vapour content 2-3 orders of magnitude lower. The mean circulation is consistent with the description in Section 2.1, exhibiting a cyclone-anticyclone pair in each of the northern and southern hemispheres and a powerful eastward-flowing zonal equatorial jet from about 20 to 30 km.

2.3.2 Longitudinally asymmetric stratospheric oscillation

Figure 2.1 shows the wind speed and temperature oscillations in my simulation of the atmosphere of the tidally locked Proxima Centauri b. The period of the LASO is much shorter ($5-6.5$ months) than that of the QBO on Earth ($26-28$ months). There is also an asymmetry between the dayside and nightside. Nightside zonal winds are more positive (eastward) than dayside winds and have shorter westward phases. Consistent with the theory that describes the QBO, the dayside-nightside asymmetries in the mean planetary-scale circulation, in particular the dayside-nightside differences in wind speeds, are the primary factor responsible for the asymmetry of the LASO. I find that the location of gravity wave sources also affects the local flow. Figure 2.1c shows temperature fluctuations with a peak-to-peak amplitude of $\sim 60-70$ K, more than an order of magnitude larger than the variation of ~ 4 K associated with the QBO (Dunkerton et al., 2015). This much larger oscillation can be explained by using Equation 2.1. In my simulation, the equatorial mean vertical shear of the zonal mean zonal wind between $30-55$ km is 15 m s^{-1} km^{-1}. Using the values R = 297 J kg^{-1} K^{-1}, H = 6800 m, $\beta = 1.8 \times 10^{-12}$ m^{-1} s^{-1}, and a meridional scale of 7500 km ($60°$ on a planet of radius 7160 km) taken from my simulation, Equation 2.1 predicts a temperature perturbation of 35 K, which matches Figure 2.1 and a peak-to-peak amplitude of $60-70$ K. The high wind speeds in the stratosphere are the source of the higher vertical shear and greater temperature oscillation compared to Earth. The relationship also depends on the β parameter, which will have a smaller value for slowly rotating planets like Proxima Centauri b. However, as a slower rotation also implies a larger meridional scale of the oscillation according to Equation 2.3, these terms on the right-hand side partially counteract each other, and I expect the vertical wind shear to have a greater effect than the rotation rate.

To confirm that the LASO is generated by the same physical mechanism as the QBO, I calculated the wave-induced acceleration due to gravity waves and compared it to the change in zonal wind direction over time. Where the oscillation is driven by gravity waves, the direction of the acceleration caused by gravity waves should match the direction of the change in the zonal wind throughout the vertical extent of the LASO. Figure 2.2a shows the filtered u' field with zonal wavenumbers smaller than 5 removed (Section 2.2.2). I find positive and negative fluctuations in wind speeds due to resolved long wavelength gravity waves, with shear zones at 30 km, 41 km, and 50 km that correspond to regions where the flow changes direction. Waves with a leftward tilt correspond to westward-propagating modes and those with a a rightward tilt correspond to eastward-propagating modes. The band of reduced u' intensity between 15 km and 30 km corresponds to the permanent superrotating equatorial jet in the troposphere. Figure 2.2b shows the zonal mean gravity wave-induced acceleration calculated using Equation 2.2 and averaged over 90 days, corresponding to approximately half of a LASO cycle. The contour lines show the change in zonal wind speed over the same 90 days. Areas of positive (negative) wind direction change match well with areas of gravity wave-induced eastward (westward) acceleration. Regions below 25−30 km show little change in zonal wind speeds and negligible gravity wave-induced acceleration.

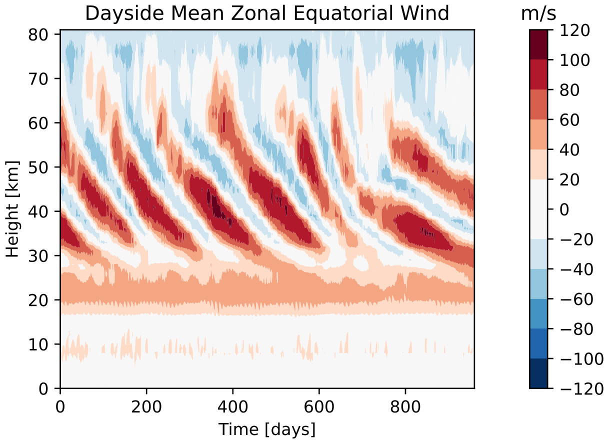

(a) Dayside zonal mean zonal wind

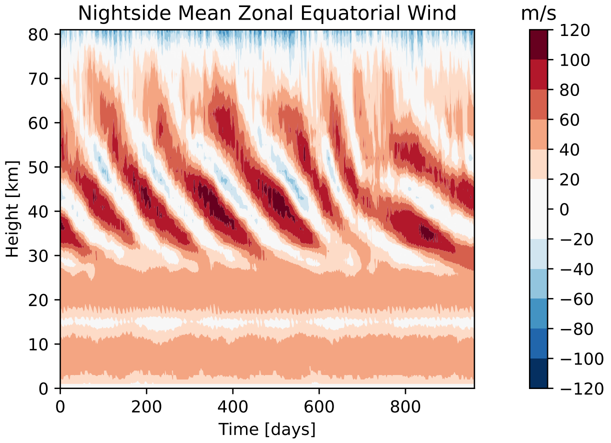

(b) Nightside zonal mean zonal wind

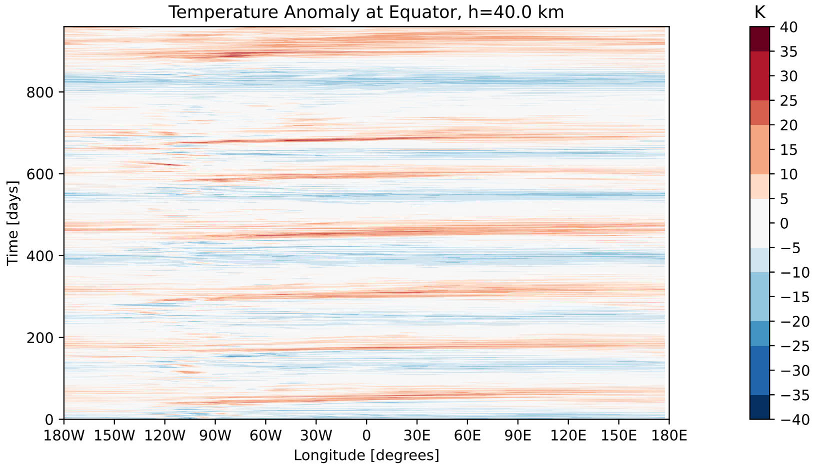

(c) Temperature anomaly at equator at 40 km

Figure 2.1: Hovmöller diagrams of a) dayside and b) nightside zonal mean equatorial winds on the simulated planet and c) the absolute temperature anomaly at 40 km. The data are sampled every six hours.

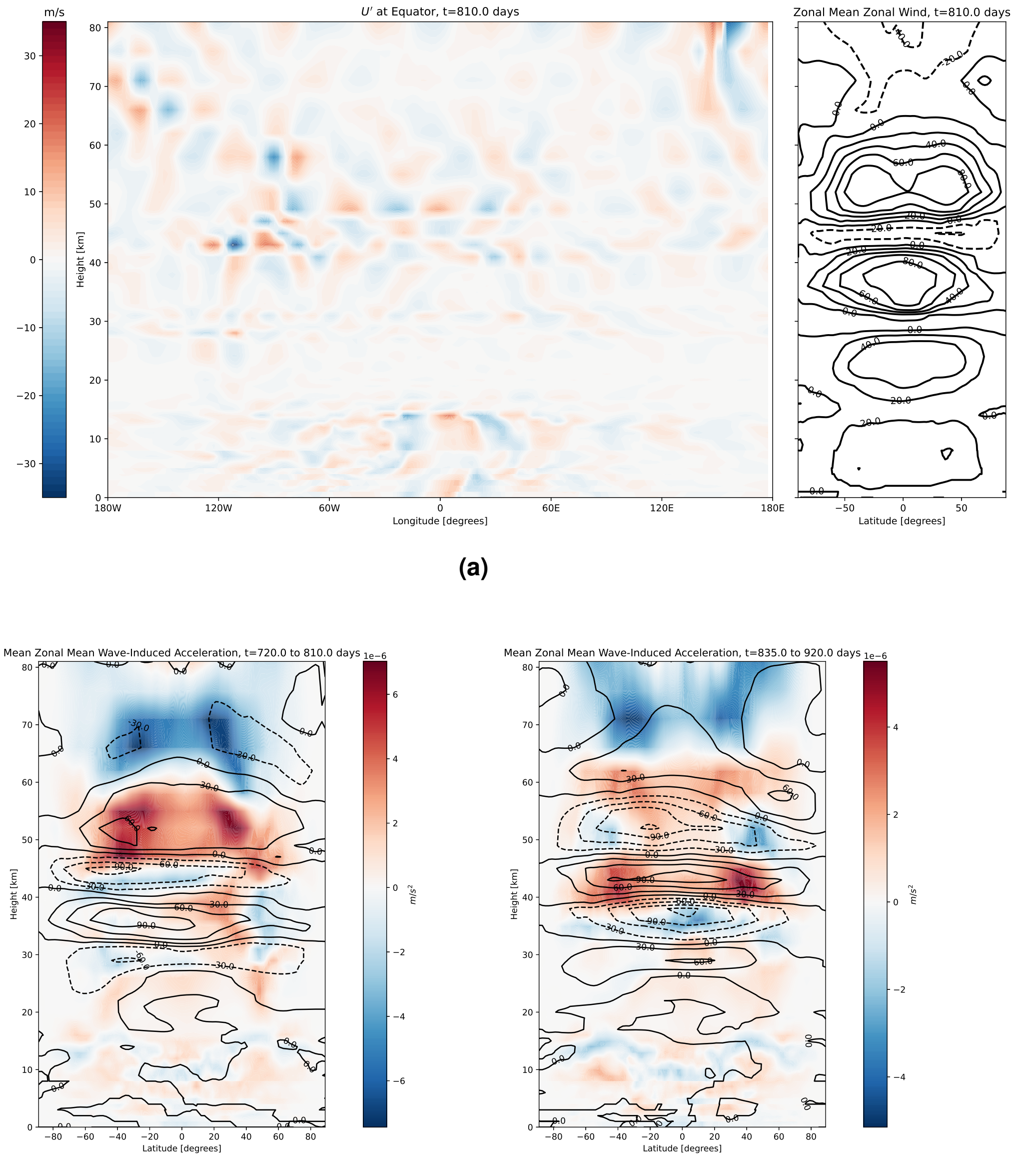
U′ at Equator, t=810.0 days

Zonal Mean Zonal Wind, t=810.0 days

Mean Zonal Mean Wave-Induced Acceleration, t=720.0 to 810.0 days

Mean Zonal Mean Wave-Induced Acceleration, t=835.0 to 920.0 days

(b) **(c)**

Figure 2.2: a) Zonal wind anomalies at the equator as a function of altitude, with zonal wavenumbers <5 removed, corresponding to a six-hour snapshot from simulation day 810 from the simulation sampling period. On the right is the zonal mean zonal wind on the same day, showing that altitudes where zonal wind anomalies in the left plot intensify correspond to shear zones where opposing jets meet. b) and c) Zonal mean wave-induced acceleration due to gravity waves, overlaid with the change in zonal mean wind speeds. The values represent 90-day means from days 720 to 810 and 835 to 920 of the simulation sampling period. The two plots show two different phases of the oscillation, with the maximum of eastward acceleration shifting downward from 50-55 km to 45-50 km in this period.

2.3.3 Latitudinal extent of LASO

The LASO extends to higher latitudes than the QBO on Earth. The latitudinal extent of the QBO, defined here by the full width at half maximum of a Gaussian fit to the horizontal cross section of the zonal wind at the height of the QBO maximum (Schenzinger, Osprey, Gray, & Butchart, 2017), is roughly 15°S-15°N (Braesicke, 2015). Figure 2.3 shows that the LASO extends from about 60°S–60°N by this definition. As the LASO on a slowly rotating tidally locked planet extends to higher latitudes, the oscillations in air temperature and in abundances of atmospheric species will cover more of the terminators and potentially have a larger impact on limb-averaged observations.

Previous work suggested that at higher latitudes the Coriolis force would counteract the acceleration due to gravity waves, limiting the QBO to equatorial regions on the Earth (Lindzen & Holton, 1968). Equation 2.3 gives a value for Earth of about L_{Earth}=10° (Baldwin et al., 2001), which underestimates the actual extent of 15° (Dunkerton & Delisi, 1985) by $\simeq$ 33%. I used spatial and temporal mean values from my simulation in Equation 2.3 as follows: the frequency of the time variation of the applied force $\sigma = 6.4 \times 10^{-8}$ s^{-1} for an oscillation of period 6 months; the radiative damping rate $\alpha = 1.5 \times 10^{-6}$ s^{-1}; the buoyancy frequency $N = 2.5 \times 10^{-2}$ s^{-1}; the depth scale of the force 10 km, and the meridional gradient of the Coriolis force at the equator $\beta = 1.8 \times 10^{-12}$ m^{-1} s^{-1}. The Coriolis force on Proxima Centauri b is an order of magnitude weaker than on Earth due to the planet's slower rotational period of 11.2 days (Ω=6.5×10^{-6} rad/s). The calculation above gives a latitudinal extent of $\simeq$45°. Scaling this value to account for the 33% underestimation gives the latitudinal range simulated by the model. The broader extent of the LASO compared to the equatorial QBO agrees with the description of slowly rotating tidally locked planets as 'all tropics' (A. P. Showman et al., 2013). A LASO on a slow rotator may therefore have a larger impact on transit spectroscopy than one on a more rapidly rotating planet.

2.3.4 Period of LASO

Another major difference between the LASO and the QBO is the period of oscillation. The period of the QBO has a large variability, with a mean value of 26–28 months (Braesicke, 2015). My calculations show that the LASO in my simulation of Proxima Centauri b's atmosphere has a period of 5–6.5 months. The period of the QBO is not directly related to the planet's rotation rate (Plumb and McEwan (1978) and Eqn. 2.4). Because a tidally locked planet does not rotate with respect to its star, the oscillation is also not related to seasonal and annual variations. The shorter period of LASO instead implies stronger wave momentum flux and wave-induced acceleration.

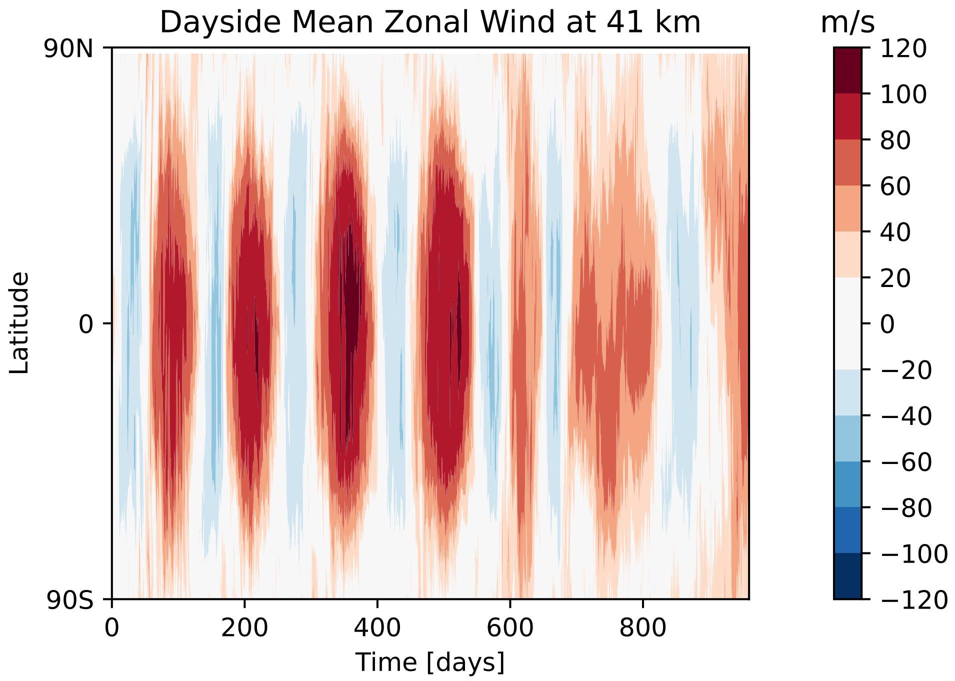

Figure 2.3: Latitudinal extent of the LASO, described by simulation data at a resolution of six hours.

On Earth, up to 80% of the QBO forcing originates from convectively generated gravity waves (Lane, 2015). Figure 2.4 shows that deep convection in my simulation of Proxima Centauri b occurs within an area of $30°$ of the substellar point. This area has the shape of a pointed oval and is asymmetrical, with convection consistently more intense at the western edge of the region. This region of deep convection is collocated with a gravity wave source (as shown in Figure 2.6b). The accepted dependence of the QBO's period on the gravity wave momentum flux as expressed in Equation 2.4 is consistent with the conclusion that greater wave momentum flux, driven by the intense convection, may account for the shorter period of the LASO compared to the QBO on Earth. Accordingly, I find higher wind speeds in the LASO than the QBO. The QBO has maximum eastward winds of 15 ms^{-1} and maximum westward winds of -30 ms^{-1} (Dunkerton et al., 2015), while the LASO's eastward wind speeds reach 100 ms^{-1} and westward winds reach -75 ms^{-1}.

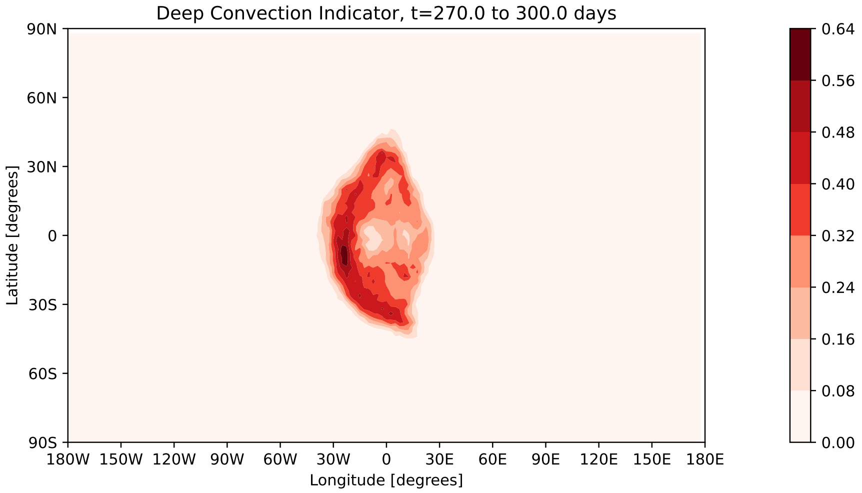

Figure 2.4: Deep convection indicator, averaged over a 30-day period (1: convection is present in the gridbox; 0: not present). In the Unified Model, convection is diagnosed by the surface buoyancy flux and an undilute parcel ascent from grid points where this flux is positive. It is then categorised as deep if the parcel reaches neutral buoyancy above $2.5\mathrm{km}$ or the freezing level (whichever is higher), and if the vertical velocity is greater than $0.02\mathrm{ms}^{-1}$ within a layer at least $1.5\mathrm{km}$ thick above the level of neutral buoyancy (Walters et al., 2019).

2.3.5 Longitudinal asymmetry of the LASO

The LASO exhibits longitudinal asymmetries that do not have an analogy on Earth. I show below that this is related to underlying asymmetries in the steady-state atmospheric dynamics of tidally locked planets and ultimately to the asymmetrical thermal forcing.

As described above, the emergence of the QBO is associated with gravity wave absorption at critical layers in the atmosphere where the speed of the background flow is similar to the phase speed of the wave, leading to wave breaking and the deposition of momentum. Longitudes and heights where the background flow is faster will absorb faster gravity waves and experience stronger acceleration, perpetuating the asymmetry. This accounts for the stronger nightside eastward winds seen in Figure 2.1b, as the nightside experiences higher eastward winds due to the Rossby wave contribution to the zonal wind, as well as for the height at which the LASO has its maximum amplitude (41 km), which is also where the standing Rossby waves are most intense.

The zonal wind does not change direction simultaneously at every longitude. Figure 2.5 shows the temporal variations of the 41 km zonal wind along the equator at two phase transitions, one from eastward to westward and the other from westward to eastward flow. In both transitions, longitudes close to the western terminator transition first, in addition to exhibiting higher wind speeds. Figure 2.5a shows that the westward winds begin to appear around 90°W on days 125–130, while other longitudes transition around days 135–140. The converse is also true

(Figure 2.5b). Wind speeds are consistently highest at 90°–120°W. Close inspection also shows that the antistellar point has a very weak westward phase, with wind speeds of only 5–10 ms^{-1} in some places, compared to 100–120 ms^{-1} during the eastward phase. Periods of westward flow at the antistellar point are comparatively brief. The weakness of the westward phase here implies lower westward acceleration, which may be due to the absorption of westward-propagating gravity waves before they travel around the planet to the nightside, a lack of critical levels available to absorb westward-propagating modes, an asymmetry in the underlying resolved gravity wave spectrum itself, or a combination of these mechanisms.

The amplitude of the LASO is largest at the western terminator and smallest at the antistellar point (Figure 2.5). This pattern cannot be explained directly by the presence of Rossby waves because the equatorial wind vector component contributed by the Rossby waves is larger at the antistellar point than at the western terminator. A possible explanation for the greater amplitude and early phase switching of the oscillation at the western terminator is the presence of a second gravity wave source in this region. The western terminator is a jet exit region where both stratospheric and tropospheric jets decrease rapidly in speed. The steep gradient in wind speeds is caused by the convergence of the two opposing wind vectors contributed by the Rossby wave cyclone-anticyclone pair. Jet exit regions are well-known to be sources of gravity waves (Plougonven & Zhang, 2014). To investigate further, I calculated the Lagrangian Rossby number (Eqn. 2.5).

Figure 2.6a shows that at 41 km, where the LASO reaches its maximum amplitude, a strong gravity wave source is present at the western terminator. In the troposphere, unbalanced flows are found in the region of deep convection (Figure 2.6b and Figure 2.4). The equatorial altitude-longitude cross-section (Figure 2.6c) confirms that areas of instability that can generate gravity waves occur preferentially westward of the substellar point in the troposphere and around the western terminator in the lower stratosphere. To link wave acceleration to the jet exit region, Figure 2.6d shows the gravity wave-induced acceleration at the equator (as calculated in Figure 2.2), overlaid with the zonal wind. The strongest acceleration is found at the jet exit region for both the tropospheric and the lowest stratospheric jets between 20–45 km. The western terminator both generates gravity waves due to the slowing of the jet speeds in this region and also absorbs high-energy gravity waves because this is where the critical levels exhibit the highest wind speeds. The result is a particularly unstable region where zonal winds reverse earlier than elsewhere and may oscillate back and forth in shorter time periods, as seen in Figure 2.5a between 125–145 days and 120°–90°W.

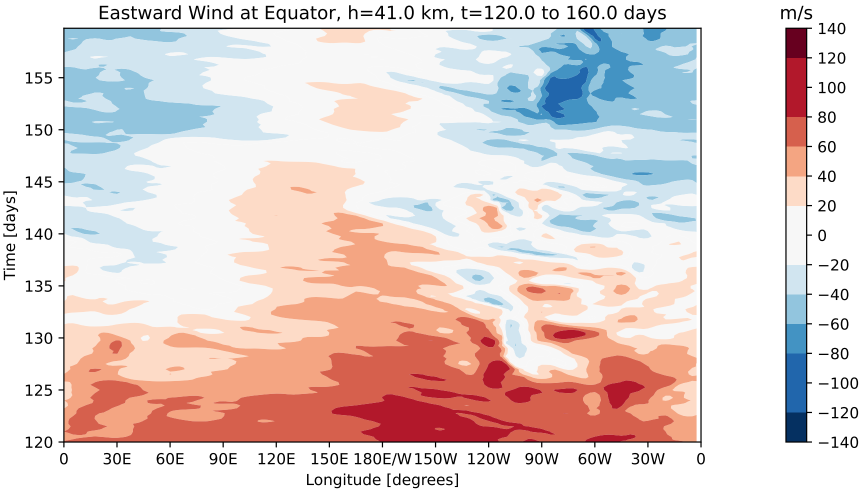

(a) Transition from eastward to westward phase at 41 km

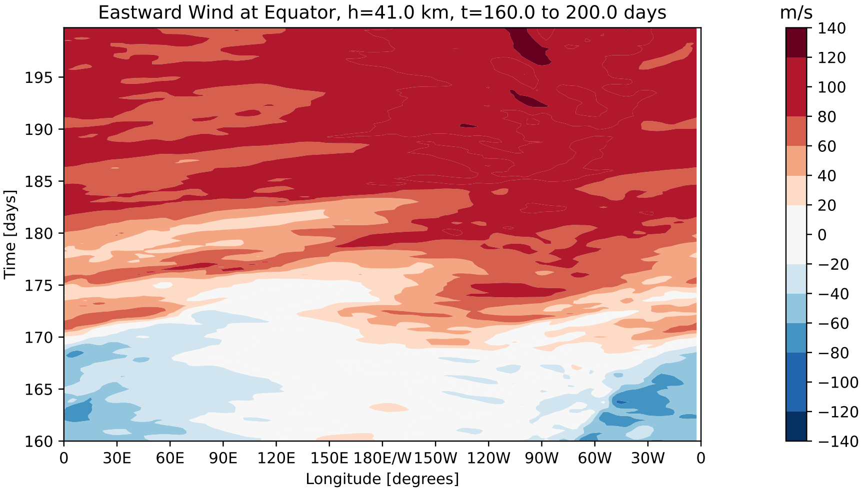

(b) Transition from westward to eastward at 41 km

Figure 2.5: Equatorial zonal wind speeds at 41 km over two 40-day periods, determined by six-hourly simulation data. The top panel shows the transition from eastward to westward winds and the bottom panel shows the transition from westward to eastward winds. Plots are centred on the antistellar point to highlight the tendency to resist westward flow in this region.

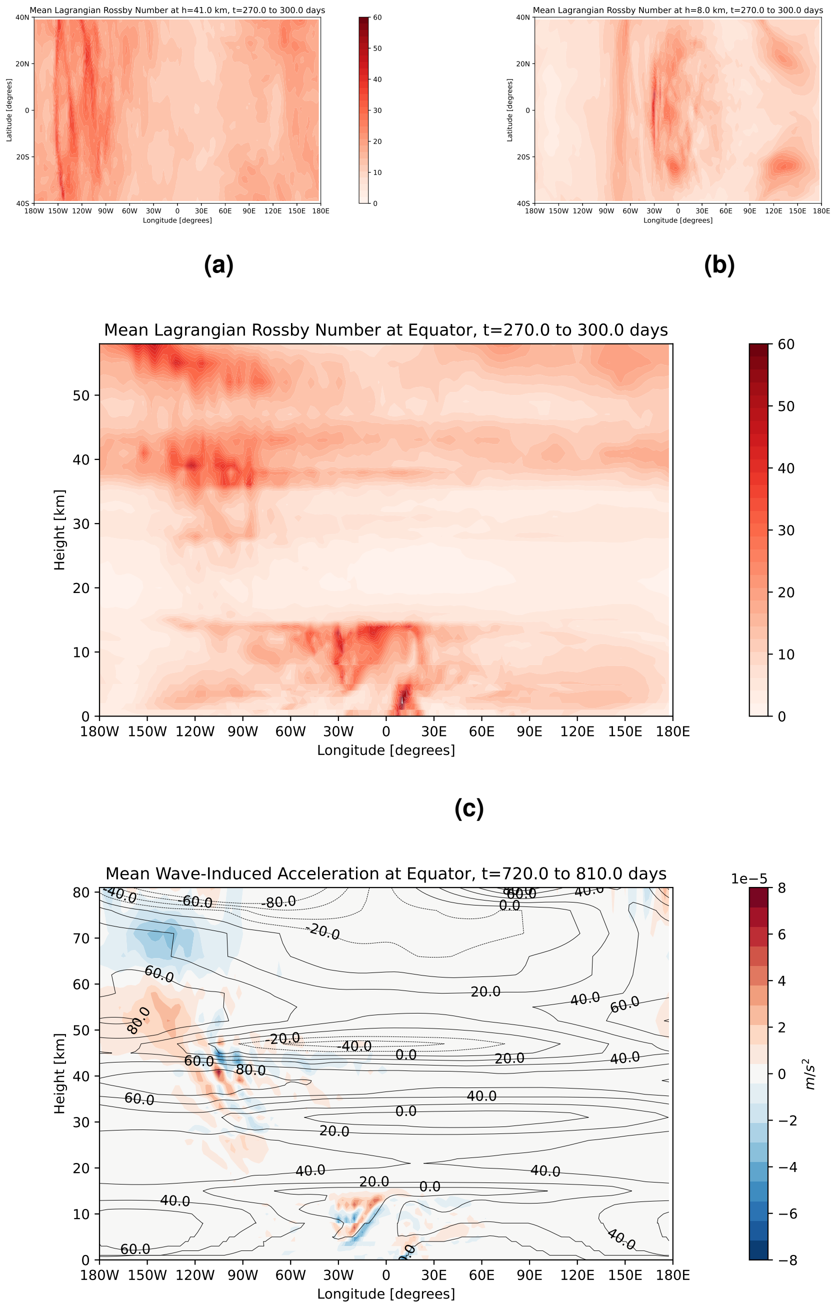

Mean Lagrangian Rossby Number at h=41.0 km, t=270.0 to 300.0 days

Mean Lagrangian Rossby Number at h=8.0 km, t=270.0 to 300.0 days

(a)

(b)

Mean Lagrangian Rossby Number at Equator, t=270.0 to 300.0 days

(c)

Mean Wave-Induced Acceleration at Equator, t=720.0 to 810.0 days

(d)

Figure 2.6: The Lagrangian Rossby number, normalised by its minimum value in the dataset and averaged over the same 30-day period shown in Figure 2.4, at a) 41 km and b) 8 km, and c) the corresponding height-longitude cross-section at the equator. I exclude the top five model levels and the high latitudes to avoid including model instability at the model top and poles. d) The height-longitude cross-section of gravity wave-induced acceleration over the same time period as Figure 2.2, overlaid with the 90-day time-mean zonal wind as contour lines.

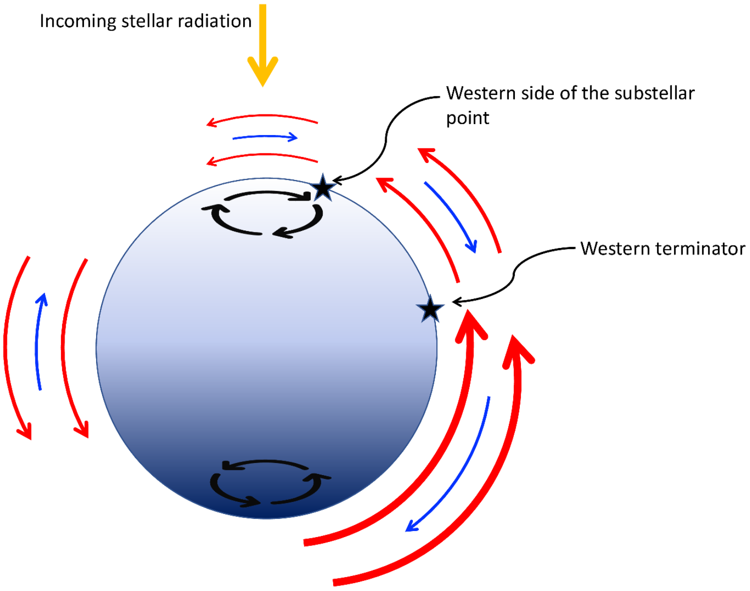

Figure 2.7: Schematic diagram of the location and interaction of Rossby waves, equatorial jets, and gravity wave sources. The perspective is looking downward from the north pole. The lighter side of the sphere is the dayside and the darker is the nightside. Red (blue) arrows indicate eastward (westward) air flow, with larger arrows representing faster wind speeds. Black spirals represent Rossby waves. The star symbol indicates gravity wave sources.

In summary, as discussed above, the LASO is shaped by interactions between multiple components of the circulation typical of tidally locked planets. Figure 2.7 shows a schematic illustration of the interplay between standing Rossby waves, the superrotating tropospheric jet, and the resolved gravity wave sources in the substellar region and at the western terminators. The diagram represents the mean circulation generated with the standard, globally invariant parameterised gravity wave source.

2.3.6 Atmospheric water vapour oscillations

On Earth, the oscillation of the zonal wind direction is associated with variations in the amount of atmospheric water vapour of the order of ±10% (Randel, Wu, Russell, Roche, & Waters, 1998; T. Wang, Zhang, Hannachi, Hirooka, & Hegglin, 2020). An analogous oscillation on exoplanets is of interest because large fluctuations in atmospheric water vapour may be observable. In my simulations, specific humidity at 41 km varies about ±50% on average, with peak oscillations up to 200% of the mean. This results in oscillations with minimum and maximum values that can differ by an order of magnitude.

To test whether a fluctuation of this magnitude would be detectable, I generated synthetic planetary spectra as observed by the NIRSpec instrument aboard JWST for the above maximum and minimum water vapour concentrations. As shown in Figure 2.8, the relative transit depths of the water vapour absorption line at 2.8 μm differ by approximately 0.13 ppm. The baseline relative transit depths calculated by the PSG for the water vapour absorption lines in my simulation are 5-10 ppm, so the difference amounts to $1-2\%$. These transit depths and fluctuations are too small to be observable for an Earth-sized planet like Proxima Centauri b, but as QBO-like phenomena have also been detected on Jupiter and Saturn in the solar system (Leovy, Friedson, & Orton, 1991; Orton et al., 1991; A. P. Showman et al., 2019), a LASO could occur on a larger planet with greater potential for observation. This could be particularly important for short-period, potentially tidally locked, super-Earth or mini-Neptune-type planets detected by missions such as the Transiting Exoplanet Survey Satellite (see Bluhm et al. (2021) for a recent example). A future telescope concept such as NASA's Large Ultraviolet Optical Infrared Surveyor (LUVOIR) may have sufficient sensitivity to detect water vapour absorption lines for terrestrial exoplanets, but the small size of the fluctuation indicates that choice of target will still be paramount for detection of a LASO or QBO-like oscillation.

2.3.7 Sensitivity tests

I performed three sensitivity tests: one with a horizontal resolution of 1° latitude by 1.25° longitude (double the resolution of the control simulation), one with a timestep of 2 minutes (compared to 20 minutes for the control), and one with the precipitation-dependent parameterised gravity wave source described in Section 2.2, which localises the launch of parameterised gravity waves in the substellar region. Table 2.3 summarises the results in comparison to the control simulation, showing that the sensitivity tests do not significantly impact my findings. The mean period ranges from $5-6.7$ months, which compares favourably to the control simulation's mean of 6 months and range of $5-6.5$ months. I did not observe significant differences in the latitudinal extent or amplitude of the oscillation of the zonal wind. The vertical wind shear is noticeably less in the 1°x1.25° simulation, leading to a smaller temperature oscillation of approximately 20K peak-to-peak, as predicted by Equation 2.1. All three tests show longitudinal asymmetry in the zonal wind, with maximum wind speeds in the nightside quadrant of 90W-180W and minima on the dayside between 0-90E. The localised gravity wave source leads to only slightly greater asymmetry than the control simulation, in line with the QBO theory that the existence and location of critical levels in the atmosphere (i.e. the background flow) is more critical in shaping the oscillation than the location of gravity wave sources. In contrast, longitudinal asymmetry is lower, though still present, in the short timestep and especially the high resolution test. Qualitatively, both the short timestep and high resolution tests also have a less regular structure, particularly at higher altitudes near the top of the vertical extent of the oscillation.

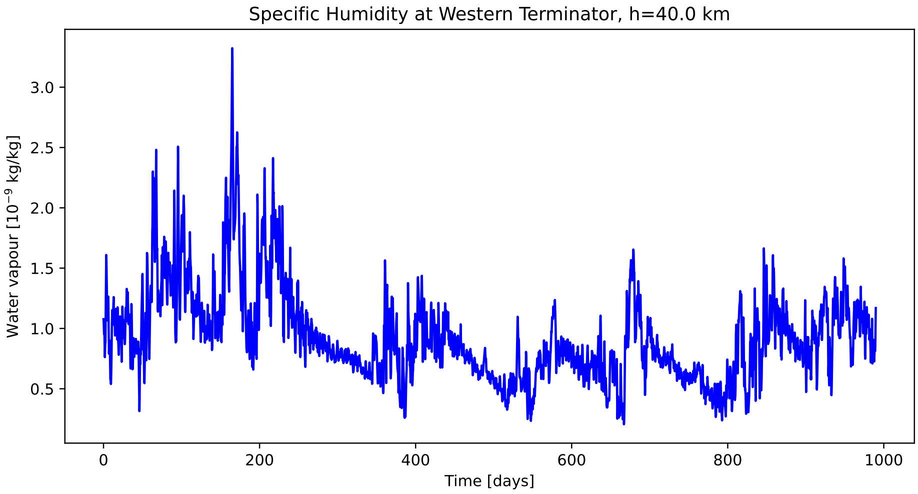

(a) Oscillation in water vapour content of the atmosphere at the western terminator at 40 km

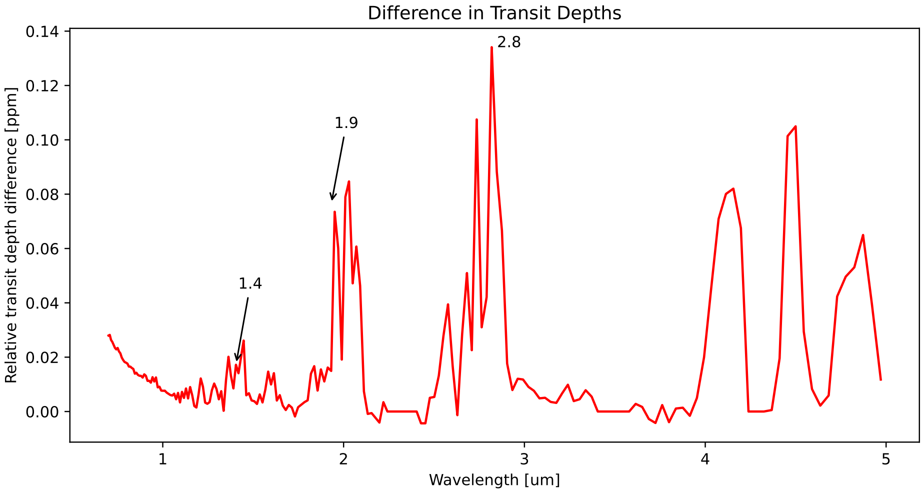

(b) Difference in relative transit depths of observations simulated during the maximum and minimum of the vapour oscillation

Figure 2.8: (a) Water vapour content averaged over 4S to 4N and 95W to 85W. The mean specific humidity is 0.93 $\times 10^{-9}$ kg/kg, with a maximum and minimum of 3.3 and 0.2 $\times 10^{-9}$ kg/kg, respectively. (b) Difference in transit depths simulated at the maximum and minimum of the oscillation, arrows highlighting water vapour absorption lines.

Simulation	Mean period (months)	Max. east/west wind at 41 km (m/s)	Latitudinal extent (°)	Mean long. asymmetry (m/s)	Mean wind shear (m/s/km)
Control	6	120/-50	60	65	15
Resolution 1°x1.25°	6.2	120/-60	60	28	5
Timestep 2 min	6.7	125/-50	60	47	15
Localised GW source	5	120/-50	60	71	11

Table 2.3: Results of three sensitivity runs compared to the control simulation. The mean longitudinal asymmetry refers to the mean difference over the simulation time between the maximum and minimum zonal wind speeds at the equator.

2.4 Discussion

Using a global 3-D climate model I show that Earth-like tidally locked planets can exhibit a longitudinally asymmetric stratospheric wind oscillation (LASO), analogous to the quasi-biennial oscillation (QBO) on Earth. As QBO-like oscillations are also known to exist on Jupiter and Saturn (Leovy et al., 1991; Orton et al., 1991; A. P. Showman et al., 2019), my finding suggests a similar conclusion for gas giants. The LASO reported in my study has implications for the climatology and observations of tidally locked exoplanets, as well as for our understanding of GCM results.

2.4.1 Oscillations in meteorological and atmospheric composition

The QBO on Earth is responsible for oscillations in the abundance of many atmospheric species, notably ozone and methane (Bowman, 1989; Huang et al., 2008; Li, Palmer, Pumphrey, Bernath, & Mahieu, 2009; Randel et al., 1998). In this study, I have focused on the characteristics and acceleration of the LASO. By including atmospheric chemical kinetics, future work could also explore LASO-induced variations in species important for observations. For example, Earth's total ozone column fluctuates by ±1 ppm ($\sim$ 4%) on the 26–28 month timescale of the QBO. A variation of this magnitude is unlikely to be detectable with existing instrumentation, but an ozone column oscillation may be larger in amplitude on a tidally locked planet than on Earth, in line with my simulation results for water vapour. Studies of ozone photochemistry on tidally locked planets (Chen et al., 2018; Yates et al., 2020) have also shown that the planet's nightside accumulates ozone in its cold traps, resulting in a zonally asymmetrical ozone layer without analogy on Earth and high levels of ozone in one hemisphere. Future work could explore how this tidally locked ozone chemistry would interact with oscillations in dayside production of ozone through stratospheric photochemistry. In addition, LASO-related temperature anomalies in my simulation reach 40–50 K ($\sim$ 25% deviation from the mean), while the QBO of temperature on Earth is limited to 1–2 K (Tegtmeier et al., 2020). Large variations in air temperature will also potentially affect measurements of thermal emission spectra from the atmosphere.

2.4.2 Sensitivity to model parameterisations

Gravity wave parametrisation schemes and differences in ability to generate a QBO-like phenomenon may account for some of the differences found in modelling studies of the same exoplanet. For example, predicted nighttime surface temperatures for Proxima Centauri b diverge by 50 K in different studies (e.g. Boutle et al. (2017); Turbet et al. (2016)), a discrepancy that can only be partly explained by differences in stellar irradiation used by these studies. Boutle et al. (2017) instead proposed that these temperature discrepancies could be explained by differences in convection parameterizations and model resolutions, which affect the water vapour profile and consequently the dayside-nightside heat transport. Gravity wave parameterisations likewise vary between models and Watkins and Cho (2010) have shown that gravity waves can have a significant impact on the development of the background flow, temperature, and heat redistribution from dayside to nightside on tidally locked planets. Gravity waves can become trapped within jets and travel longitudinally from the gravity wave source on the dayside until the jet speed develops a critical level where the wave can be absorbed (Nappo, 2012; Pitteway & Hines, 1965). Differing gravity wave schemes may therefore result in different predictions for heat redistribution and dayside-nightside temperature contrast (Watkins & Cho, 2010).

2.4.3 The importance of the western terminator for atmospheric dynamics

My results identify the western terminator as a region of particular complexity. At the equatorial western terminator, the zonal wind components contributed by the standing Rossby waves on the dayside and nightside meet and oppose each other. I have also shown in Figure 2.6 that the western terminator is a jet exit region where the flow is unbalanced and internal gravity waves are generated and locally reabsorbed. These factors lead to significant turbulence and variability due to the interplay between these elements. As transit spectroscopy is expected to be a key tool in constraining the composition of exoplanet atmospheres, understanding the dynamics of the terminator regions of tidally locked planets is important to interpreting the results of observational studies. If the time scale of an oscillation is longer than the observing window, observers may view the planet in a low-temperature/high-temperature or low-abundance/high-abundance phase of an oscillation. As I noted above, a LASO on a hot Jupiter could be intense enough to be detectable. The high amplitude of the oscillation at the western terminator, a critical region for transit spectroscopy, suggests that the LASO should be studied on tidally locked hot Jupiters to determine its possible impact on observations.

2.4.4 Reproducibility using other GCMs

I have presented the first simulation of a QBO-like phenomenon on an exoplanet. Previous exoplanet modelling studies have not observed stratospheric variability because of a prevailing focus on mean climate states and the lower atmosphere, with only few exceptions (e.g. Carone et al. (2018); Skinner and Cho (2022)). In addition, many Earth GCMs fail to generate a realistic QBO. The Stratosphere-troposphere Processes and their Role in Climate (SPARC) QBO initiative (QBOi), a systematic comparison of the performance of GCMs, including the Met Office Unified Model, in reproducing a realistic QBO, found that only five out of 47 models spontaneously generated a QBO (Butchart et al., 2018). Reproducing the LASO in another tidally locked exoplanet GCM would be beneficial to evaluate the sensitivity of the simulation results to factors such as the non-orographic gravity wave (NOGW) parameterisation. As part of the SPARC QBOi, A. C. Bushell et al. (2020) compared the ability of 13 Earth GCMs to simulate a range of observed features of the QBO. Only one model, MIROC-AGCM-LL, was able to generate a QBO with accelerations from resolved gravity waves only, and the accuracy of this simulation was the lowest; all other models in the comparison required NOGW parameterisation schemes to achieve a QBO. Across the models compared, $40-80\%$ of the wave forcing came from parameterised waves, with a mean of 70% and a value for the UM of 80%. This indicates that the gravity wave parameterisation scheme may have a large effect on the amplitude and period of the simulated oscillation. The NOGW parameterisation used in the Unified Model (Warner & McIntyre, 1996) is the most common in the SPARC QBOi comparison. A good GCM candidate for reproducing the LASO would be ExoCAM (Wolf, Kopparapu, Haqq-Misra, & Fauchez, 2022), which uses components from the National Center for Atmospheric Research Community Atmosphere Model 4 or 5 (CAM4/CAM5) and from the Community Earth System Model (CESM). A. C. Bushell et al. (2020) found that CAM5 run with 60 atmospheric levels generated the overall most realistic QBO and CESM1 was on par with the UM. Additionally, CAM5 and CESM1 use a different gravity wave parameterisation than the UM, enhancing the value of the comparison.

2.5 Conclusion

Using a global 3-D general circulation model, I reported the discovery of a phenomenon analogous to Earth's quasi-biennial oscillation (QBO) in simulations of the atmosphere of an Earth-like tidally locked planet, nominally Proxima Centauri b. As the phenomenon exhibits asymmetries related to the tidal locking, I refer to it as the longitudinally asymmetric stratospheric oscillation (LASO). The LASO begins above the tropospheric equatorial superrotating jet and extends vertically from roughly 35–55 km. It consists of a periodic reversal in the direction of the zonal winds within this region, accompanied by oscillations in temperature. I found the LASO in my simulation to have a latitudinal extent of $\pm$ 60° and a period of 5–6.5 Earth months. The shorter period compared to its Earth counterpart is explained to a first order by stronger wave driving from gravity wave generation in the deep convection zone at the substellar point. I also identified a secondary gravity wave source in the jet exit region at the western terminator. My analysis found that wind speeds in the LASO reach a maximum at the western terminator and that reversals of direction at the western terminator precede those at other longitudes. I further found that the antistellar point experiences a very weak oscillation: zonal winds are preferentially eastward-flowing, with only brief and low-speed westward phases.

My results highlight the significance of atmospheric variability in global 3-D simulations of exoplanets and point towards a need for further studies to investigate this largely uncharted territory. In this initial study, I focused on the characteristics and mechanism of the LASO and did not explore the potential effect of oscillations in abundances of atmospheric species other than water vapour on exoplanet observations. Future work in this area could use a 3-D model with online atmospheric chemistry such as presented in Yates et al. (2020) to explore such effects. While I performed sensitivity tests by varying the horizontal and temporal resolution, I expect that the LASO's fundamental dependence on the planet's mean circulation will make it sensitive to factors that alter the planet's atmospheric dynamics, such as different atmospheric compositions, the presence of land, and the planet's rotation rate. On the Earth, the QBO is also known to interact with other dynamical phenomena such as the semi-annual oscillation, Madden-Julian oscillation (Martin et al., 2021), and polar vortex. I leave such potential interactions between the LASO and similar sources of variability in the atmosphere for future work.

As the body of observational data from exoplanets grows in the coming decades, my understanding of the parameter space for planetary climate states must grow with it. This parameter space includes time-dependent atmospheric phenomena such as the one I describe in this paper which, even if they are familiar features on Earth, will inevitably take new forms on tidally locked planets. Characterisation of the sources and properties of atmospheric variability on tidally locked exoplanets promises to refine our interpretations of observations and, in the case of terrestrial planets, deepen our understanding of the Earth in the context of the larger population of planets inside and outside the solar system.

Chapter 3

Traveling planetary-scale waves cause cloud variability on tidally locked aquaplanets

(**Author contributions:** This work has been published in Cohen, Bollasina, Sergeev, Palmer, and Mayne (2023). I ran the simulations, performed the analysis, and wrote the paper. Massimo Bollasina and Paul Palmer supervised the work and edited the text. Denis Sergeev and Nathan Mayne contributed to development of the model and provided feedback on the text.)

3.1 Introduction

The capabilities of the James Webb Space Telescope (JWST) have raised the prospect of characterizing the atmospheres of transiting exoplanets through transmission spectroscopy (Beichman et al., 2014; Greene et al., 2016; Mollière et al., 2017). Particular interest has focused on the characterization of rocky and temperate planets orbiting at distances from their host stars that would allow liquid water to exist on their surfaces (Gialluca et al., 2021; Morley et al., 2017). A number of terrestrial planets have been found in this range of orbital distances, known as the habitable zone (J. F. Kasting et al., 1993), including the non-transiting Proxima Centauri b (Anglada-Escudé et al., 2016) in orbit around the closest star to Earth, Proxima Centauri, and three transiting planets in orbit around the star TRAPPIST-1 (Gillon et al., 2017). These planets are thought to be tidally locked to their host stars as a result of their close-in orbits (Barnes, 2017), and indeed tidally locked planets around M-dwarf stars may be the most common type of potentially habitable planet (Dressing & Charbonneau, 2015; R. K. Kopparapu, 2013).

A challenge for transmission spectroscopy of transiting exoplanets is the presence of clouds, which mute spectroscopic features by scattering light isotropically at the level of the cloud deck (Barstow, 2021; Helling, 2019). Clouds are believed to exist on multiple known exoplanets (Burningham et al., 2021; Helling et al., 2021; Kreidberg et al., 2014). Modelling studies of the impact of clouds on the transmission spectra of water-rich rocky planets have indicated that in most cases it would take anywhere from ten to hundreds of transits to detect atmospheric absorption features using the JWST (Fauchez et al., 2019; Komacek et al., 2020; Suissa et al., 2020). Available observations of the planets in the TRAPPIST-1 system have ruled out hydrogen-rich primordial atmospheres for these planets (de Wit et al., 2016; Garcia et al., 2022; Moran, 2018), but are unable to break the degeneracy between a cloud- or aerosol-heavy atmosphere, a high molecular mean weight atmosphere, or the absence of an atmosphere, although the JWST may be able to do so in future (Lustig-Yaeger, Meadows, & Lincowski, 2019). Some work has offered brighter prospects of the detection of water vapor on arid (icy) planets (Ding & Wordsworth, 2022) and found that stratospheric (as opposed to tropospheric) clouds would not necessarily affect observations by the JWST (Doshi, Cowan, & Huang, 2022). As water-rich planets are expected to form substantial cloud decks, this limitation is a significant obstacle to the detection of atmospheric chemistry and potential biosignatures on water-rich habitable worlds.

One possible avenue for characterizing water-rich planets is temporal variability in cloud cover. Studies of exoplanet variability are extremely limited so far, but variable wind speeds may have been detected on KELT-9b (Asnodkar et al., 2022) and variation in the offset of the peak of the phase curve of HAT-P-7b was reported by Armstrong et al. (2016) and later disputed by Lally and Vanderburg (2022). Some theoretical (Line & Parmentier, 2016; Powell et al., 2019; Welbanks & Madhusudhan, 2022) and observational (Ehrenreich et al., 2020; Mikal-Evans et al., 2022) studies have found that it may be possible to detect spatial variability in cloud cover at the planetary terminators of large exoplanets. In a one-dimensional model, Tan and Komacek (2019) found that cloud radiative feedback can drive atmospheric variability on brown dwarfs and giant planets.Hochman et al. (2022) used a dynamical systems approach to show that the climate of a tidally locked rocky planet was overall more sensitive to changes in basic parameters (CO_2 partial pressure in their study) than that of Earth, noting that tidally locked M-dwarf planets may have climate variability similar to Earth's seasons even with zero obliquity and eccentricity. Of most relevance, Song and Yang (2021) Fauchez et al. (2022), and May et al. (2021) simulated the effect of cloud variability on transmission spectra and atmospheric retrievals of TRAPPIST-1e. Song and Yang (2021) found both spatial asymmetry in transit depths when comparing the eastern and western terminators and temporal variability in the transmission spectra. In their study using the ExoCAM general circulation model, the authors found no periodicity in the time series of transit depths. In May et al. (2021), general circulation model simulations also performed with ExoCAM likewise exhibited cloud cover variability at the planetary limb. The authors combined ten synthetic spectra randomly chosen from a time series of 365 days of the planet's climate and used the resulting composite spectrum to retrieve atmospheric chemical abundances, finding that this did not result in a difference compared to the use of non-variable spectra. However, May et al. (2021) did not study the cause of the cloud variability in their simulations or look for periodicities. An understanding of the physics of cloud and climate variability is necessary to confirm that this variability is not noise and to explain why different models predict vastly different degrees of variability.

In this work, I describe a dynamical mechanism driving cloud and climate variability in the atmospheres of moist tidally locked terrestrial exoplanets and investigate its impact on time series of transmission spectra. In Section 3.2, I describe the general circulation model, simulation parameter space, and radiative transfer scheme for simulating transmission spectra. In Section 3.3, I outline a feedback loop between cloud radiative effects, incoming stellar radiation, and the dynamical state of the atmosphere that causes back-and-forth propagation or shifting of planetary-scale (Rossby) waves and regular variations in cloud cover at the planetary limb. I further discuss the interaction between the propagating Rossby gyres and the dayside cloud structure and simulate time series for the water absorption feature at 1.4 μm and the carbon dioxide feature at 2.7 μm. My results support the findings of Song and Yang (2021), May et al. (2021) and Fauchez et al. (2022) that cloud variability is unlikely to affect JWST observations, except in specific cases where the cloud structure and wave propagation may interact in a fortuitous way. In Section 3.4, I discuss my results in the context of previous work on Rossby wave structures on tidally locked planets, as well as implications of dynamical variability for the planetary climate and for observational practices. I conclude in Section 3.5.

3.2 Methods

3.2.1 Model description

The simulations are based on the Global Atmosphere 7.0 (GA7) configuration of the Met Office Unified Model (UM). Idealized versions of the UM have previously been used to simulate hot Jupiters (Christie et al., 2021; Mayne, Baraffe, Acreman, Smith, Browning, et al., 2014; Mayne et al., 2017; Zamyatina et al., 2023) and terrestrial planets (Boutle et al., 2017; Braam et al., 2022; Eager-Nash et al., 2020; Sergeev, Lewis, et al., 2022). The model uses the ENDGame (Even Newer Dynamics for General atmospheric modelling of the environment) dynamical core to solve the non-hydrostatic, fully compressible, deep-atmosphere Navier-Stokes equations (Wood et al., 2014). GA7 contains parameterizations for sub-grid scale turbulence, convection, non-orographic gravity wave drag, boundary layer processes, precipitation, and clouds. Radiative transfer is simulated using the SOCRATES (Suite Of Community RAdiative Transfer codes based on Edwards and Slingo) community radiative transfer code.

Parameter	Control ProxB	Warm ProxB	Control TRAP-1e	Warm TRAP-1e	Dry TRAP-1e
Semi-major axis (AU)	0.0485	0.0423	0.029	0.025	0.029
Stellar irradiance (W m^{-2})	881.7	1100.2	837.7	1392.9	837.7
Orbital period (Earth days)	11.2	9.2	6.1	4.2	6.1
Rotation speed (rad s^{-1})	6.501×10^{-6}	7.933×10^{-6}	1.192×10^{-5}	1.746×10^{-5}	1.192×10^{-5}
Eccentricity (·)	0	0	0	0	0
Obliquity (·)	0	0	0	0	0
Radius (km)	7160	7160	5797	5797	5797
Acceleration due to gravity (m s^{-2})	10.9	10.9	9.1	9.1	9.1
CO_2 (ppmv)	378	378	400	400	400
Number of levels (·)	60	60	39	39	39
Model top (km)	85	85	80	80	80

Table 3.1: Model parameters for all simulations

All simulations are run at a resolution of 2° latitude by 2.5° longitude. The substellar point is defined to be at 0° longitude and latitude, while the antistellar point is located at 180° longitude and the eastern and western terminators at 90°E and 90°W, respectively. “Days” refers to Earth days throughout this work.

The UM has a fully prognostic cloud scheme, the Prognostic Cloud fraction and Prognostic Condensate (PC2) scheme (Wilson, Bushell, Kerr-Munslow, Price, & Morcrette, 2008). The scheme has three prognostic cloud fractions (liquid, ice, and mixed-phase), as well as water vapor and liquid and frozen condensate. These prognostic variables are updated in increments by processes in the model, including advection, convection, and precipitation. The column cloud fraction is determined by exponential random overlap. The moist atmosphere configuration includes water vapor with evaporation and precipitation and an otherwise 100 % nitrogen atmosphere with fixed trace CO_2. In the TRAPPIST-1 Habitable Atmosphere Intercomparison (THAI) (Sergeev, Fauchez, et al., 2022), the UM’s cloud scheme produced a mean cloud fraction in the middle of the comparison (60 %), compared to the extremes of the Laboratoire de Météorologie Dynamique - Generic model (LMD-G, at 28 %) and the Resolving Orbital and Climate Keys of Earth and Extraterrestrial Environments with Dynamics model (ROCKE-3D, at 77 %).

3.2.2 Simulation parameters

I performed five simulations:

1. A “control” moist Proxima Centauri b with planetary and orbital parameters as described in Anglada-Escudé et al. (2016) (Control ProxB)
2. A “warm” moist Proxima Centauri b with planetary and orbital parameters corresponding to the inner edge of Proxima Centauri’s habitable zone (Warm ProxB)
3. A “control” moist TRAPPIST-1e with planetary and orbital parameters as described in Gillon et al. (2017) (Control TRAP-1e)
4. A “warm” moist TRAPPIST-1e with planetary and orbital parameters corresponding to the inner edge of TRAPPIST-1’s habitable zone (Warm TRAP-1e)

5. A "dry" TRAPPIST-1e atmosphere identical to the control case aside from the dry atmosphere (Dry TRAP-1e)

Table 3.1 lists the values of the parameters varied between each simulation. These parameters were chosen to facilitate comparison with previous UM studies of the two planets. The simulation set-up for Proxima Centauri b is based on Boutle et al. (2017) and Cohen et al. (2022), using a model top of 85 km with 60 vertical levels, quadratically stretched to give greater resolution near the surface. The planet is simulated with a slab ocean (Frierson et al., 2006) which has a mixing depth of 2.4 m, representing a heat capacity of 10^7 J K^{-1} m^{-2}. The stellar spectrum for Proxima Centauri, modelled as a quiescent M-dwarf, was taken from BT-Settl (Rajpurohit et al., 2013) with $T_{eff} = 3000$ K, g= $1000\mathrm{ms}^{-2}$, and metallicity $= 0.3$ dex. The Proxima Centauri b simulations were spun up from an equilibrium state of a previous simulation performed using the UM with the same configuration.

For TRAPPIST-1e, I use the simulation parameters of the TRAPPIST-1 Habitable Atmosphere Intercomparison for both the dry and the moist atmosphere cases (Fauchez et al., 2021, 2022; Sergeev, Fauchez, et al., 2022; Turbet et al., 2022). In this instance, the models use 39 vertical levels with a top of 80 km. The planet's surface in the moist case is a slab ocean with a mixing layer of 1 m, representing a heat capacity of 4×10^6 J K^{-1} m^{-2}. The spectrum is taken from BT-Settl (Rajpurohit et al., 2013) with $T_{eff} = 2600$ K and Fe/H=0. The TRAPPIST-1e simulations were spun up from an initial state of an isothermal (300K) dry atmosphere at rest with zero winds, following the THAI protocol (Fauchez et al., 2020). Unlike in the THAI project, my simulations were run with the UM's gravity wave drag scheme switched on, resulting in some differences in the wind structure.

All the simulations correspond to tidally locked planets. The Control ProxB, Warm ProxB, Control TRAP-1e, and Dry TRAP-1e simulations were run until a balance between incoming and outgoing radiation at top-of-atmosphere was achieved. Control ProxB, Warm ProxB, and Control TRAP-1e ran for 6,000 days and the period from day 5,000 to 6,000 was sampled for analysis. The Warm TRAP-1e simulation underwent a runaway greenhouse effect, with convection reaching the model top after approximately 4,000 days. I sampled a 990-day period (day 3,000 to the crash just before day 4,000) and include the results here to study the extreme limit of the habitable zone and in particular the potential effect of cloud variability on observations of close-in rocky planets (Venus analogues). As the Dry TRAP-1e simulation achieved radiative balance faster than the moist atmospheres, I ran the simulation for 4,000 days and used the period from day 3,000 to 4,000 for analysis. In the results reported below,"day 10" and similar formulations refer to the day of the sample period, not the day of the simulation.

I performed one sensitivity test to investigate the effect of slab ocean depth on the period and amplitude of the variability. The slab ocean could potentially affect atmospheric variability because sea surface temperature is a direct forcing of the atmospheric circulation. I repeated the Control TRAP-1e simulation with a 50 m slab ocean instead of 1.0 m. I found no significant differences in the period and amplitude of the cloud cover oscillation described below and negligible differences in the climatology.

3.2.3 NASA Planetary Spectrum Generator

I use the NASA Planetary Spectrum Generator (Villanueva et al., 2018), publicly available at `https://psg.gsfc.nasa.gov/` (PSG), to simulate time series of water vapor and carbon dioxide features of the four moist atmosphere simulations as observed by the JWST's NIRSpec (Near Infrared Spectrograph) instrument. I omit the dry case as it has no time-varying atmospheric chemistry or clouds. The NIRSpec instrument's range covers water vapor features in the infrared at 1.4, 1.8, and 2.7 $\mu\mathrm{m}$, as well as CO_2 features at 2.1, 2.7, and 4.3 $\mu\mathrm{m}$ (Ahrer et al., 2023). For each simulated atmosphere, I prescribe the orbital, planetary, and stellar parameters shown in Table 3.1, together with the pressure, temperature, altitude, H_2O, N_2, and CO_2 data from the UM. For the Proxima Centauri b simulations, the 85 km model top was sufficient for the PSG to calculate a spectrum, and I use only the model output data. For the TRAPPIST-1e simulations, however, the 80 km model top was slightly too low to enable the PSG to model the spectrum. I used the Met Office's *iris* package's built-in linear extrapolation method to extend the temperature, H_2O, ice cloud, liquid cloud, N_2 and CO_2 profiles to one extra atmospheric level with an altitude of 85 km and half the pressure of the layer immediately below (MetOffice, 2010). Previous works have used the PSG to generate a spectrum for each grid box and averaged the spectra for a final output representing the signal during transit (Komacek et al., 2020; May et al., 2021; Suissa et al., 2020). To reduce the computational expense of simulating long time series for multiple simulations and absorption features, I instead average the atmospheric values for each day around the limb first, generate a transit spectrum for each day, and extract and plot the absorption features against time.

3.3 Results

3.3.1 Climatology

Boutle et al. (2017) and Sergeev et al. (2020) present a detailed climatology of Proxima Centauri b as simulated by the UM. Similarly, a full description of the climatology of TRAPPIST-1e as simulated by the UM with a dry and moist atmosphere is given in Turbet et al. (2022) and Sergeev, Fauchez, et al. (2022), respectively. I give a brief overview of the equilibrium climates of all five simulations here.

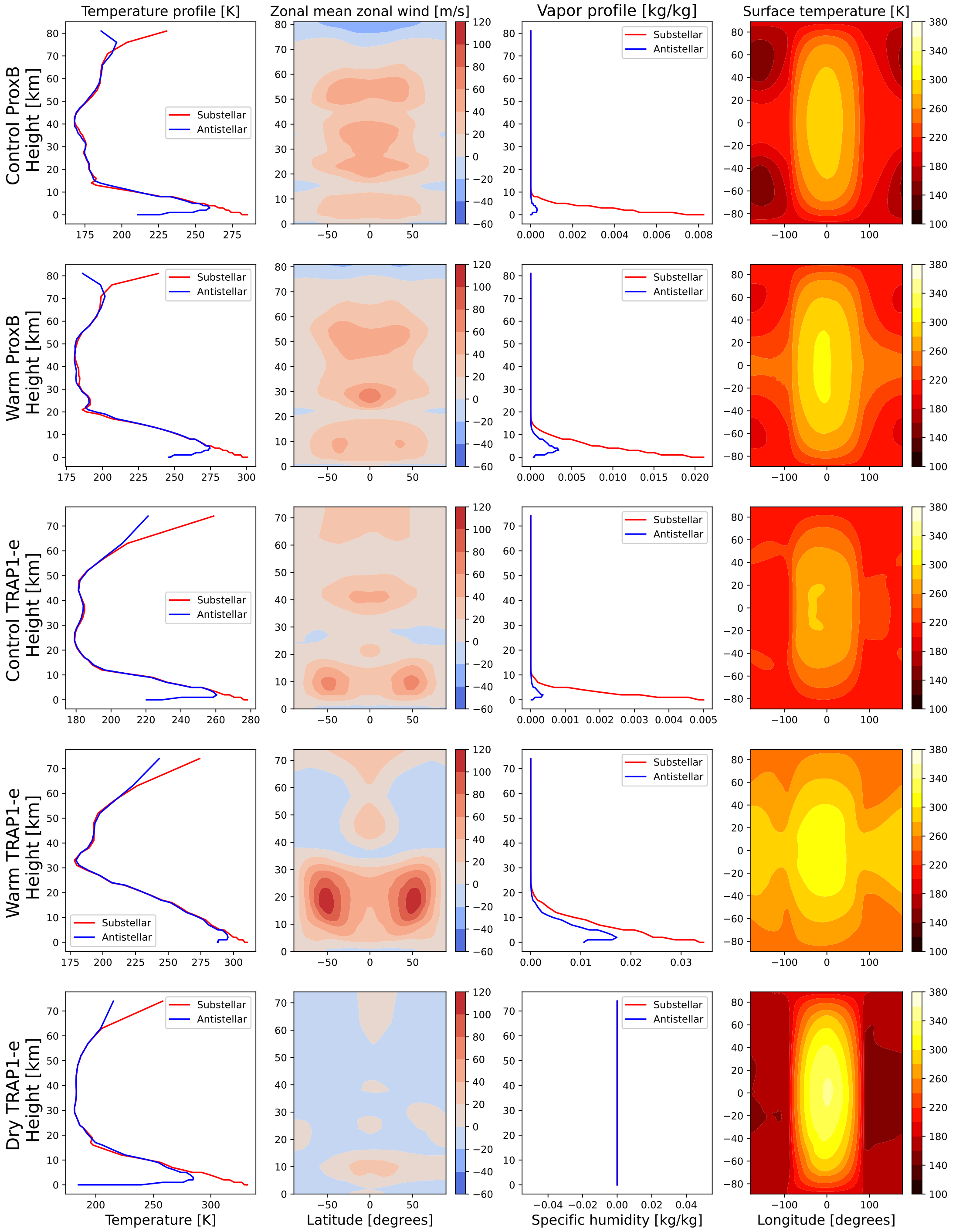

Figure 3.1: Comparative climatology of the five simulations, showing (from left to right) the vertical temperature profile at the substellar and antistellar point, the zonal mean zonal wind, the vertical water vapor profile at the substellar and antistellar point, and the surface temperature. From top row to bottom row: Control ProxB, Warm ProxB, Control TRAP-1e, Warm TRAP-1e, Dry TRAP-1e. All values are 300-day means.

Quantity	Control ProxB	Warm ProxB	Control TRAP-1e	Warm TRAP-1e	Dry TRAP-1e
Mean air temperature (sub) (K)	211.4	229.9	217.9	250.7	240.3
Max air temperature (sub) (K)	285.1	300.6	278.0	310.5	331.6
Min air temperature (sub) (K)	167.8	180.6	179.2	178.2	181.4
Mean air temperature (anti) (K)	201.6	220.6	210.4	246.3	222.1
Max air temperature (anti) (K)	259.7	274.7	260.6	295.8	284.7
Min air temperature (anti) (K)	167.9	180.4	179.0	179.4	181.4
Mean zonal mean zonal wind (m/s)	17.1	18.4	15. 6	25.2	-1.2
Max zonal mean zonal wind (m/s)	59.0	73.5	69.6	113.9	24.8
Min zonal mean zonal wind (m/s)	-35.4	-24.3	-6.4	-17.4	-20.1
Mean specific humidity (sub) (kg/kg)	1.5×10^{-3}	4.9×10^{-3}	1.0×10^{-3}	10.5×10^{-3}	0
Max specific humidity (sub) (kg/kg)	8.2×10^{-3}	21.0×10^{-3}	5.0×10^{-3}	34.5×10^{-3}	0
Min specific humidity (sub) (kg/kg)	0.5×10^{-7}	4.8×10^{-7}	0.1×10^{-7}	2.5×10^{-7}	0
Mean specific humidity (anti) (kg/kg)	0.4×10^{-4}	6.2×10^{-4}	0.6×10^{-4}	52.9×10^{-4}	0
Max specific humidity (anti) (kg/kg)	3.0×10^{-4}	33.9×10^{-4}	3.5×10^{-4}	171.8×10^{-4}	0
Min specific humidity (anti) (kg/kg)	0.5×10^{-7}	5.3×10^{-7}	0.1×10^{-7}	2.4×10^{-7}	0
Mean surface temperature (K)	219.1	243.4	231.0	276.2	212.9
Max surface temperature (K)	286.3	301.8	281.6	312.3	342.5
Min surface temperature (K)	149.5	196.5	205.2	250.4	157.3

Table 3.2: Mean, maximum, and minimum values for each plot shown in Figure 3.1. Values are given separately for the substellar and antistellar profiles of temperature and specific humidity.

Figure 3.1 shows the vertical temperature structure, zonal mean zonal wind, vertical humidity profile, and the spatial distribution of surface temperature of each simulation. All simulations display a nightside temperature inversion, although in the Warm TRAP-1e case it is very small and the temperature profile is nearly identical on the dayside and nightside. The specific humidity profiles are likewise consistent for Control ProxB, Warm ProxB, and Control TRAP-1e, with much greater humidity on the dayside and an arid nightside. Only the Warm TRAP-1e (incipient runaway) simulation has substantial humidity on the nightside. A comparison of the zonal mean zonal wind of the Control vs. Warm ProxB and Control vs. Warm TRAP-1e cases supports an increase in zonal wind speeds for planets orbiting closer in. The Proxima Centauri b simulations have a broad equatorial jet in the troposphere and a series of vertically stacked opposing jets in the stratosphere in a longitudinally asymmetric stratospheric oscillation (LASO) as described in Chapter 2. In contrast, the Control and Warm TRAPPIST-1e simulations form a mid-latitude tropospheric jet in each hemisphere. In these simulations, unlike in the THAI project, the planet also generates a LASO in the equatorial region due to the acceleration of the flow contributed by the gravity wave drag scheme.

The zonal mean zonal wind for the Dry TRAP-1e case differs from that reported in THAI (Turbet et al., 2022) for the equivalent N_2-dominated atmosphere case. Turbet et al. (2022) reported a stable state with two mid-latitude jets, while my result is a broad equatorial jet more similar to that of Proxima Centauri b or the CO_2-dominated atmosphere case in Turbet et al. (2022). Recent work has shown that UM simulations of TRAPPIST1-e exhibit climate bistability, with one stable dynamical state corresponding to an equatorial jet and the other to two mid-latitude jets (Sergeev, Lewis, et al., 2022). It may be that the inclusion of gravity waves, which affect the dynamical structure of the atmosphere and heat transport between dayside and nightside, tipped this simulation into the equatorial jet state. Using a series of daily snapshots, I found that my Dry TRAP-1e simulation had considerably greater day-to-day wind variability in the troposphere than the equivalent publicly available THAI Ben1 simulation that lacked gravity waves. This increase in variability is likely due to non-linear interaction between the gravity wave scheme and other elements of the circulation. The long-term mean horizontal flow was, however, very similar between the two simulations, including the positions of the Rossby gyres, with the primary difference being the lack of fast mid-latitude jets in the mean. The zonal wind magnitude for the Dry TRAP-1e case is in line with that shown in Turbet et al. (2022) and considerably less than that in the moist atmosphere cases. The tropospheric jet structure influences the location and shifting of Rossby wave structures discussed below, as the zonal wind magnitude is a component of the Rossby wave phase speed and Rossby waves can be advected by the flow.

3.3.2 Wave oscillation and mechanism

All five simulations exhibit the presence of zonal wavenumber-1 Rossby waves. In all the moist cases, these waves shift eastwards and westwards around an equilibrium position with a regular period. The zonal wavenumber-1 Rossby wave response arises due to the spatially periodic heating caused by irradiation of the permanent dayside of a tidally locked planet and lack of irradiation of the nightside (Gill, 1980; Matsuno, 1966; A. P. Showman & Polvani, 2010, 2011). Dayside heating causes a region of wind divergence around the substellar point in the upper atmosphere (Hammond & Lewis, 2021). A region of divergence superimposed on an absolute vorticity gradient creates a Rossby wave source as described in Sardeshmukh and Hoskins (1988) in the substellar region. Past work has reported that the eastward flow in tidally locked planet simulations causes a phase shift in the zonal wavenumber-1 Rossby wave response dependent on the long-term mean zonal wind speed (Hammond & Pierrehumbert, 2018; S. Wang & Yang, 2021). I observe this long-term mean phase shift in my simulations, but find that in a time-resolved analysis, the wave response shift (i.e., location of the Rossby minima and maxima) varies periodically. This wave oscillation induces regular cloud cover drops at the eastern terminator in two of my simulations: Control ProxB and Warm ProxB.

The wave shift causes cloud cover variations in the Proxima Centauri b simulations and not the TRAPPIST-1e simulations because the Rossby waves form in the mid-latitudes and therefore interact with the substellar cloud. The gyres in Control ProxB and Warm ProxB are centered around 45-60N/S and extend to nearly the poles and equator, while the substellar cloud region reaches from 60S to 60N. In Control TRAP-1e, the eastern gyres are centered around 60-70N/S, while the clouds only extend to roughly 30N/S: the latitude range of the gyres does not overlap with that of the substellar cloud. In Warm TRAP-1e, the bulk of the cloud forms higher up in the atmosphere and equatorwards of 15N/S, while the gyres are again located at 60-70N/S. The latitudinal position of the gyres may be influenced by the position of the zonal jets on the two planets. As seen in Figure 3.1, Proxima Centauri b's equatorial jet

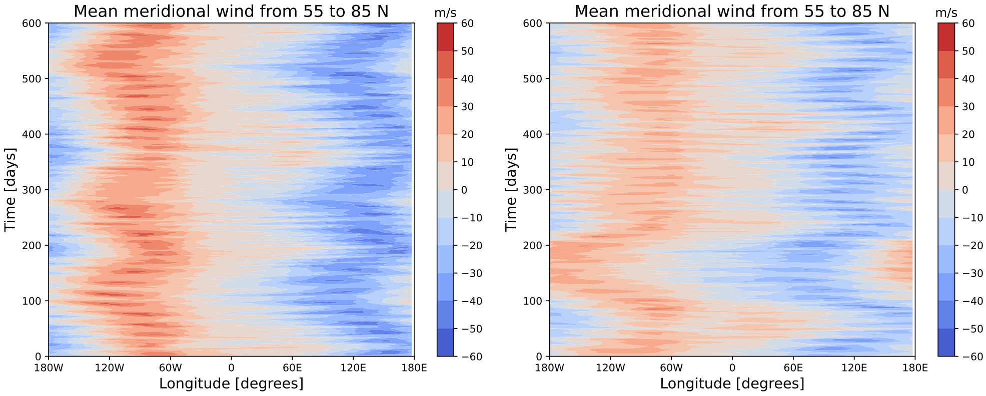

(a) Control ProxB **(b)** Warm ProxB

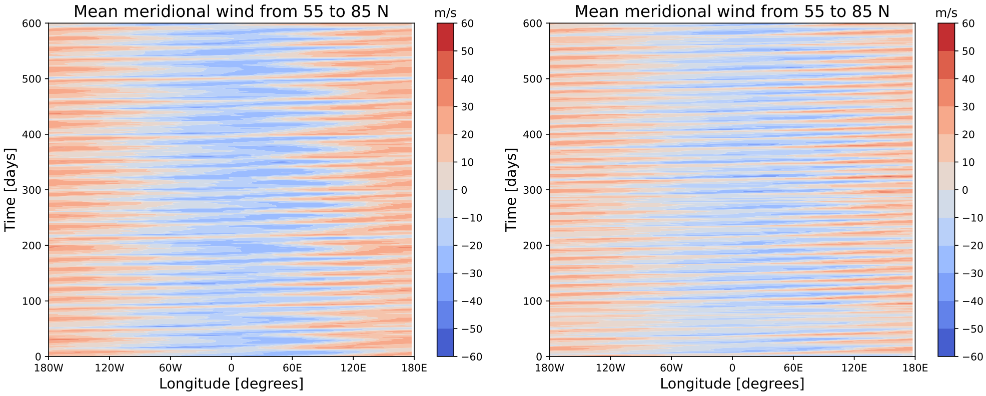

(c) Control TRAP-1e **(d)** Warm TRAP-1e

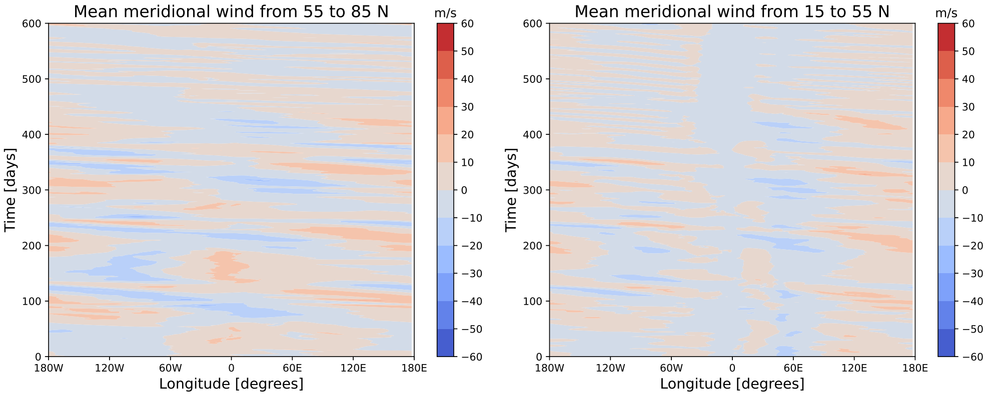

(e) Dry TRAP-1e, high latitudes **(f)** Dry TRAP-1e, low latitudes

Figure 3.2: Time-longitude diagrams of the mid-latitude (55 to 85N) averaged meridional wind at an altitude of 2.96 km above the surface. Subplot f) also shows the low latitudes for Dry TRAP-1e. Positive values correspond to northward flow, while negative values represent southward flow.

extends to about 55N/S, while the mid-latitude jets on TRAPPIST-1e extend further polewards to approximately the latitude of the Rossby vortices. Previous work simulating TRAPPIST-1e with the UM has also shown that the circulation of this planet can take on one of two regimes: a single equatorial jet or two mid-latitude jets (Sergeev, Lewis, et al., 2022). This study found that in the single equatorial jet regime, as in my Proxima Centauri b simulations, the gyres form further equatorwards than in the double mid-latitude jet regime.

Figure 3.2 represents the waves as fluctuations in the mean mid-latitude meridional wind at a height of 2.96 km. Investigation of the vertical vorticity profile and inspection of the eddy rotational component at different atmospheric levels showed that the Rossby wave-associated vorticity and wind speeds in the vertical region where clouds form are greatest at this height. Accordingly, single-level plots in my results are shown at 2.96 km. Results for other levels are qualitatively similar but typically of smaller magnitude. In Figure 3.2 a) to d), the longitudes at which the mean meridional wind alternates between northward and southward represent the longitudinal range of the oscillation in the moist atmosphere cases. The Dry TRAP-1e case is shown in Figure 3.2 e) and f). As is visible in the long-term mean flow of Dry TRAP-1e depicted in Figure 3.3 e), the western gyres in this simulation form at mid-to-high latitudes (60-90N/S), while the eastern gyres form at low latitudes (0-45N/S). The latitude range chosen in Figure 3.2 e) includes the western gyres, which tend to propagate west, dissolve, and reform near the substellar longitude, but occasionally also propagate eastwards or remain stationary. The eastern gyres are always stationary: their longitudinal position can be seen at 90E in Figure 3.2 f). To understand the mechanism driving the moist oscillation, I analyzed and compared the Control and Dry TRAP-1e simulations.

Figure 3.3 shows the wind pattern at 2.96 km for Control TRAP-1e and Dry TRAP-1e in the long-term mean and at three different simulation times, chosen to correspond to the easternmost, westernmost, and again easternmost location of the gyres in the Control TRAP-1e simulation, covering a full cycle of motion. In the control simulation, Rossby gyres are clearly visible in the northern and southern polar regions of the eastern hemisphere, for example at 60N and 60-90E in Figure 3.3 b). These gyres propagate eastwards and westwards such that the centers of the gyres shift from between 30-60E to 120-150E on an approximately 20-day cycle, with a long-term mean position of 85E. A matching western pair is less apparent due to interactions with other elements of the flow. In the dry simulation, the eastern gyres form at lower latitudes and remain stationary, while the western gyres propagate exclusively westwards, dissolve, and reform near the substellar longitude.

I explain the motion of the gyres using the theory of Rossby waves. Following e.g., Holton and Hakim (2013) or Vallis (2017), the phase speed of travelling Rossby waves is given by:

$$c_p = \bar{U} - \frac{\beta + \bar{U} k_d^2}{k^2 + l^2 + k_d^2}, \tag{3.1}$$

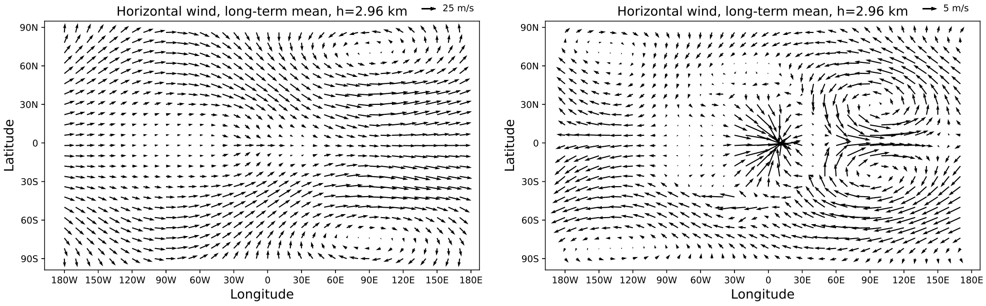

(a) Control TRAP-1e, long-term mean

(b) Dry TRAP-1e, long-term mean

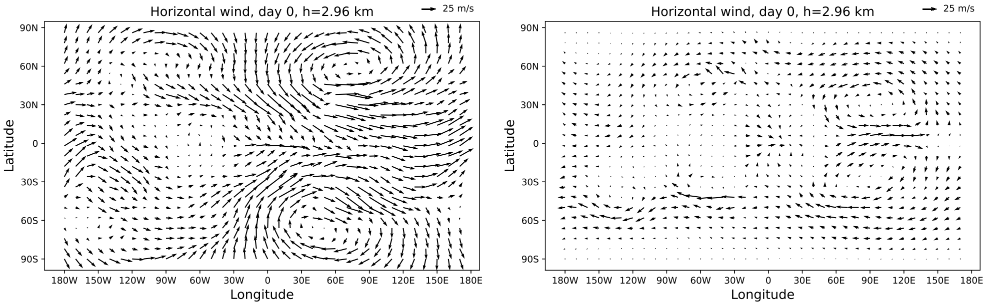

(c) Control TRAP-1e, day 0

(d) Dry TRAP-1e, day 0

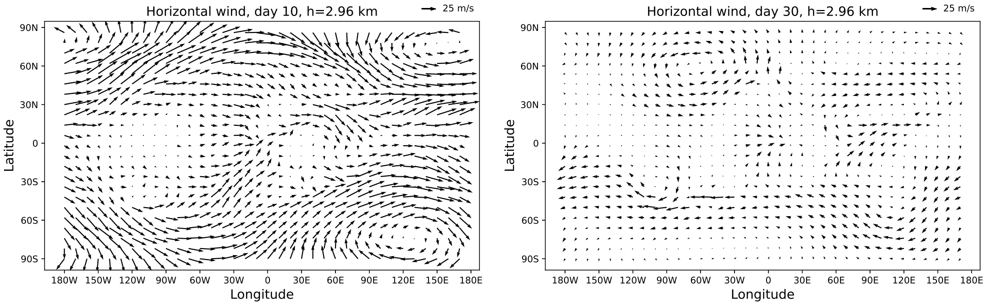

(e) Control TRAP-1e, day 10

(f) Dry TRAP-1e, day 30

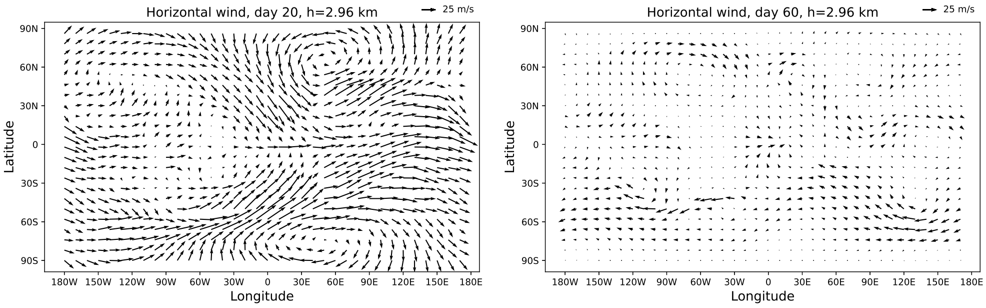

(g) Control TRAP-1e, day 20

(h) Dry TRAP-1e, day 60

Figure 3.3: Long-term mean of the general circulation for Control TRAP-1e and Dry TRAP-1e, as well as daily snapshots of days 0, 10, and 20 and days 0, 30, and 60, respectively. Note the differing quiver scale in c).

where $\bar{U}$ is the zonal mean zonal wind speed, β is the Rossby parameter $\frac{2\Omega cos\phi}{r}$ (with Ω the planet's rotation rate in radians/second, ϕ the latitude in radians, and r the planet's radius), and *k* and *l* are the zonal and meridional wavenumbers in units of m^{-1}. The variable k_d is the wavenumber corresponding to the Rossby deformation radius $\frac{1}{L_d}$ rather than the planet's radius, where L_d is defined in quasigeostrophic theory as $\frac{NH}{f_0}$, with N the Brunt-Väisälä frequency, H the scale height (6800 m for my simulations), and f_0 the Coriolis parameter at a given latitude. This form of the Rossby wave phase velocity equation takes into account vertical stratification and propagation within a GCM. For stationary Rossby waves such as those in my simulations, the theoretical phase speed corresponds to a longitudinal shift in the wave response location as the waves are advected by the zonal flow.

To determine why the Rossby gyres oscillate in the moist atmosphere cases only, I compared the Rossby wave phase velocity for Control TRAP-1e and Dry TRAP-1e. Figure 3.4 a) shows time series of the phase velocity of the Rossby wave with the highest power spectral density (PSD) in the flow, the zonal wavenumber-1 wave, for these two simulations. To confirm that only this wave contributes significantly to the phase speed, I extracted the wavenumbers of the highest powered waves in the flow on each simulation day. I first performed a Helmholtz decomposition of the wind field at 2.96 km to calculate the eddy rotational component as in Hammond and Lewis (2021). I then input the magnitude of the eddy rotational component, which I equate to the Rossby waves, into a 2-D Fourier transform and extracted the zonal (k) and meridional (l) wavenumbers of the wave with the maximum PSD on each simulation day. My results confirmed that the wave with k=1 and l=0 is consistently the highest powered wave. Finally, I calculated a day- and latitude-specific Rossby wave phase velocity as per Equation 3.1. In this calculation, I used the time-varying daily value of the zonal mean zonal wind U and Brunt-Väisälä frequency N, and further subtracted the long-term mean zonal mean wind to account for the long-term phase shift of the wave response described in S. Wang and Yang (2021) and Hammond and Pierrehumbert (2018). Figure 3.4 a) shows that, in the moist simulation, the Rossby wave phase velocity oscillates between positive (eastward) and negative (westward) values on an approximately 20-day cycle, while it remains negative in the dry case over the same time period.

In Figure 3.4 b), I then plot the Rossby wave phase velocity for Control TRAP-1e as in a), together with the longitude of the center of the northeast Rossby gyre. I tracked the gyre center by searching for the longitude in the northeast quarter of the globe where the meridional wind changes direction for each simulation day. The dashed black line represents the equilibrium position of the gyre at 85E and is aligned with the zero point of the phase velocity on the plot. This plot shows the close and regular correlation between the gyre location at the given latitude and the Rossby wave phase speed at that same latitude in both period and amplitude. According to the interpretation that the phase speed of a stationary Rossby wave represents the wave's longitudinal position, a positive phase speed should correspond to a gyre longitude east of the equilibrium point. My phase velocity curve conforms to this prediction except for a small, consistent offset from the gyre longitude curve. This offset is caused by the limitation of using the zonal wind at only one latitude in Eq. 3.1, in particular a latitude at which the Rossby gyre itself also contributes to the zonal wind. Using the global mean zonal wind instead of the latitude-specific zonal wind in the phase velocity calculation reduces the offset between the two curves in Fig. 3.4 b) to nearly zero, but in turn weakens the correlation between the amplitudes of the curves. As the gyre extends over roughly 20 degrees latitude, treating it as a point particle with a single location is inadequate to precisely predict its motion; however, the strong correlation in period and amplitude in Fig. 3.4 b) supports the interpretation of the phase velocity as representative of the longitudinal shift in the wave response over time.

The formation of Rossby gyres in simulations of tidally locked planets is believed to be related to the spatially periodic thermal forcing (Gill, 1980; Matsuno, 1966; A. P. Showman & Polvani, 2010, 2011). As my model's stellar spectra do not vary with time and the planet is tidally locked with zero eccentricity or obliquity, atmospheric processes must be responsible for the temporal variability in my simulations. To determine why the Rossby wave phase velocity varies periodically with time, I searched for correlations between quantities thought to play a role in the Matsuno-Gill response to periodic forcing. Figure 3.5 compares the variations over time of the vertical cross sections of dayside mean air temperature, vertical wind, zonal wind, net surface shortwave flux, and the PSD of the zonal wavenumber 1 Rossby wave (identified as the 1-0 wave) and, separately, the sum of the PSDs of the Rossby waves identified as 1-1, 2-1, 2-2, and 3-2 waves, where the first digit refers to the zonal wavenumber and the second digit refers to the meridional wavenumber. I show the 1-0 wave separately from other long Rossby waves to underline the central role played by the cloud radiative feedback in enhancing the Matsuno-Gill response specifically.

Regular 20-day cycles are visible in all quantities in the moist atmosphere case, but are absent in the dry atmosphere. The air temperature, vertical wind, and shortwave surface heating increases precede the increase in the Rossby wave power. For example, Figure 3.5 a), c), and g) show a peak in these three quantities at around 510 days, while the spike in the 1-0 Rossby wave (red line in Figure 3.5 g)) and increase in the zonal wind speed occur at 518-520 days. This pattern repeats ten times over the period displayed in the plots. Figure 3.6 further shows variability in the dayside mean total (sum of ice and liquid) cloud cover on the same 20-day cycle. The cloud mass fraction grows during the heating/rising and drops during the cooling/subsiding part of the cycle.

I posit an internal feedback between the dayside cloud cover and the intensity of the Matsuno-Gill response. A decrease in cloud cover allows more shortwave radiation to reach the surface, leading to atmospheric heating and subsequent ascending motion of the air mass. The 1-0 Rossby wave responds to the increase in forcing, boosting its power spectral density relative to the other constituent Rossby waves in the wind field. At the same time, the zonal wind speed

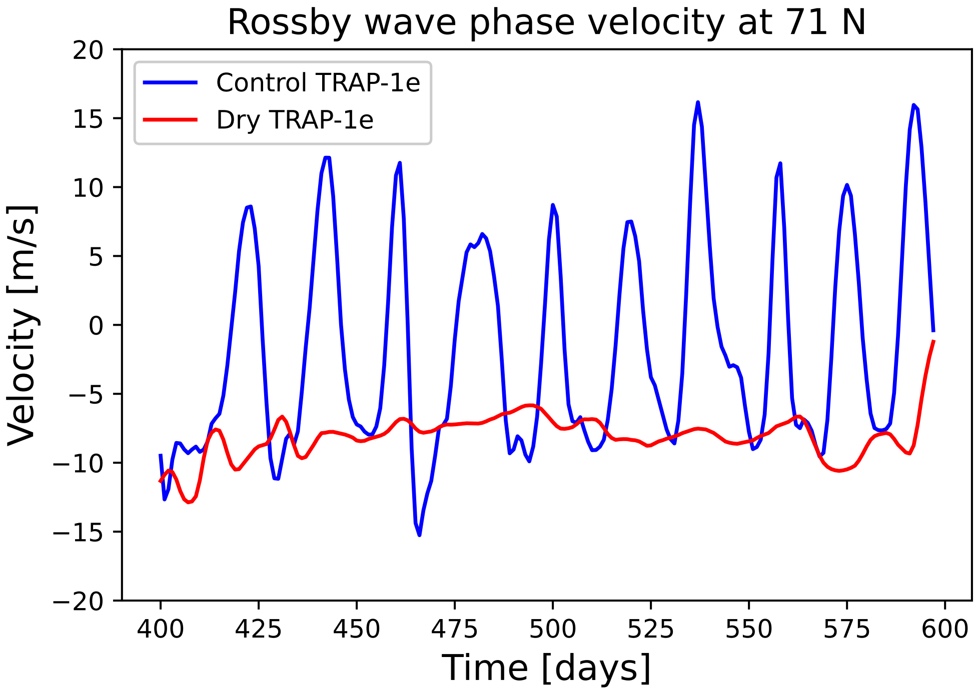

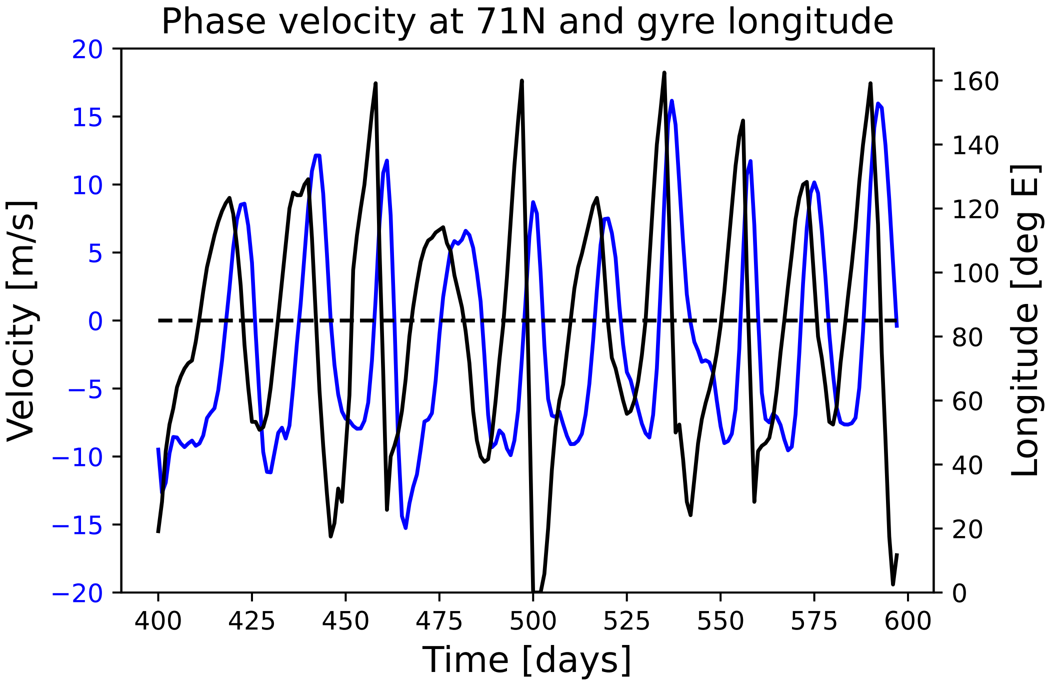

Figure 3.4: Top: Time series of Rossby wave phase velocity at 71N for Control and Dry TRAP-1e simulations. Bottom: Time series of Rossby wave phase velocity at 71N overlaid with the longitudinal position of the northeast Rossby gyre for Control TRAP-1e. A 3-day rolling mean has been applied to all curves.

Quantity	Control ProxB	Warm ProxB	Control TRAP-1e	Warm TRAP-1e
Rotation period (days)	11.2	9.2	6.1	4.2
Oscillation period (days)	157.5	120	19.4	16.2
Mean global zonal mean zonal wind (m/s)	5.3	4.1	17.8	15.1
Mean equator-pole temperature gradient (K/m)	-2.55×10^{-6}	-2.761×10^{-6}	-3.92×10^{-6}	-3.76×10^{-6}

Table 3.3: Rotation period, period of Rossby gyre oscillation, mean zonal mean zonal wind, and mean meridional temperature gradient for each of the four moist atmosphere cases. The periodicity was determined from the cloud cover oscillation shown in Figure 3.8. The meaning period for the bottom two quantities was chosen to be the same as in Figure 3.1, the first 300 days of the sampling period for each simulation.

increases, shifting the 1-0 wave structure further eastwards. To support this interpretation, I show in Figure 3.5 g) and h) both the PSD of the 1-0 wave and the summed PSD of a number of other large-scale waves, namely the 1-1, 2-1, 2-2, and 3-2 waves. At the troughs of the cycle, the PSD of the 1-0 wave is roughly equal to that of the other waves combined, and occasionally even drops below it. At the peaks, however, the PSD of the 1-0 wave increases substantially more than that of the sum of the remaining waves, indicating that this wave disproportionately receives energy during the cycle, as would be expected from its direct relationship to the Matsuno-Gill periodic forcing pattern. (Note that in the dry atmosphere case, the PSD of all waves is an order of magnitude smaller than in the moist case despite the larger shortwave flux and atmospheric temperature anomalies, highlighting the important role of moisture.)

When cloud cover increases again, less radiation reaches the surface, the air mass cools and subsides, the zonal wind speed slows, and the 1-0 Rossby wave becomes weaker and is shifted westwards from its equilibrium position. It is possible that the location of the Rossby gyres in turn affects the cloud cover, closing the causal loop, but I believe it is unlikely that the Rossby waves are the only or main factor in the density of the clouds. The zonal wind speed, which influences both the Rossby wave phase velocity and the stability of the dayside cloud cover, is also affected by the changes in the thermodynamic properties of the dayside atmosphere shown above (Figure 3.5 e)). Untangling these intricate relationships requires a better understanding of the factors controlling the zonal wind speed on tidally locked planets than is currently available. In addition, the cloud layer is likely to be sensitive to multiple processes in the atmosphere in addition to the zonal wind variation, including the intensity of convection, specific humidity, and the advective and radiative time scales.

The period of the oscillation, given in Table 3.3, varies substantially between the four moist atmosphere cases. Understanding why the period is longer in some simulations is important because a slower oscillation implies the planet will have a longer period of clear skies at the limb, potentially allowing for repeat observations when conditions are favorable. I find that the oscillation period monotonically decreases in parallel with the rotation period, but the relationship is not linear. I expect the rotation period to influence the Rossby wave phase velocity

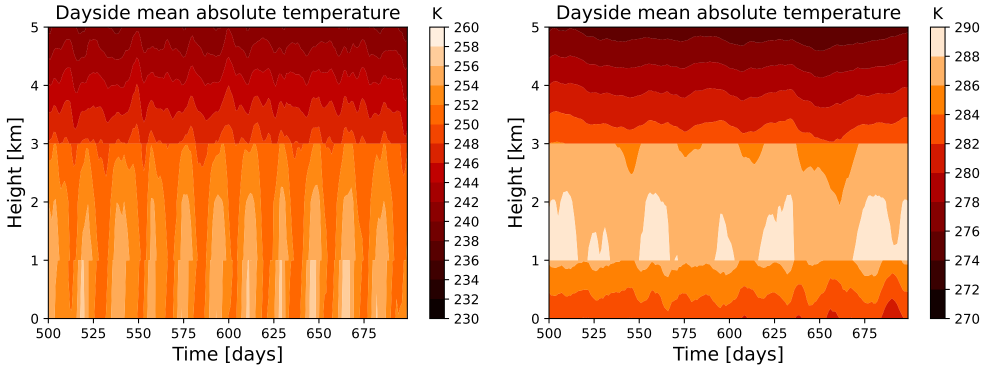

(a) Control TRAP-1e

(b) Dry TRAP-1e

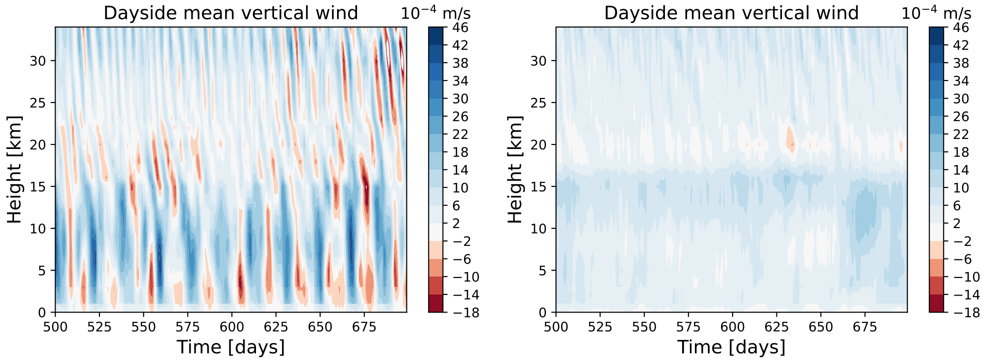

(c) Control TRAP-1e

(d) Dry TRAP-1e

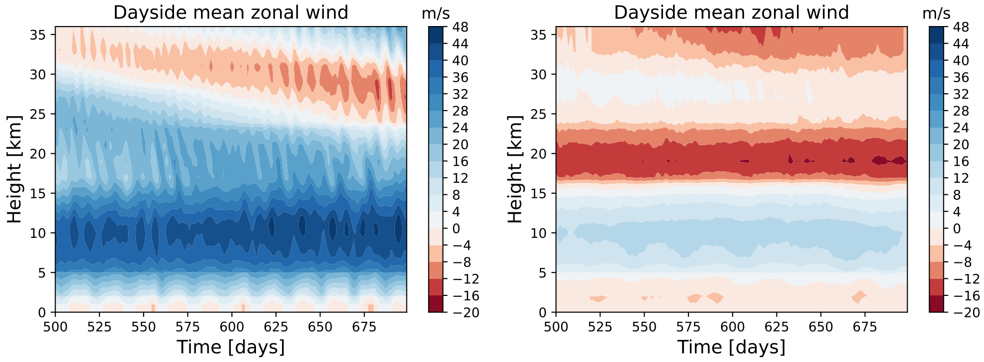

(e) Control TRAP-1e

(f) Dry TRAP-1e

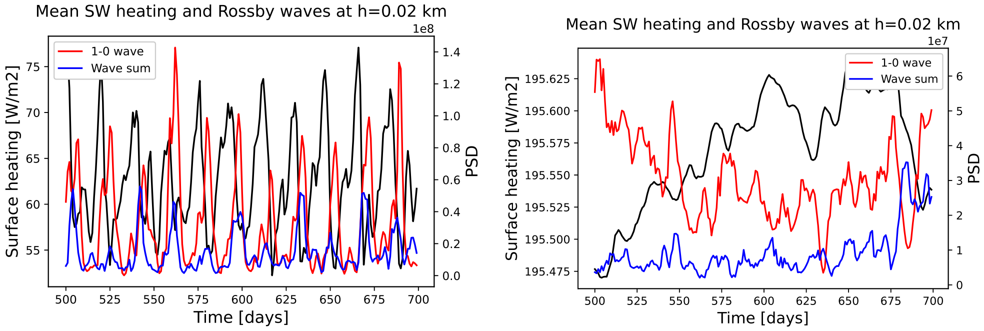

(g) Control TRAP-1e

(h) Dry TRAP-1e

Figure 3.5: Top three rows: Vertical profiles of dayside mean air temperature, vertical wind, and zonal wind over time for moist atmosphere Control TRAP-1e and dry atmosphere Dry TRAP-1e. The vertical range of a) and b) is 0 to 5 km to show the temperature oscillation near the surface. Due to the low resolution, this close-in view results in discontinuities between vertical levels. The discontinuities are not visible in c)-f) because the vertical range shown is 0 to 35 km. Bottom row: Time series of the dayside mean net downward shortwave flux close to the planet's surface (black), shown with the power spectral density of the zonal wavenumber 1 Rossby wave (red) and the sum of the power spectral density of the waves with zonal and meridional wavenumbers 1-1, 2-1, 2-2, and 3-2 (blue). Note the different limits of the y-axis.

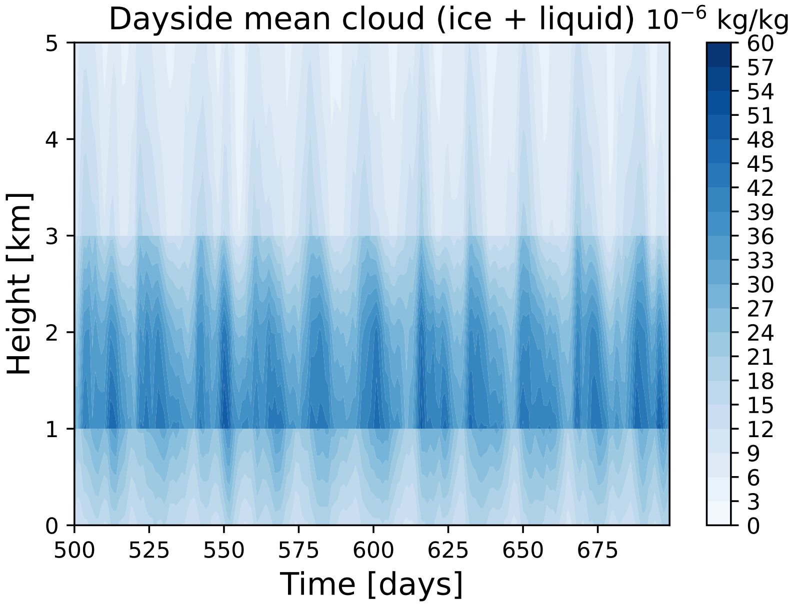

Figure 3.6: Vertical profile of dayside mean total cloud cover (sum of ice and liquid) over time for the Control TRAP-1e simulation. As in Figure 3.5 a) and b), the short vertical range of 0 to 5 km results in discontinuities between vertical levels due to the low resolution of the simulation.

directly through β. However, other factors are clearly in play. While the rotation period decreases by similar amounts (2-3 days) between each simulation, there is a disproportionately large difference between the oscillation periods of the Proxima Centauri b and TRAPPIST-1e simulations. I believe the non-linearity can be explained by the additional influence of the zonal wind on the Rossby wave phase velocity as defined in Equation 3.1. Figure 3.7 shows latitude-time diagrams of the Rossby wave phase velocity for each simulation. Both the eastward and westward phase of the oscillation display higher phase velocities in the TRAPPIST-1e simulations as compared to Proxima Centauri b, accounting for the much shorter oscillation periods of the former. Effectively, the more rapid background zonal flow is shifting the wave response east and west of its equilibrium point more quickly in the TRAPPIST-1e cases.

The phase velocities differ because the zonal mean wind, reported in Table 3.3, jumps significantly between the Proxima Centauri b (4-5 m/s) and TRAPPIST-1e (15-18 m/s) simulations. In particular, Figure 3.1 shows that the zonal mean wind speeds are higher at the mid-latitudes where the gyres are centered in the TRAPPIST-1e cases than the Proxima Centauri b cases. This is because Control and Warm TRAP-1e are both in the double mid-latitude jet circulation regime described by Sergeev, Lewis, et al. (2022), while Control and Warm ProxB are both in the single equatorial jet regime. Sergeev, Lewis, et al. (2022) found that the single jet regime is characterized by transport of angular momentum to the equator by the stationary eddy term of the axial angular momentum equation driven by wave-jet resonance between the equatorial jet and the zonal wavenumber-1 Rossby wave (consistent with the findings of e.g., S. Wang and Yang (2021), Hammond and Pierrehumbert (2018), and Tsai et al. (2014)). The double jet regime, on the other hand, forms when the mean advection and transient eddy terms of the momentum budget become large at the mid-latitudes and the stationary eddy term decreases at the equator: the mid-latitude jets speed up while the equatorial jet slows down. As the stationary gyres form in the mid-latitudes, it is the wind speeds in the mid-latitudes that control the magnitude of the Rossby wave phase velocity.

Sergeev, Lewis, et al. (2022) explores the development of both the single jet and the double jet regimes during the model spin-up period. As shown in Table 3.3, the TRAPPIST-1e simulations have a larger equator-to-pole temperature gradient than the Proxima Centauri b simulations. This larger temperature gradient may cause greater baroclinic instability, promoting the formation of baroclinic mid-latitude jets. However, the exact reasons why a simulated planet is nudged into one regime or the other may be varied and are difficult to isolate in a model as complex as the UM. According to the weak temperature gradient theory applicable to slowly rotating tidally locked planets (Pierrehumbert & Hammond, 2019), the equator-pole temperature gradient should increase with increasing rotation rate, which is consistent with the values in Table 3.3. The discontinuity between the two Proxima Centauri b and the two TRAPPIST-1e simulations is a reflection of the shift from the single jet to the double jet regime. These patterns broadly suggest that more slowly rotating planets with weaker equator-pole temperature gradients and a single equatorial jet are likely to have longer oscillation periods and longer windows of cloudless sky at the terminators.

3.3.3 Cloud variability and observables

The migration of Rossby gyres impacts the amount of moisture transport and thus cloud condensate at the planetary terminators. All four of the moist atmosphere simulations display cloud cover variability at the terminators, shown in Figure 3.8. The Control and Warm ProxB runs in Figure 3.8 a) and b), respectively, exhibit large fluctuations in cloud condensate in the observable regions of the planet, ranging from near 0 to 7×10^{-7} kg/kg and 2.5×10^{-6} kg/kg, respectively, on a time scale matching the migratory cycle of the Rossby gyres (120 days/160 days). The TRAPPIST-1e simulations do not undergo these long-period cycles, but show regular smaller magnitude fluctuations on an approximately 20-day time scale.

Figure 3.9 depicts the interaction between the wind field and the dayside clouds. Figure 3.9 a) and b) are two stages in the Rossby gyre migratory cycle for the Warm ProxB simulation, corresponding to a cloud condensate maximum and minimum. During the maximum, the eastern pair of Rossby gyres is at the extreme western part of its propagation path, where it intersects with the region of heavy cloud cover around the substellar point. During the minimum, the gyres are at the extreme eastern part of the propagation path and do not interact with the dayside clouds. In the TRAPPIST-1e case, shown in Figure 3.9 c) and d), the Rossby

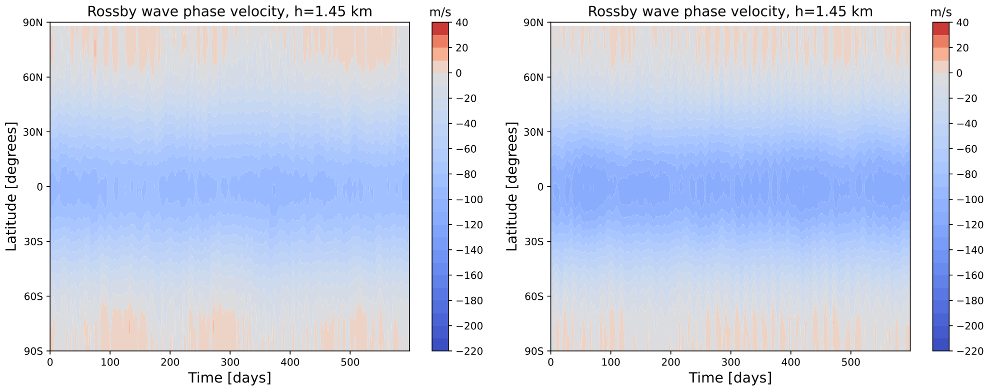

Rossby wave phase velocity, h=1.45 km

Rossby wave phase velocity, h=1.45 km

(a) Control ProxB **(b)** Warm ProxB

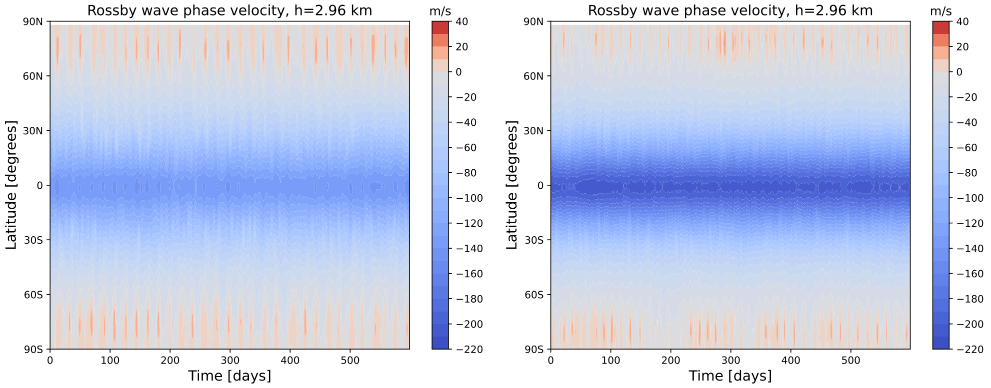

Rossby wave phase velocity, h=2.96 km

Rossby wave phase velocity, h=2.96 km

(c) Control TRAP-1e **(d)** Warm TRAP-1e

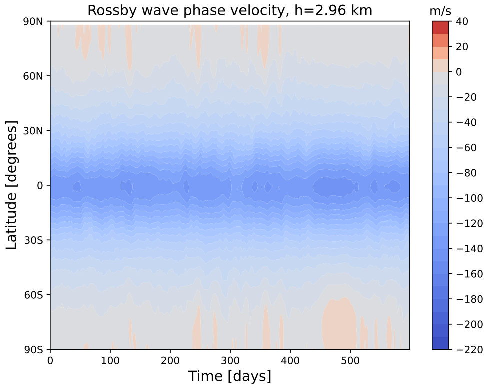

Rossby wave phase velocity, h=2.96 km

(e) Dry TRAP-1e

Figure 3.7: Latitude-time diagrams of Rossby wave phase velocity for each simulation at h=2.96 km height. Positive values correspond to eastward flow, while negative values represent westward flow. The phase velocity is calculated with subtraction of the mean zonal wind as in Figure 3.4.

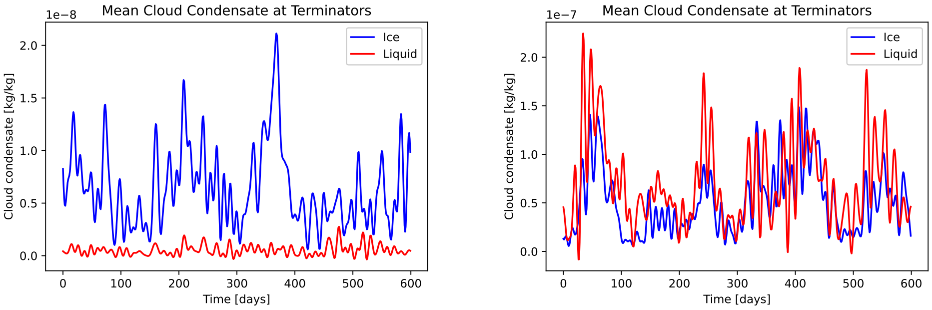

(a) Control ProxB

(b) Warm ProxB

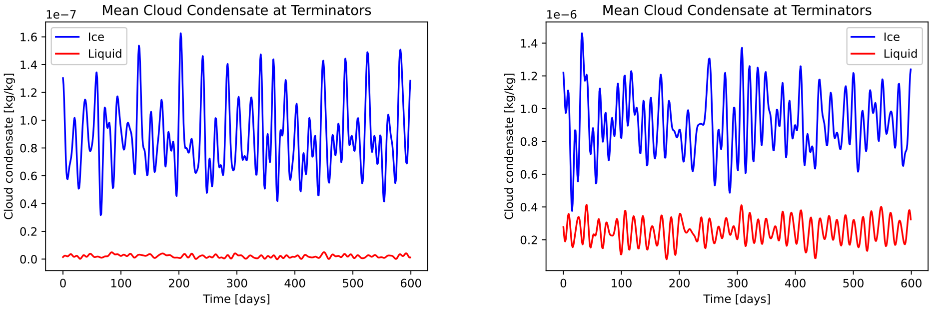

(c) Control TRAP-1e

(d) Warm TRAP-1e

Figure 3.8: Mean cloud condensate (mixing ratio, kg/kg) over time at the planetary limb for each of the four moist atmosphere simulations. Liquid and ice cloud are shown separately. Each type of cloud is averaged over all latitudes and all heights on the eastern and western terminator. The data has been filtered to remove cycles with periods shorter than 10 days. Note the different limits of the y-axis.

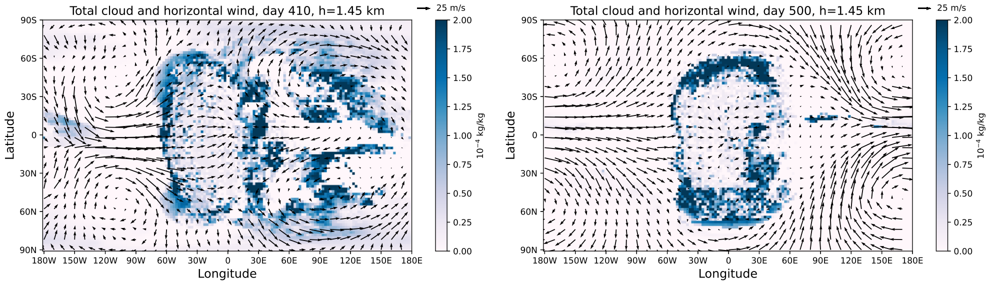

(a) Warm ProxB, day 410

(b) Warm ProxB, day 500

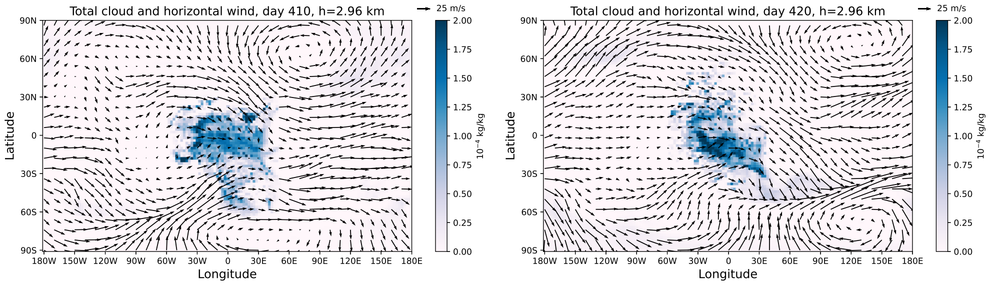

(c) Control TRAP-1e, day 410

(d) Control TRAP-1e, day 420

Figure 3.9: Wind vectors overlaid on the total cloud condensate (sum of ice and liquid) at the given height for Warm ProxB and Control TRAP-1e simulations. The images are daily snapshots chosen to illustrate the eastmost and westmost phases of the Rossby gyre migration for each planet.

gyres are too far polewards to interact with the dayside cloud cover. The short-period cycles shown in Figure 3.8 c) are likely a direct reflection of the fluctuation in cloud condensate and moisture described in 3.3.2 and shown in Figures 3.5 and 3.6, on which the longer-period effect from the traveling wave structures is overlaid.

The magnitude and periodicity of the variation in cloud cover at the planetary limb is highly sensitive to not only the Rossby wave propagation, but also the dayside cloud structure. As demonstrated by the TRAPPIST-1e cases, the amount of cloud at the terminator will not be affected by the Rossby wave oscillation unless the Rossby gyres form at low or mid-latitudes where they can advect cloud from the substellar region. Figure 3.10 shows cross-sections of the dayside cloud layer at the equator and at longitude 0 for the four moist atmosphere simulations. The extent of the cloud cover in longitude, latitude, and altitude depends on the temperature and moisture profile of each simulated planet, but as the longitude, latitude, and even peak altitude of the Rossby waves also vary in different simulations, the parameter space of the resulting wave-cloud interaction is complex.

To explore the potential impact of wave-cloud interactions on observations, I simulated transit spectra for the Control ProxB, Warm ProxB, Control TRAP-1e, and Warm TRAP-1e simulations, excluding the Dry TRAP-1e simulation as it does not form clouds. I constructed time series of two absorption features, shown in Figure 3.11. I chose the water line at 1.4 μm

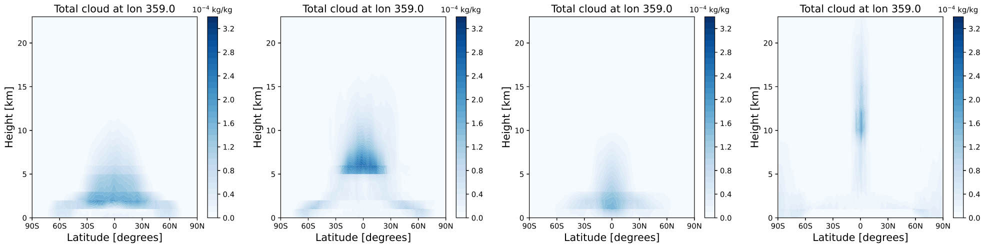

(a) Control ProxB **(b)** Warm ProxB **(c)** Control TRAP-1e **(d)** Warm TRAP-1e

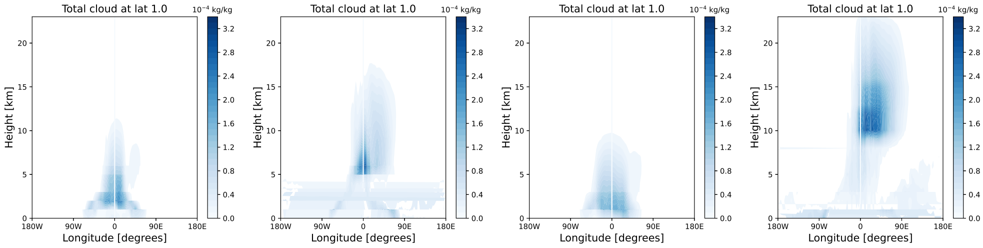

(e) Control ProxB **(f)** Warm ProxB **(g)** Control TRAP-1e **(h)** Warm TRAP-1e

Figure 3.10: Longitudinal and latitudinal cross-sections of the dayside cloud layer for the four moist atmosphere simulations. The total cloud is the sum of ice and liquid cloud condensate. The images depict 120-day means.

because it does not overlap with any CO_2 features and the CO_2 feature at 2.7 μm because it is a strong line in the available NIRSpec spectrum and does not overlap with the N_2-N_2 collision-induced absorption at 4.3 μm. As the CO_2 abundance in the simulations is fixed, variability in the transit depth of this feature can only be due to differences in the muting effect of cloud cover or due to temperature fluctuations and not due to variations in CO_2 content. For the water feature, variations in transit depth may also be due to differences in water vapor content on different days, caused by other factors such as the LASO and random fluctuation (model noise). However, the time series for the H_2O and CO_2 are well-correlated, supporting clouds as a factor in the variability. In the Control and Warm ProxB simulations in Figure 3.11 a)-d), the time series show clear long-period variation in addition to small continuous fluctuations, but the relative difference in the transit depths for these simulations is only 4-5 %. The percentage variation for the Warm TRAP-1e simulation is the largest in the comparison at 18-20 %, but the transit depths are profoundly muted compared to Control TRAP-1e because of the high cloud deck visible in Figure 3.10 d) and h). In addition, while the Control and Warm ProxB time series have extended periods of larger transit depths, corresponding to the longer period of the cloud cover oscillation for this planet, the TRAP-1e runs lack these multi-week periods of stronger transit signals due to their shorter Rossby wave cycle as described in Section 3.3.2.

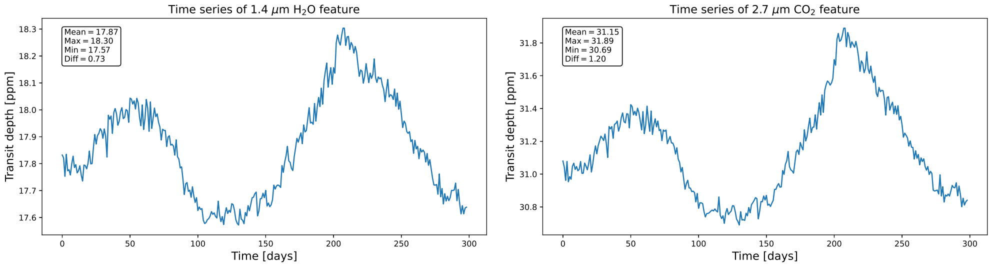

(a) Water feature, Control ProxB **(b)** CO_2 feature, Control ProxB

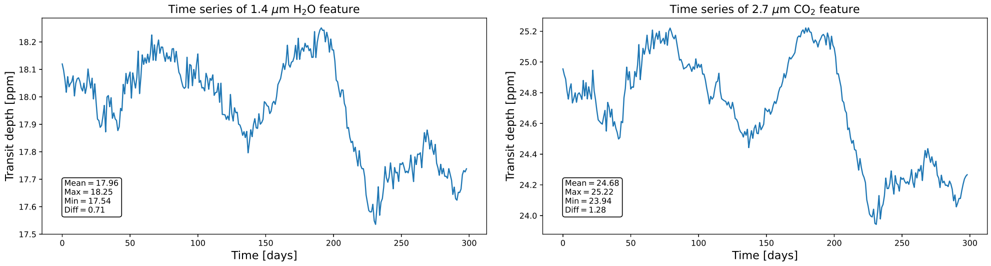

(c) Water feature, Warm ProxB **(d)** CO_2 feature, Warm ProxB

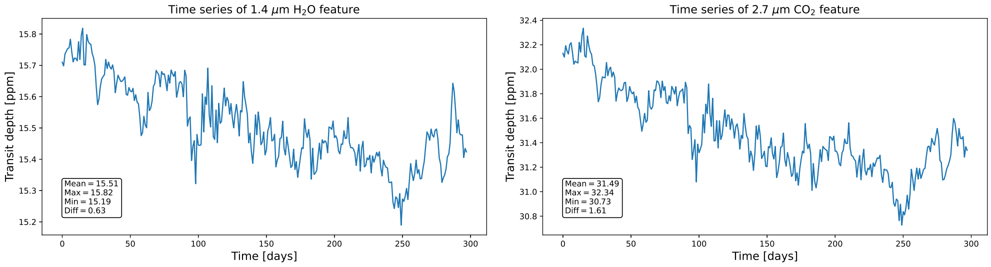

(e) Water feature, Control TRAP-1e **(f)** CO_2 feature, Control TRAP-1e

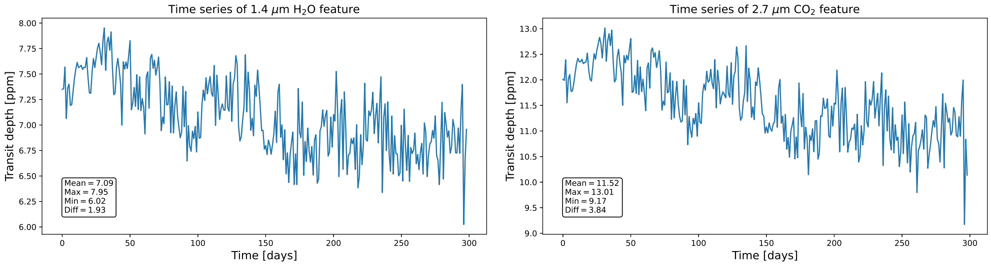

(g) Water feature, Warm TRAP-1e **(h)** CO_2 feature, Warm TRAP-1e

Figure 3.11: Time series of the 1.4 μm water absorption feature and 2.7 μm CO_2 absorption feature for the Control ProxB, Warm ProxB, Control TRAP-1e, and Warm TRAP-1e simulations. A sample of 300 days is taken to cover the 157.5 and 120 day oscillation periods in the Control and Warm Proxima Centauri b simulations, respectively. The values shown exclude the solid surface radius of the planet and represent only the opaque component of the atmosphere.

3.4 Discussion

My results support the existence of internal atmospheric variability on tidally locked aquaplanets even in the absence of a varying stellar spectrum or stellar activity, rotation with respect to the host star, obliquity, and eccentricity. The stabilizing feedback between the dayside cloud cover and atmospheric temperature, identified in previous work on the inner edge of the habitable zone for tidally locked Earth-like planets (R. k. Kopparapu et al., 2016; J. Yang, Boué, Fabrycky, & Abbot, 2014; J. Yang et al., 2013), induces periodicity in the atmospheric dynamics. Edson, Lee, Bannon, Kasting, and Pollard (2011) postulated that the large amplitude of the zonal wavenumber 1 Rossby wave on slowly rotating planets with superrotating atmospheres is caused by resonance between this wave and the spatially periodic heating. My finding of a disproportionate increase in the power spectral density of the $1-0$ wave directly after an increase in net surface shortwave flux supports their hypothesis.

The increase in surface heating is caused by a drop in total cloud cover in the dayside, reducing the cloud albedo. This periodic reduction in cloud cover may be affected by the propagation of the Rossby gyres in a closed feedback loop, but it is likely that other aspects of the circulation, especially the magnitude of the zonal and vertical winds and intensity of convection in the substellar region also play a role. The potential relationship between atmospheric moisture and cloud-radiative feedback is reminiscent of theories of the Madden-Julian Oscillation (MJO) (C. Zhang, 2005; C. Zhang, Adames, Khouider, Wang, & Yang, 2020), particularly the moisture-mode hypothesis, which also posits a planetary wave response. In the moisture-mode theory of the MJO, clouds trap longwave radiation in the troposphere, leading to enhanced areas of column moisture, convection, and precipitation. These areas are collocated with corresponding areas of dry air and suppressed convection to their east. The spatially periodic heating anomalies (which are regions of divergence) cause a planetary wave response which is the moist atmosphere analogue of the Matsuno-Gill dry atmosphere wave response. The planetary wave response in turn advects moisture horizontally eastwards, propagating the precipitation/moisture anomaly eastwards. As there is no consensus about the mechanism of the MJO, however, and the complexity of the factors influencing the cloud cover on the dayside is high, I limit my analysis to identifying the immediate cause of the Rossby gyre oscillation and its effects on observables, and defer detailed analysis of the moist atmosphere feedbacks between clouds, convection, specific humidity, and the zonal wind, as well as further comparison to Earth analogues to future studies.

My simulations of transit spectra show that the variable cloud cover caused by traveling Rossby waves could affect transit depths, though for my chosen planets the effect is too small to be observable with current instruments. May et al. (2021) reported a transit depth variation due to cloud cover on the order of 10 ppm for their 10^{-4} bars of CO_2 (with one bar of N_2 TRAPPIST-1e simulation with ExoCAM (Wolf et al., 2022), which is comparable to the THAI Hab 1 set-up (Sergeev, Fauchez, et al., 2022) and to my Control TRAP-1e experiment. THAI

Part III (Fauchez et al., 2021) found the standard deviation of the variation of the continuum level for Hab 1 to be 3 ppm for ExoCAM and 1 ppm for the UM, compared to my min-max difference of 1.26 ppm for for the 2.7 μm feature. Song and Yang (2021) found the amplitude of temporal variability in their simulated transmission spectra, also for data generated by ExoCAM, to be on the order of 20 ppm. The slightly smaller degree of variation in my results compared to May et al. (2021) and Song and Yang (2021) is in line with the finding in Sergeev, Fauchez, et al. (2022) and Fauchez et al. (2021) that ExoCAM displays the greatest degree of cloud variability out of the four models included in the comparison. My quantitative findings agree with the results of these previous works and support the conclusion that atmospheric variability due to clouds will be below the noise floor of JWST.

From a qualitative perspective, the impact of Rossby waves on observations is highly sensitive to the location of both the Rossby gyres and the cloud deck. If clouds form on or extend to the planetary terminators, migrations by Rossby gyres could regularly clear this region for periods of time as long as the planet's transit. Based on my simulations, this scenario is most plausible on slowly-rotating planets where the gyre oscillation period is long and the atmospheric state at the planetary limb may persist for longer. A warmer planet with more cloud would show greater variability in transit depths as advection by the Rossby wave gyres results in long periods of heavy cloud cover and periods of entirely clear sky. Without prior knowledge of the cloud structure, cycle duration, and cycle phase, it is impossible to predict when clearing events might occur and to time observations to avoid flattened, featureless spectra due to clouds (de Wit et al., 2016; Diamond-Lowe et al., 2018; Garcia et al., 2022; Knutson et al., 2014; Kreidberg et al., 2014). However, as the body of data from transit spectroscopy grows, atmospheric and climate variability should be considered when combining or interpreting data from different observing periods. In addition, as our theoretical understanding of climate variability on exoplanets improves, it may be beneficial to obtain data from consecutive transits instead of randomly chosen ones, as consecutive observations are more likely to represent a real atmospheric state rather than an averaged, composite one.

Traveling Rossby gyres could also affect the chemical composition of the planet's atmosphere. Several studies using chemistry-climate models have found that different chemical environments form on the dayside and nightside of tidally locked planets due to the presence or absence of photochemistry (Braam et al., 2022; Chen et al., 2018; Yates et al., 2020). In particular, the nightside gyres can build up high concentrations of species that are destroyed on the irradiated dayside (Ridgway et al., 2023). In my simulations of TRAPPIST-1e, however, the nightside gyres frequently travel back and forth over the eastern terminator, exposing chemically enriched nightside air to radiation. This process may reduce chemical differences between the dayside and nightside, leading to a more homogeneous planetary climate.

The specific features of this atmospheric oscillation, including the period, the latitudes and longitudes of the Rossby gyres, their size, the distance they travel, and how much cloud (if any) they advect are dependent on model set-up, especially the cloud parameterization. The THAI project found significant differences in the cloud water paths predicted by the four models included in the intercomparison, with the UM in the middle of the pack (Sergeev, Fauchez, et al., 2022). The location of the Rossby gyres also differs between models and between simulations with varying parameters. To date, only Skinner and Cho (2022) have studied the Rossby wave lifecycle in a tidally locked planet simulation. In their high-resolution, hot gas giant simulations, Rossby gyres (or “modons”) fully circumnavigate the planet in the westward direction, periodically dissipate, and then reform and begin circulating again. I did not observe circumnavigation even in a matching high-resolution simulation performed with the control Proxima Centauri b model. Numerous factors such as the temperature structure of the atmosphere and the presence of clouds may influence the motion of Rossby waves in simulations of tidally locked planets. A better understanding of the sensitivity and evolution of these waves in atmospheric models of tidally locked planets is key to understanding climate variability and a fruitful avenue for future work.

3.5 Conclusion

I describe a mechanism in the atmosphere of tidally locked terrestrial exoplanets in which feedbacks between clouds and incoming stellar radiation influence the dynamical state of the atmosphere, especially the zonal wavenumber-1 Rossby response to the thermal forcing, leading to alternating eastward and westward propagation of the Rossby gyres previously characterized as largely stationary. This proposed mechanism is as follows: 1) a decrease in substellar cloud cover reduces cloud albedo and increases the shortwave heating at the substellar surface of the planet; 2) the greater substellar atmospheric heating increases the peak-to-trough amplitude of the spatially periodic heating pattern, i.e. it increases the difference between dayside and nightside temperatures, and thereby enhances the Matsuno-Gill equatorial Rossby wave response, as shown in my spectral analysis of Rossby waves in the flow over time; 3) zonal mean wind speed also increases, shifting the Rossby wave response eastward of its equilibrium position and away from the substellar cloud region; 4) this results in decreased cloud cover at the eastern terminator. When substellar cloud cover increases again, the cycle “runs in reverse”: shortwave heating and atmospheric temperature drop, the Matsuno-Gill response weakens, the zonal wind slows, and the Rossby gyres shift westward.

The oscillation in the location of the Rossby gyres can only affect the distribution of clouds if the path of the Rossby gyre migration intersects with the dayside cloud cover. In my simulations of Proxima Centauri b, this interaction results in periodic clear and cloudy days at the planet’s eastern terminator, while in my simulations of TRAPPIST-1e, the Rossby gyres are located too far polewards to interact with the dayside clouds. Time series of synthetic spectra generated for a 300-day sample of the climate oscillation confirmed that the variation in cloud cover and atmospheric humidity associated with the feedback mechanism results in a time-varying transmission spectrum, but the magnitude of the variation in transit depths is too small to be detectable for my simulated planets. The mechanism is most likely to be observationally relevant on warm, slowly-rotating planets, as the long period of the Rossby gyre oscillation may clear the planetary terminators of cloud cover for extended stretches of time.

This study and my previous work in Chapter 2 identify physical mechanisms of variability which cause cycles in the planetary climate even in idealised exoplanet models without eccentricity, obliquity, or changes in the stellar spectrum. More complex environments on real planets are no doubt subject to additional sources of variability. As the body of exoplanet observations grows in the age of JWST and other upcoming telescopes, consideration of long-term climate variability and of weather on other planets can help interpret observations taken at different times, construct time series, and inform observing and data processing practices.

Chapter 4

Haze optical depth in exoplanet atmospheres varies with rotation rate: Implications for observations

(**Author contributions:** This work has been resubmitted after peer review to The Astrophysical Journal. I developed the haze transport and radiative transfer code, ran the simulations, analysed the output, and wrote the text. Adiv Paradise is the developer and maintainer of the ExoPlaSim source code. Paola Tiranti tested the haze transport and radiative transfer code. Paul Palmer and Massimo Bollasina supervised the project and edited the text.)

4.1 Introduction

Transmission spectroscopy promises insights into the atmospheres of a vast range of exoplanets, from the largest and hottest gas giants Ehrenreich et al. (2020) to sub-Earth-sized rocky worlds Lustig-Yaeger et al. (2019). Even before the launch and beginning of operations of the James Webb Space Telescope (JWST), attempts had been made to characterise exoplanet atmospheres with the Hubble Space Telescope (Damiano et al., 2022; Knutson et al., 2014; Libby-Roberts et al., 2022, 2020), the Very Large Telescope (Bean et al., 2011), and the Spitzer Space Telescope (Knutson et al., 2011), with mixed results: the spectra were often featureless, allowing limited inferences to be made about the planet's atmospheric chemistry and composition (Kreidberg et al., 2014). The greater sensitivity of the instruments on the JWST has partially overcome these limitations. For example, Ahrer et al. (2023) reported direct detection of carbon dioxide in the atmosphere of WASP-39 b, previously only hinted at by Spitzer data (Wakeford et al., 2017). On the other hand, Lustig-Yaeger et al. (2023) reported a featureless transmission spectrum for LHS 475 b, a warm Earth-sized planet, potentially caused by a high cloud deck, a thin atmosphere, or no atmosphere. Moran et al. (2023) found a spectrum for warm super-Earth GJ 486 b that statistically diverged from flat but could not be fit by any atmospheric model.

One cause of featureless transmission spectra that remains a challenge, including for the JWST and especially for observing Earth-like rocky planets, is the presence of clouds and hazes in a planet's atmosphere. An extensive literature exists on the topics of cloud and haze formation in exoplanet atmospheres and the impact they have on observations, including reviews by Barstow (2021) and Helling (2019) for clouds and Gao et al. (2021) for hazes. Theoretical predictions and laboratory work indicate that photochemically-produced hazes may be common in many types of exoplanets, including hot gas giants Gao et al. (2020) and sub-Neptunes (Crossfield & Kreidberg, 2017; He et al., 2018b; Hörst et al., 2018; Kawashima & Ikoma, 2018), but also on Earth-like planets (G. Arney, Domagal-Goldman, & Meadows, 2018; G. N. Arney et al., 2017; Bergin et al., 2023) and the early Earth itself (G. Arney et al., 2016; J. D. Haqq-Misra, Domagal-Goldman, Kasting, & Kasting, 2008; Trainer et al., 2004; Wolf & Toon, 2010). In addition, observations of some planets have hinted at the existence of hazes due to the presence of a steep scattering slope at short wavelengths of the spectrum Ohno and Kawashima (2020); Pont et al. (2008) or, in the case of GJ 1214 b, a high Bond albedo of 0.51 combined with a featureless transmission spectrum (Kempton et al., 2023).

Theoretical studies of photochemical hazes on terrestrial planets have typically used the existing literature on organic hazes found on Titan, called tholins, as their starting point. For example, G. N. Arney et al. (2017) used a 1-D coupled photochemical-climate model to simulate the effects of different stellar spectra on organic haze formation, using optical constants reported for Titan tholins by Khare et al. (1984). This study found that stellar spectra had a substantial impact on haze formation even within stellar classes: while the flaring M-dwarf (M3.5V) AD Leo produced only a thin haze layer at the top of the atmosphere, the quiescent M-dwarf (M4V) GJ 876 produced a haze layer 4-5 orders of magnitude thicker. As the simulations were 1-D and do not include transport by the planetary circulation, however, they may not represent the thickness of the haze layer at the planetary limb, the region of interest for transmission spectroscopy. Steinrueck et al. (2021) and Parmentier et al. (2013) studied the effect of the general circulation of hot Jupiters HD 189733 b and HD 209458 b on the gravitational settling of passive (i.e., not radiatively active) haze particles within the atmosphere. In their simulations, vertical mixing resulted in a relatively uniform abundance of small radius particles around the limb, but larger particles (with the size cut-off varying depending on the planet) displayed both spatial and temporal variability at the terminator. One-dimensional simulations are not able to capture this spatial variability.

The complexity of the formation and radiative impact of photochemical hazes—including coagulation and growth, sedimentation and transport, and effects on atmospheric heating profiles with consequent feedbacks on the circulation—make their representation in models a challenging task. In a recent work, Steinrueck et al. (2023) simulated HD 189733 b with radiatively active tracers and haze optical properties from either soot-like particles or Titan-like tholins. They found that Titan-like organic hazes had a dramatic effect on the planetary general circulation, changing its structure sufficiently for the 3-D haze distribution to be very different from that simulated without the haze radiative effects. The soot-like hazes had no such impact. In parallel, a recent study by Mak et al. (2023) used haze profiles from G. N. Arney et al. (2017) to simulate radiatively active organic haze on the Archean Earth in a sophisticated 3-D general circulation model (GCM), the Met Office Unified Model. A notable finding is that organic haze could either cool or warm the planet depending on the thickness of the haze layer, further complicating the picture of haze-atmosphere coupled interactions. It is clear that while sophisticated 3-D haze studies such as these are urgently needed, faster models are also crucial to begin covering the vast parameter space represented by exoplanet hazes.

In this study, I present a fast, idealised 3-D GCM with radiatively active hazes to bridge the gap between 1-D models and complex 3-D GCMs. The model, ExoPlaSim, is highly computationally efficient and was developed to map large parameter spaces and identify targets for simulation by more sophisticated GCMs (J. Haqq-Misra, Wolf, Fauchez, Shields, & Kopparapu, 2022; Paradise, Macdonald, Menou, Lee, & Fan, 2022). Exoplanet GCMs inclusive of haze modelling were not available until very recently, but Steinrueck et al. (2023), Mak et al. (2023), and the ExoPlaSim extension now raise the prospect of applying a sampling protocol as described in J. Haqq-Misra et al. (2022) to the study of exoplanet hazes.

I use ExoPlaSim to perform a parameter space sweep of 3-D haze distribution on tidally locked terrestrial planets as a function of planetary rotation rate, with a focus on the terminator region. Although 1-D models of haze production and haze microphysics can examine how much haze may form at any location on a tidally locked planet, they do not account for horizontal transport from other haze-producing regions. The haze abundance at the planetary limb, where transmission studies probe, depends not only on local production, but also on horizontal transport from the dayside's substellar region, where photochemical haze production should peak. My study thus aims to predict the terminator haze abundance for planets with different rotation periods given a fixed haze production amount on the dayside. The model and haze parameterisation as well as the numerical experiments are described in Section 4.2. In Section 4.3, I present my results and in Section 4.4 I discuss their significance, potential conclusions for selecting observational targets, and the limitations of my study and planned further work. Conclusions are presented in Section 4.5.

4.2 Methods

4.2.1 Model

I use the intermediate complexity GCM ExoPlaSim to perform my study. ExoPlaSim, documented in Paradise et al. (2022), is based on the Planet Simulator (Fraedrich, Jansen, Kirk, Luksch, & Lunkeit, 2005; Lunkheit et al., 2011), an Earth system model developed to maximise computational speed and portability. ExoPlaSim contains a spectral core and is optimised to run at T21 resolution (32 latitudes and 64 longitudes) with 10 vertical levels, which I maintain in my study. The model has a slab ocean and simulates moist atmospheric processes with vertical diffusion representing vertical mixing, Kuo-type deep convection (Kuo, 1965, 1974), Tiedtke shallow convection (Tiedtke, 1983), and dry convective adjustment. ExoPlaSim includes a radiative transfer module with two shortwave bands, a blue band from 0.3 to 0.75 μm and a red band from 0.75 to 14 μm, as well as one longwave band. The blue shortwave band ($\lambda < 0.75\mu$m) represents Rayleigh scattering in the lowest atmospheric level, cloud scattering, water vapour absorption, and optional ozone absorption (not used in my study), while the red band ($\lambda > 0.75\mu$m) includes water vapour absorption and both scattering and absorption by clouds (Lunkheit et al., 2011).

Paradise et al. (2022) modified the existing PlaSim source code to accommodate planets with a wide range of surface pressures, rotation rates, and stellar types, including tidally locked planets orbiting M-dwarf stars. At its standard T21 resolution, ExoPlaSim can compute a year of climate in roughly one minute of runtime (Paradise & Menou, 2017). ExoPlaSim has been used in previous studies of the habitability of Earth-like exoplanets (J. Checlair, Menou, & Abbot, 2017; J. H. Checlair, Olson, Jansen, & Abbot, 2019; Paradise & Menou, 2017; Paradise, Menou, Valencia, & Lee, 2019) and is particularly suited for simulations over long timescales (Chen, Li, Paradise, & Kopparapu, 2023) or large, unconstrained parameter spaces (Macdonald, Paradise, Menou, & Lee, 2022). I refer to J. Haqq-Misra et al. (2022) and Paradise et al. (2022) for detailed description of the model and its performance compared to other GCMs.

To represent haze particles circulating in the atmosphere, I used ExoPlaSim's built-in grid-space tracer transport module, supplemented by a gravitational settling scheme based on Steinrueck et al. (2021) and Parmentier et al. (2013). The radiative effects of the haze are taken into account in a parameterisation for a scattering and absorbing aerosol given by Stephens (1978). I refer to Appendix A for a complete description of these parameterisations. With the haze module included, I was able to compute one year of model time in eight minutes when running on 32 processors.

4.2.2 Haze optical constants

To simulate the effect of radiatively active hazes in the atmosphere, I use the complex refractive indices reported in He et al. (2023). In this study, the authors generated haze analogs in the PHAZER chamber set-up of Johns Hopkins University (He et al., 2017) with an AC plasma energy source. The gas mixture used to approximate a water-rich 300 K atmosphere at 1000x solar metallicity was 56.0% H_2O, 11.0% CH_4, 10.0% CO_2, 6.4% N_2, 1.9% H_2, and 14.7% He. Although my simulated atmospheres of nitrogen gas with interactive water vapour and trace carbon dioxide and methane do not precisely replicate this gas mixture, the laboratory set-up and haze analogs produced in He et al. (2023) are a better fit for simulations of water-rich rocky planets than the previously widely used optical constants measured for organic tholins in a Titan-like atmosphere in Khare et al. (1984). I further choose to simulate this haze because the authors report both the complex refractive index and the density, a necessary input for the gravitational settling scheme, and because a large amount of haze was produced at 300 K, making it appropriate for simulations of hazy temperate planets. Ultimately, however, I expect photochemical haze compositions and production rates to be sensitive to the particular conditions on a planet and not easily generalised across atmospheres (Corrales, Gavilan, Teal, & Kempton, 2023; He et al., 2018a; Moran et al., 2020). My study examines the interaction between one potential kind of organic haze and the general circulation of tidally locked planets, without aiming to predict what kinds of organic haze may actually be present on temperate tidally locked M-dwarf planets.

My simulations assume the haze particles are spherical and can be described using Mie theory (Mie, 1908). I use He et al. (2023)'s complex refractive indices between 0.4 and 14 μm, binned to 10 nm, and the Python package MiePython (Prahl, 2023) to calculate the wavelength-specific extinction, scattering, and backscattering efficiencies based on the size parameter derived from the particle radius. I use a particle of radius 500 nm based on findings from G. N. Arney et al. (2017), in which particles grew to this size for the quiescent M-class star GJ 876, and on the results of a sensitivity study of haze particle size reported in Section 4.3. A pre-prepared BT-Settl stellar spectrum, also binned to 10 nm, is then used to compute the flux-weighted mean efficiencies for each shortwave band. Table 4.1 lists the efficiencies for the two stellar spectra in my study for both shortwave bands, where band 1 indicates wavelengths $< 0.75\mu$m and band 2 indicates wavelengths $> 0.75\mu$m, as well as the stellar parameters. Comparison of the scattering and extinction efficiencies indicates that the particles are primarily scattering rather than absorbing.

Star	TRAPPIST-1	Wolf 1061
Q_{ext} (band 1)	3.42	3.00
Q_{scat} (band 1)	3.24	2.79
Q_{back} (band 1)	0.23	0.31
Q_{ext} (band 2)	2.03	2.30
Q_{scat} (band 2)	1.98	2.24
Q_{back} (band 2)	0.03	0.04
Stellar temperature (K)	2709	3408
Stellar metallicity (·)	0.045	-0.09
log (g) (·)	5.2	4.9

Table 4.1: Mie extinction efficiency, scattering efficiency, and backscattering efficiencies for two M-class stars for shortwave bands 1 ($0.3 < \lambda < 0.75\mu$m) and 2 ($0.75 < \lambda < 14\mu$m), as well as parameters defining the stellar spectra. Efficiencies are shown rounded to the fifth decimal place.

4.2.3 Source and sink

I position the haze source in the stratosphere at the top model level only in an analogy to Earth's Junge layer (Junge, Chagnon, & Manson, 1961). I assume the haze particles are photochemically produced *in situ* by shortwave radiation and settle downwards to be redistributed by the tropospheric circulation. The source term is defined as:

$$P = S_{top} \frac{SW_{top}}{SW_{max}} \tag{4.1}$$

where SW_{top} is the downward shortwave flux for each gridbox at the top level of the model and SW_{max} is the maximum downward shortwave flux out of all gridboxes at the top level. S_{top} is an arbitrary source coefficient in units of kg/kg. For a tidally locked planet, the source is at its maximum at the substellar point and falls off in all directions proportionally to the downward shortwave flux. The haze source can be dampened and reach an equilibrium of less than S_{top} if, for example, the reflective effect of a haze layer reduces the incoming shortwave flux. I fix the source coefficient for all simulations at 10^{-7} kg/kg, based on haze profiles reported in G. N. Arney et al. (2017) for an atmosphere with a methane to carbon dioxide ratio of 0.2 at an altitude of 25-30 km, the approximate height of the model top. A sink term is provided only in the bottom level. Its value is a constant 10^{-3} applied uniformly to the mass mixing ratio in the bottom model level (following Steinrueck et al. (2021)), which is assumed to be a timescale for particles settling out of the atmosphere.

Table 4.2 summarises the free parameters in the haze scheme, the values used in my simulations, and their sources.

Parameter	Value	Source
Particle radius (nm)	500	G. N. Arney et al. (2017)
Particle density (kg/m^3)	1262	He et al. (2023)
Source (kg/kg)	10^{-7}	G. N. Arney et al. (2017)
Sink ($\cdot$)	10^{-3}	Steinrueck et al. (2021)
Haze optical constants	Table 4.1	He et al. (2023)

Table 4.2: Free parameters in the haze scheme, the values chosen for my simulations, and their sources.

4.2.4 Simulation set-up

I performed a parameter space sweep of rotation rate for two idealised tidally locked aquaplanets, one representative of Earth-like terrestrial planets and one of super-Earths. For Earth-like planets, I use configuration values for TRAPPIST-1 e (Gillon et al., 2017), an ideal candidate because it is used as a benchmark in the TRAPPIST-1 Habitable Atmosphere Intercomparison (Fauchez et al., 2022; Sergeev, Fauchez, et al., 2022; Turbet et al., 2022). To extend my study to super-Earths, I use values for Wolf 1061 c (Wright, Wittenmyer, Tinney, Bentley, & Zhao, 2016). Table 4.3 summarises the parameters used in my simulations, which I take from the Arecibo Habitable Planets Catalog (Laboratory, 2023). In addition to two size classes, the simulated planets represent two ends of the habitable temperature range, with ExoPlaSim simulating TRAPPIST-1 e as an eyeball planet (a sea ice-covered nightside and liquid water only in the substellar region) and Wolf 1061 c as a planet close to a runaway greenhouse state. Wolf 1061 c approaches 9% atmospheric water vapour at the substellar point and is in a temperature and pressure regime that would lead to a runaway greenhouse in other GCMs (see J. Haqq-Misra et al. (2022) for a comparison of ExoPlaSim and ExoCAM when simulating hot near-runaway atmospheres). However, my simulations remain numerically stable and reach an equilibrium with the values given in Table 4.3, showing no further warming trend. As the failure to run away may be an artefact of the model's limitations with respect to water vapour treatment, these simulations should be seen as possible atmospheric states for warm temperate planets, rather than specific predictions for planets with the stellar constant of Wolf 1061 c. I discuss these limitations further in Section 4.4.4. The atmospheric composition of bulk nitrogen gas with interactive water vapour and trace methane and carbon dioxide in a 0.2 ratio is based on simulation parameters from G. N. Arney et al. (2017) which allowed for the formation of a thick haze layer with a substantial effect on the climate in their study.

Before carrying out the parameter space sweep, I ran each simulation for 75 model years to determine the time until radiative balance was reached at the top of the atmosphere. I found that while small net positive or negative energy anomalies continued to exist at top-of-atmosphere until 60 years of model time, the temperature, atmospheric moisture, and haze profiles reached equilibrium and no longer showed an upward or downward trend after about 20 years. Accordingly, to save computational time, I run each simulation in the parameter

Planet	TRAPPIST-1 e	Wolf 1061 c
Radius ($R_\oplus$)	0.92	1.66
Stellar constant (W/m^2)	889	1777
Gravity (m/s^2)	9.1	12.1
N_2 (bar)	0.988	0.988
CH_4 (bar)	0.002	0.002
CO_2 (bar)	0.01	0.01

Table 4.3: Planet simulation parameters. The unit of bar is equivalent to 10^5 Pascals.

space for 30 years and use the average of the final year of runtime for my analysis. All simulations are run with 1 bar (10^5 Pascal) of surface pressure at the standard T21 truncation (32 latitudes x 64 longitudes x 10 model levels) and initialised from a 250 K isothermal atmosphere. The top model level is located at 10 mbar or 25-28 km, representing the tropopause. I use a model timestep of 15 minutes.

4.2.5 Study parameter space

To test the gravitational settling scheme, I first simulate a range of particle sizes and densities as passive tracers only, following Steinrueck et al. (2021) and Parmentier et al. (2013). The particle radii include: 1 nm, 5 nm, 10 nm, 30 nm, 50 nm, 60 nm, 80 nm, 100 nm, 500 nm, and 1000 nm. These values cover a similar range as Steinrueck et al. (2021), but with greater focus on particles in the 10s of nanometers because laboratory experiments reported in He et al. (2018b) found that haze particle size distributions tended to peak in the 30-80 nm range (although for a different gas composition than studied in He et al. (2023)). This set of simulations is repeated for particle densities of 1000 kg/m^3, 1262 kg/m^3, and 1328 kg/m^3. The latter two values are reported in He et al. (2023) as the densities of the organic haze analogues created in the study experiments at 300 K and 400 K, respectively. 1000 kg/m^3 is the reference value used in Steinrueck et al. (2021) and Parmentier et al. (2013) and approximates the density of black soot. The results of these size and density sensitivity tests are in line with those of Steinrueck et al. (2021) and Parmentier et al. (2013). I briefly discuss them in Section 4.3.

In my primary parameter space, I keep all inputs for each of the simulated planets fixed, but vary the rotation period from 1 to 30 Earth days, plus two additional simulations with periods of 6 and 12 hours. This gives a total of 32 simulations for each planet, or 64 in all. I use only one haze particle size and density: 500 nm, the size to which haze particles grew in the quiescent M-dwarf simulation in G. N. Arney et al. (2017), and 1262 kg/m^3, the density of haze analogues measured in He et al. (2023) for a water-rich 300 K atmosphere, together with the Mie efficiencies listed in Table 4.1. On Earth, particles of this size are in the accumulation phase, i.e. they accumulate in the atmosphere rather than settling out rapidly or agglomerating to form larger particles. In addition to these 64 simulations with radiatively active circulating haze, I perform another 64 simulations which are identical in all respects but do not include haze. I refer to this second set as “control simulations” and use them as a comparison to determine how the haze radiative feedback affects the surface temperature and general circulation in each simulation.

The aim of this experimental design is to study the potential distributions of organic hydrocarbon hazes on temperate tidally locked rocky planets as a function of rotation period (a known value for tidally locked planets). I focus particularly on the planetary limb, the region observed during transmission spectroscopy. While photochemical haze production may be expected to be highest in the substellar region, where stellar UV flux is the greatest, the haze abundance at the limb will depend on the general circulation. In this work, I do not vary the rotation period and stellar constant together, as I wish to isolate the effect of varying rotation. Instead, the inclusion of two planets with different stellar constants, stellar spectra, and sizes points at important factors in the larger parameter space affecting haze distribution which can be explored in future studies, while allowing one-to-one comparison between the planets based on rotation period. In the text hereafter, I refer to the set of simulations based on TRAPPIST-1 e planetary parameters as TRAP and those based on Wolf 1061 c as WOLF.

4.3 Results

My simulations fall into three circulation regimes, previously described in the literature, and one transitional regime. Below I describe the general circulation and 3-D haze distribution of each regime, followed by an overview of the parameter space as a whole and a brief discussion of sensitivity to particle size and density.

4.3.1 Banded circulation regime

For rotation periods 0.25, 0.5, and 1 days, both TRAP and WOLF simulations fall into a banded circulation regime with eastward flow in the mid-latitudes and westward flow at the equator. This regime resembles the flow state for a planet with a 1-day rotation period shown in Merlis and Schneider (2010) (their Figure 6, top right), Carone, Keppens, and Decin (2015) (their Figure 14 and 15), and Noda et al. (2017) (their Figure 11 b), as well as the “rapid rotators” described by J. Haqq-Misra, Wolf, Joshi, Zhang, and Kopparapu (2018). I show the horizontal and vertical winds at the top model level in Figure 4.1 because this level is where the haze source is prescribed and where wind-haze interactions first take place.

Figure 4.2 shows the vertically integrated haze mass column and the area- and density-weighted haze mass profiles for several regions on the planet: the dayside, nightside, terminator, and the western and eastern halves of the terminator split into separate areas. The TRAP case is comparatively well-mixed, with similar vertical haze profiles in all regions and a small

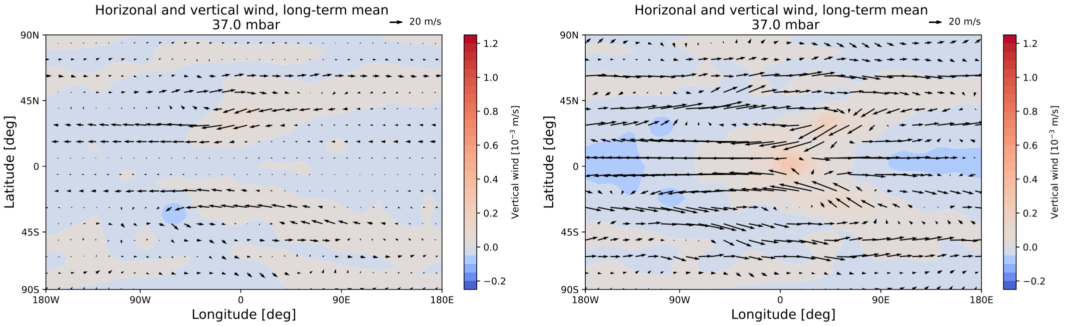

(a) TRAPPIST-1 e, top of model **(b)** Wolf 1061 c, top of model

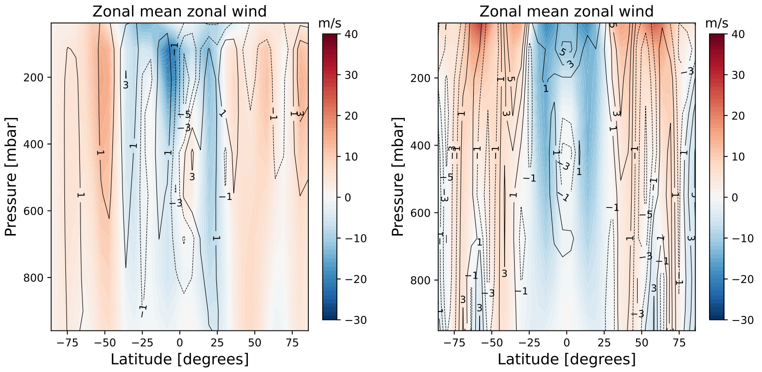

(c) TRAPPIST-1 e, zonal mean zonal wind **(d)** Wolf 1061 c, zonal mean zonal wind

Figure 4.1: Top row: Horizontal and vertical winds in circulation regime 1 for a) TRAPPIST-1 e-type planet and b) Wolf 1061 c-type planet. Bottom row: Zonal mean zonal wind for TRAP and WOLF, with contour lines showing the difference in wind speed (absolute value) between the haze simulation and an identical simulation without haze (hazy minus control). Solid lines indicate positive values and dashed lines indicate negative. The rotation period shown is 0.25 days.

gradient in the haze column from equator to pole. In contrast, the WOLF case is more spatially differentiated. Haze is concentrated closer to the equator and west of the substellar point, forming a distinct M- or W-shape. The vertical profiles reveal greater terminator asymmetry, with a hazier western terminator higher in the atmosphere, and a hazier eastern terminator below roughly 600 mbar.

In Figure 4.3, I show an estimate of the haze differential optical depth in shortwave band 1 (blue) along the line of sight when the planet is viewed from the star. As a true 3-D treatment of the line of sight requires complex calculations and remains to be integrated into atmospheric retrievals (Caldas et al., 2019; Wardenier et al., 2022), I use a fixed path length and assume the haze number density is constant along this path. Fig. 4.3 therefore represents a relative comparison of the extinction caused by the simulated TRAP and WOLF atmospheres rather than a quantitative prediction of optical depth. Like Fig. 4.2, Fig. 4.3 reveals more uniform haze mixing in the TRAP atmosphere both from equator to pole and from surface to top of the atmosphere, although there is still enhancement near the equator. In contrast, in the WOLF case haze remains largely concentrated within $\pm 40^{\circ}$. In addition, there is significant terminator asymmetry, with haze differential optical thickness decreasing above 400 mbar at the eastern terminator and remaining high to the model top at the western terminator.

4.3.2 Transitional circulation regime

TRAP simulations with a rotation period of 2 days and WOLF simulations with periods of 2 and 3 days enter into a transitional space between circulation regimes characterised by a very low amount of haze. Figure 4.4 shows that the two models have different horizontal wind structures. In the TRAP case, there is a prominent quadrupolar pattern at the model top, while the WOLF case appears more similar to the banded regime, with higher wind speeds and the beginnings of gyre formation typical of the regime described in Section 4.3.3 below. Similarly, the zonal mean zonal wind in TRAP no longer exhibits westward flow at the equator and instead forms an eastward jet with increasing wind speeds towards the mid-latitudes. In contrast, the zonal mean zonal wind in the WOLF case appears like a higher-speed, more regular version of the banded regime. However, both simulations show an increase in the magnitude and spatial extent of the upward wind on the dayside, with a corresponding increase in subsidence on the nightside.

Figure 4.5 reveals a low amount of haze throughout the atmosphere, with vertical profiles consistent across the planet at around 0.5×10^{-9} kg/m^3 for both WOLF and TRAP. The vertical haze columns and differential optical depths shown in Figure 4.6 are about 25 percent of those in the banded regime. The low haze amount could be caused by, for example, more rapid settling of particles at the planetary surface, or a failure of particles to escape the source at

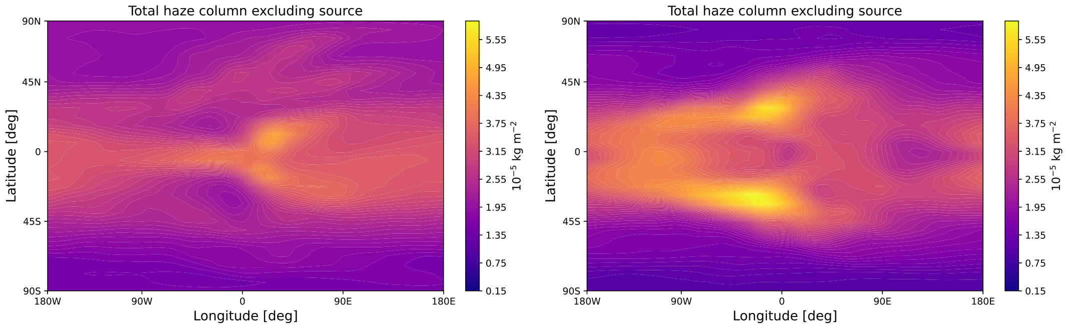

(a) TRAPPIST-1 e **(b)** Wolf 1061 c

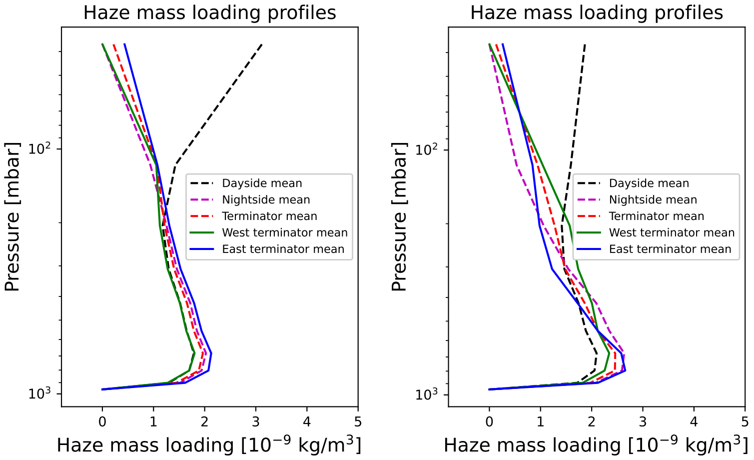

(c) TRAPPIST-1 e **(d)** Wolf 1061 c

Figure 4.2: Vertically integrated haze mass column for a) TRAP and b) WOLF and vertical haze mass profiles for c) TRAP and d) WOLF regime 1. The rotation period shown is 0.25 days.

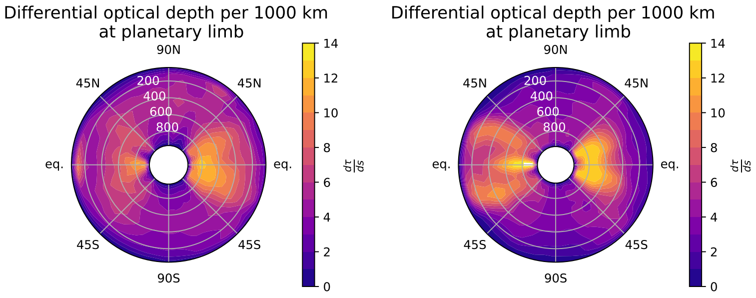

(a) TRAPPIST-1 e **(b)** Wolf 1061 c

Figure 4.3: Differential optical depth per 1000 km in shortwave band 1 at the planetary limb for a) TRAP and b) WOLF for regime 1. The white text labels show pressure in mbar. The eastern (evening) terminator is shown on the right-hand side of each plot and the western (morning) terminator on the left-hand side of each plot to maintain consistency with other figures. The rotation period shown is 0.25 days.

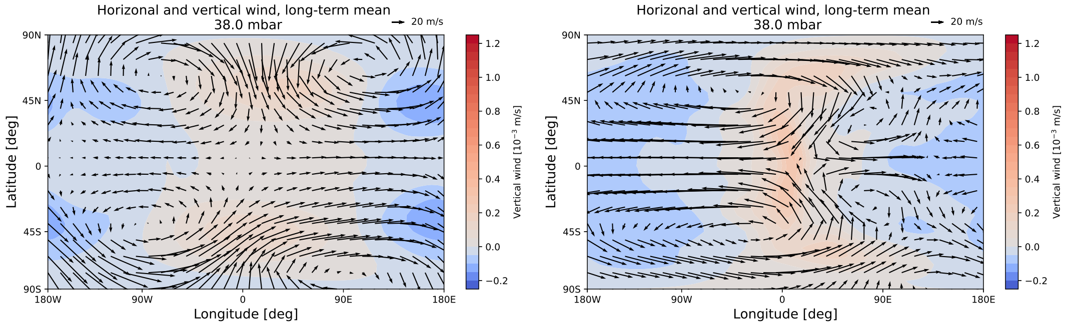

(a) TRAPPIST-1 e, top of model

(b) Wolf 1061 c, top of model

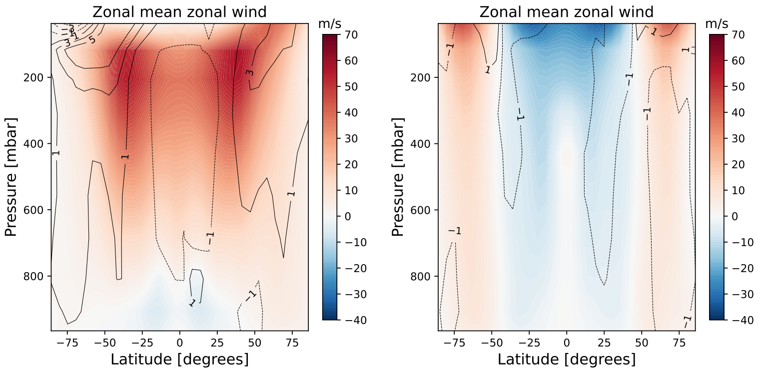

(c) TRAPPIST-1 e, zonal mean zonal wind

(d) Wolf 1061 c, zonal mean zonal wind

Figure 4.4: Top row: Horizontal and vertical winds in circulation regime 2 for a) TRAP and b) WOLF. Bottom row: Zonal mean zonal wind for c) TRAP and d) WOLF, with contour lines showing the difference in wind speed (absolute value) between the haze simulation and an identical simulation without haze (hazy minus control). Solid lines indicate positive values and dashed lines indicate negative. The rotation period shown is 2 days.

the top level. The larger extent of the area of upward wind shown in Fig. 4.4 a) and b) and uniform lack of haze throughout the atmosphere in Fig. 4.5 suggest the latter is more likely. A detailed analysis of the particle trajectories would be helpful to clarify this aspect, but is beyond the scope of this study.

4.3.3 Double jet circulation regime

For rotation periods of 3 (TRAP) or 4 (WOLF) to 12 days, both planets develop a circulation characterised by two rapid mid-latitude eastward jets. This double jet circulation regime is a common equilibrium state for simulations of TRAPPIST-1 e with its original rotation period of 6.1 days, predicted by 3 out of 4 models in the TRAPPIST-1 Habitable Atmosphere Intercomparison (Sergeev, Fauchez, et al., 2022). As shown in Figure 4.7, WOLF has substantially faster jets than TRAP, particularly near the model top. Also characteristic of this state are a pair of high-latitude Rossby gyres found near the eastern terminator, along with a less prominent matching pair at the western terminator. The gyres are key to the haze distribution in this regime. The vertical haze columns shown in Figure 4.8 display several notable features: a much hazier WOLF atmosphere than TRAP, a reversed meridional haze gradient with a clearer equator and hazier poles compared to the banded regime, the build-up of a thick haze layer in the eastern Rossby gyres, and a small north-south asymmetry in haze mass.

North-south asymmetry in simulations of tidally locked planets has been reported in other models, notably by Braam, Palmer, Decin, Cohen, and Mayne (2023) in ozone columns, by Landgren, Nadeau, Lewis, Kataria, and Hitchcock (2023) in the size of the Rossby gyres, and by Noda et al. (2017) in the surface temperature and other climate variables. This behaviour occurs in both sophisticated GCMs (the Met Office Unified Model in Braam et al. (2023)) and shallow-water models (the Shallow-Water Atmospheric Model in Python for Exoplanets in Landgren et al. (2023)). Landgren et al. (2023) hypothesise that a supercritical pitchfork bifurcation leads to north-south hemispheric asymmetry because at the convergence zone around the western terminator, where the eastward flow between the gyres encounters the westward dayside-to-nightside flow, even a small perturbation in the eastward winds leads to an uneven transfer of momentum across the equator to either the northern or southern hemisphere. The asymmetry of the gyres then causes asymmetries in the ozone column of Braam et al. (2023) and the surface temperature of Noda et al. (2017) because the gyres collect tracers and are associated with a surface temperature minimum.

The Rossby gyres are key to the high terminator differential optical depth in this regime, as shown in Figure 4.9. Braam et al. (2023) describe how the overturning circulation of the troposphere and stratosphere on a slowly rotating tidally locked planet can transport tracer-enriched air from the dayside to the nightside and deposit it in the gyres. A similar pattern

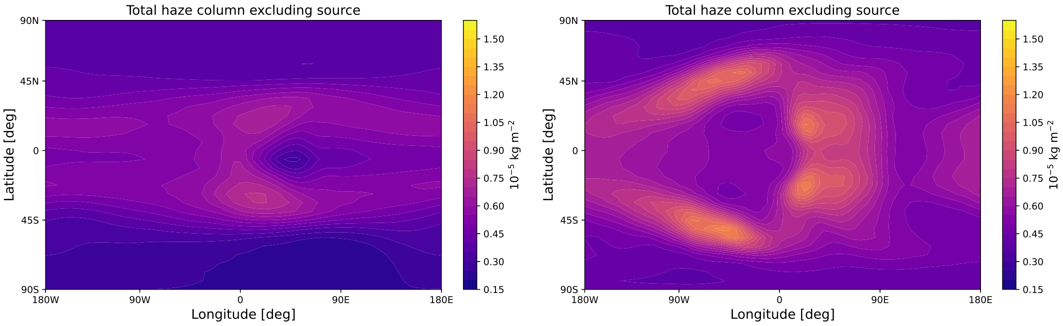

(a) TRAPPIST-1 e **(b)** Wolf 1061 c

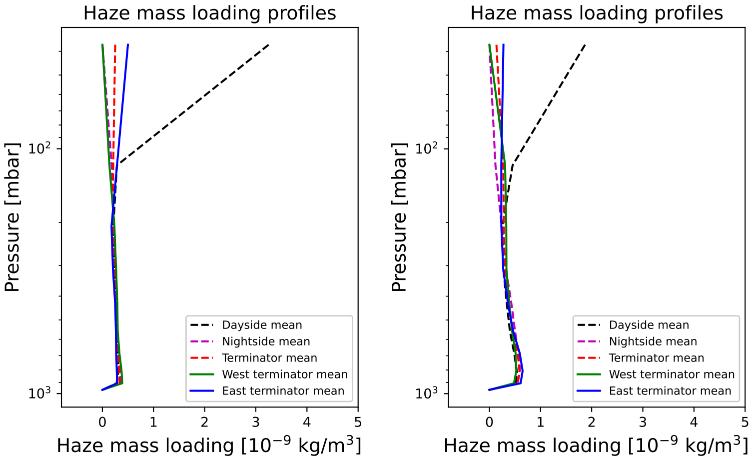

(c) TRAPPIST-1 e **(d)** Wolf 1061 c

Figure 4.5: Vertically integrated haze mass column for a) TRAP and b) WOLF and vertical haze mass profiles for c) TRAP and d) WOLF for regime 2. The rotation period shown is 2 days.

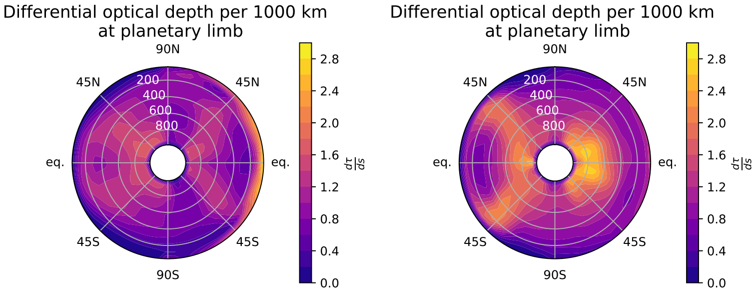

(a) TRAPPIST-1 e **(b)** Wolf 1061 c

Figure 4.6: Differential optical depth per 1000 km in shortwave band 1 at the planetary limb for a) TRAP and b) WOLF regime 2. The eastern (evening) terminator is shown on the right-hand side of each plot and the western (morning) terminator on the left-hand side of each plot to maintain consistency with other figures. The white text labels show pressure in mbar. The rotation period shown is 2 days.

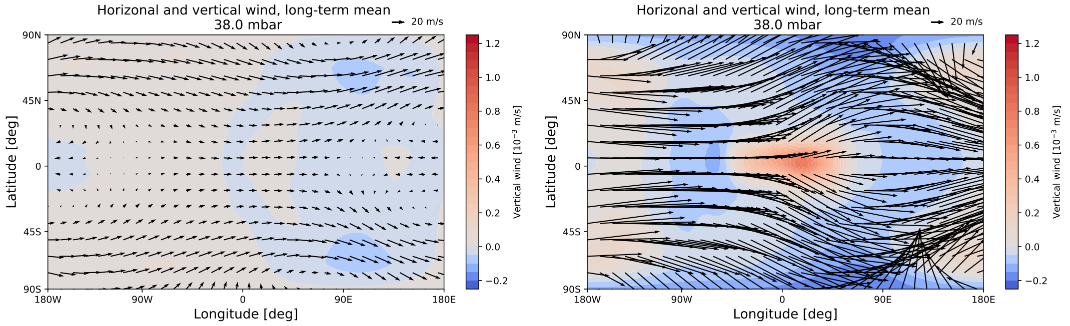

(a) TRAPPIST-1 e, top of model **(b)** Wolf 1061 c, top of model

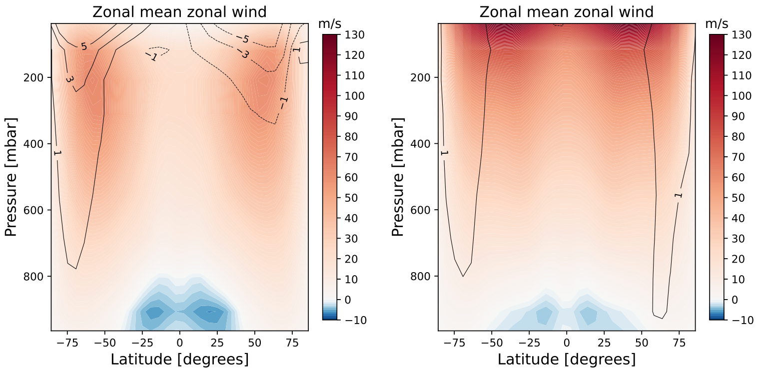

(c) TRAPPIST-1 e, zonal mean zonal wind **(d)** Wolf 1061 c, zonal mean zonal wind

Figure 4.7: Top row: Horizontal and vertical winds in circulation regime 3 for a) TRAP and b) WOLF. Bottom row: Zonal mean zonal wind for c) TRAP and d) WOLF, with contour lines showing the difference in wind speed (absolute value) between the haze simulation and an identical simulation without haze (hazy minus control). Solid lines indicate positive values and dashed lines indicate negative. The rotation period shown is 6 days.

of tracer transport is reported in Parmentier et al. (2013) (their Figure 6 for 0.5 μm particles) and Steinrueck et al. (2021) (their Figure 7 for 1.0 μm particles). The large latitudinal extent of the gyres and their presence straddling the eastern terminator leads to the poor observing prospects of this simulated regime compared to the others.

4.3.4 Single jet circulation regime

For periods of 13 to 30 days, ExoPlaSim simulates both TRAP and WOLF as planets with a single eastward jet centred at the equator. This circulation regime has been described in previous studies of rotation rate Edson et al. (2011); Noda et al. (2017) and in investigations of the equatorial superrotation on both gas and terrestrial planets (A. P. Showman & Polvani, 2010, 2011; A. P. Showman et al., 2013). Figure 4.10 c) and d) shows a broad jet covering most of the planet in both the TRAP and the WOLF cases, with higher winds speeds on WOLF, particularly near the model top, and a weaker westward flow near the poles. In the transition from the double jet to the single jet regime, the eastern Rossby gyres increase in size and migrate to the nightside of the planet.

The position of the gyres is once again key to the terminator differential optical depth shown in Figure 4.12. If the gyres continue to collect haze particles but are now located on the nightside rather than on the planetary limb, I might expect a less hazy terminator. This is the case for the TRAP simulation: the vertical haze column in Figure 4.11 a) is highest in the substellar region and within the nightside gyres, and comparatively low elsewhere. In the WOLF case, however, (Fig. 4.11 b)), the haze column is lowest in the substellar region and within the nightside gyres and highest in the region of high winds around the gyre centres. This results in a very high haze mass at the limb, this time at the western terminator. The vertical haze profiles shown in Fig. 4.11 c) and d) reveal that TRAP has a high haze layer at altitudes higher than 200 mbar and a lower amount of haze throughout the atmosphere below, while in the WOLF simulation haze mass increases steadily with atmospheric pressure. This vertical structure is consistent with Braam et al. (2023)'s description of tracer transport by an overturning dayside-nightside circulation from a high source region on the dayside to the nightside gyres. As the TRAP case develops a high haze layer, the overturning circulation can transport haze from this layer into the gyre centres. In contrast, haze settles more rapidly in the WOLF simulation and experiences the edges of the gyres as a barrier when horizontally transported from dayside to nightside. The contrast between these two cases highlights the importance of the full 3-D circulation in predicting the amount of haze in the observing region.

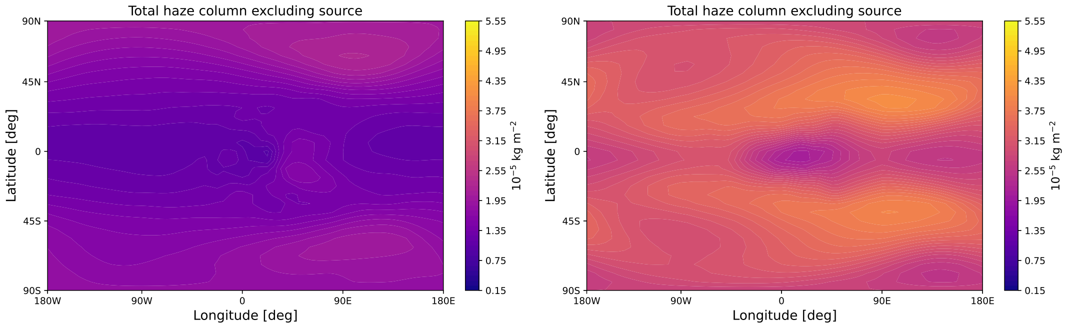

(a) TRAPPIST-1 e **(b)** Wolf 1061 c

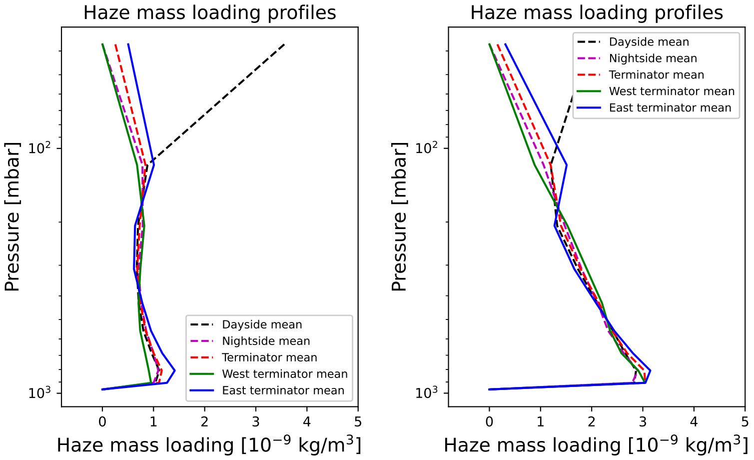

(c) TRAPPIST-1 e **(d)** Wolf 1061 c

Figure 4.8: Vertically integrated haze mass column for a) TRAP and b) WOLF and vertical haze mass profiles for c) TRAP and d) WOLF for regime 3. The rotation period shown is 6 days.

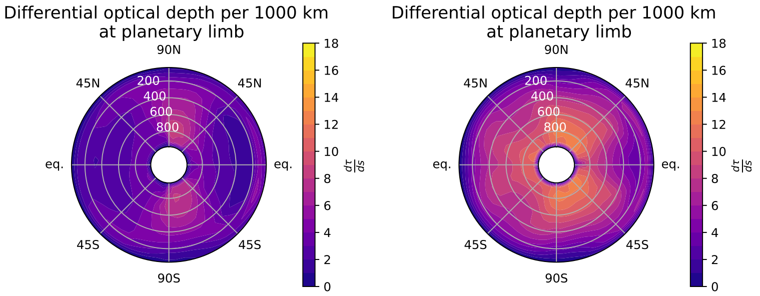

(a) TRAPPIST-1 e **(b)** Wolf 1061 c

Figure 4.9: Differential optical depth per 1000 km in shortwave band 1 at the planetary limb for a) TRAP and b) WOLF for regime 3. The white text labels show pressure in mbar. The eastern (evening) terminator is shown on the right-hand side of each plot and the western (morning) terminator on the left-hand side of each plot to maintain consistency with other figures. The rotation period shown is 6 days.

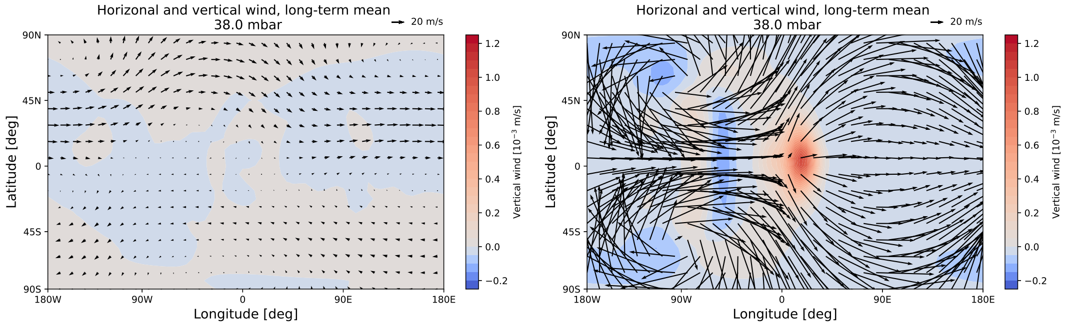

(a) TRAPPIST-1 e, top of model **(b)** Wolf 1061 c, top of model

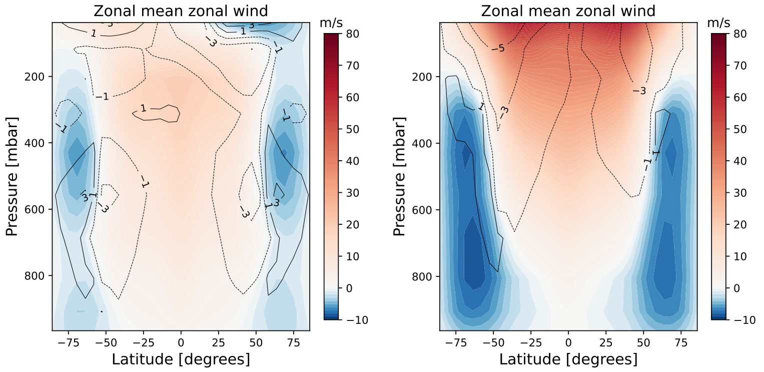

(c) TRAPPIST-1 e, zonal mean zonal wind **(d)** Wolf 1061 c, zonal mean zonal wind

Figure 4.10: Top row: Horizontal and vertical winds in circulation regime 4 for a) TRAP and b) WOLF. Bottom row: Zonal mean zonal wind for c) TRAP and d) WOLF, with contour lines showing the difference in wind speed (absolute value) between the haze simulation and an identical simulation without haze (hazy minus control). Solid lines indicate positive values and dashed lines indicate negative. The rotation period shown is 18 days.

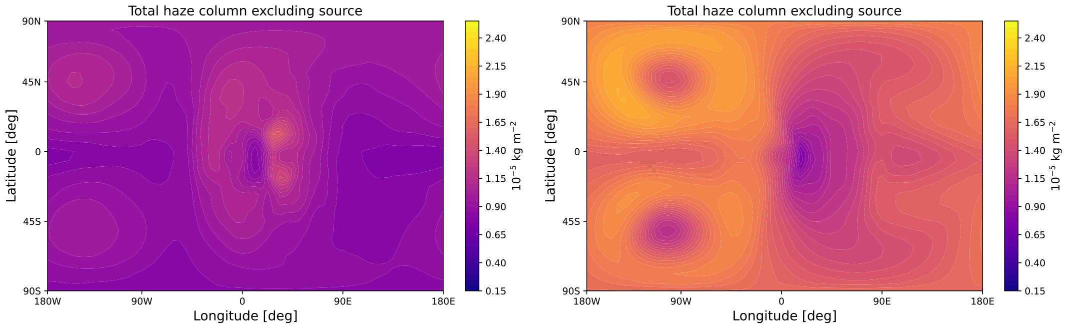

(a) TRAPPIST-1 e

(b) Wolf 1061 c

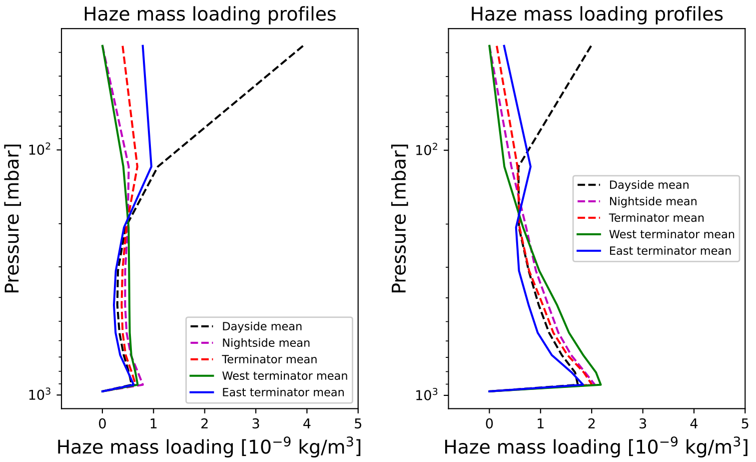

(c) TRAPPIST-1 e

(d) Wolf 1061 c

Figure 4.11: Vertically integrated haze mass column for a) TRAP and b) WOLF and vertical haze mass profiles for c) TRAP and d) WOLF for regime 4. The rotation period shown is 18 days.

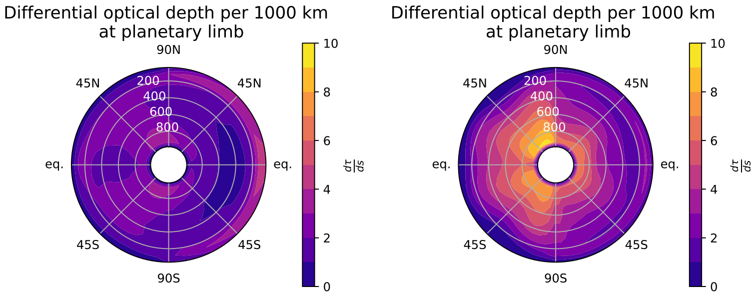

(a) TRAPPIST-1 e

(b) Wolf 1061 c

Figure 4.12: Differential optical depth per 1000 km in shortwave band 1 at the planetary limb for a) TRAP and b) WOLF for regime 4. The white text labels show pressure in mbar. The eastern (evening) terminator is shown on the right-hand side of each plot and the western (morning) terminator on the left-hand side of each plot to maintain consistency with other figures. The rotation period shown is 18 days.

4.3.5 Parameter space overview

Observing region

The four regimes described above are representative of my chosen parameter space. I now give an overview of the full parameter space as a function of rotation rate. Figure 4.13 displays the haze mass per meter squared at the planetary limb as a function of planetary rotation period. The four circulation regimes are clearly visible. Haze mass, initially high at short periods in the banded regime, drops steeply with rotation rate to the low-haze valley at 2 (TRAP) or 3 (WOLF) days. It then rises again in the double jet regime, but there are clear differences between the two planets: the TRAP case takes the rough form of a parabola, peaking at around 8 days in the middle of the double jet regime. The haze mass remains lower than in the banded regime throughout. In contrast, haze mass increases sharply in the WOLF case to a maximum at 5 days. In the WOLF simulations, the double jet regime is even hazier than the banded regime. In the single jet regime, both planets see a gradual increase with rotation period, but the total haze mass remains substantially lower than in the banded and double jet regimes. Fig. 4.13 also reveals systematic patterns in terminator asymmetry. In the double jet regime, both TRAP and WOLF have more haze mass at the eastern terminator, while in the single jet regime, the WOLF simulations now have a hazier western terminator up to a 22-day rotation period and the TRAP simulations show little asymmetry. This difference is due to the trapping of haze particles in the nightside gyres in the TRAP simulations but not in the WOLF simulations in the single jet regime.

While Fig. 4.13 could suggest that slowly rotating planets are more favourable observing targets because they generally have lower differential optical depths at the limb, it does not account for the height at which haze particles accumulate. The height of the haze layer is as important as the particle abundance, as instruments cannot probe below the haze layer if the atmosphere exceeds a certain threshold of optical depth. To quantify the impact of vertical structure on potential observations, I show in Figure 4.14 the percentage of the top model level (the tropopause) which exceeds differential optical depths of 1, 2, and 3 in shortwave band 1. Fig. 4.14 a) and b) mirror Fig. 4.13 with respect to the banded regime, haze valley, and double jet regime: the terminators are largely impenetrable in the banded and double jet regimes and anomalously clear in the transitional regime between them. However, in the single jet regime, differential optical depths are higher in more of the limb for TRAP than for WOLF, even though TRAP has less haze mass overall.

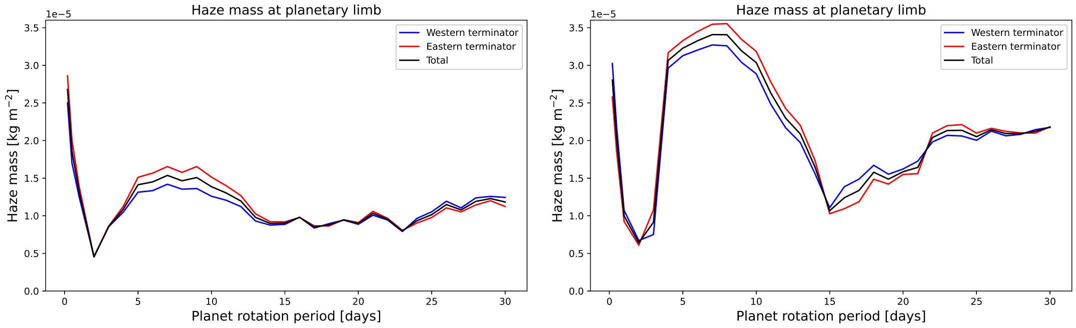

(a) TRAPPIST-1 e **(b)** Wolf 1061 c

Figure 4.13: Haze mass at the planetary limb in kg/m^2 as a function of rotation rate for a) TRAP and b) WOLF. Haze mass loading is integrated downwards as in the vertically integrated haze column and then additionally along the limb to account for differences in spacing between latitudes. The total haze mass at the limb is then divided by the surface area of the limb to further account for the difference in size between the two planets, resulting in a unit of kg/m^2.

The reason for this is revealed in Fig. 4.14 c) and d), which show the maximum differential optical depth at each atmospheric pressure level as a function of rotation period. The hazy banded regime, clear transitional regime, and hazy double jet regime are visible and consistent with Fig. 4.13 and Fig. 4.14 a) and b), but the difference in vertical structure in the single jet regime is now apparent. Haze particles continue to build up in the deeper atmosphere in the WOLF simulations as rotation period increases, but do not form a layer at the top of the model as in the TRAP simulations.

Climate impact

To examine the impact of radiatively active organic haze particles on the planetary climate, I show the global mean surface temperature and global mean water vapour column in Figure 4.15 for both my simulations with radiative effects of haze and the matching set of control simulations without haze. For most of the parameter space, the haze has little impact on the climate and effectively acts as a passive tracer. Table 4.1 shows that most of the extinction is caused by scattering rather than absorption, and that the scattering is mostly in the forward direction, as the backscattering efficiencies are small. It may be that the particles scatter light forwards through the atmosphere and towards the surface, leading to similar instellation at the surface as a clear atmosphere and therefore a similar surface temperature and water vapour column. For the TRAP case, some simulations in the double jet regime show a small anti-greenhouse effect of no more than 1-2 K, while in the WOLF case, the slowest rotators in the single jet regime show warming of up to 5 K due to the haze. The contours in Figures 4.1, 4.4, 4.7, and 4.10 c) and d) in turn show the radiative feedback of the haze on the general circulation, with positive values corresponding to regions where the hazy simulation predicts higher

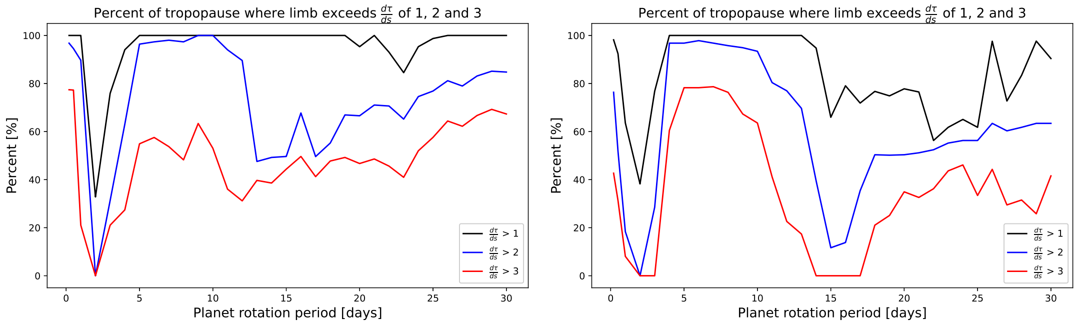

(a) TRAPPIST-1 e **(b)** Wolf 1061 c

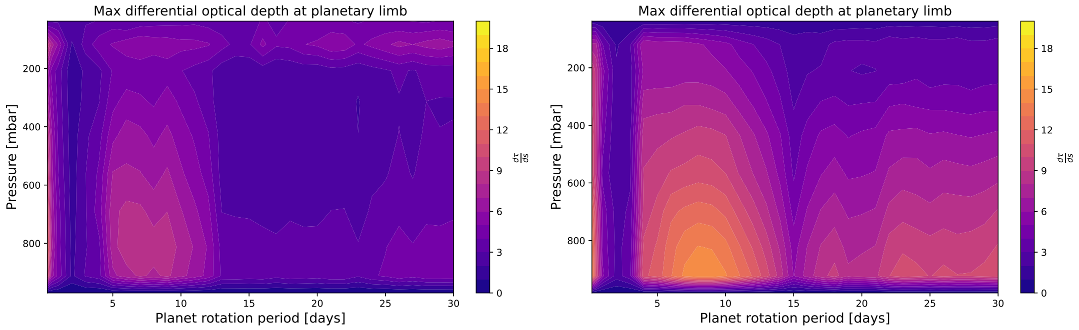

(c) TRAPPIST-1 e **(d)** Wolf 1061 c

Figure 4.14: Top row: Percentage of tropopause (top model level) with a differential optical depth for shortwave band 1 greater than 1, 2, and 3 at the planetary limb for a) TRAP and b) WOLF. Bottom row: Maximum differential optical depth for shortwave band 1 at the planetary limb as a function of atmospheric pressure and rotation rate for c) TRAP and d) WOLF. The differential optical depth is calculated for a fixed path length of 1000 km as in Fig. 4.3, 4.6, 4.9, and 4.12. As the value is sensitive to the choice of path length, these figures express the relative haziness of the atmosphere in different circulation regimes and at different altitudes, rather than a quantitative prediction of optical thickness.

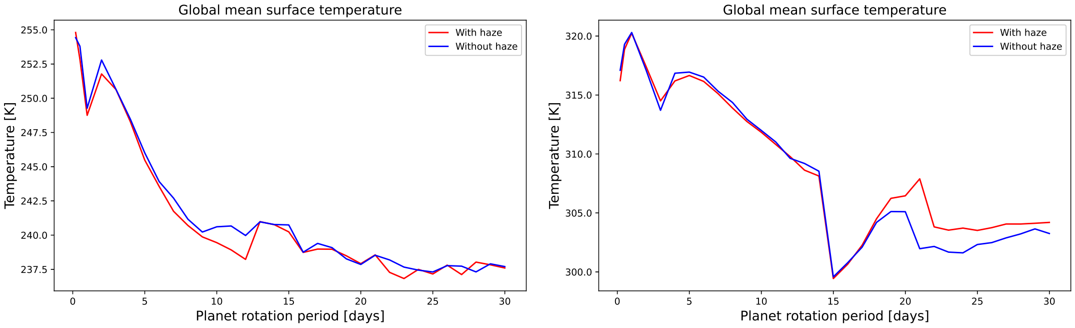

(a) TRAPPIST-1 e **(b)** Wolf 1061 c

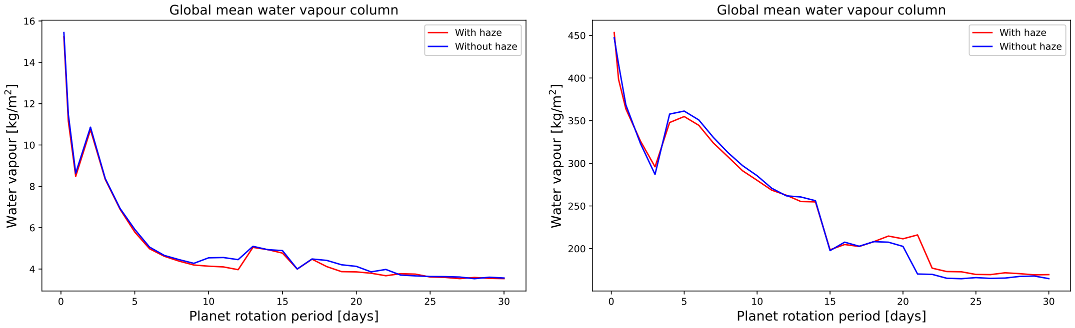

(c) TRAPPIST-1 e **(d)** Wolf 1061 c

Figure 4.15: Effect of radiatively active organic haze particles on the global mean surface temperature for a) TRAP and b) WOLF and water vapour column for c) TRAP and d) WOLF as a function of rotation period.

wind speeds than the control simulation. In general, the differences in wind speed increase with altitude. In the banded regime, the westward equatorial jet slows while the eastward mid-latitude jets accelerate. In the double jet regime, the TRAP case exhibits acceleration of the southern mid-latitude jet and slowing of the northern mid-latitude jet compared to the control, which I interpret as a perturbation in the north-south asymmetry rather than a shift in the circulation regime itself. In the WOLF case, the wind speeds are nearly identical, with very slight acceleration (+1 m/s) of both mid-latitude jets. In the single jet regime, the single equatorial jet slows for both planets. The transitional regime in the TRAP case has slightly faster mid-latitude jets than the control simulation, while the WOLF cases are again nearly identical. The magnitude of the difference is small in all simulations, with 1-3 m/s typical for most of the atmosphere.

4.3.6 Sensitivity to particle size and density

I performed a preliminary parameter space study of particle size and density to test the gravitational settling scheme, as well as the sensitivity of the haze distribution to these inputs. The particle sizes and densities tested are described in Section 4.2. As my results broadly reproduce the findings of Steinrueck et al. (2021) and Parmentier et al. (2013), which contain detailed analyses of the settling behavior, I only summarise them here. The haze distribution falls into either a “small particle” regime, in which the particles are not affected by gravitational settling and the equilibrium mass mixing ratios are insensitive to size and density, or a “large particle” regime in which haze particles begin to settle under gravity and collect in the lower atmosphere. In the large particle regime, total haze mass decreases with particle size and density, as particles settle out of the atmosphere faster. The transition between the regimes occurs at around 100 nm, placing the chosen 500 nm particles well into the large particle regime. I also found that a particle size of 500 nm resulted in the largest extinction efficiencies for the given haze refractive indices and stellar spectra. I therefore expect that my simulated particle size will have the most substantial climate impact out of the large particles in the tested range. Based on these tests, I believe the results presented above are robust to particle size and density for the given initial haze source and these two simulated planets. However, my findings – including that the particles act as passive tracers – do not necessarily generalise to other planets or stars, whose spectra will result in different Mie efficiencies, or to a higher haze source than used in my simulations.

4.4 Discussion

4.4.1 Circulation regimes

The progression of circulation regimes with rotation period parallels the study of moist atmospheric circulation as a function of rotation period conducted by Noda et al. (2017), J. Haqq-Misra et al. (2018), and Edson et al. (2011), and to a lesser extent the dry circulation regimes modelled by Carone et al. (2015), and Merlis and Schneider (2010). There is good agreement between models when it comes to short-period planets: Noda et al. (2017)’s type-IV circulation, J. Haqq-Misra et al. (2018)’s rapid rotators, and tidally locked simulations with a 1-day period in Carone et al. (2015), Edson et al. (2011), and Merlis and Schneider (2010) all resemble my banded regime.

While both the single and double jet states appear in simulations of tidally locked planets, not all studies distinguish between them and, even if both are identified, the transitions between them occur at different rotation periods. Noda et al. (2017) describe their type-II circulation, applicable to their simulations with rotation periods from 6.7-20 days, as characterised by a stationary Rossby wave on a broad equatorial westerly jet. This description corresponds to my single jet regime (13 to 30 day rotation periods). The authors note that as the simulated planet spins faster, the equatorial jet slows as transient mid-latitude disturbances begin to transport eastward momentum from the equator toward the poles, a mechanism indicating a shift to a mid-latitude jet state. In a study of a climate bistability between the double jet and single jet circulation regimes for sophisticated GCM simulations of TRAPPIST-1 e (rotation period of 6.1 days), Sergeev, Lewis, et al. (2022) investigates a phenomenon in which some simulation initial conditions result in a transfer of angular momentum towards the equator (single jet regime) and others towards the poles (double jet regime). Their Figure 7 depicts the single and double jet regimes as nearly identical to those in ExoPlaSim in terms of Rossby gyre location and jet structure. J. Haqq-Misra et al. (2018) categorise planets in both of these states as “Rhines rotators”, a regime characterised by a combination of a thermally direct overturning circulation from dayside to nightside and the presence of zonal jets. Their Figure 9 shows both a single jet structure (the 3300 K case) and a double jet structure (the 3000 K case). However, as their study varies stellar type, stellar constant, and rotation period in tandem to represent physically consistent tidally locked planets, there are several confounding factors compared to my parameter space of rotation period only. Carone et al. (2015) in turn define circulation regimes based on the ratio of the tropical and extratropical Rossby radius of deformation to the planet’s radius, i.e., based on whether tropical or extratropical Rossby waves can “fit” on the planet. Their tropical Rossby wave-dominated regime matches my single jet regime and their extratropical Rossby wave-dominated regime matches my double jet regime (schematically shown in their Figure 2) with respect to the position of the Rossby gyres. However, they find that slower rotators tend towards two mid-latitude jets and faster rotators towards a single fast equatorial jet. Edson et al. (2011) in contrast find mid-latitude jets at rotation periods of 3 and 4 days, as well as a structure that could be a single jet or transitional between double and single jets at 5 days (their Figure 4). As their parameter space only covers periods of 1, 3, 4, 5, and 100 days, it is not possible to make further comparisons.

If the single and double jet states can indeed be viewed as variations of a single regime (the Rhines rotators of J. Haqq-Misra et al. (2018) or type-II circulation of Noda et al. (2017)) distinguished by whether angular momentum is transferred either towards the equator or towards the poles (Sergeev, Lewis, et al., 2022), different studies may have inconsistent results for the same rotation period if other factors, such as choice of temperature forcing or stellar constant, dry vs. moist atmosphere, or the presence clouds, are not kept constant or if implementations of model physics differ. As my work shows, however, distinguishing between these states is crucial to explaining the haze distribution, as the location of the Rossby gyres is central to how hazy the terminators become. Further work on the emergence of the single and double jets in the vein of Sergeev, Lewis, et al. (2022), particularly in more idealised models that enable better investigation of underlying mechanisms, is necessary to clarify the relationship between these states and the various factors that influence them. Conversely, if it becomes possible to diagnose haze distribution through, for example, asymmetry in the haze layer altitude between the leading and trailing limb of a transmission spectrum, this could be evidence for a particular circulation regime.

Finally, with respect to the low-haze transitional regime between the banded and double jet regimes, I can compare my results to Noda et al. (2017) and Carone et al. (2015). Although both studies simulated planets with 2-day rotation periods, neither display the results of this experiment. Noda et al. (2017) identify a type-III circulation regime with periods from 1.25 to 2 days, characterised by a circulation similar to that of type-II (broad eastward jet with stationary Rossby waves) but with significant north-south asymmetry in values such as surface temperature and geopotential height, as well as long-term periodic variability in this asymmetry. Carone et al. (2015) show results from their 3-day period simulation, which is characterised by the presence of both tropical and extra-tropical Rossby waves. As neither these results nor ours form a consistent picture, clearly further theoretical work is needed in understanding planets with rotation periods of approximately 1-3 days. Tidally locked planets with rotation periods this short are unlikely to be temperate, but may still form photochemical hazes.

4.4.2 Distribution and effects of haze

I can compare my results to the passive haze tracer studies of Steinrueck et al. (2021) and Parmentier et al. (2013) and the radiatively active haze tracer studies of Steinrueck et al. (2023) and Mak et al. (2023). Steinrueck et al. (2021) and Parmentier et al. (2013) investigated gravitational settling and vertical mixing of passive haze tracers with varying radii in simulations of hot Jupiters HD 189733 b and HD 209458 b, respectively. As in my Section 4.3.6, in both studies haze particles fall into two regimes based on size: particles with a radius larger than the mean free path of the background gas fall with a terminal velocity independent of the pressure, while particles smaller than the mean free path have terminal velocities inversely proportional to the pressure. If all else is held equal, an N_2 atmosphere should have a larger mean free path than an H_2 atmosphere, shifting the transition from small to large particle regime towards larger particles. However, other factors such as gravity (21.93 m/s^2 in Steinrueck et al. (2021) and 9.81 m/s^2 in Parmentier et al. (2013)) and viscosity (dependent on local temperature, which is much higher in both hot Jupiter studies) also come into play. Steinrueck et al. (2021) place the transition at 10-30 nm, compared to my 100 nm. In the small particle regime, Steinrueck et al. (2021) also report particle trapping in nightside vortices which extend across the morning terminator, while in the large particle regime, the vortices are depleted of hazes.

In recent work, Steinrueck et al. (2023) and Mak et al. (2023) performed radiatively active haze tracer simulations of hot Jupiter HD 189733 b and the Archaean Earth, respectively, both using optical constants for organic hazes analogous to Titan's tholins reported in Khare et al. (1984). Steinrueck et al. (2023) found that Titan-like hazes increase the net heating rate across a broad range of atmospheric pressures, significantly influencing the atmospheric circulation and therefore changing the haze distribution compared to the passive tracer simulations. In contrast, Mak et al. (2023) found that for the Archean Earth only a thin haze layer leads to atmospheric heating, while thicker haze layers (6 out of their 7 simulations) lead to atmospheric cooling. I note that although both the optical constants and the stellar spectra used in these studies differ from my own, Mak et al. (2023)'s simulated atmosphere is similar to ours and indeed also based on the chemical compositions used in G. N. Arney et al. (2017) (nitrogen atmosphere with 0.2 ratio of CH_4 to CO_2).

While Braam et al. (2023) focus on ozone distribution, the mechanism they identify for transport of tracers from a dayside photochemical source to the nightside Rossby gyres is relevant to my results. This study shows that the overturning circulation on a tidally locked planet can advect tracers from the dayside in the upper atmosphere and deposit them in the areas of low geopotential height within the nightside gyres. The analysis primarily discusses the stratosphere because this is where ozone is produced, but the same mechanism could explain why haze particles collect in the nightside gyres in the TRAP simulations which form a high dayside haze layer, but not in the WOLF simulations which are lacking such a high layer.

As this discussion shows, drawing broad conclusions about the distribution and climate impact of photochemical hazes is difficult. This is not only because of the limited amount of literature available, but also because of the sensitivities that literature reveals. Haze particles may collect inside Rossby gyres or remain circulating outside them, depending on whether the gyres are fed by a high altitude haze layer. Haze may either warm or cool the planet's surface and atmosphere, depending on its optical properties and the thickness of the haze layer. Haze particles may affect the general circulation significantly if they absorb light and change the temperature structure of an atmosphere, or they may act as passive tracers. Understanding which of these effects is in play for a particular exoplanet cannot be predicted in advance, but requires observational data to guide modelling efforts.

4.4.3 Implications for observations and future work

In my study, I varied the rotation rate of each of the simulated planets while keeping all other parameters constant. This allows me to attribute changes across the parameter space solely to rotation rate and circulation regime, without having to consider the confounding effects of different haze production rates, stellar spectra, stellar constants, atmospheric compositions, and numerous other, often unconstrained factors. On the other hand, my simulations may not all correspond to real atmospheric states, as I do not co-vary rotation period, stellar constant, stellar type, and haze production rate, which are or could be linked for tidally locked planets. To better relate my simulations to the known exoplanet population, I identify below a number of temperate tidally locked rocky planets whose rotation periods place them within my parameter space.

The double jet TRAP simulation presented in Section 4.3.3 is physically self-consistent, as it takes the rotation period (6 days), stellar spectrum, and stellar constant, as well as planet radius and mass from the real planet TRAPPIST-1 e. TRAPPIST-1 e is one of the most frequently modelled exoplanets and serves as a benchmark for GCM studies of rocky tidally locked worlds. Moist simulations of the planet as part of the Trappist-1 Habitable Atmosphere Intercomparison (THAI) predicted a double jet circulation regime in three out of four cases (Sergeev, Fauchez, et al., 2022). The TRAPPIST-1 system has already been observed multiple times (Greene et al., 2023; Krishnamurthy et al., 2021; Lim et al., 2023; Lincowski et al., 2023; Zieba et al., 2023) and TRAPPIST-1 e is likely to be an observing target in the future. Other rocky, presumably tidally locked planets whose rotation periods place them within the double jet regime in my parameter space include Teegarden's star b (Zechmeister et al., 2019) at 4.9 days and LP 890-9 c (Delrez et al., 2022) at 8.5 days.

The single jet WOLF simulation presented in Section 4.3.4 is likewise physically self-consistent, with the rotation period (18 days), stellar spectrum, stellar constant, planet radius, and planet mass of Wolf 1061 c. As noted in Sections 4.2.4 and 4.4.4, however, these values would likely lead to a runaway greenhouse regime in other GCMs. A direct comparison is not possible as this planet has not been modelled in GCM simulations before, but a frequently studied example of a planet usually simulated with a single superrotating jet is Proxima Centauri b (Boutle et al., 2017; Turbet et al., 2016), with a rotation period of 11.2 days. A transiting planet orbiting an M-class star with a similar stellar constant and rotation period as Wolf 1061 c is Kepler-1649 c (Vanderburg et al., 2020) at 19.5 days and a stellar constant of about 1.23 times that of Earth. A planet with a rotation period that places it in the single jet regime, but a stellar constant closer to that of TRAPPIST-1 e is GJ 1061 d (Anglada-Escudé et al., 2013) at 13 days and a stellar constant about 0.69 times that of Earth.

As discussed in Section 4.4.1, however, models do not always predict the same circulation regime for a given rotation period. The ability to constrain a planet's circulation regime from observations would be a significant step forward in our understanding of exoplanet atmospheric dynamics. My simulation results show distinct terminator asymmetry and limb silhouettes associated with each circulation regime. I propose that, for planets with optically thick haze, it may be possible to detect evidence of a circulation regime through separate atmospheric retrievals of the leading and trailing limb (Song & Yang, 2021) or through retrieval of the planet's transmission string (Grant & Wakeford, 2023). I plan to test this approach in future work by producing simulated observations for my identified circulation regimes. However, simulating transmission spectra requires a larger atmospheric pressure range than included in my parameter space study, and the stratospheric circulation is also relevant to the haze distribution. It is possible that the low-haze troposphere of regime 2 (the transitional regime) is a result of particle trapping at the tropopause or in the stratosphere, which would in fact lead to a higher haze layer and poorer observational prospects. It may also be the case that the Rossby gyres extend into the stratosphere, again trapping haze particles at lower pressures. I will therefore extend the top of my model into the stratosphere for the purpose of simulating observations, as well as studying the potential stratospheric circulation.

4.4.4 Limitations

Previous work reporting north-south asymmetry in GCM simulations of tidally locked planets has shown that the asymmetry may reverse periodically, i.e. the northern hemisphere may be warmer than the southern for some period of time, followed by a period in which the southern is warmer than the northern (Noda et al., 2017). As I use the average of one year for my analysis, my results do not reflect any such switching, and a long-term average (several times the period of the oscillation) could result in no differences between the northern and southern hemispheres. Since, however, transmission spectroscopy cannot distinguish latitudinal variations and any north-south asymmetry would therefore not affect observations, I chose a shorter averaging period to keep the simulation runtimes and output sizes at manageable levels.

As stated in Section 4.2.4, the model inputs for the WOLF simulations would likely lead to a runaway greenhouse regime in other, more sophisticated GCMs. J. Haqq-Misra et al. (2022) found that ExoPlaSim underpredicts the surface temperature and stratospheric water vapour content compared to ExoCAM (their Table 3), an effect that is more pronounced in hotter simulations. Paradise et al. (2022) states as a possible explanation that ExoPlaSim treats water vapour as a trace gas, such that increases in water vapour pressure do not lead to increases in surface pressure and resulting effects on dynamics and climate. In addition, the absorptivity of water vapour in shortwave band 2 ($\lambda > 0.75 \mu$m) relies on a parameterisation that is tuned to the solar spectrum and is likely less accurate for M-class stellar spectra. Paradise et al. (2022) contains further details about these model limitations and potential future development work to remedy them. Some modelling work has indicated that tidally locked planets may be able to maintain surface habitable temperatures even with atmospheric water vapour content that would normally indicate a greenhouse regime (R. k. Kopparapu et al., 2017), as a result of a feedback whereby increasing dayside temperatures lead to increasing dayside cloud albedo (J. Yang et al., 2013); however, ExoPlaSim has not been validated for these regimes (Paradise et al., 2022). The WOLF simulations are therefore better seen as theoretical atmospheric states for warm temperate planets, rather than specific predictions for the stellar constant of Wolf 1061 c.

The haze scheme is highly idealised and does not account for sinks (chemical sinks, wet deposition) aside from gravitational settling onto the surface, a particle size distribution (which may vary with time due to particle growth and loss), or radiative effects dependent on wavelength. The haze source is taken from 1-D modelling in G. N. Arney et al. (2017) and prescribed within the model, not generated internally by self-consistent chemistry or haze microphysics. Accordingly, my results should be seen as first order estimates of the interaction between the atmospheric circulation and radiatively active haze particles. The strength of ExoPlaSim and the haze scheme is their computational efficiency and ability to map large parameter spaces and isolate relationships between a small number of factors. The free parameters in the haze scheme, including optical constants, particle size and density, and haze source strength and location, as well as the many model parameters relevant to the circulation and haze distribution (including stellar constant, stellar type, planet gravity, and others) leave a large parameter space still to be explored. I examine only one type of organic haze, which may vary in its optical properties from other laboratory haze analogues, as indeed real organic hazes may vary from planet to planet depending on factors such as trace gas abundances, stellar spectrum, and atmospheric temperature. Future work could, for example, study the effect of the organic haze data published in Corrales et al. (2023) by way of comparison with my study.

I intend to follow up the present work with a smaller, more computationally intensive study of a select number of cases from my parameter space at a higher vertical and horizontal resolution and with a higher model top to investigate the transport of haze to and within the stratosphere and generate simulated transmission spectra. The source code of ExoPlaSim, including the haze scheme, is open source and freely available for further work by other researchers.

4.5 Conclusion

I developed a haze module to simulate haze transport and radiative effects in a fast, open source intermediate complexity general circulation model, ExoPlaSim. I used the model to study the 3-D haze distribution for a tidally locked Earth-like (TRAPPIST-1 e-based) and super-Earth-like (Wolf 1061 c-based) planet with rotation periods ranging from 0.25 to 30 days in idealised simulations. The aim of my study was to identify characteristic haze distribution regimes which could potentially be distinguished by observations of the planetary limb. My simulations fall into three primary circulation regimes, which have also been identified in previous literature: a banded regime (rapid rotators), a double jet regime (intermediate rotation periods), and a single jet regime (slow rotators). The banded regime tends to have haze particles well-mixed throughout the atmosphere, while in the other two regimes, haze collects either inside or around the Rossby gyres associated with the stationary Rossby waves typical of the atmospheric circulation of tidally locked planets. As the Rossby gyres are associated with large amounts of haze, their location–on the planetary limb or on the nightside–has a controlling effect on the haze differential optical depth at the terminator. My simulations in the double jet and single jet regimes also show east-west terminator asymmetry, which could be observable. Overall, the simulations in my study with the lowest differential optical depths at the top of the atmosphere were the slowly rotating super-Earths, in which haze particles settled deeper into the atmosphere around the nightside Rossby gyres. My chosen haze optical constants resulted in a haze layer which had little effect on the surface temperature of the planet or feedback on the general circulation. The organic hazes in my simulations therefore act largely as passive tracers; however, this finding cannot be generalised to other hazes or laboratory haze analogues, which much be examined individually.

ExoPlaSim's computational efficiency allows me to explore a larger parameter space than is feasible with more complex GCMs. I intend to follow this work with a smaller set of higher resolution and higher model top simulations selected from the parameter space described in my results in Section 4.3. This will allow me to explore the impact on the haze distribution of including the stratospheric circulation and to generate simulated transmission spectra and transmission strings.

Chapter 5

Discussion

5.1 Summary of results

In the preceding chapters, I have explored how several physical processes in tidally locked exoplanet atmospheres that can only be simulated in 3-D models may affect observations of the planetary terminator in transmission spectroscopy. These physical processes fall under two broad headings: atmospheric waves and their global effects, and the horizontal transport of light-extinguishing aerosols.

In Chapter 2, I described a stratospheric wind and water vapour oscillation analogous to the quasi-biennial oscillation on Earth. The oscillation is caused by the deposition of gravity wave pseudomomentum in stratospheric regions where the phase speed of the gravity wave is similar in magnitude to the speed of the background flow. This process causes the stratosphere to form a vertically stacked series of jets flowing in alternating directions in a pattern which propagates downwards over time. Unlike Earth's QBO, this oscillation exhibits major longitudinal asymmetries in the magnitude of the associated wind speeds, with a maximum at the western terminator and a minimum at the substellar point, as well as a much shorter period. As the QBO is associated with a corresponding periodic variation in the abundances of atmospheric species (water vapour, ozone, etc.), I also simulated the transit depth of water vapour absorption lines over time. If the amplitude of the transit depth variation were large enough, it could be possible to diagnose the existence of such an oscillation on an exoplanet or, given enough historical data, predict when water vapour abundances are higher and observe the planet during this phase of the oscillation. I found that the effects on transit spectra are too small to be observable for an Earth-like planet; however, similar oscillations could exist on gas giants and cause measurable variations in spectral signatures.

In Chapter 3, I explored a relationship between cloud radiative feedback at the substellar point, the Matsuno-Gill response to periodic thermal forcing, and cloud abundance at the terminator. I found that changes in the amount of cloud in the substellar region affect the substellar forcing, increasing or decreasing the background zonal wind and therefore shifting the zonal wavenumber-1 standing Rossby wave in such a way that the eastern Rossby gyres traverse a path of over 100 degrees of longitude. In their westernmost position, the gyres advect cloud from the substellar point to the terminators, while in their easternmost position, the gyres do not overlap with the substellar region of cloud and cannot advect cloud towards the limb. Simulated transmission spectra show a periodic rise and fall in the transit depths of water vapour and carbon dioxide with the same period as the dynamical oscillation. Even during the transit depth maxima, however, these absorption lines are not deep enough to be detectable. This is true even of simulations of a planet at the inner edge of the habitable zone, with a theoretically improved planet-to-star ratio, because the cloud deck forms higher up in this warmer atmosphere. Given the relationships between rotation rate, stellar forcing, amount of cloud, and Rossby gyre location for tidally locked water-rich planets, it is unclear whether any particular configuration of orbital distance and stellar type has a higher likelihood of having cloudless periods at the planetary limb.

In Chapter 4, I studied the effect of planetary rotation rate (and therefore circulation regime) on the 3-D spatial distribution of organic haze particles and especially on the haze abundance at the planetary limb. In broad agreement with the existing literature, my simulations fell into three distinct regimes: a banded regime (fast rotators), a double jet regime (intermediate rotators), and a single jet regime (slow rotators). Each regime is associated with a characteristic haze distribution at the terminator because the circulation transports haze away from the prescribed source in the model in a different way. Repeating the rotation rate parameter space for both an Earth-size and a super-Earth-sized planet showed that other factors, especially stellar forcing, but also the gravity and size of the planet, can also affect the haze distribution and merit further study. It is possible that detected signatures of hazes in exoplanet transmission spectra could be used to draw inferences about the underlying deep circulation, especially based on asymmetries in haze layer altitude between the morning and evening terminators. In my parameter space, the slowly-rotating super-Earth simulations were the most promising candidates for observation, as haze particles collected around the nightside vortices relatively low in the atmosphere without forming a high haze layer.

5.2 Implications of results

Taking a broad view, my research suggests several conclusions: that Earth-like planets remain poor observational prospects, that existing scientific software tools are misaligned with the objectives of exoplanet science, but also that temporal and spatial variability in exoplanet transmission spectra may in the future become powerful tools for drawing conclusions about a planet's atmosphere and climate.

The simulated transmission spectra included in Chapters 2 and 3 show not only that these dynamical oscillations in the model are not observable for Earth-like planets, but also that water vapour is not detectable even at the most favourable phase of the oscillation. The water vapour transit depths at the LASO peak and at the cloud oscillation trough remain smaller than JWST's ability to detect, largely because the planet-star ratio and heavy mean molecular weight of the atmosphere are more important factors than the vapour abundance. This means it may not be possible to confirm the presence of water on potentially habitable rocky worlds, even during periods when the terminators are relatively cloudless. The findings are in line with prior research on the detectability of water vapour on potentially habitable worlds (Komacek et al., 2020; Suissa et al., 2020) and close loopholes related to variability.

While the Unified Model makes it possible to study phenomena such as atmospheric variability with a high degree of sophistication compared to other exoplanet GCMs, the results remain unobservable. This calls into question the use of sophisticated, computationally expensive models to study terrestrial exoplanets for purposes of interpreting observations. On the other hand, the results of Chapters 3 and 4 highlight the importance of 3-D effects in modelling because of, among other things, transport of clouds and hazes. This conflict reveals a gap in the scientific software ecosystem: fast, low-resolution, simplified 3-D atmosphere models with a modular design and a high model top. Given the vast parameter space represented by the exoplanet population, faster and more flexible models that can map this parameter space at reasonable computational cost are at least as necessary as sophisticated but slow coupled chemistry-climate models. As a modular, intermediate complexity GCM, ExoPlaSim represents a step in this direction, though it is hampered by difficulties simulating deep atmospheres with higher model tops. The development of 3-D models that prioritise quantity over quality would be a valuable innovation for exoplanet science, even if performed under the aegis of informatics or computational fluid dynamics, without offering immediate scientific findings about exoplanets. Such exoplanet-specific GCMs could dispense with some model features more useful to Earth science–such as higher resolution near the surface–in favour of designs oriented towards the specific challenges of modelling exoplanets. A next step, already being explored by the exoplanet community, is to incorporate these findings into atmospheric retrievals through parameterisations or into machine learning approaches through 3-D forward models.

If sufficient advances in modelling are made, the spatial and temporal variability described in this thesis promise novel insights into planetary climates. Chapters 3 and 4 describe differences in cloud and haze abundances between the eastern and western terminator as a direct result of the general circulation. Observing such limb asymmetries in aerosol and gaseous species abundances and incorporating them into retrievals could help constrain the circulation regime, in particular the presence and location of Rossby gyres. Tracer simulations consistently indicate that the gyres are a unique, chemically enriched region of the atmosphere (Braam et al., 2023; Parmentier et al., 2013; Steinrueck et al., 2021; Yates et al., 2020). If the gyres extend across the limb as in the double jet regime, transit spectroscopy will probe this region during egress (but not during ingress). Limb asymmetries could then be due to the gyres rather than temperature differences (as proposed in Ehrenreich et al. (2020)) or redistribution from the substellar point by jets. If, as explored in Chapter 3, the gyres also regularly shift and cross between the dayside and nightside, they will periodically be exposed to the host star's light, triggering photochemical reactions and perturbing their internal chemical environment. This could have implications for detections of chemical disequilibrium, which could have origins in dynamical causes rather than, say, biological processes.

An understanding of atmospheric variability is ultimately indispensable to interpreting observations. Solar system planets exhibit many kinds of variability: the quasi-quadrennial and quasi-periodic oscillations on Jupiter and Saturn, respectively (analogues to Earth's QBO and semi-annual oscillation); the seasonal methane cycle of Mars; the sporadic Venusian ozone layer; and variations in thermal structure and chemical composition on Titan. As individual exoplanets are observed on multiple occasions and the archive of exoplanet data grows, a theoretical understanding of potential forms of atmospheric variability will become necessary to distinguish genuine physical phenomena from sources of noise and error.

5.3 Future work

This thesis suggests several avenues for future work. One simple approach would be to expand these studies to larger, more observable planets. Stratospheric oscillations are physically possible and could be more easily detected on gas planets. It is as yet unexplored whether stationary Rossby waves on tidally locked sub-Neptunes and hot Jupiters shift locations and what impact this could have on the regional atmospheric composition and on observations. Likewise, repeating the parameter space study in Chapter 4 with a low mean molecular weight atmosphere (hydrogen/helium) could yield different results, as the atmospheric composition will affect viscosity and settling velocities.

One significant area where theoretical understanding remains lacking is the formation and role of the stationary Rossby waves and Rossby gyres on tidally locked planets. How consistent is the location of the gyres in simulations by different models? Do other models besides the Unified Model predict regular shifts in the gyre location? If so, what is the period of this oscillation? What is the chemical environment in the gyres predicted by coupled chemistry-climate models? How does this environment change in response to periodic exposure to radiation when the gyres are on the dayside? One important question is how far the gyres extend into the upper atmosphere and whether they continue to show enhanced tracer profiles at higher altitudes. A fruitful approach might be to simulate the environment in the gyres, rather than at the substellar or antistellar point, using existing 1-D chemistry or aerosol codes. A next step could be to simulate periodic irradiation of the equilibrium chemical environment in the gyres.

The additions to ExoPlaSim also open up potential for exploration of a much larger parameter space of aerosols. Recent and upcoming laboratory studies of exoplanet aerosols are making complex refractive indices of photochemical hazes available to modellers (He et al., 2018a, 2023). ExoPlaSim allows for rapid investigation of the impact of different hazes on a planet's general circulation and climate, as well as of the sensitivity of the haze distribution to source location, source strength, particle size, particle density, and the other existing parameters characterising the model. A few potential approaches could be: to compare the impact of various laboratory-created haze analogues, soot-like hazes, and Titan's tholins on the general circulation; to vary the source mass mixing ratio for a given haze to determine when the haze abundance becomes radiatively and observationally relevant; or to systematically vary the stellar forcing and spectrum to identify associated haze distribution regimes.

To follow up on Chapter 4, I have run simulations of the eight cases described with a model top fixed at 1 μbar and the haze source maintained in the same location just above the tropopause. This will allow me to compare the haze distribution in the upper atmosphere across the parameter space, to generate simulated transmission spectra and potentially transmission strings, and to perform atmospheric retrievals using the simulation data. The aim of this follow-up work is to determine whether the circulation regimes can be distinguished by, for example, differences in transit depths, and to test whether separate retrievals of the eastern and western terminators can leverage terminator asymmetry to draw conclusions about the circulation and spatial variability in atmospheric composition.

The goal of such future work would be to test whether the theoretical predictions in this thesis are observable. An observation of a periodic reversal of wind direction or warming and cooling of the atmosphere on a gas giant could confirm the existence of a LASO. Terminator asymmetry on a hazy exoplanet or a transmission string matching one of the optical depth profiles shown in Chapter 4 could indicate a planet with a double jet circulation regime. These findings would enrich our understanding of other planets, expanding them from unresolved points with a few known chemical species in the atmosphere to dynamic worlds with winds, weather, and climate. Atmospheric dynamics in turn play a role in contextualising detections of chemical disequilibrium and determining whether such disequilibrium is a potential biosignature. As the James Webb Space Telescope and many upcoming missions begin to characterise exoplanet atmospheres in greater and greater detail, 4-D simulations will become ever more important in bringing together different observations into a coherent picture of a planet – and it is these global views which will ultimately help us understand how the Earth fits into the exoplanet population and whether the world we inhabit is truly unique.

Appendix A

Haze transport and radiative transfer parameterisations

A.1 Gravitational settling scheme

ExoPlaSim includes a gridspace tracer transport module with a flux-form semi-Lagrangian transport scheme based on S.-J. Lin and Rood (1996) and S.-J. Lin, Chao, Sud, and Walker (1994) that can be used to calculate the passive transport of gas-phase tracers. Vertical transport is calculated by a piecewise parabolic method as described in Colella and Woodward (1984). To represent solid-phase particle transport, I repurposed the advection fluxes in the zonal, meridional, and vertical directions from the existing flux-form scheme and added an additional vertical flux from gravitational settling based on Steinrueck et al. (2021) and Parmentier et al. (2013).

According to this parameterisation, the haze mass mixing ratio is described by the equation:

$$\frac{D\chi}{Dt} = -g\frac{\partial(\rho_g \chi V_s)}{\partial p} + P + L, \tag{A.1}$$

where $\frac{D}{Dt}$ is the total derivative, χ is the mass mixing ratio (kg/kg), g is the gravitational constant (m/s^2), ρ_g is the surrounding gas density (kg/m^3), V_s is the terminal velocity of the falling particles (m/s), p is the pressure (Pa), P is the production term (kg/kg), and L is the loss term (kg/kg). The first term on the right-hand side represents gravitational settling of a solid-phase particle under gravity. The terminal velocity is given by:

$$V_s = \frac{2\beta a^2 g(\rho_p - \rho_g)}{2\eta}, \tag{A.2}$$

where a is the particle radius (m), g is the gravitational constant (m/s^2), ρ_p is the particle density (kg/m^3), ρ_g is the surrounding gas density (kg/m^3), β is the Cunningham correction factor (dimensionless), and η is the viscosity (Pa · s). The Cunningham factor is a correction to the Stokes' drag force to account for the case in which the mean free path of the gas is similar to the particle size. Stokes' law assumes a no-slip condition, but this assumption is not valid for small particles, which experience the surrounding gas as a non-continuous medium. In this case, drag is generated by particles interacting with the surrounding individual gas molecules rather than by the viscosity of the gas. The Cunningham factor accounts for this effect and is defined by:

$$\beta = 1 + Kn(1.256 + 0.4e^{-1.1/Kn}), \tag{A.3}$$

where *Kn* is the Knudsen number, the ratio of the mean free path λ of the gas to the particle size *a*. The mean free path is calculated as:

$$\lambda = \frac{k_b T}{\sqrt{2}\pi d^2 P}, \tag{A.4}$$

where k_B is the Boltzmann constant, *T* is the air temperature (K), *d* is the molecular diameter of the surrounding gas (m), and *P* is the air pressure (Pa). The viscosity is calculated using a parameterisation described by Rosner (1986):

$$\eta = \frac{5}{16} \frac{\sqrt{\pi m k_b T}}{\pi d^2} \frac{(k_b T/\varepsilon)^{0.16}}{1.22}, \tag{A.5}$$

where *m* is the molecular mass (kg) and ε is the depth of the Lennard-Jones potential well. I use the following values for N_2 gas: m = 4.652×10^{-26} kg, d = 3.64×10^{-10} m, and $\varepsilon = 95.5 k_b$ T. The parameterisation represents particles with a single, uniform radius.

A.2 Haze radiative transfer scheme

ExoPlaSim's shortwave radiation module is based on the work of Lacis and Hansen (1974) for the clear sky fraction, with cloud parameterizations from Stephens (1984) and Stephens (1978) for the cloud cover fraction. The model uses a two-stream method to represent multi-scattering by clouds in two shortwave bands and a diffusivity factor of 0.5 for diffuse light. Cloud is treated as scattering but not absorbing in shortwave band 1 (blue), and as both scattering and absorbing in shortwave band 2 (red). I added a haze radiative transfer scheme based on the cloud scheme, with adaptations to include empirically measured optical data for hazes rather than internally calculated values from parameterisations as for the clouds. Haze radiative effects are included only for the clear sky fraction; in cloudy areas, cloud scattering and/or absorption is assumed to dominate the radiative transfer.

A.2.1 Cloud scheme

The cloud treatment for shortwave band 1 is given in the Planet Simulator Reference Manual. I do not reproduce it here, as my additions to code are based only on the cloud scheme for shortwave band 2. The cloud treatment in shortwave band 2, representing both scattering and absorption, is as follows:

$$Tr_{C2} = \frac{4u}{R}, \tag{A.6}$$

where *Tr* is the transmissivity through a layer of cloud and,

$$u^2 = \frac{(1 - \omega_0 + 2\beta_2\omega_0)}{(1 - \omega_0)}, \tag{A.7}$$

where ω_0 is the single scattering albedo (the ratio of the scattering efficiency to the total extinction efficiency and β_2 is the backscatter ratio (the backscattered fraction of monodirectional incident radiation at a given zenith angle, calculated from a parameterisation based on fields within the model) for shortwave band 2, and

$$R = (u+1)^2 exp(\tau_{eff}) - (u-1)^2 exp(-\tau_{eff}), \tag{A.8}$$

where τ_{eff} is the effective optical depth. The value of τ_{eff} is calculated using a parameterisation based on the cloud liquid water path, the single scattering albedo, the backscatter ratio, and the cosine of the solar zenith angle taken from Stephens (1978). The PlaSim Reference Manual provides more detailed information about this parameterisation.

In addition, the reflectivity from a layer of cloud is given by:

$$Re_{C2} = \frac{[exp(\tau_{eff}) - exp(-\tau_{eff})](u^2 - 1)}{R}, \tag{A.9}$$

where *u*, *R*, and τ_{eff} are as given above. The transmissivity *Tr* and the reflectivity *Re* are unitless and are expressed as fractions with a value between 0 and 1. Detailed derivations of all the above equations are given in the PlaSim Reference Manual and in Stephens (1978).

A.2.2 Haze scheme

The haze treatment in both shortwave bands 1 and 2 uses the same equations for *Tr*, *Re*, *u* and *R* as the cloud scheme above. The haze optical depth of a haze layer is given as:

$$\tau_N = NQ_{ext}\pi r^2 \delta z, \tag{A.10}$$

where *N* is the number density in particles per m^3, Q_{ext} is the extinction efficiency, *r* is the particle radius in meters, and δz is the layer thickness in meters. The effective optical depth τ_{eff} is then given by:

$$\tau_{eff} = \frac{[(1-\omega_0)(1-\omega_0+2\beta\omega_0)]^{1/2}\tau_N}{\mu_0}, \tag{A.11}$$

in the formulation given by Stephens (1978) for an absorbing and scattering medium, where ω_0 is the single scattering albedo (the ratio of the scattering efficiency to the extinction efficiency), β is the backscatter ratio (calculated for the haze as Q_{back}/Q_{scat}, the ratio of the backscattering efficiency to the scattering efficiency), and μ_0 is the cosine of the solar zenith angle. Instead of being determined by parameterisations within the model, the values of Q_{ext}, Q_{back}, and Q_{scat} are read in from an external data file after being pre-calculated from the haze complex refractive index and are then used to calculate ω_0 and β.

A.3 Mie efficiency calculations

I use the Python package MiePython (Prahl, 2023) to calculate the Mie extinction, scattering, and backscattering efficiencies. MiePython uses algorithms based on Wiscombe (1980) to calculate these efficiencies. The online documentation for the MiePython package contains detailed descriptions of the formulas used and examples of calculations, as well as validations against test cases reported in Wiscombe (1980) and Bohren and Huffman (1998). I reproduce below the formulas used by the MiePython packages to calculate the extinction, scattering, and backscattering efficiencies:

Extinction efficiency:

$$Q_{ext} = \frac{2}{x^2}\Sigma_{n=1}^{\infty}(2n+1)(|a_n|^2+|b_n|^2) \tag{A.12}$$

Scattering efficiency:

$$Q_{scat} = \frac{2}{x^2}\Sigma_{n=1}^{\infty}(2n+1)\cdot Re\{a_n+b_n\} \tag{A.13}$$

where in both cases *x* is the size parameter of the particle, $\frac{2\pi a}{\lambda_{vac}}$, with *a* the particle radius and λ_{vac} the wavelength of incoming light in a vacuum, and

$$a_n = \frac{[D_n(mx)/m+n/x]\psi_n(x)-\psi_{n-1}(x)}{[D_n(mx)/m+n/x]\xi_n(x)-\xi_{n-1}(x)} \tag{A.14}$$

$$b_n = \frac{[mD_n(mx)+n/x]\psi_n(x)-\psi_{n-1}(x)}{[mD_n(mx)+n/x]\xi_n(x)-\xi_{n-1}(x)} \tag{A.15}$$

where *x* is again the size parameter, *m* is the complex refractive index of the particle, and ψ and ξ are equivalent to:

$$\psi_n(x) = xj_n(x) \tag{A.16}$$

$$\xi_n(x) = xj_n(x) + ixy_n(x) \tag{A.17}$$

Here $j_n(x)$ and $y_n(x)$ are spherical Bessel functions. The factor D_n in Equations A.14 and A.15 is the logarithmic derivative computed using the continued fraction method developed by Lentz (1990). As the description of this method is lengthy and is fully documented in Prahl (2023) and Lentz (1990), I refer the reader to these publications for a full derivation.

Finally, I calculate the backscattering efficiency using MiePython as:

$$Q_{back} = \frac{1}{x^2}|\Sigma_{n=1}^{\infty}(2n+1)(-1)^2(a_n-b_n)|^2 \tag{A.18}$$

where a_n and b_n are defined as in Equations A.14 and A.15 above.

The calculation of the backscattering efficiency by MiePython is based on a definition of the backscattering cross-section used in optics, which differs by a factor of 4π from the definition used in meteorology. I quote from the American Meteorological Society's Glossary of Meteorology:

“ Backscattering cross-section:

For plane-wave radiation incident on a scattering object or a scattering medium, the ratio of the intensity scattered in the direction toward the source to the incident irradiance.

So defined, the backscattering cross section has units of area per unit solid angle, for example, square meters per steradian.

In common usage, synonymous with radar cross section, although this can be confusing because the radar cross section is 4π times the backscattering cross section as defined in 1) and has units of area, for example, square meters.”

(American Meteorological Society, 2023: Backscattering cross section,

https://glossary.ametsoc.org/wiki/Backscattering_cross_section)

By this definition, MiePython computes the radar cross-section, which can in some cases be larger than the scattering cross-section. However, the radiative transfer scheme described in Appendix Section **??** requires as input the backscatter ratio, the proportion of incident light scattered back towards the source. This ratio must be less than or equal to one and the backscattering cross-section must be less than or equal to the total scattering cross-section. To arrive at the meteorological definition of the backscattering cross-section, therefore, the value computed by MiePython must be divided by a factor of 4π. As the backscattering efficiency differs from the backscattering cross-section only by a factor of the geometric cross-section (constant for a given particle radius, as in my simulations), I take the backscattering efficiency calculated by MiePython and divide it by a factor of 4π to obtain the values of the backscattering efficiencies given in Table 4.1.

The Mie efficiencies input into the ExoPlaSim model need not be calculated using MiePython, but can be obtained by other methods chosen by the user. However, care should be taken that the backscattering efficiency used is equivalent to the American Meteorological Society definition and that its value does not exceed that of the scattering efficiency.

Bibliography

Abbot, D. S., Bloch-Johnson, J., Checlair, J., Farahat, N. X., Graham, R. J., Plotkin, D., … Spaulding-Astudillo, F. (2018, February). Decrease in Hysteresis of Planetary Climate for Planets with Long Solar Days. *The Astrophysical Journal*, *854*(1), 3. Retrieved 2021-11-17, from `https://doi.org/10.3847/1538-4357/aaa70f` (Publisher: American Astronomical Society) doi: 10.3847/1538-4357/aaa70f

Ahrer, E.-M., Alderson, L., Batalha, N. M., Batalha, N. E., Bean, J. L., Beatty, T. G., … JWST Transiting Exoplanet Community Early Release Science Team (2023, February). Identification of carbon dioxide in an exoplanet atmosphere. *Nature*, *614*(7949), 649–652. Retrieved 2023-03-21, from `https://www.nature.com/articles/s41586-022-05269-w` (Number: 7949 Publisher: Nature Publishing Group) doi: 10.1038/s41586-022-05269-w

Alexander, M. J., & Holton, J. R. (1997, February). A Model Study of Zonal Forcing in the Equatorial Stratosphere by Convectively Induced Gravity Waves. *Journal of the Atmospheric Sciences*, *54*(3), 408–419. Retrieved 2022-01-29, from `https://journals.ametsoc.org/view/journals/atsc/54/3/1520-0469_1997_054_0408_amsozf_2.0.co_2.xml` (Publisher: American Meteorological Society Section: Journal of the Atmospheric Sciences) doi: 10.1175/1520-0469(1997)054<0408:AMSOZF>2.0.CO;2

Anglada-Escudé, G., Amado, P. J., Barnes, J., Berdiñas, Z. M., Butler, R. P., Coleman, G. A. L., … Zechmeister, M. (2016, August). A terrestrial planet candidate in a temperate orbit around Proxima Centauri. *Nature*, *536*(7617), 437–440. Retrieved 2020-11-17, from `http://www.nature.com/articles/nature19106` doi: 10.1038/nature19106

Anglada-Escudé, G., Tuomi, M., Gerlach, E., Barnes, R., Heller, R., Jenkins, J. S., … Jones, H. R. A. (2013, August). A dynamically-packed planetary system around GJ 667C with three super-Earths in its habitable zone. *Astronomy & Astrophysics*, *556*, A126. Retrieved 2023-10-02, from `https://www.aanda.org/articles/aa/abs/2013/08/aa21331-13/aa21331-13.html` (Publisher: EDP Sciences) doi: 10.1051/0004-6361/201321331

Armstrong, D. J., de Mooij, E., Barstow, J., Osborn, H. P., Blake, J., & Saniee, N. F. (2016, December). Variability in the atmosphere of the hot giant planet HAT-P-7 b. *Nature Astronomy*, *1*(1), 0004. (Place: London Publisher: Nature Publishing Group WOS:000406527100005) doi: 10.1038/s41550-016-0004

Arney, G., Domagal-Goldman, S. D., & Meadows, V. S. (2018, March). Organic Haze as a Biosignature in Anoxic Earth-like Atmospheres. *Astrobiology*, *18*(3), 311–329. Retrieved 2020-10-30, from `http://www.liebertpub.com/doi/10.1089/ast.2017.1666` doi: 10.1089/ast.2017.1666

Arney, G., Domagal-Goldman, S. D., Meadows, V. S., Wolf, E. T., Schwieterman, E., Charnay, B., … Trainer, M. G. (2016, November). The Pale Orange Dot: The Spectrum and Habitability of Hazy Archean Earth. *Astrobiology*, *16*(11), 873–899. Retrieved 2020-10-16, from `http://www.liebertpub.com/doi/10.1089/ast.2015.1422` doi: 10.1089/ast.2015.1422

Arney, G. N., Meadows, V. S., Domagal-Goldman, S. D., Deming, D., Robinson, T. D., Tovar, G., … Schwieterman, E. (2017, February). Pale Orange Dots: The Impact of Organic Haze on the Habitability and Detectability of Earthlike Exoplanets. *The Astrophysical Journal*, *836*(1), 49. Retrieved 2023-03-17, from `https://dx.doi.org/10.3847/1538-4357/836/1/49` (Publisher: The American Astronomical Society) doi: 10.3847/1538-4357/836/1/49

Asnodkar, A. P., Wang, J., Eastman, J. D., Cauley, P. W., Gaudi, B. S., Ilyin, I., & Strassmeier, K. (2022, March). Variable and Supersonic Winds in the Atmosphere of an Ultrahot Giant Planet. *The Astronomical Journal*, *163*(4), 155. Retrieved 2022-11-17, from `https://dx.doi.org/10.3847/1538-3881/ac51d2` (Publisher: The American Astronomical Society) doi: 10.3847/1538-3881/ac51d2

Baldwin, M. P., Gray, L. J., Dunkerton, T. J., Hamilton, K., Haynes, P. H., Randel, W. J., … Takahashi, M. (2001). The quasi-biennial oscillation. *REVIEWS OF GEOPHYSICS*, 52. doi: https://doi.org/10.1029/1999RG000073

Barclay, T., Pepper, J., & Quintana, E. V. (2018, October). A Revised Exoplanet Yield from the Transiting Exoplanet Survey Satellite (TESS). *The Astrophysical Journal Supplement Series*, *239*(1), 2. Retrieved 2021-05-05, from `https://doi.org/10.3847/1538-4365/aae3e9` (Publisher: American Astronomical Society) doi: 10.3847/1538-4365/aae3e9

Barnes, R. (2017, December). Tidal locking of habitable exoplanets. *Celestial Mechanics and Dynamical Astronomy*, *129*(4), 509–536. Retrieved 2020-11-09, from `https://doi.org/10.1007/s10569-017-9783-7` doi: 10.1007/s10569-017-9783-7

Barstow, J. K. (2021, February). The curse of clouds. *Astronomy & Geophysics*, *62*(1), 1.36–1.42. Retrieved 2022-11-17, from `https://doi.org/10.1093/astrogeo/atab044` doi: 10.1093/astrogeo/atab044

Bean, J. L., Désert, J.-M., Kabath, P., Stalder, B., Seager, S., Kempton, E. M.-R., ... Seifahrt, A. (2011, November). The optical and near-infrared transmission spectrum of the super-Earth GJ 1214b: Further evidence of a metal-rich atmosphere. *The Astrophysical Journal*, *743*(1), 92. Retrieved 2023-05-23, from `https://dx.doi.org/10.1088/0004-637X/743/1/92` (Publisher: The American Astronomical Society) doi: 10.1088/0004-637X/743/1/92

Beichman, C., Benneke, B., Knutson, H., Smith, R., Lagage, P.-O., Dressing, C., ... Sing, D. (2014, December). Observations of Transiting Exoplanets with the James Webb Space Telescope (JWST). *Publications of the Astronomical Society of the Pacific*, *126*(946), 1134. Retrieved 2021-05-13, from `https://iopscience.iop.org/article/10.1086/679566/meta` (Publisher: IOP Publishing) doi: 10.1086/679566

Bergin, E. A., Kempton, E. M.-R., Hirschmann, M., Bastelberger, S. T., Teal, D. J., Blake, G. A., ... Li, J. (2023, May). Exoplanet Volatile Carbon Content as a Natural Pathway for Haze Formation. *The Astrophysical Journal Letters*, *949*(1), L17. Retrieved 2023-07-13, from `https://dx.doi.org/10.3847/2041-8213/acd377` (Publisher: The American Astronomical Society) doi: 10.3847/2041-8213/acd377

Berta, Z. K., Charbonneau, D., Désert, J.-M., Kempton, E. M.-R., McCullough, P. R., Burke, C. J., ... Homeier, D. (2012, February). The flat transmission spectrum of the super-Earth GJ1214b from Wide Field Camera 3 on the Hubble Space Telescope. *The Astrophysical Journal*, *747*(1), 35. Retrieved 2023-05-23, from `https://dx.doi.org/10.1088/0004-637X/747/1/35` (Publisher: The American Astronomical Society) doi: 10.1088/0004-637X/747/1/35

Bluhm, P., Palle, E., Molaverdikhani, K., Kemmer, J., Hatzes, A. P., Kossakowski, D., ... Osorio, M. R. Z. (2021, June). An ultra-short-period transiting super-Earth orbiting the M3 dwarf TOI-1685. *Astronomy & Astrophysics*, *650*, A78. Retrieved 2021-11-15, from `http://arxiv.org/abs/2103.01016` (arXiv: 2103.01016) doi: 10.1051/0004-6361/202140688

Bohren, C., & Huffman, D. (1998). *Absorption and Scattering of Light by Small Particles.* WILEY-VCH Verlag GmbH & Co. KGaA. Retrieved from `https://onlinelibrary.wiley.com/doi/book/10.1002/9783527618156` doi: 10.1002/9783527618156

Bonfils, X., Delfosse, X., Udry, S., Forveille, T., Mayor, M., Perrier, C., ... Bertaux, J.-L. (2013, January). The HARPS search for southern extra-solar planets - XXXI. The M-dwarf sample. *Astronomy & Astrophysics*, *549*, A109. Retrieved 2023-05-12, from `https://www.aanda.org/articles/aa/abs/2013/01/aa14704-10/aa14704-10.html` (Publisher: EDP Sciences) doi: 10.1051/0004-6361/201014704

Booker, J. R., & Bretherton, F. P. (1967, February). The critical layer for internal gravity waves in a shear flow. *Journal of Fluid Mechanics*, *27*(3), 513–539. Retrieved 2021-09-03, from `https://www.cambridge.org/core/journals/journal-of-fluid-mechanics/article/critical-layer-for-internal-gravity-waves-in-a-shear-flow/8D72D50D8C40AFCC668E7047B2300EEF` (Publisher: Cambridge University Press) doi: 10.1017/S0022112067000515

Boutle, I. A., Joshi, M., Lambert, F. H., Mayne, N. J., Lyster, D., Manners, J., ... Kohary, K. (2020, June). Mineral dust increases the habitability of terrestrial planets but confounds biomarker detection. *Nature Communications*, *11*(1), 2731. Retrieved 2021-03-09, from `https://www.nature.com/articles/s41467-020-16543-8` (Number: 1 Publisher: Nature Publishing Group) doi: 10.1038/s41467-020-16543-8

Boutle, I. A., Mayne, N. J., Drummond, B., Manners, J., Goyal, J., Lambert, F. H., ... Earnshaw, P. D. (2017, May). Exploring the climate of Proxima B with the Met Office Unified Model. *Astronomy & Astrophysics*, *601*, A120. Retrieved 2020-10-14, from `https://www.aanda.org/articles/aa/abs/2017/05/aa30020-16/aa30020-16.html` (Publisher: EDP Sciences) doi: 10.1051/0004-6361/201630020

Bowman, K. P. (1989, November). Global Patterns of the Quasi-biennial Oscillation in Total Ozone. *Journal of the Atmospheric Sciences*, *46*(21), 3328–3343. Retrieved 2021-09-06, from `https://journals.ametsoc.org/view/journals/atsc/46/21/1520-0469_1989_046_3328_gpotqb_2_0_co_2.xml` (Publisher: American Meteorological Society Section: Journal of the Atmospheric Sciences) doi: 10.1175/1520-0469(1989)046<3328:GPOTQB>2.0.CO;2

Braam, M., Palmer, P. I., Decin, L., Cohen, M., & Mayne, N. J. (2023, November). Stratospheric dayside-to-nightside circulation drives the 3D ozone distribution on synchronously rotating rocky exoplanets. *Monthly Notices of the Royal Astronomical Society*, *526*(1), 263–278. Retrieved 2023-10-04, from `https://doi.org/10.1093/mnras/stad2704` doi: 10.1093/mnras/stad2704

Braam, M., Palmer, P. I., Decin, L., Ridgway, R. J., Zamyatina, M., Mayne, N. J., ... Abraham, N. L. (2022, September). Lightning-induced chemistry on tidally-locked Earth-like exoplanets. *Monthly Notices of the Royal Astronomical Society*, stac2722. Retrieved 2022-10-12, from `https://doi.org/10.1093/mnras/stac2722` doi: 10.1093/mnras/stac2722

Braesicke, P. (2015, January). MIDDLE ATMOSPHERE | Zonal Mean Climatology. In G. R. North, J. Pyle, & F. Zhang (Eds.), *Encyclopedia of Atmospheric Sciences (Second Edition)* (pp. 50–56). Oxford: Academic Press. Retrieved 2021-08-10, from `https://www.sciencedirect.com/science/article/pii/B9780123822253002279` doi: 10.1016/B978-0-12-382225-3.00227-9

Brogi, M., Kok, R. J. d., Albrecht, S., Snellen, I. A. G., Birkby, J. L., & Schwarz, H. (2016, January). Rotation and winds of exoplanet HD 189733 b measured with high-dispersion transmission spectroscopy. *The Astrophysical Journal*, *817*(2), 106. Retrieved 2021-05-13, from `https://iopscience.iop.org/article/10.3847/0004-637X/817/2/106` doi: 10.3847/0004-637X/817/2/106

Brown, T. M., Charbonneau, D., Gilliland, R. L., Noyes, R. W., & Burrows, A. (2001, May). Hubble Space Telescope Time-Series Photometry of the Transiting Planet of HD 209458. *The Astrophysical Journal*, *552*(2), 699–709. Retrieved 2021-05-11, from `http://arxiv.org/abs/astro-ph/0101336` (arXiv: astro-ph/0101336) doi: 10.1086/320580

Burningham, B., Faherty, J. K., Gonzales, E. C., Marley, M. S., Visscher, C., Lupu, R., ... Saumon, D. (2021, September). Cloud busting: enstatite and quartz clouds in the atmosphere of 2M2224-0158. *Monthly Notices of the Royal Astronomical Society*, *506*(2), 1944–1961. Retrieved 2022-08-12, from `https://doi.org/10.1093/mnras/stab1361` doi: 10.1093/mnras/stab1361

Bushell, A. (2021). *UMDP 034: Non-Orographic (Spectral) Gravity Wave Parametrization* (Tech. Rep. No. 34). Exeter, United Kingdom: Met Office. Retrieved from `https://code.metoffice.gov.uk/doc/um/latest/papers/umdp_034.pdf`

Bushell, A. C., Anstey, J. A., Butchart, N., Kawatani, Y., Osprey, S. M., Richter, J. H., ... Yukimoto, S. (2020). Evaluation of the Quasi-Biennial Oscillation in global climate models for the SPARC QBO-initiative. *Quarterly Journal of the Royal Meteorological Society*, *148*(744), 1459–1489. Retrieved 2022-01-13, from `https://onlinelibrary.wiley.com/doi/abs/10.1002/qj.3765` (_eprint: https://onlinelibrary.wiley.com/doi/pdf/10.1002/qj.3765) doi: 10.1002/qj.3765

Bushell, A. C., Butchart, N., Derbyshire, S. H., Jackson, D. R., Shutts, G. J., Vosper, S. B., & Webster, S. (2015, November). Parameterized Gravity Wave Momentum Fluxes from Sources Related to Convection and Large-Scale Precipitation Processes in a Global Atmosphere Model. *Journal of the Atmospheric Sciences*, *72*(11), 4349–4371. Retrieved 2021-09-22, from `https://journals.ametsoc.org/view/journals/atsc/72/11/jas-d-15-0022.1.xml` (Publisher: American Meteorological Society Section: Journal of the Atmospheric Sciences) doi: 10.1175/JAS-D-15-0022.1

Butchart, N., Anstey, J. A., Hamilton, K., Osprey, S., McLandress, C., Bushell, A. C., ... Yukimoto, S. (2018, March). Overview of experiment design and comparison of models participating in phase 1 of the SPARC Quasi-Biennial Oscillation initiative (QBOi). *Geoscientific Model Development*, *11*(3), 1009–1032. Retrieved 2022-01-13, from `https://gmd.copernicus.org/articles/11/1009/2018/` (Publisher: Copernicus GmbH) doi: 10.5194/gmd-11-1009-2018

Caldas, A., Leconte, J., Selsis, F., Waldmann, I. P., Bordé, P., Rocchetto, M., & Charnay, B. (2019, March). Effects of a fully 3D atmospheric structure on exoplanet transmission spectra: retrieval biases due to day–night temperature gradients. *Astronomy & Astrophysics*, *623*, A161. Retrieved 2021-03-01, from `https://www.aanda.org/articles/aa/abs/2019/03/aa34384-18/aa34384-18.html` (Publisher: EDP Sciences) doi: 10.1051/0004-6361/201834384

Carone, L., Keppens, R., & Decin, L. (2015, November). Connecting the dots – II. Phase changes in the climate dynamics of tidally locked terrestrial exoplanets. *Monthly Notices of the Royal Astronomical Society*, *453*(3), 2412–2437. Retrieved 2023-06-14, from `https://doi.org/10.1093/mnras/stv1752` doi: 10.1093/mnras/stv1752

Carone, L., Keppens, R., Decin, L., & Henning, T. (2018, February). Stratosphere circulation on tidally locked ExoEarths. *Monthly Notices of the Royal Astronomical Society*, *473*(4), 4672–4685. Retrieved 2020-10-07, from `https://academic.oup.com/mnras/article/473/4/4672/4564445` (Publisher: Oxford Academic) doi: 10.1093/mnras/stx2732

Catanzarite, J., & Shao, M. (2011, September). The Occurrence Rate of Earth Analog Planets Orbiting Sunlike Stars. *The Astrophysical Journal*, *738*(2), 151. Retrieved 2021-05-10, from `http://arxiv.org/abs/1103.1443` (arXiv: 1103.1443) doi: 10.1088/0004-637X/738/2/151

Catling, D., & Kasting, J. (2017). *Atmospheric Evolution on Inhabited and Lifeless Worlds*. Cambridge University Press. Retrieved 2021-05-11, from `https://www.cambridge.org/core/books/atmospheric-evolution-on-inhabited-and-lifeless-worlds/CB3EE1D3F18A1DB234342E1FF410FC61`

Charbonneau, D., Brown, T. M., Latham, D. W., & Mayor, M. (1999, December). Detection of Planetary Transits Across a Sun-like Star. *The Astrophysical Journal*, *529*(1), L45. Retrieved 2021-05-11, from `https://iopscience.iop.org/article/10.1086/312457/meta` (Publisher: IOP Publishing) doi: 10.1086/312457

Charbonneau, D., Brown, T. M., Noyes, R. W., & Gilliland, R. L. (2002, March). Detection of an Extrasolar Planet Atmosphere*. *The Astrophysical Journal*, *568*(1), 377. Retrieved 2023-07-05, from `https://iopscience.iop.org/article/10.1086/338770/meta` (Publisher: IOP Publishing) doi: 10.1086/338770

Checlair, J., Menou, K., & Abbot, D. S. (2017, August). No Snowball on Habitable Tidally Locked Planets. *The Astrophysical Journal*, *845*(2), 132. Retrieved 2021-11-17, from `https://doi.org/10.3847/1538-4357/aa80e1` (Publisher: American Astronomical Society) doi: 10.3847/1538-4357/aa80e1

Checlair, J. H., Olson, S. L., Jansen, M. F., & Abbot, D. S. (2019, October). No Snowball on Habitable Tidally Locked Planets with a Dynamic Ocean. *The Astrophysical Journal*, *884*(2), L46. Retrieved 2021-11-17, from `https://doi.org/10.3847/2041-8213/ab487d` (Publisher: American Astronomical Society) doi: 10.3847/2041-8213/ab487d

Chen, H., Li, G., Paradise, A., & Kopparapu, R. K. (2023, March). Sporadic Spin-orbit Variations in Compact Multiplanet Systems and Their Influence on Exoplanet Climate. *The Astrophysical Journal Letters*, *946*(2), L32. Retrieved 2023-06-07, from `https://dx.doi.org/10.3847/2041-8213/acbd33` (Publisher: The American Astronomical Society) doi: 10.3847/2041-8213/acbd33

Chen, H., Wolf, E. T., Kopparapu, R., Domagal-Goldman, S., & Horton, D. E. (2018, November). Biosignature Anisotropy Modeled on Temperate Tidally Locked M-dwarf Planets. *The Astrophysical Journal*, *868*(1), L6. Retrieved 2021-02-22, from `https://doi.org/10.3847/2041-8213/aaedb2` (Publisher: American Astronomical Society) doi: 10.3847/2041-8213/aaedb2

Christie, D. A., Mayne, N. J., Lines, S., Parmentier, V., Manners, J., Boutle, I., ... Kohary, K. (2021, September). The impact of mixing treatments on cloud modelling in 3D simulations of hot Jupiters. *Monthly Notices of the Royal Astronomical Society*, *506*(3), 4500–4515. Retrieved 2022-10-12, from `https://doi.org/10.1093/mnras/stab2027` doi: 10.1093/mnras/stab2027

Cohen, M., Bollasina, M. A., Palmer, P. I., Sergeev, D. E., Boutle, I. A., Mayne, N. J., & Manners, J. (2022, May). Longitudinally Asymmetric Stratospheric Oscillation on a Tidally Locked Exoplanet. *The Astrophysical Journal*, *930*(2), 152. Retrieved 2022-08-02, from `https://doi.org/10.3847/1538-4357/ac625d` (Publisher: American Astronomical Society) doi: 10.3847/1538-4357/ac625d

Cohen, M., Bollasina, M. A., Sergeev, D. E., Palmer, P. I., & Mayne, N. J. (2023, April). Traveling Planetary-scale Waves Cause Cloud Variability on Tidally Locked Aquaplanets. *The Planetary Science Journal*, *4*(4), 68. Retrieved 2023-07-03, from `https://iopscience.iop.org/article/10.3847/PSJ/acc9c4/meta` (Publisher: IOP Publishing) doi: 10.3847/PSJ/acc9c4

Colella, P., & Woodward, P. R. (1984, April). The Piecewise Parabolic Method (PPM) for gas-dynamical simulations. *Journal of Computational Physics*, *54*(1), 174–201. Retrieved 2022-02-23, from `https://www.sciencedirect.com/science/article/pii/0021999184901438` doi: 10.1016/0021-9991(84)90143-8

Corrales, L., Gavilan, L., Teal, D. J., & Kempton, E. M.-R. (2023, February). Photochemical Hazes Can Trace the C/O Ratio in Exoplanet Atmospheres. *The Astrophysical Journal Letters*, *943*(2), L26. Retrieved 2023-09-01, from `https://dx.doi.org/10.3847/2041-8213/acaf86` (Publisher: The American Astronomical Society) doi: 10.3847/2041-8213/acaf86

Crossfield, I. J. M., Barman, T., Hansen, B. M. S., & Howard, A. W. (2013, November). Warm ice giant GJ 3470b - I. A flat transmission spectrum indicates a hazy, low-methane, and/or metal-rich atmosphere. *Astronomy & Astrophysics*, *559*, A33. Retrieved 2023-05-23, from `https://www.aanda.org/articles/aa/abs/2013/11/aa22278-13/aa22278-13.html` (Publisher: EDP Sciences) doi: 10.1051/0004-6361/201322278

Crossfield, I. J. M., & Kreidberg, L. (2017, November). Trends in Atmospheric Properties of Neptune-size Exoplanets. *The Astronomical Journal*, *154*(6), 261. Retrieved 2023-05-23, from `https://dx.doi.org/10.3847/1538-3881/aa9279` (Publisher: The American Astronomical Society) doi: 10.3847/1538-3881/aa9279

Damiano, M., Hu, R., Barclay, T., Zieba, S., Kreidberg, L., Brande, J., ... Quintana, E. V. (2022, October). A Transmission Spectrum of the Sub-Earth Planet L98-59 b in 1.1–1.7 µm. *The Astronomical Journal*, *164*(5), 225. Retrieved 2023-05-23, from `https://dx.doi.org/10.3847/1538-3881/ac9472` (Publisher: The American Astronomical Society) doi: 10.3847/1538-3881/ac9472

Debras, F., Mayne, N., Baraffe, I., Goffrey, T., & Thuburn, J. (2019, November). Eigenvectors, Circulation, and Linear Instabilities for Planetary Science in 3 Dimensions (ECLIPS3D). *Astronomy & Astrophysics*, *631*, A36. Retrieved 2021-11-15, from `https://www.aanda.org/articles/aa/abs/2019/11/aa35582-19/aa35582-19.html` (Publisher: EDP Sciences) doi: 10.1051/0004-6361/201935582

Debras, F., Mayne, N., Baraffe, I., Jaupart, E., Mourier, P., Laibe, G., ... Thuburn, J. (2020, January). Acceleration of superrotation in simulated hot Jupiter atmospheres. *Astronomy & Astrophysics*, *633*, A2. Retrieved 2021-08-16, from `https://www.aanda.org/articles/aa/abs/2020/01/aa36110-19/aa36110-19.html` (Publisher: EDP Sciences) doi: 10.1051/0004-6361/201936110

Del Genio, A. D., & Zhou, W. (1996, April). Simulations of Superrotation on Slowly Rotating Planets: Sensitivity to Rotation and Initial Condition. *Icarus*, *120*(2), 332–343. Retrieved 2021-05-11, from `https://www.sciencedirect.com/science/article/pii/S0019103596900548` doi: 10.1006/icar.1996.0054

Delrez, L., Murray, C. A., Pozuelos, F. J., Narita, N., Ducrot, E., Timmermans, M., ... Gillon, M. (2022, November). Two temperate super-Earths transiting a nearby late-type M dwarf. *Astronomy & Astrophysics*, *667*, A59. Retrieved 2023-10-02, from `https://www.aanda.org/articles/aa/abs/2022/11/aa44041-22/aa44041-22.html` (Publisher: EDP Sciences) doi: 10.1051/0004-6361/202244041

Demory, B.-O., Gillon, M., de Wit, J., Madhusudhan, N., Bolmont, E., Heng, K., ... Queloz, D. (2016, April). A map of the large day-night temperature gradient of a super-Earth exoplanet. *Nature*, *532*(7598), 207–209. Retrieved 2021-05-13, from `http://arxiv.org/abs/1604.05725` (arXiv: 1604.05725) doi: 10.1038/nature17169

de Wit, J., Wakeford, H. R., Gillon, M., Lewis, N. K., Valenti, J. A., Demory, B.-O., ... Van Grootel, V. (2016, September). A combined transmission spectrum of the Earth-sized exoplanets TRAPPIST-1 b and c. *Nature*, *537*(7618), 69–72. Retrieved 2022-08-12, from `https://www.nature.com/articles/nature18641` (Number: 7618 Publisher: Nature Publishing Group) doi: 10.1038/nature18641

Diamond-Lowe, H., Berta-Thompson, Z., Charbonneau, D., & Kempton, E. M.-R. (2018, July). Ground-based Optical Transmission Spectroscopy of the Small, Rocky Exoplanet GJ 1132b. *The Astronomical Journal*, *156*(2), 42. Retrieved 2021-05-13, from `https://doi.org/10.3847/1538-3881/aac6dd` (Publisher: American Astronomical Society) doi: 10.3847/1538-3881/aac6dd

Ding, F., & Wordsworth, R. D. (2022, January). Prospects for Water Vapor Detection in the Atmospheres of Temperate and Arid Rocky Exoplanets around M-dwarf Stars. *The Astrophysical Journal Letters*, *925*(1), L8. Retrieved 2022-08-12, from `https://doi.org/10.3847/2041-8213/ac4a5d` (Publisher: American Astronomical Society) doi: 10.3847/2041-8213/ac4a5d

Doshi, D., Cowan, N. B., & Huang, Y. (2022, September). Stratospheric clouds do not impede JWST transit spectroscopy for exoplanets with Earth-like atmospheres. *Monthly Notices of the Royal Astronomical Society*, *515*(2), 1982–1992. Retrieved 2023-03-21, from `https://doi.org/10.1093/mnras/stac1869` doi: 10.1093/mnras/stac1869

Dressing, C. D., & Charbonneau, D. (2015, June). The occurrence of potentially habitable planets orbiting M dwarfs estimated from the full Kepler dataset and an empirical measurement of the detection sensitivity. *The Astrophysical Journal*, *807*(1), 45. Retrieved 2020-11-09, from `https://doi.org/10.1088%2F0004-637x%2F807%2F1%2F45` (Publisher: American Astronomical Society) doi: 10.1088/0004-637X/807/1/45

Dunkerton, T. J. (1997). The role of gravity waves in the quasi-biennial oscillation. *Journal of Geophysical Research: Atmospheres*, *102*(D22), 26053–26076. Retrieved 2021-06-07, from `https://agupubs.onlinelibrary.wiley.com/doi/abs/10.1029/96JD02999` (_eprint: https://agupubs.onlinelibrary.wiley.com/doi/pdf/10.1029/96JD02999) doi: https://doi.org/10.1029/96JD02999

Dunkerton, T. J., Anstey, J. A., & Gray, L. J. (2015, January). MIDDLE ATMOSPHERE | Quasi-Biennial Oscillation. In G. R. North, J. Pyle, & F. Zhang (Eds.), *Encyclopedia of Atmospheric Sciences (Second Edition)* (pp. 18–25). Oxford: Academic Press. Retrieved 2021-08-09, from `https://www.sciencedirect.com/science/article/pii/B9780123822253002322` doi: 10.1016/B978-0-12-382225-3.00232-2

Dunkerton, T. J., & Delisi, D. P. (1985, February). Climatology of the Equatorial Lower Stratosphere. *Journal of the Atmospheric Sciences*, *42*(4), 376–396. Retrieved 2021-09-03, from `https://journals.ametsoc.org/view/journals/atsc/42/4/1520-0469_1985_042_0376_cotels_2_0_co_2.xml` (Publisher: American Meteorological Society Section: Journal of the Atmospheric Sciences) doi: 10.1175/1520-0469(1985)042<0376:COTELS>2.0.CO;2

Dymont, A. H., Yu, X., Ohno, K., Zhang, X., & Fortney, J. J. (2021, December). Cleaning our Hazy Lens: Statistical Trends in Transmission Spectra of Warm Exoplanets. *arXiv:2112.06173 [astro-ph]*. Retrieved 2021-12-14, from `http://arxiv.org/abs/2112.06173` (arXiv: 2112.06173)

Eager-Nash, J. K., Reichelt, D. J., Mayne, N. J., Lambert, F. H., Sergeev, D. E., Ridgway, R. J., ... Kohary, K. (2020, July). Implications of different stellar spectra for the climate of tidally locked Earth-like exoplanets. *Astronomy & Astrophysics*, *639*, A99. Retrieved 2023-03-21, from `https://www.aanda.org/articles/aa/abs/2020/07/aa38089-20/aa38089-20.html` (Publisher: EDP Sciences) doi: 10.1051/0004-6361/202038089

Edson, A., Lee, S., Bannon, P., Kasting, J. F., & Pollard, D. (2011, March). Atmospheric circulations of terrestrial planets orbiting low-mass stars. *Icarus*, *212*(1), 1–13. Retrieved 2022-07-07, from `https://www.sciencedirect.com/science/article/pii/S0019103510004422` doi: 10.1016/j.icarus.2010.11.023

Edwards, B., Mugnai, L., Tinetti, G., Pascale, E., & Sarkar, S. (2019, May). An Updated Study of Potential Targets for Ariel. *The Astronomical Journal*, *157*(6), 242. Retrieved 2020-09-22, from `https://iopscience.iop.org/article/10.3847/1538-3881/ab1cb9` doi: 10.3847/1538-3881/ab1cb9

Edwards, B., Rice, M., Zingales, T., Tessenyi, M., Waldmann, I., Tinetti, G., … Sarkar, S. (2019, April). Exoplanet spectroscopy and photometry with the Twinkle space telescope. *Experimental Astronomy*, *47*(1), 29–63. Retrieved 2021-05-13, from `https://doi.org/10.1007/s10686-018-9611-4` doi: 10.1007/s10686-018-9611-4

Ehrenreich, D., Lovis, C., Allart, R., Zapatero Osorio, M. R., Pepe, F., Cristiani, S., … Zerbi, F. (2020, April). Nightside condensation of iron in an ultrahot giant exoplanet. *Nature*, *580*(7805), 597–601. Retrieved 2021-01-16, from `https://www.nature.com/articles/s41586-020-2107-1` (Number: 7805 Publisher: Nature Publishing Group) doi: 10.1038/s41586-020-2107-1

Ern, M., & Preusse, P. (2009). Quantification of the contribution of equatorial Kelvin waves to the QBO wind reversal in the stratosphere. *Geophysical Research Letters*, *36*(21). Retrieved 2022-01-29, from `https://www.proquest.com/openview/5a305e1df092e68af0d45a1e8542ddf6/1?pq-origsite=gscholar&cbl=54723` doi: DOI:10.1029/2009GL040493

Evan, S., Alexander, M. J., & Dudhia, J. (2012). WRF simulations of convectively generated gravity waves in opposite QBO phases. *Journal of Geophysical Research: Atmospheres*, *117*(D12). Retrieved 2022-01-16, from `https://onlinelibrary.wiley.com/doi/abs/10.1029/2011JD017302` (_eprint: https://onlinelibrary.wiley.com/doi/pdf/10.1029/2011JD017302) doi: 10.1029/2011JD017302

Fauchez, T. J., Turbet, M., Sergeev, D. E., Mayne, N. J., Spiga, A., Sohl, L., … Bouldin, N. (2021, June). TRAPPIST Habitable Atmosphere Intercomparison (THAI) Workshop Report. *The Planetary Science Journal*, *2*(3), 106. Retrieved 2022-08-03, from `https://iopscience.iop.org/article/10.3847/PSJ/abf4df/meta` (Publisher: IOP Publishing) doi: 10.3847/PSJ/abf4df

Fauchez, T. J., Turbet, M., Villanueva, G. L., Wolf, E. T., Arney, G., Kopparapu, R. K., … Stevenson, K. B. (2019, December). Impact of Clouds and Hazes on the Simulated JWST Transmission Spectra of Habitable Zone Planets in the TRAPPIST-1 System. *The Astrophysical Journal*, *887*(2), 194. Retrieved 2020-10-02, from `https://doi.org/10.3847%2F1538-4357%2Fab5862` (Publisher: American Astronomical Society) doi: 10.3847/1538-4357/ab5862

Fauchez, T. J., Turbet, M., Wolf, E. T., Boutle, I., Way, M. J., Del Genio, A. D., ... Domagal Goldman, S. D. (2020, February). TRAPPIST-1 Habitable Atmosphere Intercomparison (THAI): motivations and protocol version 1.0. *Geoscientific Model Development*, *13*(2), 707–716. Retrieved 2021-02-01, from `https://gmd.copernicus.org/articles/13/707/2020/` (Publisher: Copernicus GmbH) doi: https://doi.org/10.5194/gmd-13-707-2020

Fauchez, T. J., Villanueva, G. L., Sergeev, D. E., Turbet, M., Boutle, I. A., Tsigaridis, K., ... Mayne, N. J. (2022, September). The TRAPPIST-1 Habitable Atmosphere Intercomparison (THAI). III. Simulated Observables—the Return of the Spectrum. *The Planetary Science Journal*, *3*(9), 213. Retrieved 2022-10-12, from `https://iopscience.iop.org/article/10.3847/PSJ/ac6cf1/meta` (Publisher: IOP Publishing) doi: 10.3847/PSJ/ac6cf1

Feliz, D. L., Plavchan, P., Bianco, S. N., Jimenez, M., Collins, K. I., Alvarado, B. V., & Stassun, K. G. (2021, May). NEMESIS: Exoplanet Transit Survey of Nearby M-Dwarfs in TESS FFIs I. *The Astronomical Journal*, *161*(5), 247. Retrieved 2021-05-11, from `http://arxiv.org/abs/2103.05647` (arXiv: 2103.05647) doi: 10.3847/1538-3881/abedb3

Folonier, H. A., & Ferraz-Mello, S. (2017, December). Tidal synchronization of an anelastic multi-layered body: Titan's synchronous rotation. *Celestial Mechanics and Dynamical Astronomy*, *129*(4), 359–396. Retrieved 2021-05-11, from `http://arxiv.org/abs/1706.08603` (arXiv: 1706.08603) doi: 10.1007/s10569-017-9777-5

Fossati, L., Haswell, C. A., Froning, C. S., Hebb, L., Holmes, S., Kolb, U., ... Wilson, D. (2010, May). METALS IN THE EXOSPHERE OF THE HIGHLY IRRADIATED PLANET WASP-12b. *The Astrophysical Journal*, *714*(2), L222–L227. Retrieved 2021-05-13, from `https://iopscience.iop.org/article/10.1088/2041-8205/714/2/L222` doi: 10.1088/2041-8205/714/2/L222

Fraedrich, K., Jansen, H., Kirk, E., Luksch, U., & Lunkeit, F. (2005, July). The Planet Simulator: Towards a user friendly model. *Meteorologische Zeitschrift*, 299–304. Retrieved 2023-05-30, from `https://www.schweizerbart.de/papers/metz/detail/14/54202/The_Planet_Simulator_Towards_a_user_friendly_model?af=crossref` (Publisher: Schweizerbart'sche Verlagsbuchhandlung) doi: 10.1127/0941-2948/2005/0043

Fraine, J., Deming, D., Benneke, B., Knutson, H., Jordán, A., Espinoza, N., ... Todorov, K. (2014). Water vapour absorption in the clear atmosphere of a Neptune-sized exoplanet. *Nature*(513), 526–529. Retrieved 2021-05-13, from `https://www.nature.com/articles/nature13785` doi: https://doi.org/10.1038/nature13785

Frierson, D. M. W., Held, I. M., & Zurita-Gotor, P. (2006, October). A Gray-Radiation Aquaplanet Moist GCM. Part I: Static Stability and Eddy Scale. *Journal of Atmospheric Sciences*, *63*(10), 2548–2566. Retrieved 2021-01-05, from `https://journals.ametsoc.org/view/journals/atsc/63/10/jas3753.1.xml` (Publisher: American Meteorological Society Section: Journal of Atmospheric Sciences) doi: 10.1175/JAS3753.1

Gao, P., Thorngren, D. P., Lee, G. K. H., Fortney, J. J., Morley, C. V., Wakeford, H. R., ... Zhang, X. (2020, October). Aerosol composition of hot giant exoplanets dominated by silicates and hydrocarbon hazes. *Nature Astronomy*, *4*(10), 951–956. Retrieved 2021-02-12, from `https://www.nature.com/articles/s41550-020-1114-3` (Number: 10 Publisher: Nature Publishing Group) doi: 10.1038/s41550-020-1114-3

Gao, P., Wakeford, H. R., Moran, S. E., & Parmentier, V. (2021). Aerosols in Exoplanet Atmospheres. *Journal of Geophysical Research: Planets*, *126*(4), e2020JE006655. Retrieved 2023-05-01, from `https://onlinelibrary.wiley.com/doi/abs/10.1029/2020JE006655` (_eprint: https://onlinelibrary.wiley.com/doi/pdf/10.1029/2020JE006655) doi: 10.1029/2020JE006655

Garcia, L. J., Moran, S. E., Rackham, B. V., Wakeford, H. R., Gillon, M., de Wit, J., & Lewis, N. K. (2022, April). HST/WFC3 transmission spectroscopy of the cold rocky planet TRAPPIST-1h. *Astronomy & Astrophysics*. Retrieved 2022-08-12, from `https://www.aanda.org/10.1051/0004-6361/202142603` doi: 10.1051/0004-6361/202142603

Garfinkel, C. I., Gerber, E. P., Shamir, O., Rao, J., Jucker, M., White, I. P., & Paldor, N. (2021, April). *A QBO cookbook: Sensitivity of the Quasi-Biennial Oscillation to resolution, resolved waves, and parameterized gravity waves* [preprint]. Retrieved 2021-04-21, from `http://www.essoar.org/doi/10.1002/essoar.10506774.1` (Archive Location: world Publisher: Earth and Space Science Open Archive Section: Atmospheric Sciences) doi: 10.1002/essoar.10506774.1

Gialluca, M. T., Robinson, T. D., Rugheimer, S., & Wunderlich, F. (2021, May). Characterizing Atmospheres of Transiting Earth-like Exoplanets Orbiting M Dwarfs with James Webb Space Telescope. *Publications of the Astronomical Society of the Pacific*, *133*(1023), 054401. Retrieved 2022-08-12, from `https://doi.org/10.1088/1538-3873/abf367` (Publisher: IOP Publishing) doi: 10.1088/1538-3873/abf367

Gibson, N. P., Aigrain, S., Barstow, J. K., Evans, T. M., Fletcher, L. N., & Irwin, P. G. J. (2013, February). A Gemini ground-based transmission spectrum of WASP-29b: a featureless spectrum from 515 to 720 nm. *Monthly Notices of the Royal Astronomical Society*, *428*(4), 3680–3692. Retrieved 2023-05-23, from `https://doi.org/10.1093/mnras/sts307` doi: 10.1093/mnras/sts307

Gill, A. E. (1980). Some simple solutions for heat-induced tropical circulation. *Quarterly Journal of the Royal Meteorological Society*, *106*(449), 447–462. Retrieved 2021-05-04, from `https://rmets.onlinelibrary.wiley.com/doi/abs/10.1002/qj.49710644905` (_eprint: https://rmets.onlinelibrary.wiley.com/doi/pdf/10.1002/qj.49710644905) doi: https://doi.org/10.1002/qj.49710644905

Gillon, M., Triaud, A. H. M. J., Demory, B.-O., Jehin, E., Agol, E., Deck, K. M., ... Queloz, D. (2017, February). Seven temperate terrestrial planets around the nearby ultracool dwarf star TRAPPIST-1. *Nature*, *542*(7642), 456–460. Retrieved 2021-05-13, from `https://www.nature.com/articles/nature21360` (Number: 7642 Publisher: Nature Publishing Group) doi: 10.1038/nature21360

Grant, D., & Wakeford, H. R. (2023, March). Transmission strings: a technique for spatially mapping exoplanet atmospheres around their terminators. *Monthly Notices of the Royal Astronomical Society*, *519*(4), 5114–5127. Retrieved 2023-08-08, from `https://doi.org/10.1093/mnras/stac3632` doi: 10.1093/mnras/stac3632

Greene, T. P., Bell, T. J., Ducrot, E., Dyrek, A., Lagage, P.-O., & Fortney, J. J. (2023, June). Thermal emission from the Earth-sized exoplanet TRAPPIST-1 b using JWST. *Nature*, *618*(7963), 39–42. Retrieved 2023-10-02, from `https://www.nature.com/articles/s41586-023-05951-7` (Number: 7963 Publisher: Nature Publishing Group) doi: 10.1038/s41586-023-05951-7

Greene, T. P., Line, M. R., Montero, C., Fortney, J. J., Lustig-Yaeger, J., & Luther, K. (2016, January). Characterizing transiting exoplanet atmospheres with*JWST*. *The Astrophysical Journal*, *817*(1), 17. Retrieved 2021-05-13, from `https://iopscience.iop.org/article/10.3847/0004-637X/817/1/17` doi: 10.3847/0004-637X/817/1/17

Guenther, M. N., Zhan, Z., Seager, S., Rimmer, P. B., Ranjan, S., Stassun, K. G., ... Ting, E. B. (2020, February). Stellar Flares from the First TESS Data Release: Exploring a New Sample of M Dwarfs. *Astronomical Journal*, *159*(2), 60. (Place: Bristol Publisher: Iop Publishing Ltd WOS:000520500700001) doi: 10.3847/1538-3881/ab5d3a

Hammond, M., & Lewis, N. T. (2021, March). The rotational and divergent components of atmospheric circulation on tidally locked planets. *Proceedings of the National Academy of Sciences*, *118*(13). Retrieved 2021-11-19, from `https://www.pnas.org/content/118/13/e2022705118` (Publisher: National Academy of Sciences Section: Physical Sciences) doi: 10.1073/pnas.2022705118

Hammond, M., & Pierrehumbert, R. T. (2018, December). Wave-mean Flow Interactions in the Atmospheric Circulation of Tidally Locked Planets. *The Astrophysical Journal*, *869*(1), 65. Retrieved 2023-01-27, from `https://dx.doi.org/10.3847/1538-4357/aaec03` (Publisher: The American Astronomical Society) doi: 10.3847/1538-4357/aaec03

Hammond, M., Tsai, S.-M., & Pierrehumbert, R. T. (2020, September). The Equatorial Jet Speed on Tidally Locked Planets. I. Terrestrial Planets. *The Astrophysical Journal*, *901*(1), 78. Retrieved 2021-05-18, from `https://iopscience.iop.org/article/10.3847/1538-4357/abb08b` doi: 10.3847/1538-4357/abb08b

Haqq-Misra, J., Wolf, E. T., Fauchez, T. J., Shields, A. L., & Kopparapu, R. K. (2022, November). The Sparse Atmospheric Model Sampling Analysis (SAMOSA) Intercomparison: Motivations and Protocol Version 1.0: A CUISINES Model Intercomparison Project. *The Planetary Science Journal*, *3*(11), 260. Retrieved 2023-06-07, from `https://iopscience.iop.org/article/10.3847/PSJ/ac9479/meta` (Publisher: IOP Publishing) doi: 10.3847/PSJ/ac9479

Haqq-Misra, J., Wolf, E. T., Joshi, M., Zhang, X., & Kopparapu, R. K. (2018, January). Demarcating Circulation Regimes of Synchronously Rotating Terrestrial Planets within the Habitable Zone. *The Astrophysical Journal*, *852*(2), 67. Retrieved 2023-06-14, from `https://dx.doi.org/10.3847/1538-4357/aa9f1f` (Publisher: The American Astronomical Society) doi: 10.3847/1538-4357/aa9f1f

Haqq-Misra, J. D., Domagal-Goldman, S. D., Kasting, P. J., & Kasting, J. F. (2008, December). A Revised, Hazy Methane Greenhouse for the Archean Earth. *Astrobiology*, *8*(6), 1127–1137. Retrieved 2020-11-11, from `https://www.liebertpub.com/doi/10.1089/ast.2007.0197` (Publisher: Mary Ann Liebert, Inc., publishers) doi: 10.1089/ast.2007.0197

Hardegree-Ullman, K. K., Cushing, M. C., Muirhead, P. S., & Christiansen, J. L. (2019, July). Kepler Planet Occurrence Rates for Mid-Type M Dwarfs as a Function of Spectral Type. *The Astronomical Journal*, *158*(2), 75. Retrieved 2021-05-10, from `http://arxiv.org/abs/1905.05900` (arXiv: 1905.05900) doi: 10.3847/1538-3881/ab21d2

Haynes, P. H. (1998). The latitudinal structure of the quasi-biennial oscillation. *Quarterly Journal of the Royal Meteorological Society*, *124*(552), 2645–2670. Retrieved 2021-03-30, from `https://rmets.onlinelibrary.wiley.com/doi/abs/10.1002/qj.49712455206` (_eprint: https://rmets.onlinelibrary.wiley.com/doi/pdf/10.1002/qj.49712455206) doi: https://doi.org/10.1002/qj.49712455206

He, C., Hörst, S. M., Lewis, N. K., Yu, X., Moses, J. I., Kempton, E. M.-R., … Vuitton, V. (2018a, March). Laboratory Simulations of Haze Formation in the Atmospheres of Super-Earths and Mini-Neptunes: Particle Color and Size Distribution. *The Astrophysical Journal Letters*, *856*(1), L3. Retrieved 2023-03-21, from `https://dx.doi.org/10.3847/2041-8213/aab42b` (Publisher: The American Astronomical Society) doi: 10.3847/2041-8213/aab42b

He, C., Hörst, S. M., Lewis, N. K., Yu, X., Moses, J. I., Kempton, E. M.-R., … Vuitton, V. (2018b, July). Photochemical Haze Formation in the Atmospheres of Super-Earths and Mini-Neptunes. *The Astronomical Journal*, *156*(1), 38. Retrieved 2020-10-16, from `https://iopscience.iop.org/article/10.3847/1538-3881/aac883` doi: 10.3847/1538-3881/aac883

He, C., Hörst, S. M., Riemer, S., Sebree, J. A., Pauley, N., & Vuitton, V. (2017, June). Carbon Monoxide Affecting Planetary Atmospheric Chemistry. *The Astrophysical Journal Letters*, *841*(2), L31. Retrieved 2023-09-29, from `https://dx.doi.org/10.3847/2041-8213/aa74cc` (Publisher: The American Astronomical Society) doi: 10.3847/2041-8213/aa74cc

He, C., Radke, M., Moran, S. E., Horst, S. M., Lewis, N. K., Moses, J. I., … Vuitton, V. (2023, January). *Optical Properties of Organic Hazes in Water-rich Exoplanet Atmospheres: Implications for Observations with JWST.* arXiv. Retrieved 2023-01-10, from `http://arxiv.org/abs/2301.02745` (arXiv:2301.02745 [astro-ph]) doi: 10.48550/arXiv.2301.02745

Heath, M. J., Doyle, L. R., Joshi, M. M., & Haberle, R. M. (1999, August). Habitability of Planets Around Red Dwarf Stars. *Origins of life and evolution of the biosphere*, *29*(4), 405–424. Retrieved 2020-11-09, from `https://doi.org/10.1023/A:1006596718708` doi: 10.1023/A:1006596718708

Helling, C. (2019). Exoplanet Clouds. *Annual Review of Earth and Planetary Sciences*, *47*(1), 583–606. Retrieved 2023-06-05, from `https://doi.org/10.1146/annurev-earth-053018-060401` (_eprint: https://doi.org/10.1146/annurev-earth-053018-060401) doi: 10.1146/annurev-earth-053018-060401

Helling, C., Lewis, D., Samra, D., Carone, L., Graham, V., Herbort, O., ... Mayne, N. (2021, May). Cloud property trends in hot and ultra-hot giant gas planets (WASP-43b, WASP-103b, WASP-121b, HAT-P-7b, and WASP-18b). *Astronomy & Astrophysics*, *649*, A44. Retrieved 2022-08-12, from `https://www.aanda.org/articles/aa/abs/2021/05/aa39911-20/aa39911-20.html` (Publisher: EDP Sciences) doi: 10.1051/0004-6361/202039911

Henry, T. J., Jao, W.-C., Subasavage, J. P., Beaulieu, T. D., Ianna, P. A., Costa, E., & Méndez, R. A. (2006, October). The Solar Neighborhood. XVII. Parallax Results from the CTIOPI 0.9 m Program: 20 New Members of the RECONS 10 Parsec Sample. *The Astronomical Journal*, *132*(6), 2360. Retrieved 2023-05-12, from `https://dx.doi.org/10.1086/508233` doi: 10.1086/508233

Hochman, A., Luca, P. D., & Komacek, T. D. (2022, October). Greater Climate Sensitivity and Variability on TRAPPIST-1e than Earth. *The Astrophysical Journal*, *938*(2), 114. Retrieved 2023-01-09, from `https://dx.doi.org/10.3847/1538-4357/ac866f` (Publisher: The American Astronomical Society) doi: 10.3847/1538-4357/ac866f

Holton, J. R., & Hakim, G. H. (2013). *An Introduction to Dynamic Meteorology* (Fifth ed.). Oxford, UK: Academic Press.

Huang, F. T., Mayr, H. G., Reber, C. A., Russell, J. M., Mlynczak, M. G., & Mengel, J. G. (2008). Ozone quasi-biennial oscillations (QBO), semiannual oscillations (SAO), and correlations with temperature in the mesosphere, lower thermosphere, and stratosphere, based on measurements from SABER on TIMED and MLS on UARS. *Journal of Geophysical Research: Space Physics*, *113*(A1). Retrieved 2021-09-06, from `https://agupubs.onlinelibrary.wiley.com/doi/abs/10.1029/2007JA012634` (_eprint: https://agupubs.onlinelibrary.wiley.com/doi/pdf/10.1029/2007JA012634) doi: 10.1029/2007JA012634

Hörst, S. M., He, C., Lewis, N. K., Kempton, E. M.-R., Marley, M. S., Morley, C. V., ... Vuitton, V. (2018, April). Haze production rates in super-Earth and mini-Neptune atmosphere experiments. *Nature Astronomy*, *2*(4), 303–306. Retrieved 2020-10-05, from `https://www.nature.com/articles/s41550-018-0397-0` (Number: 4 Publisher: Nature Publishing Group) doi: 10.1038/s41550-018-0397-0

Imamura, T., Mitchell, J., Lebonnois, S., Kaspi, Y., Showman, A. P., & Korablev, O. (2020, July). Superrotation in Planetary Atmospheres. *Space Science Reviews*, *216*(5), 87. Retrieved 2020-10-02, from `https://doi.org/10.1007/s11214-020-00703-9` doi: 10.1007/s11214-020-00703-9

Jason, S., Tennyson, J., Pascale, E., Williams, J., Johnson, G., Vora, A., . . . Sweeting, M. (2016). TWINKLE: A NEW IDEA FOR COMMERCIAL ASTROPHYSICS MISSIONS. In (p. 15). Valletta, Malta.

Joshi, M. M., Haberle, R. M., & Reynolds, R. T. (1997, October). Simulations of the Atmospheres of Synchronously Rotating Terrestrial Planets Orbiting M Dwarfs: Conditions for Atmospheric Collapse and the Implications for Habitability. *Icarus*, *129*(2), 450–465. Retrieved 2021-05-10, from `https://www.sciencedirect.com/science/article/pii/S0019103597957936` doi: 10.1006/icar.1997.5793

Junge, C. E., Chagnon, C. W., & Manson, J. E. (1961, May). A World-wide Stratospheric Aerosol Layer. *Science*, *133*(3463), 1478–1479. Retrieved 2023-07-08, from `https://www.science.org/doi/10.1126/science.133.3463.1478.b` (Publisher: American Association for the Advancement of Science) doi: 10.1126/science.133.3463.1478.b

Kasting, J. (2012). *How to Find a Habitable Planet*. Princeton University Press. Retrieved 2021-05-11, from `https://books.google.co.uk/books/about/How_to_Find_a_Habitable_Planet.html?id=xPqEeB-SRvUC&redir_esc=y`

Kasting, J. F., Whitmire, D. P., & Reynolds, R. T. (1993, January). Habitable Zones around Main Sequence Stars. *Icarus*, *101*(1), 108–128. Retrieved 2021-05-10, from `https://www.sciencedirect.com/science/article/pii/S0019103583710109` doi: 10.1006/icar.1993.1010

Kawashima, Y., & Ikoma, M. (2018, January). Theoretical Transmission Spectra of Exoplanet Atmospheres with Hydrocarbon Haze: Effect of Creation, Growth, and Settling of Haze Particles. I. Model Description and First Results. *The Astrophysical Journal*, *853*(1), 7. Retrieved 2023-04-24, from `https://dx.doi.org/10.3847/1538-4357/aaa0c5` (Publisher: The American Astronomical Society) doi: 10.3847/1538-4357/aaa0c5

Kempton, E. M.-R., Zhang, M., Bean, J. L., Steinrueck, M. E., Piette, A. A. A., Parmentier, V., . . . McGill, P. (2023, May). A reflective, metal-rich atmosphere for GJ 1214b from its JWST phase curve. *Nature*, 1–2. Retrieved 2023-05-10, from `https://www.nature.com/articles/s41586-023-06159-5` (Publisher: Nature Publishing Group) doi: 10.1038/s41586-023-06159-5

Khare, B. N., Sagan, C., Arakawa, E. T., Suits, F., Callcott, T. A., & Williams, M. W. (1984, October). Optical constants of organic tholins produced in a simulated Titanian atmosphere: From soft x-ray to microwave frequencies. *Icarus*, *60*(1), 127–137. Retrieved 2023-06-05, from `https://www.sciencedirect.com/science/article/pii/0019103584901428` doi: 10.1016/0019-1035(84)90142-8

Knutson, H. A., Benneke, B., Deming, D., & Homeier, D. (2014, January). A featureless transmission spectrum for the Neptune-mass exoplanet GJ 436b. *Nature*, *505*(7481), 66–68. Retrieved 2020-11-20, from `http://www.nature.com/articles/nature12887` doi: 10.1038/nature12887

Knutson, H. A., Charbonneau, D., Allen, L. E., Fortney, J. J., Agol, E., Cowan, N. B., ... Megeath, S. T. (2007, May). A map of the day–night contrast of the extrasolar planet HD 189733b. *Nature*, *447*(7141), 183–186. Retrieved 2021-05-11, from `https://www.nature.com/articles/nature05782` (Number: 7141 Publisher: Nature Publishing Group) doi: 10.1038/nature05782

Knutson, H. A., Charbonneau, D., Cowan, N. B., Fortney, J. J., Showman, A. P., Agol, E., ... Allen, L. E. (2008, December). Multiwavelength constraints on the day-night circulation patterns of HD 189733b. *The Astrophysical Journal*, *690*(1), 822–836. Retrieved 2021-05-11, from `https://doi.org/10.1088/0004-637x/690/1/822` (Publisher: American Astronomical Society) doi: 10.1088/0004-637X/690/1/822

Knutson, H. A., Madhusudhan, N., Cowan, N. B., Christiansen, J. L., Agol, E., Deming, D., ... Seager, S. (2011, June). A Spitzer transmission spectrum for the exoplanet GJ 436b, evidence for stellar variability, and constraints on dayside flux variations. *The Astrophysical Journal*, *735*(1), 27. Retrieved 2023-06-05, from `https://dx.doi.org/10.1088/0004-637X/735/1/27` (Publisher: The American Astronomical Society) doi: 10.1088/0004-637X/735/1/27

Koll, D. D. B., & Abbot, D. S. (2016, July). Temperature structure and atmospheric circulation of dry rocky tidally locked exoplanets. *The Astrophysical Journal*, *825*(2), 99. Retrieved 2021-02-05, from `https://doi.org/10.3847/0004-637x/825/2/99` (Publisher: American Astronomical Society) doi: 10.3847/0004-637X/825/2/99

Komacek, T. D., & Abbot, D. S. (2019, February). The Atmospheric Circulation and Climate of Terrestrial Planets Orbiting Sun-like and M Dwarf Stars over a Broad Range of Planetary Parameters. *The Astrophysical Journal*, *871*(2), 245. Retrieved 2020-10-05, from `https://doi.org/10.3847%2F1538-4357%2Faafb33` (Publisher: American Astronomical Society) doi: 10.3847/1538-4357/aafb33

Komacek, T. D., Fauchez, T. J., Wolf, E. T., & Abbot, D. S. (2020, January). Clouds will Likely Prevent the Detection of Water Vapor in $\less$i$\greater$JWST$\less$/i$\greater$ Transmission Spectra of Terrestrial Exoplanets. *The Astrophysical Journal*, *888*(2), L20. Retrieved 2022-08-12, from `https://doi.org/10.3847/2041-8213/ab6200` (Publisher: American Astronomical Society) doi: 10.3847/2041-8213/ab6200

Komacek, T. D., Showman, A. P., & Tan, X. (2017, February). Atmospheric Circulation of Hot Jupiters: Dayside–Nightside Temperature Differences. II. Comparison with Observations. *The Astrophysical Journal*, *835*(2), 198. Retrieved 2022-01-17, from `https://iopscience.iop.org/article/10.3847/1538-4357/835/2/198` doi: 10.3847/1538-4357/835/2/198

Kopparapu, R. K. (2013, March). A revised estimate of the occurrence rate of terrestrial planets in the habitable zones around Kepler M-dwarfs. *The Astrophysical Journal*, *767*(1), L8. Retrieved 2021-05-10, from `https://doi.org/10.1088/2041-8205/767/1/18` (Publisher: American Astronomical Society) doi: 10.1088/2041-8205/767/1/L8

Kopparapu, R. k., Wolf, E. T., Arney, G., Batalha, N. E., Haqq-Misra, J., Grimm, S. L., & Heng, K. (2017, August). Habitable Moist Atmospheres on Terrestrial Planets near the Inner Edge of the Habitable Zone around M Dwarfs. *The Astrophysical Journal*, *845*(1), 5. Retrieved 2020-10-14, from `https://iopscience.iop.org/article/10.3847/1538-4357/aa7cf9` doi: 10.3847/1538-4357/aa7cf9

Kopparapu, R. k., Wolf, E. T., Haqq-Misra, J., Yang, J., Kasting, J. F., Meadows, V., ... Mahadevan, S. (2016, March). The inner edge of the habitable zone for synchronously rotating planets around low-mass stars using general circulation models. *The Astrophysical Journal*, *819*(1), 84. Retrieved 2020-11-16, from `https://doi.org/10.3847%2F0004-637x%2F819%2F1%2F84` (Publisher: American Astronomical Society) doi: 10.3847/0004-637X/819/1/84

Kraucunas, I., & Hartmann, D. L. (2005, February). Equatorial Superrotation and the Factors Controlling the Zonal-Mean Zonal Winds in the Tropical Upper Troposphere. *Journal of the Atmospheric Sciences*, *62*(2), 371–389. Retrieved 2021-04-09, from `https://journals.ametsoc.org/view/journals/atsc/62/2/jas-3365.1.xml` (Publisher: American Meteorological Society Section: Journal of the Atmospheric Sciences) doi: 10.1175/JAS-3365.1

Kreidberg, L., Bean, J. L., Désert, J.-M., Benneke, B., Deming, D., Stevenson, K. B., ... Homeier, D. (2014, January). Clouds in the atmosphere of the super-Earth exoplanet GJ 1214b. *Nature*, *505*(7481), 69–72. Retrieved 2023-05-23, from `https://www.nature.com/articles/nature12888` (Number: 7481 Publisher: Nature Publishing Group) doi: 10.1038/nature12888

Krishnamurthy, V., Hirano, T., Stefánsson, G., Ninan, J. P., Mahadevan, S., Gaidos, E., ... Wisniewski, J. (2021, August). Nondetection of Helium in the Upper Atmospheres of TRAPPIST-1b, e, and f*. *The Astronomical Journal*, *162*(3), 82. Retrieved 2023-05-23, from `https://dx.doi.org/10.3847/1538-3881/ac0d57` (Publisher: The American Astronomical Society) doi: 10.3847/1538-3881/ac0d57

Kunimoto, M., & Matthews, J. M. (2020, May). Searching the Entirety of Kepler Data. II. Occurrence Rate Estimates for FGK Stars. *The Astronomical Journal*, *159*(6), 248. Retrieved 2023-05-12, from `https://dx.doi.org/10.3847/1538-3881/ab88b0` (Publisher: The American Astronomical Society) doi: 10.3847/1538-3881/ab88b0

Kuo, H. L. (1965, January). On Formation and Intensification of Tropical Cyclones Through Latent Heat Release by Cumulus Convection. *Journal of the Atmospheric Sciences*, *22*(1), 40–63. Retrieved 2023-05-30, from `https://journals.ametsoc.org/view/journals/atsc/22/1/1520-0469_1965_022_0040_ofaiot_2_0_co_2.xml` (Publisher: American Meteorological Society Section: Journal of the Atmospheric Sciences) doi: 10.1175/1520-0469(1965)022<0040:OFAIOT>2.0.CO;2

Kuo, H. L. (1974, July). Further Studies of the Parameterization of the Influence of Cumulus Convection on Large-Scale Flow. *Journal of the Atmospheric Sciences*, *31*(5), 1232–1240. Retrieved 2023-05-30, from `https://journals.ametsoc.org/view/journals/atsc/31/5/1520-0469_1974_031_1232_fsotpo_2_0_co_2.xml` (Publisher: American Meteorological Society Section: Journal of the Atmospheric Sciences) doi: 10.1175/1520-0469(1974)031<1232:FSOTPO>2.0.CO;2

Labonté, M.-P., & Merlis, T. M. (2020, June). Sensitivity of the Atmospheric Water Cycle within the Habitable Zone of a Tidally Locked, Earth-like Exoplanet. *The Astrophysical Journal*, *896*(1), 31. Retrieved 2020-10-16, from `https://iopscience.iop.org/article/10.3847/1538-4357/ab9102` doi: 10.3847/1538-4357/ab9102

Laboratory, P. H. (2023). *PHL @ UPR Arecibo - The Habitable Exoplanets Catalog.* Retrieved 2023-04-03, from `https://phl.upr.edu/projects/habitable-exoplanets-catalog`

Lacis, A. A., & Hansen, J. (1974, January). A Parameterization for the Absorption of Solar Radiation in the Earth's Atmosphere. *Journal of the Atmospheric Sciences*, *31*(1), 118–133. Retrieved 2023-05-04, from `https://journals.ametsoc.org/view/journals/atsc/31/1/1520-0469_1974_031_0118_apftao_2_0_co_2.xml` (Publisher: American Meteorological Society Section: Journal of the Atmospheric Sciences) doi: 10.1175/1520-0469(1974)031<0118:APFTAO>2.0.CO;2

Lacy, B. I., & Burrows, A. (2020, December). JWST Transit Spectra. I. Exploring Potential Biases and Opportunities in Retrievals of Tidally Locked Hot Jupiters with Clouds and Hazes. *The Astrophysical Journal*, *905*(2), 131. Retrieved 2022-06-20, from `https://iopscience.iop.org/article/10.3847/1538-4357/abc01c` doi: 10.3847/1538-4357/abc01c

Lally, M., & Vanderburg, A. (2022, March). Reassessing the Evidence for Time Variability in the Atmosphere of the Exoplanet HAT-P-7 b. *The Astronomical Journal*, *163*(4), 181. Retrieved 2022-11-17, from `https://dx.doi.org/10.3847/1538-3881/ac53a8` (Publisher: The American Astronomical Society) doi: 10.3847/1538-3881/ac53a8

Landgren, E., Nadeau, A., Lewis, N., Kataria, T., & Hitchcock, P. (2023, May). *A Shallow Water Model Exploration of Atmospheric Circulation on Sub-Neptunes: Effects of Radiative Forcing and Rotation Period.* arXiv. Retrieved 2023-06-12, from `http://arxiv.org/abs/2305.19479` (arXiv:2305.19479 [astro-ph]) doi: 10.48550/arXiv.2305.19479

Lane, T. P. (2015, January). GRAVITY WAVES | Convectively Generated Gravity Waves. In G. R. North, J. Pyle, & F. Zhang (Eds.), *Encyclopedia of Atmospheric Sciences (Second Edition)* (pp. 171–179). Oxford: Academic Press. Retrieved 2021-08-10, from `https://www.sciencedirect.com/science/article/pii/B9780123822253004898` doi: 10.1016/B978-0-12-382225-3.00489-8

Leconte, J., Forget, F., Charnay, B., Wordsworth, R., & Pottier, A. (2013, December). Increased insolation threshold for runaway greenhouse processes on Earth-like planets. *Nature*, *504*(7479), 268–271. Retrieved 2021-05-05, from `https://www.nature.com/articles/nature12827` (Number: 7479 Publisher: Nature Publishing Group) doi: 10.1038/nature12827

Lentz, W. (1990). Continued fraction calculation of spherical Bessel functions. *Computers in Physics*, *4*(4), 403–407. doi: 10.1063/1.168382

Leovy, C. B., Friedson, A. J., & Orton, G. S. (1991, December). The quasiquadrennial oscillation of Jupiter's equatorial stratosphere. *Nature*, *354*(6352), 380–382. Retrieved 2021-08-12, from `https://www.nature.com/articles/354380a0` (Bandiera_abtest: a Cg_type: Nature Research Journals Number: 6352 Primary_atype: Research Publisher: Nature Publishing Group) doi: 10.1038/354380a0

Li, Q., Palmer, P. I., Pumphrey, H. C., Bernath, P., & Mahieu, E. (2009, November). What drives the observed variability of HCN in the troposphere and lower stratosphere? *Atmospheric Chemistry and Physics*, *9*(21), 8531–8543. Retrieved 2021-11-02, from `https://acp.copernicus.org/articles/9/8531/2009/` (Publisher: Copernicus GmbH) doi: 10.5194/acp-9-8531-2009

Libby-Roberts, J. E., Berta-Thompson, Z. K., Diamond-Lowe, H., Gully-Santiago, M. A., Irwin, J. M., Kempton, E. M.-R., ... Newton, E. R. (2022, July). The Featureless HST/WFC3 Transmission Spectrum of the Rocky Exoplanet GJ 1132b: No Evidence for a Cloud-free Primordial Atmosphere and Constraints on Starspot Contamination. *The Astronomical Journal*, *164*(2), 59. Retrieved 2023-05-23, from `https://dx.doi.org/10.3847/1538-3881/ac75de` (Publisher: The American Astronomical Society) doi: 10.3847/1538-3881/ac75de

Libby-Roberts, J. E., Berta-Thompson, Z. K., Désert, J.-M., Masuda, K., Morley, C. V., Lopez, E. D., ... Winn, J. N. (2020, January). The Featureless Transmission Spectra of Two Super-puff Planets. *The Astronomical Journal*, *159*(2), 57. Retrieved 2023-05-23, from `https://dx.doi.org/10.3847/1538-3881/ab5d36` (Publisher: The American Astronomical Society) doi: 10.3847/1538-3881/ab5d36

Lim, O., Benneke, B., Doyon, R., MacDonald, R. J., Piaulet, C., Artigau, , ... Darveau-Bernier, A. (2023, September). Atmospheric Reconnaissance of TRAPPIST-1 b with JWST/NIRISS: Evidence for Strong Stellar Contamination in the Transmission Spectra. *The Astrophysical Journal Letters*, *955*(1), L22. Retrieved 2023-10-02, from `https://dx.doi.org/10.3847/2041-8213/acf7c4` (Publisher: The American Astronomical Society) doi: 10.3847/2041-8213/acf7c4

Lin, S.-J., Chao, W. C., Sud, Y. C., & Walker, G. K. (1994, July). A Class of the van Leer-type Transport Schemes and Its Application to the Moisture Transport in a General Circulation Model. *Monthly Weather Review*, *122*(7), 1575–1593. Retrieved 2022-02-16, from `https://journals.ametsoc.org/view/journals/mwre/122/7/1520-0493_1994_122_1575_acotvl_2_0_co_2.xml` (Publisher: American Meteorological Society Section: Monthly Weather Review) doi: 10.1175/1520-0493(1994)122<1575:ACOTVL>2.0.CO;2

Lin, S.-J., & Rood, R. B. (1996, September). Multidimensional Flux-Form Semi-Lagrangian Transport Schemes. *Monthly Weather Review*, *124*(9), 2046–2070. Retrieved 2022-02-16, from `https://journals.ametsoc.org/view/journals/mwre/124/9/1520-0493_1996_124_2046_mffslt_2_0_co_2.xml` (Publisher: American Meteorological Society Section: Monthly Weather Review) doi: 10.1175/1520-0493(1996)124<2046:MFFSLT>2.0.CO;2

Lin, Y.-L. (2007). *Mesoscale Dynamics*. Cambridge: Cambridge University Press. Retrieved 2021-07-22, from `https://www.cambridge.org/core/books/mesoscale-dynamics/FBBF93FD4782DBE8CC30BDDB2AE53D56` doi: 10.1017/CBO9780511619649

Lincowski, A. P., Meadows, V. S., Zieba, S., Kreidberg, L., Morley, C., Gillon, M., . . . Tamburo, P. (2023, September). Potential Atmospheric Compositions of TRAPPIST-1 c Constrained by JWST/MIRI Observations at 15 μm. *The Astrophysical Journal Letters*, *955*(1), L7. Retrieved 2023-10-02, from `https://dx.doi.org/10.3847/2041-8213/acee02` (Publisher: The American Astronomical Society) doi: 10.3847/2041-8213/acee02

Lindzen, R., & Holton, J. (1968, November). A Theory of the Quasi-Biennial Oscillation. *J. Atmos. Sci.*, *25*, 1095–1107. doi: 10.1175/1520-0469(1968)025<1095:ATOTQB>2.0.CO;2

Line, M. R., & Parmentier, V. (2016, March). The influence of nonuniform cloud cover on transit transmission spectra. *The Astrophysical Journal*, *820*(1), 78. Retrieved 2021-02-12, from `https://doi.org/10.3847/0004-637x/820/1/78` (Publisher: American Astronomical Society) doi: 10.3847/0004-637X/820/1/78

Lines, S., Manners, J., Mayne, N. J., Goyal, J., Carter, A. L., Boutle, I. A., . . . Sing, D. K. (2018, November). Exonephology: transmission spectra from a 3D simulated cloudy atmosphere of HD 209458b. *Monthly Notices of the Royal Astronomical Society*, *481*(1), 194–205. Retrieved 2021-11-15, from `https://doi.org/10.1093/mnras/sty2275` doi: 10.1093/mnras/sty2275

Louden, T., & Wheatley, P. J. (2015, November). Spatially resolved eastward winds and rotation of HD 189733b. *The Astrophysical Journal*, *814*(2), L24. Retrieved 2021-05-11, from `https://iopscience.iop.org/article/10.1088/2041-8205/814/2/L24` doi: 10.1088/2041-8205/814/2/L24

Lucarini, V., Pascale, S., Boschi, R., Kirk, E., & Iro, N. (2013). Habitability and Multistability in Earth-like Planets. *Astronomische Nachrichten*, *334*(6), 576–588. Retrieved 2020-11-16, from `https://onlinelibrary.wiley.com/doi/abs/10.1002/asna.201311903` (_eprint: https://onlinelibrary.wiley.com/doi/pdf/10.1002/asna.201311903) doi: https://doi.org/10.1002/asna.201311903

Lunkheit, F., Borth, H., Boettinger, M., Fraedrich, K., Jansen, H., Kirk, E., . . . Wan, H. (2011). *Planet Simulator Reference Manual.* University of Hamburg. Retrieved from `https://www.mi.uni-hamburg.de/en/arbeitsgruppen/theoretische-meteorologie/modelle/sources/psreferencemanual-1.pdf`

Lustig-Yaeger, J., Fu, G., May, E. M., Ceballos, K. N. O., Moran, S. E., Peacock, S., . . . Wakeford, H. R. (2023, January). *A JWST transmission spectrum of a nearby Earth-sized exoplanet.* arXiv. Retrieved 2023-06-05, from `http://arxiv.org/abs/2301.04191` (arXiv:2301.04191 [astro-ph])

Lustig-Yaeger, J., Meadows, V. S., & Lincowski, A. P. (2019, June). The Detectability and Characterization of the TRAPPIST-1 Exoplanet Atmospheres with JWST. *The Astronomical Journal*, *158*(1), 27. Retrieved 2022-10-12, from `https://doi.org/10.3847/1538-3881/ab21e0` (Publisher: American Astronomical Society) doi: 10.3847/1538-3881/ab21e0

Macdonald, E., Paradise, A., Menou, K., & Lee, C. (2022, June). Climate uncertainties caused by unknown land distribution on habitable M-Earths. *Monthly Notices of the Royal Astronomical Society*, *513*(2), 2761–2769. Retrieved 2023-05-05, from `https://doi.org/10.1093/mnras/stac1040` doi: 10.1093/mnras/stac1040

Madhusudhan, N. (2018). *Atmospheric retrieval of exoplanets*. Springer International Publishing. Retrieved 2023-05-16, from `https://www.repository.cam.ac.uk/handle/1810/316284`

Madhusudhan, N. (2019, August). Exoplanetary Atmospheres: Key Insights, Challenges and Prospects. *Annual Review of Astronomy and Astrophysics*, *57*(1), 617–663. Retrieved 2021-06-01, from `http://arxiv.org/abs/1904.03190` (arXiv: 1904.03190) doi: 10.1146/annurev-astro-081817-051846

Mak, M. T., Mayne, N. J., Sergeev, D. E., Manners, J., Eager-Nash, J. K., Arney, G., ... Kohary, K. (2023). 3D Simulations of the Archean Earth Including Photochemical Haze Profiles. *Journal of Geophysical Research: Atmospheres*, *128*(20), e2023JD039343. Retrieved 2023-10-20, from `https://onlinelibrary.wiley.com/doi/abs/10.1029/2023JD039343` (_eprint: https://onlinelibrary.wiley.com/doi/pdf/10.1029/2023JD039343) doi: 10.1029/2023JD039343

Martin, Z., Son, S.-W., Butler, A., Hendon, H., Kim, H., Sobel, A., ... Zhang, C. (2021, June). The influence of the quasi-biennial oscillation on the Madden–Julian oscillation. *Nature Reviews Earth & Environment*, 1–13. Retrieved 2021-06-21, from `https://www.nature.com/articles/s43017-021-00173-9` (Bandiera_abtest: a Cg_type: Nature Research Journals Primary_atype: Reviews Publisher: Nature Publishing Group Subject_term: Atmospheric science;Projection and prediction Subject_term_id: atmospheric-science;projection-and-prediction) doi: 10.1038/s43017-021-00173-9

Matsuno, T. (1966). Quasi-Geostrophic Motions in the Equatorial Area. *Journal of the Meteorological Society of Japan. Ser. II*, *44*(1), 25–43. Retrieved 2021-04-09, from `https://www.jstage.jst.go.jp/article/jmsj1965/44/1/44_1_25/_article` doi: 10.2151/jmsj1965.44.1_25

May, E. M., Taylor, J., Komacek, T. D., Line, M. R., & Parmentier, V. (2021, April). Water Ice Cloud Variability and Multi-epoch Transmission Spectra of TRAPPIST-1e. *The Astrophysical Journal Letters*, *911*(2), L30. Retrieved 2022-08-12, from `https://doi.org/10.3847/2041-8213/abeeff` (Publisher: American Astronomical Society) doi: 10.3847/2041-8213/abeeff

Mayne, N. J., Baraffe, I., Acreman, D. M., Smith, C., Browning, M. K., Amundsen, D. S., ... Jackson, D. R. (2014, January). The unified model, a fully-compressible, non-hydrostatic, deep atmosphere global circulation model, applied to hot Jupiters - ENDGame for a HD 209458b test case. *Astronomy & Astrophysics*, *561*, A1. Retrieved 2021-08-11, from `https://www.aanda.org/articles/aa/abs/2014/01/aa22174-13/aa22174-13.html` (Publisher: EDP Sciences) doi: 10.1051/0004-6361/201322174

Mayne, N. J., Baraffe, I., Acreman, D. M., Smith, C., Wood, N., Amundsen, D. S., ... Jackson, D. R. (2014, December). Using the UM dynamical cores to reproduce idealised 3-D flows. *Geoscientific Model Development*, *7*(6), 3059–3087. Retrieved 2021-08-11, from `https://gmd.copernicus.org/articles/7/3059/2014/` (Publisher: Copernicus GmbH) doi: 10.5194/gmd-7-3059-2014

Mayne, N. J., Debras, F., Baraffe, I., Thuburn, J., Amundsen, D. S., Acreman, D. M., ... Wood, N. (2017, August). Results from a set of three-dimensional numerical experiments of a hot Jupiter atmosphere. *Astronomy & Astrophysics*, *604*, A79. Retrieved 2022-02-24, from `http://www.aanda.org/10.1051/0004-6361/201730465` doi: 10.1051/0004-6361/201730465

Merlis, T. M., & Schneider, T. (2010). Atmospheric Dynamics of Earth-Like Tidally Locked Aquaplanets. *Journal of Advances in Modeling Earth Systems*, *2*(4). Retrieved 2020-10-31, from `https://agupubs.onlinelibrary.wiley.com/doi/abs/10.3894/JAMES.2010.2.13` (_eprint: https://agupubs.onlinelibrary.wiley.com/doi/pdf/10.3894/JAMES.2010.2.13) doi: 10.3894/JAMES.2010.2.13

MetOffice. (2010). *Iris: A Python package for analysing and visualising meteorological and oceanographic data sets.* Retrieved from `https://scitools-iris.readthedocs.io/en/stable/`

Mie, G. (1908). Beiträge zur Optik trüber Medien, speziell kolloidaler Metallösungen. *Annalen der Physik*, *330*(3), 377–445. Retrieved 2023-05-19, from `https://onlinelibrary.wiley.com/doi/abs/10.1002/andp.19083300302` (_eprint: https://onlinelibrary.wiley.com/doi/pdf/10.1002/andp.19083300302) doi: 10.1002/andp.19083300302

Mikal-Evans, T., Sing, D. K., Barstow, J. K., Kataria, T., Goyal, J., Lewis, N., ... Spake, J. J. (2022, February). Diurnal variations in the stratosphere of the ultrahot giant exoplanet WASP-121b. *Nature Astronomy*, 1–9. Retrieved 2022-02-22, from `https://www.nature.com/articles/s41550-021-01592-w` (Publisher: Nature Publishing Group) doi: 10.1038/s41550-021-01592-w

Mitchell, J. L., & Vallis, G. K. (2010). The transition to superrotation in terrestrial atmospheres. *Journal of Geophysical Research: Planets*, *115*(E12). Retrieved 2021-05-11, from `https://agupubs.onlinelibrary.wiley.com/doi/abs/10.1029/2010JE003587` (_eprint: https://agupubs.onlinelibrary.wiley.com/doi/pdf/10.1029/2010JE003587) doi: https://doi.org/10.1029/2010JE003587

Mollière, P., Boekel, R. v., Bouwman, J., Henning, T., Lagage, P.-O., & Min, M. (2017, April). Observing transiting planets with JWST - Prime targets and their synthetic spectral observations. *Astronomy & Astrophysics*, *600*, A10. Retrieved 2020-10-05, from `https://www.aanda.org/articles/aa/abs/2017/04/aa29800-16/aa29800-16.html` (Publisher: EDP Sciences) doi: 10.1051/0004-6361/201629800

Moran, S. E. (2018). Limits on Clouds and Hazes for the TRAPPIST-1 Planets. *The Astronomical Journal*, 11.

Moran, S. E., Hörst, S. M., Vuitton, V., He, C., Lewis, N. K., Flandinet, L., ... Valenti, J. A. (2020, May). Chemistry of Temperate Super-Earth and Mini-Neptune Atmospheric Hazes from Laboratory Experiments. *The Planetary Science Journal*, *1*(1), 17. Retrieved 2023-09-27, from `https://iopscience.iop.org/article/10.3847/PSJ/ab8eae/meta` (Publisher: IOP Publishing) doi: 10.3847/PSJ/ab8eae

Moran, S. E., Stevenson, K. B., Sing, D. K., MacDonald, R. J., Kirk, J., Lustig-Yaeger, J., ... Wakeford, H. R. (2023, May). High Tide or Riptide on the Cosmic Shoreline? A Water-rich Atmosphere or Stellar Contamination for the Warm Super-Earth GJ 486b from JWST Observations. *The Astrophysical Journal Letters*, *948*(1), L11. Retrieved 2023-06-05, from `https://dx.doi.org/10.3847/2041-8213/accb9c` (Publisher: The American Astronomical Society) doi: 10.3847/2041-8213/accb9c

Morley, C. V., Kreidberg, L., Rustamkulov, Z., Robinson, T., & Fortney, J. J. (2017, November). Observing the Atmospheres of Known Temperate Earth-sized Planets withJWST. *The Astrophysical Journal*, *850*(2), 121. Retrieved 2020-11-26, from `https://doi.org/10.3847%2F1538-4357%2Faa927b` (Publisher: American Astronomical Society) doi: 10.3847/1538-4357/aa927b

Nappo, C. J. (2012, January). Ducted Gravity Waves. In C. J. Nappo (Ed.), *International Geophysics* (Vol. 102, pp. 87–116). Academic Press. Retrieved 2021-09-06, from `https://www.sciencedirect.com/science/article/pii/B9780123852236000045` doi: 10.1016/B978-0-12-385223-6.00004-5

Noda, S., Ishiwatari, M., Nakajima, K., Takahashi, Y. O., Takehiro, S., Onishi, M., ... Hayashi, Y. Y. (2017, January). The circulation pattern and day-night heat transport in the atmosphere of a synchronously rotating aquaplanet: Dependence on planetary rotation rate. *Icarus*, *282*, 1–18. Retrieved 2022-06-21, from `https://www.sciencedirect.com/science/article/pii/S0019103516305668` doi: 10.1016/j.icarus.2016.09.004

Ohno, K., & Kawashima, Y. (2020, June). Super-Rayleigh Slopes in Transmission Spectra of Exoplanets Generated by Photochemical Haze. *The Astrophysical Journal Letters*, *895*(2), L47. Retrieved 2020-11-18, from `https://iopscience.iop.org/article/10.3847/2041-8213/ab93d7/meta` (Publisher: IOP Publishing) doi: 10.3847/2041-8213/ab93d7

Orton, G. S., Friedson, A. J., Baines, K. H., Martin, T. Z., West, R. A., Caldwell, J., ... Shure, M. (1991, April). Thermal Maps of Jupiter: Spatial Organization and Time Dependence of Stratospheric Temperatures, 1980 to 1990. *Science*, *252*(5005), 537–542. Retrieved 2021-08-12, from `https://science.sciencemag.org/content/252/5005/537` (Publisher: American Association for the Advancement of Science Section: Research Articles) doi: 10.1126/science.252.5005.537

Paradise, A., Macdonald, E., Menou, K., Lee, C., & Fan, B. L. (2022, April). ExoPlaSim: Extending the Planet Simulator for exoplanets. *Monthly Notices of the Royal Astronomical Society*, *511*(3), 3272–3303. Retrieved 2023-05-30, from `https://doi.org/10.1093/mnras/stac172` doi: 10.1093/mnras/stac172

Paradise, A., & Menou, K. (2017, October). GCM Simulations of Unstable Climates in the Habitable Zone. *The Astrophysical Journal*, *848*(1), 33. Retrieved 2021-11-17, from `https://doi.org/10.3847/1538-4357/aa8b1c` (Publisher: American Astronomical Society) doi: 10.3847/1538-4357/aa8b1c

Paradise, A., Menou, K., Valencia, D., & Lee, C. (2019). Habitable Snowballs: Temperate Land Conditions, Liquid Water, and Implications for CO2 Weathering. *Journal of Geophysical Research: Planets*, *124*(8), 2087–2100. Retrieved 2021-11-17, from `https://onlinelibrary.wiley.com/doi/abs/10.1029/2019JE005917` (_eprint: https://onlinelibrary.wiley.com/doi/pdf/10.1029/2019JE005917) doi: 10.1029/2019JE005917

Parmentier, V., Showman, A. P., & Lian, Y. (2013, October). 3D mixing in hot Jupiters atmospheres - I. Application to the day/night cold trap in HD 209458b. *Astronomy & Astrophysics*, *558*, A91. Retrieved 2023-04-28, from `https://www.aanda.org/articles/aa/abs/2013/10/aa21132-13/aa21132-13.html` (Publisher: EDP Sciences) doi: 10.1051/0004-6361/201321132

Perryman, M. (2018). *The Exoplanet Handbook* (2nd ed.). Cambridge: Cambridge University Press. Retrieved 2021-05-10, from `https://www.cambridge.org/core/books/exoplanet-handbook/750759E015FDCF469D141F0046198519` doi: 10.1017/9781108304160

Petigura, E. A., Howard, A. W., & Marcy, G. W. (2013, November). Prevalence of Earth-size planets orbiting Sun-like stars. *Proceedings of the National Academy of Sciences*. Retrieved 2021-05-10, from `https://www.pnas.org/content/early/2013/10/31/1319909110` (Publisher: National Academy of Sciences Section: Physical Sciences) doi: 10.1073/pnas.1319909110

Piani, C., Durran, D., Alexander, M. J., & Holton, J. R. (2000, November). A Numerical Study of Three-Dimensional Gravity Waves Triggered by Deep Tropical Convection and Their Role in the Dynamics of the QBO. *Journal of the Atmospheric Sciences*, *57*(22), 3689–3702. Retrieved 2022-01-29, from `https://journals.ametsoc.org/view/journals/atsc/57/22/1520-0469_2000_057_3689_ansotd_2.0.co_2.xml` (Publisher: American Meteorological Society Section: Journal of the Atmospheric Sciences) doi: 10.1175/1520-0469(2000)057<3689:ANSOTD>2.0.CO;2

Pierrehumbert, R. T., & Hammond, M. (2019). Atmospheric Circulation of Tide-Locked Exoplanets. *Annual Review of Fluid Mechanics*, *51*(1), 275–303. Retrieved 2020-12-09, from `https://doi.org/10.1146/annurev-fluid-010518-040516` (_eprint: https://doi.org/10.1146/annurev-fluid-010518-040516) doi: 10.1146/annurev-fluid-010518-040516

Pitteway, M. L. V., & Hines, C. O. (1965, December). The reflection and ducting of atmospheric acoustic–gravity waves. *Canadian Journal of Physics*, *43*(12), 2222–2243. Retrieved 2021-09-06, from `https://cdnsciencepub.com/doi/10.1139/p65-217` (Publisher: NRC Research Press) doi: 10.1139/p65-217

Plougonven, R., & Zhang, F. (2014). Internal gravity waves from atmospheric jets and fronts. *Reviews of Geophysics*, *52*(1), 33–76. Retrieved 2021-07-08, from `https://agupubs.onlinelibrary.wiley.com/doi/abs/10.1002/2012RG000419` (_eprint: https://agupubs.onlinelibrary.wiley.com/doi/pdf/10.1002/2012RG000419) doi: 10.1002/2012RG000419

Plumb, R. A. (1977, December). The Interaction of Two Internal Waves with the Mean Flow: Implications for the Theory of the Quasi-Biennial Oscillation. *Journal of the Atmospheric Sciences*, *34*(12), 1847–1858. Retrieved 2021-03-15, from `https://journals.ametsoc.org/view/journals/atsc/34/12/1520-0469_1977_034_1847_tiotiw_2_0_co_2.xml` (Publisher: American Meteorological Society Section: Journal of the Atmospheric Sciences) doi: 10.1175/1520-0469(1977)034<1847:TIOTIW>2.0.CO;2

Plumb, R. A., & McEwan, A. D. (1978, October). The Instability of a Forced Standing Wave in a Viscous Stratified Fluid: A Laboratory Analogue of .the Quasi-Biennial Oscillation. *Journal of the Atmospheric Sciences*, *35*(10), 1827–1839. Retrieved 2021-03-19, from `https://journals.ametsoc.org/view/journals/atsc/35/10/1520-0469_1978_035_1827_tioafs_2_0_co_2.xml` (Publisher: American Meteorological Society Section: Journal of the Atmospheric Sciences) doi: 10.1175/1520-0469(1978)035<1827:TIOAFS>2.0.CO;2

Pont, F., Knutson, H., Gilliland, R. L., Moutou, C., & Charbonneau, D. (2008, March). Detection of atmospheric haze on an extrasolar planet: the 0.55–1.05 µm transmission spectrum of HD 189733b with the Hubble Space Telescope. *Monthly Notices of the Royal Astronomical Society*, *385*(1), 109–118. Retrieved 2023-05-23, from `https://doi.org/10.1111/j.1365-2966.2008.12852.x` doi: 10.1111/j.1365-2966.2008.12852.x

Popp, M., Schmidt, H., & Marotzke, J. (2016, February). Transition to a Moist Greenhouse with CO 2 and solar forcing. *Nature Communications*, *7*(1), 10627. Retrieved 2020-11-16, from `https://www.nature.com/articles/ncomms10627` (Number: 1 Publisher: Nature Publishing Group) doi: 10.1038/ncomms10627

Powell, D., Louden, T., Kreidberg, L., Zhang, X., Gao, P., & Parmentier, V. (2019, December). Transit Signatures of Inhomogeneous Clouds on Hot Jupiters: Insights from Microphysical Cloud Modeling. *Astrophysical Journal*, *887*(2), 170. (Place: Bristol Publisher: Iop Publishing Ltd WOS:000506012000064) doi: 10.3847/1538-4357/ab55d9

Prahl, S. (2023, May). *miepython.* Zenodo. Retrieved 2023-06-05, from `https://zenodo.org/record/7949403` doi: 10.5281/zenodo.7949403

Quintana, E. V., Barclay, T., Raymond, S. N., Rowe, J. F., Bolmont, E., Caldwell, D. A., ... Selsis, F. (2014, April). An Earth-Sized Planet in the Habitable Zone of a Cool Star. *Science*, *344*(6181), 277–280. Retrieved 2021-06-06, from `https://www.sciencemag.org/lookup/doi/10.1126/science.1249403` doi: 10.1126/science.1249403

Rajpurohit, A. S., Reylé, C., Allard, F., Homeier, D., Schultheis, M., Bessell, M. S., & Robin, A. C. (2013, August). The effective temperature scale of M dwarfs. *Astronomy & Astrophysics*, *556*, A15. Retrieved 2023-03-21, from `https://www.aanda.org/articles/aa/abs/2013/08/aa21346-13/aa21346-13.html` (Publisher: EDP Sciences) doi: 10.1051/0004-6361/201321346

Randel, W. J., Wu, F., Russell, J. M., Roche, A., & Waters, J. W. (1998, January). Seasonal Cycles and QBO Variations in Stratospheric CH4 and H2O Observed in UARS HALOE Data. *Journal of the Atmospheric Sciences*, *55*(2), 163–185. Retrieved 2021-09-06, from `https://journals.ametsoc.org/view/journals/atsc/55/2/1520-0469_1998_055_0163_scaqvi_2.0.co_2.xml` (Publisher: American Meteorological Society Section: Journal of the Atmospheric Sciences) doi: 10.1175/1520-0469(1998)055<0163:SCAQVI>2.0.CO;2

Rauscher, E., Menou, K., Seager, S., Deming, D., Cho, J. Y.-K., & Hansen, B. M. S. (2007, August). Toward Eclipse Mapping of Hot Jupiters. *The Astrophysical Journal*, *664*(2), 1199. Retrieved 2023-08-08, from `https://iopscience.iop.org/article/10.1086/519213/meta` (Publisher: IOP Publishing) doi: 10.1086/519213

Read, P. L., & Lebonnois, S. (2018, May). Superrotation on Venus, on Titan, and Elsewhere. *Annual Review of Earth and Planetary Sciences*, *46*(1), 175–202. Retrieved 2020-10-02, from `https://www-annualreviews-org.ezproxy.is.ed.ac.uk/doi/10.1146/annurev-earth-082517-010137` (Publisher: Annual Reviews) doi: 10.1146/annurev-earth-082517-010137

Ridgway, R. J., Zamyatina, M., Mayne, N. J., Manners, J., Lambert, F. H., Braam, M., ... Kohary, K. (2023, January). 3D modelling of the impact of stellar activity on tidally locked terrestrial exoplanets: atmospheric composition and habitability. *Monthly Notices of the Royal Astronomical Society*, *518*(2), 2472–2496. Retrieved 2023-03-20, from `https://doi.org/10.1093/mnras/stac3105` doi: 10.1093/mnras/stac3105

Rosner, D. E. (1986). *Transport processes in chemically reacting flow systems*. Butterworth-Heinemann. Retrieved 2023-06-05, from `https://www.sciencedirect.com/book/9780409951783/transport-processes-in-chemically-reacting-flow-systems?via=ihub=`

Rushby, A. J., Johnson, M., Mills, B. J. W., Watson, A. J., & Claire, M. W. (2018, May). Long-Term Planetary Habitability and the Carbonate-Silicate Cycle. *Astrobiology*, *18*(5), 469–480. (Place: New Rochelle Publisher: Mary Ann Liebert, Inc WOS:000432861500001) doi: 10.1089/ast.2017.1693

Sardeshmukh, P. D., & Hoskins, B. J. (1988, April). The Generation of Global Rotational Flow by Steady Idealized Tropical Divergence. *Journal of Atmospheric Sciences*, *45*, 1228–1251. Retrieved 2023-02-20, from `https://ui.adsabs.harvard.edu/abs/1988JAtS...45.1228S` (ADS Bibcode: 1988JAtS...45.1228S) doi: 10.1175/1520-0469(1988)045<1228:TGOGRF>2.0.CO;2

Scaife, A. A., Butchart, N., Warner, C. D., Stainforth, D., Norton, W., & Austin, J. (2000). Realistic quasi-biennial oscillations in a simulation of the global climate. *Geophysical Research Letters*, *27*(21), 3481–3484. Retrieved 2021-03-15, from `https://agupubs.onlinelibrary.wiley.com/doi/abs/10.1029/2000GL011625` (_eprint: https://agupubs.onlinelibrary.wiley.com/doi/pdf/10.1029/2000GL011625) doi: https://doi.org/10.1029/2000GL011625

Scaife, A. A., Butchart, N., Warner, C. D., & Swinbank, R. (2002, May). Impact of a Spectral Gravity Wave Parameterization on the Stratosphere in the Met Office Unified Model. *Journal of the Atmospheric Sciences*, *59*(9), 1473–1489. Retrieved 2021-03-15, from `https://journals.ametsoc.org/view/journals/atsc/59/9/1520-0469_2002_059_1473_ioasgw_2.0.co_2.xml` (Publisher: American Meteorological Society Section: Journal of the Atmospheric Sciences) doi: 10.1175/1520-0469(2002)059<1473:IOASGW>2.0.CO;2

Scalo, J., Kaltenegger, L., Segura, A., Fridlund, M., Ribas, I., Kulikov, Y. N., … Lammer, H. (2007, February). M Stars as Targets for Terrestrial Exoplanet Searches And Biosignature Detection. *Astrobiology*, *7*(1), 85–166. Retrieved 2020-10-14, from `https://www.liebertpub.com/doi/abs/10.1089/ast.2006.0125` (Publisher: Mary Ann Liebert, Inc., publishers) doi: 10.1089/ast.2006.0125

Schenzinger, V., Osprey, S., Gray, L., & Butchart, N. (2017, June). Defining metrics of the Quasi-Biennial Oscillation in global climate models. *Geoscientific Model Development*, *10*(6), 2157–2168. Retrieved 2021-07-30, from `https://gmd.copernicus.org/articles/10/2157/2017/` doi: 10.5194/gmd-10-2157-2017

Schwieterman, E. W., Kiang, N. Y., Parenteau, M. N., Harman, C. E., DasSarma, S., Fisher, T. M., … Lyons, T. W. (2018, June). Exoplanet Biosignatures: A Review of Remotely Detectable Signs of Life. *Astrobiology*, *18*(6), 663–708. Retrieved 2022-05-02, from `https://www.ncbi.nlm.nih.gov/pmc/articles/PMC6016574/` doi: 10.1089/ast.2017.1729

Sebastian, D., Pedersen, P. P., Murray, C. A., Ducrot, E., Garcia, L. J., Burdanov, A., . . . Thompson, S. (2020). Development of the SPECULOOS exoplanet search project. *Proceedings of SPIE - The International Society for Optical Engineering*, *11445*(Ground-based and Airborne Telescopes VIII). Retrieved 2023-05-16, from `https://www.repository.cam.ac.uk/handle/1810/325227` (Publisher: SPIE) doi: 10.1117/12.2563563

Seeley, J. T., & Wordsworth, R. D. (2021, November). Episodic deluges in simulated hothouse climates. *Nature*, *599*(7883), 74–79. Retrieved 2021-11-08, from `https://www.nature.com/articles/s41586-021-03919-z` (Bandiera_abtest: a Cg_type: Nature Research Journals Number: 7883 Primary_atype: Research Publisher: Nature Publishing Group Subject_term: Atmospheric dynamics;Climate and Earth system modelling;Phase transitions and critical phenomena Subject_term_id: atmospheric-dynamics;climate-and-earth-system-modelling;phase-transitions-and-critical-phenomena) doi: 10.1038/s41586-021-03919-z

Sergeev, D. E., Fauchez, T. J., Turbet, M., Boutle, I. A., Tsigaridis, K., Way, M. J., . . . Mayne, N. J. (2022, September). The TRAPPIST-1 Habitable Atmosphere Intercomparison (THAI). II. Moist Cases—The Two Waterworlds. *The Planetary Science Journal*, *3*(9), 212. Retrieved 2022-11-17, from `https://iopscience.iop.org/article/10.3847/PSJ/ac6cf2/meta` (Publisher: IOP Publishing) doi: 10.3847/PSJ/ac6cf2

Sergeev, D. E., Lambert, F. H., Mayne, N. J., Boutle, I. A., Manners, J., & Kohary, K. (2020, May). Atmospheric Convection Plays a Key Role in the Climate of Tidally Locked Terrestrial Exoplanets: Insights from High-resolution Simulations. *Astrophysical Journal*, *894*(2), 84. (Place: Bristol Publisher: Iop Publishing Ltd WOS:000533292900001) doi: 10.3847/1538-4357/ab8882

Sergeev, D. E., Lewis, N. T., Lambert, F. H., Mayne, N. J., Boutle, I. A., Manners, J., & Kohary, K. (2022, September). Bistability of the Atmospheric Circulation on TRAPPIST-1e. *The Planetary Science Journal*, *3*(9), 214. Retrieved 2022-10-12, from `https://iopscience.iop.org/article/10.3847/PSJ/ac83be/meta` (Publisher: IOP Publishing) doi: 10.3847/PSJ/ac83be

Showman, A., Cho, J., & Menou, K. (2010). Atmospheric Circulation of Exoplanets. In *Exoplanets.* Tucson, Arizona: University of Arizona Press. Retrieved 2023-05-24, from `https://www.semanticscholar.org/paper/Atmospheric-Circulation-of-Exoplanets-Showman-Cho/760a66fdf3ad5ef417e051aa617c90f44229e2d8`

Showman, A. P., & Polvani, L. M. (2010). The Matsuno-Gill model and equatorial superrotation. *Geophysical Research Letters*, *37*(18). Retrieved 2021-04-09, from `https://agupubs.onlinelibrary.wiley.com/doi/abs/10.1029/2010GL044343` (_eprint: https://agupubs.onlinelibrary.wiley.com/doi/pdf/10.1029/2010GL044343) doi: https://doi.org/10.1029/2010GL044343

Showman, A. P., & Polvani, L. M. (2011, August). Equatorial superrotation on tidally locked exoplanets. *The Astrophysical Journal*, *738*(1), 71. Retrieved 2020-10-02, from `https://doi.org/10.1088%2F0004-637x%2F738%2F1%2F71` (Publisher: IOP Publishing) doi: 10.1088/0004-637X/738/1/71

Showman, A. P., Tan, X., & Zhang, X. (2019, September). Atmospheric Circulation of Brown Dwarfs and Jupiter and Saturn-like Planets: Zonal Jets, Long-term Variability, and QBO-type Oscillations. *The Astrophysical Journal*, *883*(1), 4. Retrieved 2021-09-17, from `http://arxiv.org/abs/1807.08433` (arXiv: 1807.08433) doi: 10.3847/1538-4357/ab384a

Showman, A. P., Wordsworth, R. D., Merlis, T. M., & Kaspi, Y. (2013). Atmospheric Circulation of Terrestrial Exoplanets. In *Comparative Climatology of Terrestrial Planets* (pp. 277–329). University of Arizona Press. Retrieved from `https://arxiv.org/pdf/1306.2418.pdf`

Skinner, J. W., & Cho, J. Y.-K. (2022, April). Modons on tidally synchronized extrasolar planets. *Monthly Notices of the Royal Astronomical Society*, *511*(3), 3584–3601. Retrieved 2022-11-17, from `https://doi.org/10.1093/mnras/stab2809` doi: 10.1093/mnras/stab2809

Song, X., & Yang, J. (2021). Asymmetry and Variability in the Transmission Spectra of Tidally Locked Habitable Planets. *Frontiers in Astronomy and Space Sciences*, *8*. Retrieved 2022-11-22, from `https://www.frontiersin.org/articles/10.3389/fspas.2021.708023`

Steinrueck, M. E., Koskinen, T., Lavvas, P., Parmentier, V., Zieba, S., Tan, X., … Kreidberg, L. (2023, July). Photochemical Hazes Dramatically Alter Temperature Structure and Atmospheric Circulation in 3D Simulations of Hot Jupiters. *The Astrophysical Journal*, *951*(2), 117. Retrieved 2023-07-13, from `https://dx.doi.org/10.3847/1538-4357/acd4bb` (Publisher: The American Astronomical Society) doi: 10.3847/1538-4357/acd4bb

Steinrueck, M. E., Showman, A. P., Lavvas, P., Koskinen, T., Tan, X., & Zhang, X. (2021, June). 3D simulations of photochemical hazes in the atmosphere of hot Jupiter HD 189733b. *Monthly Notices of the Royal Astronomical Society*, *504*(2), 2783–2799. Retrieved 2023-04-28, from `https://doi.org/10.1093/mnras/stab1053` doi: 10.1093/mnras/stab1053

Stephens, G. L. (1978, November). Radiation Profiles in Extended Water Clouds. I: Theory. *Journal of the Atmospheric Sciences*, *35*(11), 2111–2122. Retrieved 2023-05-04, from `https://journals.ametsoc.org/view/journals/atsc/35/11/1520-0469_1978_035_2111_rpiewc_2_0_co_2.xml` (Publisher: American Meteorological Society Section: Journal of the Atmospheric Sciences) doi: 10.1175/1520-0469(1978)035<2111:RPIEWC>2.0.CO;2

Stephens, G. L. (1984, April). The Parameterization of Radiation for Numerical Weather Prediction and Climate Models. *Monthly Weather Review*, *112*(4), 826–867. Retrieved 2023-05-04, from `https://journals.ametsoc.org/view/journals/mwre/112/4/1520-0493_1984_112_0826_tporfn_2_0_co_2.xml` (Publisher: American Meteorological Society Section: Monthly Weather Review) doi: 10.1175/1520-0493(1984)112<0826:TPORFN>2.0.CO;2

Sugimoto, N., Fujisawa, Y., Kashimura, H., Noguchi, K., Kuroda, T., Takagi, M., & Hayashi, Y.-Y. (2021, June). Generation of gravity waves from thermal tides in the Venus atmosphere. *Nature Communications*, *12*(1), 3682. Retrieved 2021-07-05, from `https://www.nature.com/articles/s41467-021-24002-1` (Bandiera_abtest: a Cc_license_type: cc_by Cg_type: Nature Research Journals Number: 1 Primary_atype: Research Publisher: Nature Publishing Group Subject_term: Atmospheric dynamics;Computational science Subject_term_id: atmospheric-dynamics;computational-science) doi: 10.1038/s41467-021-24002-1

Suissa, G., Mandell, A. M., Wolf, E. T., Villanueva, G. L., Fauchez, T., & Kopparapu, R. k. (2020, March). Dim Prospects for Transmission Spectra of Ocean Earths around M Stars. *The Astrophysical Journal*, *891*(1), 58. Retrieved 2020-10-14, from `https://iopscience.iop.org/article/10.3847/1538-4357/ab72f9` doi: 10.3847/1538-4357/ab72f9

Tan, X., & Komacek, T. D. (2019, November). The Atmospheric Circulation of Ultra-hot Jupiters. *The Astrophysical Journal*, *886*(1), 26. Retrieved 2023-01-26, from `https://dx.doi.org/10.3847/1538-4357/ab4a76` (Publisher: The American Astronomical Society) doi: 10.3847/1538-4357/ab4a76

Tarter, J. C., Backus, P. R., Mancinelli, R. L., Aurnou, J. M., Backman, D. E., Basri, G. S., ... Young, R. E. (2007, April). A Reappraisal of The Habitability of Planets around M Dwarf Stars. *Astrobiology*, *7*(1), 30–65. Retrieved 2020-11-02, from `https://www.liebertpub.com/doi/abs/10.1089/ast.2006.0124` (Publisher: Mary Ann Liebert, Inc. 2 Madison Avenue Larchmont, NY 10538 USA) doi: 10.1089/ast.2006.0124

Tegtmeier, S., Anstey, J., Davis, S., Ivanciu, I., Jia, Y., McPhee, D., & Kedzierski, R. P. (2020). Zonal Asymmetry of the QBO Temperature Signal in the Tropical Tropopause Region. *Geophysical Research Letters*, *47*(24), e2020GL089533. Retrieved 2021-09-06, from `https://agupubs.onlinelibrary.wiley.com/doi/abs/10.1029/2020GL089533` (_eprint: https://agupubs.onlinelibrary.wiley.com/doi/pdf/10.1029/2020GL089533) doi: 10.1029/2020GL089533

Tiedtke, M. (1983). The sensitivity of the time-mean large-scale flow to cumulus convection in the ECMWF model. In *Workshop on Convection in Large-scale Numerical Models, 28 November to 1 December 1983.* Reading: ECMWF.

Tilley, M. A., Segura, A., Meadows, V., Hawley, S., & Davenport, J. (2018, August). Modeling Repeated M Dwarf Flaring at an Earth-like Planet in the Habitable Zone: Atmospheric Effects for an Unmagnetized Planet. *Astrobiology*, *19*(1), 64–86. Retrieved 2020-09-28, from `https://www.liebertpub.com/doi/10.1089/ast.2017.1794` (Publisher: Mary Ann Liebert, Inc., publishers) doi: 10.1089/ast.2017.1794

Tinetti, G., Deroo, P., Swain, M. R., Griffith, C. A., Vasisht, G., Brown, L. R., ... McCullough, P. (2010, April). Probing the terminator region of the hot Jupiter XO-1b with transmission spectroscopy. *The Astrophysical Journal*, *712*(2), L139–L142. Retrieved 2021-05-13, from `https://iopscience.iop.org/article/10.1088/2041-8205/712/2/L139` doi: 10.1088/2041-8205/712/2/L139

Tinetti, G., Drossart, P., Eccleston, P., Hartogh, P., Heske, A., Leconte, J., ... Zwart, F. (2018, November). A chemical survey of exoplanets with ARIEL. *Experimental Astronomy*, *46*(1), 135–209. (Place: Dordrecht Publisher: Springer WOS:000450662900006) doi: 10.1007/s10686-018-9598-x

Trainer, M. G., Pavlov, A. A., Curtis, D. B., Mckay, C. P., Worsnop, D. R., Delia, A. E., ... Tolbert, D. M. A. (2004, December). Haze Aerosols in the Atmosphere of Early Earth: Manna from Heaven. *Astrobiology*, *4*(4), 409–419. Retrieved 2020-11-11, from `https://www.liebertpub.com/doi/abs/10.1089/ast.2004.4.409` (Publisher: Mary Ann Liebert, Inc. 2 Madison Avenue Larchmont, NY 10538 USA) doi: 10.1089/ast.2004.4.409

Tsai, S.-M., Dobbs-Dixon, I., & Gu, P.-G. (2014, September). Three-dimensional structures of equatorial waves and the resulting super-rotation in the atmosphere of a tidally locked hot Jupiter. *The Astrophysical Journal*, *793*(2), 141. Retrieved 2021-03-31, from `https://doi.org/10.1088/0004-637x/793/2/141` (Publisher: American Astronomical Society) doi: 10.1088/0004-637X/793/2/141

Tsiaras, A., Rocchetto, M., Waldmann, I. P., Venot, O., Varley, R., Morello, G., … Tennyson, J. (2016, March). DETECTION OF AN ATMOSPHERE AROUND THE SUPER-EARTH 55 CANCRI E. *The Astrophysical Journal*, *820*(2), 99. Retrieved 2021-05-13, from `https://doi.org/10.3847/0004-637x/820/2/99` (Publisher: American Astronomical Society) doi: 10.3847/0004-637X/820/2/99

Turbet, M., Fauchez, T. J., Sergeev, D. E., Boutle, I. A., Tsigaridis, K., Way, M. J., … Sohl, L. (2022, September). The TRAPPIST-1 Habitable Atmosphere Intercomparison (THAI). I. Dry Cases—The Fellowship of the GCMs. *The Planetary Science Journal*, *3*(9), 211. Retrieved 2022-11-17, from `https://iopscience.iop.org/article/10.3847/PSJ/ac6cf0/meta` (Publisher: IOP Publishing) doi: 10.3847/PSJ/ac6cf0

Turbet, M., Leconte, J., Selsis, F., Bolmont, E., Forget, F., Ribas, I., … Anglada-Escude, G. (2016, December). The habitability of Proxima Centauri b II. Possible climates and observability. *Astronomy & Astrophysics*, *596*, A112. (Place: Les Ulis Cedex A Publisher: Edp Sciences S A WOS:000390797900110) doi: 10.1051/0004-6361/201629577

Turbet, M., & Selsis, F. (2021, April). Main ways in which stars influence the climate and surface habitability of their planets. *arXiv:2104.06391 [astro-ph]*. Retrieved 2021-04-14, from `http://arxiv.org/abs/2104.06391` (arXiv: 2104.06391)

Vallis, G. K. (2017). *Atmospheric and Oceanic Fluid Dynamics: Fundamentals and Large-Scale Circulation* (2nd ed.). Cambridge: Cambridge University Press. Retrieved 2021-05-04, from `https://www.cambridge.org/core/books/atmospheric-and-oceanic-fluid-dynamics/41379BDDC4257CBE11143C466F6428A4` doi: 10.1017/9781107588417

Vanderburg, A., Rowden, P., Bryson, S., Coughlin, J., Batalha, N., Collins, K. A., … Quinn, S. N. (2020, April). A Habitable-zone Earth-sized Planet Rescued from False Positive Status. *The Astrophysical Journal Letters*, *893*(1), L27. Retrieved 2023-10-02, from `https://dx.doi.org/10.3847/2041-8213/ab84e5` (Publisher: The American Astronomical Society) doi: 10.3847/2041-8213/ab84e5

Venot, O., Drummond, B., Miguel, Y., Waldmann, I. P., Pascale, E., & Zingales, T. (2018, November). A better characterization of the chemical composition of exoplanets atmospheres with ARIEL. *Experimental Astronomy*, *46*(1), 101–134. Retrieved 2020-10-05, from `https://doi.org/10.1007/s10686-018-9597-y` doi: 10.1007/s10686-018-9597-y

Vida, K., Olah, K., Kovari, Z., van Driel-Gesztelyi, L., Moor, A., & Pal, A. (2019, October). Flaring Activity of Proxima Centauri from TESS Observations: Quasiperiodic Oscillations during Flare Decay and Inferences on the Habitability of Proxima b. *Astrophysical Journal*, *884*(2), 160. (Place: Bristol Publisher: Iop Publishing Ltd WOS:000501817800002) doi: 10.3847/1538-4357/ab41f5

Villanueva, G. L., Smith, M. D., Protopapa, S., Faggi, S., & Mandell, A. M. (2018, September). Planetary Spectrum Generator: An accurate online radiative transfer suite for atmospheres, comets, small bodies and exoplanets. *Journal of Quantitative Spectroscopy and Radiative Transfer*, *217*, 86–104. Retrieved 2021-09-10, from `https://www.sciencedirect.com/science/article/pii/S0022407318301572` doi: 10.1016/j.jqsrt.2018.05.023

Wakeford, H. R., Sing, D. K., Deming, D., Lewis, N. K., Goyal, J., Wilson, T. J., … Mandell, A. M. (2017, December). The Complete Transmission Spectrum of WASP-39b with a Precise Water Constraint. *The Astronomical Journal*, *155*(1), 29. Retrieved 2023-07-08, from `https://dx.doi.org/10.3847/1538-3881/aa9e4e` (Publisher: The American Astronomical Society) doi: 10.3847/1538-3881/aa9e4e

Walters, D., Baran, A. J., Boutle, I., Brooks, M., Earnshaw, P., Edwards, J., … Zerroukat, M. (2019, May). The Met Office Unified Model Global Atmosphere 7.0/7.1 and JULES Global Land 7.0 configurations. *Geoscientific Model Development*, *12*(5), 1909–1963. Retrieved 2021-11-15, from `https://gmd.copernicus.org/articles/12/1909/2019/` (Publisher: Copernicus GmbH) doi: 10.5194/gmd-12-1909-2019

Wandel, A. (2018, April). On the Biohabitability of M-dwarf Planets. *The Astrophysical Journal*, *856*(2), 165. Retrieved 2020-10-30, from `https://doi.org/10.3847%2F1538-4357%2Faaae6e` (Publisher: American Astronomical Society) doi: 10.3847/1538-4357/aaae6e

Wang, J., Mawet, D., Ruane, G., Delorme, J.-R., Klimovich, N. S., & Hu, R. (2017, September). Baseline requirements for detecting biosignatures with the HabEx and LUVOIR mission concepts. In S. Shaklan (Ed.), (p. Art. No. 104000Z). Bellingham, WA: Society of Photo-Optical Instrumentation Engineers. Retrieved 2023-05-16, from `https://resolver.caltech.edu/CaltechAUTHORS:20180216-134344780` (Conference Name: Techniques and Instrumentation for Detection of Exoplanets VIII Issue: 10400 Meeting Name: Techniques and Instrumentation for Detection of Exoplanets VIII Number: 10400)

Wang, S., & Yang, J. (2021, January). Phase Shift of Planetary Waves and Wave–Jet Resonance on Tidally Locked Planets. *The Astrophysical Journal*, *907*(1), 28. Retrieved 2023-02-17, from `https://dx.doi.org/10.3847/1538-4357/abcf2a` (Publisher: The American Astronomical Society) doi: 10.3847/1538-4357/abcf2a

Wang, T., Zhang, Q., Hannachi, A., Hirooka, T., & Hegglin, M. I. (2020). Tropical water vapour in the lower stratosphere and its relationship to tropical/extratropical dynamical processes in ERA5. *Quarterly Journal of the Royal Meteorological Society*, *146*(730), 2432–2449. Retrieved 2021-09-10, from `https://rmets.onlinelibrary.wiley.com/doi/abs/10.1002/qj.3801` (_eprint: https://rmets.onlinelibrary.wiley.com/doi/pdf/10.1002/qj.3801) doi: 10.1002/qj.3801

Wardenier, J. P., Parmentier, V., & Lee, E. K. H. (2022, February). All along the line of sight: a closer look at opening angles and absorption regions in the atmospheres of transiting exoplanets. *Monthly Notices of the Royal Astronomical Society*, *510*(1), 620–629. Retrieved 2023-05-16, from `https://doi.org/10.1093/mnras/stab3432` doi: 10.1093/mnras/stab3432

Warner, C. D., & McIntyre, M. E. (1996, November). On the Propagation and Dissipation of Gravity Wave Spectra through a Realistic Middle Atmosphere. *Journal of the Atmospheric Sciences*, *53*(22), 3213–3235. Retrieved 2021-09-22, from `https://journals.ametsoc.org/view/journals/atsc/53/22/1520-0469_1996_053_3213_otpado_2_0_co_2.xml` (Publisher: American Meteorological Society Section: Journal of the Atmospheric Sciences) doi: 10.1175/1520-0469(1996)053<3213:OTPADO>2.0.CO;2

Warner, C. D., & McIntyre, M. E. (2001, July). An Ultrasimple Spectral Parameterization for Nonorographic Gravity Waves. *Journal of the Atmospheric Sciences*, *58*(14), 1837–1857. Retrieved 2021-09-22, from `https://journals.ametsoc.org/view/journals/atsc/58/14/1520-0469_2001_058_1837_auspfn_2.0.co_2.xml` (Publisher: American Meteorological Society Section: Journal of the Atmospheric Sciences) doi: 10.1175/1520-0469(2001)058<1837:AUSPFN>2.0.CO;2

Watkins, C., & Cho, J. Y.-K. (2010, May). Gravity Waves on Hot Extrasolar Planets: I. Propagation and Interaction with the Background. *The Astrophysical Journal*, *714*(1), 904–914. Retrieved 2021-07-12, from `http://arxiv.org/abs/1003.4818` (arXiv: 1003.4818) doi: 10.1088/0004-637X/714/1/904

Welbanks, L., & Madhusudhan, N. (2022, July). On Atmospheric Retrievals of Exoplanets with Inhomogeneous Terminators. *The Astrophysical Journal*, *933*(1), 79. Retrieved 2022-11-17, from `https://dx.doi.org/10.3847/1538-4357/ac6df1` (Publisher: The American Astronomical Society) doi: 10.3847/1538-4357/ac6df1

Williams, P. K. G., Charbonneau, D., Cooper, C. S., Showman, A. P., & Fortney, J. J. (2006, October). Resolving the Surfaces of Extrasolar Planets with Secondary Eclipse Light Curves. *The Astrophysical Journal*, *649*(2), 1020. Retrieved 2023-08-08, from `https://iopscience.iop.org/article/10.1086/506468/meta` (Publisher: IOP Publishing) doi: 10.1086/506468

Wilson, D. R., Bushell, A. C., Kerr-Munslow, A. M., Price, J. D., & Morcrette, C. J. (2008). PC2: A prognostic cloud fraction and condensation scheme. I: Scheme description. *Quarterly Journal of the Royal Meteorological Society*, *134*(637), 2093–2107. Retrieved 2022-08-03, from `https://onlinelibrary.wiley.com/doi/abs/10.1002/qj.333` (_eprint: https://onlinelibrary.wiley.com/doi/pdf/10.1002/qj.333) doi: 10.1002/qj.333

Wiscombe, W. J. (1980, May). Improved Mie scattering algorithms. *Applied Optics*, *19*(9), 1505–1509. Retrieved 2023-09-15, from `https://opg.optica.org/ao/abstract.cfm?uri=ao-19-9-1505` (Publisher: Optica Publishing Group) doi: 10.1364/AO.19.001505

Wolf, E. T. (2017, April). Assessing the Habitability of the TRAPPIST-1 System Using a 3D Climate Model. *The Astrophysical Journal*, *839*(1), L1. Retrieved 2020-10-01, from `https://doi.org/10.3847%2F2041-8213%2Faa693a` (Publisher: American Astronomical Society) doi: 10.3847/2041-8213/aa693a

Wolf, E. T., Kopparapu, R., Haqq-Misra, J., & Fauchez, T. J. (2022, January). ExoCAM: A 3D Climate Model for Exoplanet Atmospheres. *The Planetary Science Journal*, *3*(1), 7. Retrieved 2022-11-17, from `https://iopscience.iop.org/article/10.3847/PSJ/ac3f3d/meta` (Publisher: IOP Publishing) doi: 10.3847/PSJ/ac3f3d

Wolf, E. T., & Toon, O. B. (2010, June). Fractal Organic Hazes Provided an Ultraviolet Shield for Early Earth. *Science*, *328*, 1266. Retrieved 2022-01-25, from `https://ui.adsabs.harvard.edu/abs/2010Sci...328.1266W` (ADS Bibcode: 2010Sci...328.1266W) doi: 10.1126/science.1183260

Wolszczan, A., & Frail, D. A. (1992, January). A planetary system around the millisecond pulsar PSR1257 + 12. *Nature*, *355*(6356), 145–147. Retrieved 2021-06-06, from `https://www.nature.com/articles/355145a0` (Number: 6356 Publisher: Nature Publishing Group) doi: 10.1038/355145a0

Wong, I., Shporer, A., Zhou, G., Kitzmann, D., Komacek, T. D., Tan, X., … Villaseñor, J. N. (2021, November). TOI-2109: An Ultrahot Gas Giant on a 16 hr Orbit. *The Astronomical Journal*, *162*(6), 256. Retrieved 2022-01-17, from `https://doi.org/10.3847/1538-3881/ac26bd` (Publisher: American Astronomical Society) doi: 10.3847/1538-3881/ac26bd

Wood, N., Staniforth, A., White, A., Allen, T., Diamantakis, M., Gross, M., … Thuburn, J. (2014). An inherently mass-conserving semi-implicit semi-Lagrangian discretization of the deep-atmosphere global non-hydrostatic equations. *Quarterly Journal of the Royal Meteorological Society*, *140*(682), 1505–1520. Retrieved 2022-10-12, from `https://onlinelibrary.wiley.com/doi/abs/10.1002/qj.2235` (_eprint: https://onlinelibrary.wiley.com/doi/pdf/10.1002/qj.2235) doi: 10.1002/qj.2235

Wordsworth, R. (2015, June). Atmospheric heat redistribution and collapse on tidally locked rocky planets. *The Astrophysical Journal*, *806*(2), 180. Retrieved 2021-05-11, from `https://doi.org/10.1088/0004-637x/806/2/180` (Publisher: American Astronomical Society) doi: 10.1088/0004-637X/806/2/180

Wordsworth, R. (2021, May). How Likely Are Snowball Episodes Near the Inner Edge of the Habitable Zone? *The Astrophysical Journal Letters*, *912*(1), L14. Retrieved 2023-05-12, from `https://dx.doi.org/10.3847/2041-8213/abf7c7` (Publisher: The American Astronomical Society) doi: 10.3847/2041-8213/abf7c7

Wright, D. J., Wittenmyer, R. A., Tinney, C. G., Bentley, J. S., & Zhao, J. (2016, January). THREE PLANETS ORBITING WOLF 1061. *The Astrophysical Journal Letters*, *817*(2), L20. Retrieved 2023-06-06, from `https://dx.doi.org/10.3847/2041-8205/817/2/L20` (Publisher: The American Astronomical Society) doi: 10.3847/2041-8205/817/2/L20

Wyttenbach, A., Ehrenreich, D., Lovis, C., Udry, S., & Pepe, F. (2015, May). Spectrally resolved detection of sodium in the atmosphere of HD 189733b with the HARPS spectrograph. *Astronomy & Astrophysics*, *577*, A62. Retrieved 2021-05-13, from `http://www.aanda.org/10.1051/0004-6361/201525729` doi: 10.1051/0004-6361/201525729

Yang, J., Boué, G., Fabrycky, D. C., & Abbot, D. S. (2014, April). Strong dependence of the inner edge of the habitable zone on planetary rotation rate. *The Astrophysical Journal*, *787*(1), L2. Retrieved 2020-10-05, from `https://doi.org/10.1088%2F2041-8205%2F787%2F1%2Fl2` (Publisher: IOP Publishing) doi: 10.1088/2041-8205/787/1/L2

Yang, J., Cowan, N. B., & Abbot, D. S. (2013, June). Stabilizing cloud feedback dramatically expands the habitable zone of tidally locked planets. *The Astrophysical Journal*, *771*(2), L45. Retrieved 2020-10-05, from `https://doi.org/10.1088%2F2041-8205%2F771%2F2%2Fl45` (Publisher: IOP Publishing) doi: 10.1088/2041-8205/771/2/L45

Yang, J.-Y., Xie, J.-W., & Zhou, J.-L. (2020, March). Occurrence and Architecture of Kepler Planetary Systems as Functions of Stellar Mass and Effective Temperature. *The Astronomical Journal*, *159*(4), 164. Retrieved 2021-05-10, from `http://arxiv.org/abs/2002.02840` (arXiv: 2002.02840) doi: 10.3847/1538-3881/ab7373

Yates, J. S., Palmer, P. I., Manners, J., Boutle, I., Kohary, K., Mayne, N., & Abraham, L. (2020, February). Ozone chemistry on tidally locked M dwarf planets. *Monthly Notices of the Royal Astronomical Society*, *492*(2), 1691–1705. Retrieved 2023-03-21, from `https://doi.org/10.1093/mnras/stz3520` doi: 10.1093/mnras/stz3520

Zamyatina, M., Hébrard, E., Drummond, B., Mayne, N. J., Manners, J., Christie, D. A., … Kohary, K. (2023, February). Observability of signatures of transport-induced chemistry in clear atmospheres of hot gas giant exoplanets. *Monthly Notices of the Royal Astronomical Society*, *519*(2), 3129–3153. Retrieved 2023-03-20, from `https://doi.org/10.1093/mnras/stac3432` doi: 10.1093/mnras/stac3432

Zechmeister, M., Dreizler, S., Ribas, I., Reiners, A., Caballero, J. A., Bauer, F. F., … Osorio, M. R. Z. (2019, July). The CARMENES search for exoplanets around M dwarfs - Two temperate Earth-mass planet candidates around Teegarden's Star. *Astronomy & Astrophysics*, *627*, A49. Retrieved 2023-10-02, from `https://www.aanda.org/articles/aa/abs/2019/07/aa35460-19/aa35460-19.html` (Publisher: EDP Sciences) doi: 10.1051/0004-6361/201935460

Zhang, C. (2005). Madden-Julian Oscillation. *Reviews of Geophysics*, *43*(2). Retrieved 2022-08-08, from `https://onlinelibrary.wiley.com/doi/abs/10.1029/2004RG000158` (_eprint: https://onlinelibrary.wiley.com/doi/pdf/10.1029/2004RG000158) doi: 10.1029/2004RG000158

Zhang, C., Adames, A. F., Khouider, B., Wang, B., & Yang, D. (2020). Four Theories of the Madden-Julian Oscillation. *Reviews of Geophysics*, *58*(3), e2019RG000685. Retrieved 2022-08-08, from `https://onlinelibrary.wiley.com/doi/abs/10.1029/2019RG000685` (_eprint: https://onlinelibrary.wiley.com/doi/pdf/10.1029/2019RG000685) doi: 10.1029/2019RG000685

Zhang, F., Koch, S. E., Davis, C. A., & Kaplan, M. L. (2000, June). A survey of unbalanced flow diagnostics and their application. *Advances in Atmospheric Sciences*, *17*(2), 165–183. Retrieved 2021-07-08, from `http://link.springer.com/10.1007/s00376-000-0001-1` doi: 10.1007/s00376-000-0001-1

Zieba, S., Kreidberg, L., Ducrot, E., Gillon, M., Morley, C., Schaefer, L., … Suissa, G. (2023, August). No thick carbon dioxide atmosphere on the rocky exoplanet TRAPPIST-1 c. *Nature*, *620*(7975), 746–749. Retrieved 2023-10-02, from `https://www.nature.com/articles/s41586-023-06232-z` (Number: 7975 Publisher: Nature Publishing Group) doi: 10.1038/s41586-023-06232-z